

**MATERIALS INTEGRATION FOR HIGH-
PERFORMANCE PHOTOVOLTAICS BY
WAFER BONDING**

Thesis by
James Michael Zahler

In Partial Fulfillment of the Requirements
for the Degree of
Doctor of Philosophy

California Institute of Technology
Pasadena, CA

2005
(Submitted April 21, 2005)

© 2005

James Michael Zahler

All Rights Reserved

Acknowledgements

No thesis is an individual endeavor, and this thesis would not have been possible without the assistance of my collaborators and advisor and would have been unendurable without the support of my coworkers, friends, and family. I apologize in advance to anyone whom I might omit in this brief acknowledgement, but it is late and I am running out of time!

In the summer of 2000, Harry Atwater agreed to allow me to transfer to his group from the chemical engineering department. I was discouraged and doubtful about my future at Caltech and in graduate school in general. Since giving me that chance he has been a great advisor with no shortage of encouragement or ideas. I am never sure if this is by design, but Harry has managed to inspire me to work hard and has given me countless ideas to pursue while always allowing me to feel that I have nearly complete freedom to pursue experiments that are interesting to me.

While in Harry's group I had the good fortune to work closely with two post-doctoral scholars, Chang-Geun Ahn and Anna Fontcuberta i Morral. Chang-Geun was extremely helpful in getting the Ge/Si bonding project going and in optical and electrical characterization experiments. Anna was tough to work with because her energy level is so darned high, but she has also been very supportive and her high energy approach to research has pushed me to work harder and faster than I might have by myself. Without Anna's hard work and encouragement, the InP/Si bonding work and the spectroscopic studies of hydrogen in InP and Ge would not have gone nearly as far as they did.

In the course of my thesis I have worked with many collaborators without whom many of the results in this thesis would have been impossible. The work began with Ge/Si bonding for triple-junction cells with funding from Tecstar, and while working with Tecstar I was assisted in solar cell growth and design by Charlie Chu and Peter Iles. Following Emcore's acquisition of Tecstar, GaAs growth was continued at Spectrolab, and the assistance of Richard King and others there is greatly appreciated. The growth of test structures on InP/Si bonded samples was performed by Mark Wanlass at the National Renewable Energy Laboratory (NREL). Optical characterization of GaAs and InGaAs on Ge/Si and InP/Si, respectively, were conducted by Richard Ahrenkiel, also from NREL. The spectroscopic studies of hydrogen in Ge and InP would not have been possible without the equipment and insight of Yves Chabal and his research group at Rutgers University. The transmission electron micrographs in this thesis were made by Carol Garland at Caltech.

In a break with tradition, I will not write a little anecdote about each Atwater Group member, but I will say that the group has been great to work with. The conversations and good times shared with them throughout my thesis have helped me maintain my sanity, and I have received advice from them more times than I can remember. They have been a wonderful group of people to work with even as students have come and gone throughout the years. In particular I have greatly enjoyed the time spent with (in alphabetical order) Julie Biteen, Rhett and Julie Brewer, Jason Holt, Brendan Kayes, Pieter Kik, Maribeth Mason, Regina Ragan, Christine Richardson, Jen Ruglovsky, Luke Sweatlock, and Robb Walters.

As with most graduate students, I have had the support of a wonderful family. Without the support, motivation, and love of my parents throughout my life many of my achievements would not have been possible – this thesis is no exception. Finally, unlike many graduate students, I have had the love and support of my wife Amy (and our new daughter Ava). We have been through many highs and lows in the last six years, most of them due to my graduate work, and we have worked through all of those challenges and come through them smiling (through gritted teeth). Thank you Amy, without your support this would have been much, much harder.

Abstract

The fundamental efficiency limit for state of the art triple-junction photovoltaic devices is being approached. By allowing integration of non-lattice-matched materials in monolithic structures, wafer bonding enables novel photovoltaic devices that have a greater number of subcells to improve the discretization of the solar spectrum, thus extending the efficiency limit of the devices. Additionally, wafer bonding enables the integration of non-lattice-matched materials with foreign substrates to confer desirable properties associated with the handle substrate on the solar cell structure, such as reduced mass, increased thermal conductivity, and improved mechanical toughness. This thesis outlines process development and characterization of wafer bonding integration technologies essential for transferring conventional triple-junction solar cell designs to potentially lower cost Ge/Si epitaxial templates. These epitaxial templates consist of a thin film of single-crystal Ge on a Si handle substrate. Additionally, a novel four-junction solar cell design consisting of non-lattice matched subcells of GaInP, GaAs, InGaAsP, and InGaAs based on InP/Si wafer-bonded epitaxial templates is proposed and InP/Si template fabrication and characterization is pursued.

In this thesis the detailed-balance theory of the thermodynamic limiting performance of solar cell efficiency is applied to several device designs enabled by wafer bonding and layer exfoliation. The application of the detailed-balance theory to the novel four-junction cell described above shows that operating under 100 suns at 300 K a maximum efficiency of 54.9% is achievable with subcell bandgaps of 1.90, 1.42, 1.02, and 0.60 eV, a material combination

achievable by integrating two wide-bandgap subcells lattice matched to GaAs and two narrow-bandgap subcells lattice matched to InP.

Wafer bonding and layer transfer processes with sufficient quality to enable subsequent material characterization are demonstrated for both Ge/Si and InP/Si structures. The H-induced exfoliation process in each of these materials is studied using TEM, AFM, and FTIR to elucidate the chemical states of hydrogen leading to exfoliation. Additionally, the electrical properties of wafer-bonded interfaces between bulk-Ge/Si and bulk-InP/Si structures are shown to exhibit Ohmic, low-resistance electrical contact. Further studies of p-p isotype heterojunctions in Ge/Si indicate that significant conduction paths exist through defects at the bonded interface. The first known instance of epitaxy of III-V compound semiconductors on wafer-bonded Ge/Si epitaxial templates is demonstrated. Additionally, InGaAs is grown on InP/Si templates that have been improved by removal of damage induced by the ion implantation and exfoliation processes.

Related Publications

The research described in this thesis has been described in several publications and submitted papers. Many of these are rather general, touching on many topics. For this reason, they are not associated with any specific chapters in the listing below.

“A detailed-balance efficiency analysis of the promise of wafer-bonding-enabled photovoltaic designs,” J.M. Zahler, A. Fontcuberta i Morral, H.A. Atwater (in process)

“Spectroscopic studies of the physical and chemical role of hydrogen in the H-induced exfoliation of Ge,” J.M. Zahler, A. Fontcuberta i Morral, H.A. Atwater, Y.J. Chabal (in process)

“Electrical properties of the Ge/Si wafer-bonded interface,” J.M. Zahler, C.-G. Ahn, A. Fontcuberta i Morral, H.A. Atwater (in process)

“Spectroscopic studies of the thermal evolution of hydrogen bonding in InP and consequences for the mechanism of hydrogen-induced exfoliation of InP,” A. Fontcuberta i Morral, J. M. Zahler, Harry A. Atwater, Y. J. Chabal, (in process)

“InGaAs/InP double heterostructures on In/Si templates fabricated by wafer bonding and hydrogen induced exfoliation of InP,” A. Fontcuberta i Morral, J. M. Zahler, S. P. Ahrenkiel, M. Wanlass, Harry. A. Atwater, *Appl. Phys. Lett.* 83 (2003), 5413.

“Wafer bonding and layer transfer processes for 4-junction high efficiency solar cells,” J.M. Zahler, A. Fontcuberta i Morral, C.-G. Ahn, H.A. Atwater, M.W. Wanlass, C.Chu, P.A. Iles, *29th. IEEE Photovoltaic Specialists Conference*. New Orleans, LA, May 2002.

“Ge layer transfer to Si for photovoltaic applications,” J.M. Zahler, C.-G. Ahn, S. Zaghi, H.A. Atwater, C. Chu, P. Iles, *Thin Solid Films*, 403-404 (2002), p.558-562.

Contents

Acknowledgements	iii
Abstract	v
Related Publications	vii
Contents	ix
List of Figures.....	xvii
List of Tables	xxxv
Chapter 1: Introduction.....	1
1.1 Photovoltaic Devices	1
1.1.1 Photovoltaics as a Critical Step toward a Sustainable Energy Economy.....	1
1.1.2 A Performance and Economic History of Photovoltaic Devices.....	4
1.1.3 Photovoltaic Operating Principle.....	6
1.1.4 Fundamental and Practical Limits to Photovoltaic Efficiency.....	7
1.1.4.1 Fundamental Limits to Photovoltaic Efficiency	7
1.1.4.2 Practical Limitations to Photovoltaic Efficiency	9
1.1.4.3 Solar Cell Designs for Improved Limiting Efficiency	9
1.2 Materials Integration.....	12
1.2.1 Traditional Epitaxial Strategies.....	12

1.2.1.1	Fundamental Limits of Heteroepitaxy	13
1.2.1.2	Heteroepitaxial Ge/Si Integration	14
1.2.1.3	Heteroepitaxial III-V/Si Integration.....	15
1.2.1.3.1	Polar on Non-Polar Heteroepitaxy	15
1.2.1.3.2	Heteroepitaxial GaAs/Si and InP/Si Integration.....	16
1.2.2	Materials Integration by Wafer Bonding and Layer Transfer.....	17
1.2.2.1	General Principle of Wafer Bonding.....	18
1.2.2.2	Processes for Layer Thinning.....	18
1.3	Application of Materials Integration by Wafer Bonding and Layer Transfer to Photovoltaics	20
1.3.1	Ge/Si Wafer Bonded Substrates for Dual- and Triple-Junction Solar Cells	20
1.3.2	InP/Si Wafer Bonded Substrates for a Proposed Four-Junction Solar Cell	23
1.3.3	Photovoltaic Device Requirements for Virtual Substrates Fabricated by Wafer Bonding and Layer Transfer	26
1.4	Organization of Thesis.....	27
1.5	References	30
Chapter 2: Detailed Balance Calculation of the Thermodynamic Limiting Efficiency of Wafer-Bonding Enabled Solar Cells		35
2.1	The Detailed-Balance Theory of Photovoltaic Efficiency.....	35
2.1.1	Formulation of the Detailed-Balance Theory for a Single-Junction Solar Cell...	36
2.1.2	Detailed-Balance Efficiency Calculation for a Single-Junction Solar Cell	39
2.2	Detailed-Balance Efficiency of Multi-Junction Solar Cell Structures.....	46
2.2.1	Multi-Junction Solar Cell Electrical Connectivity.....	49
2.2.2	Detailed-Balance Efficiency Formulation for Tandem, Multi-Junction Solar Cells	50

2.2.3	Detailed-Balance Efficiency Calculation of Tandem, Dual- and Triple-Junction Solar Cells.....	52
2.3	Detailed-Balance Efficiency Calculation of Wafer-Bonded, Multi-Junction Solar Cells	56
2.3.1	Detailed-Balance Efficiency Calculation of a Triple-Junction Wafer-Bonded Solar Cell Fabricated on an Active Si Subcell.....	57
2.3.1	Detailed-Balance Efficiency Calculation of a Four-Junction Wafer-Bonded Solar Cell.....	62
2.3.2.1	Detailed-Balance Efficiency Calculation of an Ideal Wafer-Bonded Four-Junction Solar Cell.....	64
2.3.2.2	Detailed-Balance Efficiency Calculation of a Wafer-Bonded Four-Junction GaInP/GaAs/InGaAsP/InGaAs Solar Cell.....	65
2.3.2.3	Detailed-Balance Efficiency Calculation of a Wafer-Bonded Four-Junction GaInP/GaAs/Si/Ge Solar Cell.....	67
2.3.3	Detailed-Balance Efficiency Calculation of a Five-Junction, Independently-Connected Solar Cell Enabled by Wafer Bonding	70
2.4	Summary.....	72
2.5	References	75
Chapter 3: Materials Integration by Wafer Bonding and Layer Transfer		77
3.1	Challenges of Wafer Bonding and Layer Transfer.....	77
3.1.1	Surface Activation	78
3.1.2	Surface Morphology: Particles and Surface Roughness	80
3.1.3	Layer Thinning	83
3.1.4	Thermal Processing Issues for Wafer Bonding Integration of Dissimilar Materials	85

3.1.4.1	Coefficients of Thermal Expansion the Group IV and III-V Semiconductors of Interest.....	85
3.1.4.2	Thermally-Induced Stress in Bulk-Bonded Structures.....	85
3.1.4.3	Stress and Substrate Morphology during Thermal Processing of Thin-Film Wafer-Bonded Heterostructures.....	89
3.1.4.3.1	Substrate Shape during MOCVD	90
3.1.4.3.2	Substrate Deformation and Stress Following Photovoltaic Device Growth.....	92
3.1.4.3.3	Photovoltaic Device Film Stability in Operation from 200 to 400 K	94
3.2	Wafer Bonding Process and Results.....	94
3.2.1	Generalized Wafer Bonding Process for Ge/Si and InP/Si Wafer Bonding	95
3.2.2	Ge/Si Wafer Bonding Process and Results	98
3.2.2.1	AFM Characterization of Wafer Bonded Heterostructures.....	102
3.2.2	InP/Si Wafer Bonding Process and Results	106
3.2.2.1	AFM Characterization of Wafer Bonded Heterostructures.....	107
3.3	Summary.....	107
3.4	References	110
Chapter 4: The Role of H in the H-induced Layer Exfoliation of Ge and InP		115
4.1	H-Induced Exfoliation of Ge	116
4.1.1	Summary of the Qualitative Model for the H-induced Exfoliation of Si.....	116
4.1.2	Experimental Procedure.....	117
4.1.3	Results and Interpretation	122
4.1.3.1	Transmission Electron Microscopy.....	122

4.1.3.2	Atomic Force Microscopy	127
4.1.3.3	Infrared Spectroscopy	128
4.1.3.3.1	Identification of Discrete Defect Modes at Low Temperature.....	129
4.1.3.3.2	Spectral Evolution of the Sub-Critical 2×10^{16} cm ⁻² Dose	134
4.1.3.3.3	Spectral Evolution of the Low-Temperature Blistering 1×10^{17} cm ⁻² Dose.....	136
4.1.3.3.4	Spectral Evolution of the Retarded-Blistering 5×10^{16} cm ⁻² Dose ...	140
4.1.4	Discussion.....	143
4.1.4.1	Comparison to Previous Work.....	143
4.1.4.1.1	Stein et al. H-implanted Ge	143
4.1.4.1.2	Weldon et al. Study of H-induced Si Exfoliation.....	146
4.1.4.1.3	Summary of Comparison to Previous Work	146
4.1.4.2	Comparison of Blistering and Non-blistering Implant Conditions	147
4.1.4.2.1	Identification of Surface Modes Following Film Exfoliation	148
4.1.4.2.2	Identification of Internal Surface Modes Prior to Exfoliation.....	152
4.1.4.2.3	Comparison of Exfoliation Precursor Modes from 2000 to 2050 cm ⁻¹	156
4.1.4.2.4	Summary of Comparison of Blistering and Non-blistering Implant Conditions	159
4.1.5	Conclusions.....	160
4.2	H-induced Exfoliation of InP	161
4.2.1	An Introduction to Hydrogen in H-implanted InP	161
4.2.1	Experimental Procedure.....	163
4.2.2	Results and Interpretation	165
4.2.2.1	Transmission Electron Microscopy.....	165
4.2.2.3	Infrared Spectroscopy	166

4.2.3	Discussion.....	171
4.2.4	Conclusions.....	179
4.3	Summary.....	180
4.4	References	182
Chapter 5: Electrical Properties of Wafer-Bonded Interfaces		185
5.1	Electrical Properties of Heavily-Doped Wafer-Bonded Interfaces	186
5.1.1	Schemes for Enabling Low-Resistance Bonded Interfaces	186
5.1.2	Heavily Doped Ge/Si Wafer-Bonded Heterostructures	189
5.1.2.1	Experimental Procedure	189
5.1.2.2	Results and Analysis	190
5.1.2.3	Discussion	190
5.1.3	Heavily Doped InP/Si Wafer-Bonded Heterostructures	195
5.1.3.1	Experimental Procedure	195
5.1.3.2	Results and Analysis	197
5.1.3.2.1	Current-Voltage Data	197
5.1.3.2.2	Infrared Spectroscopy	198
5.1.3.2.3	Transmission Electron Microscopy	198
5.1.3.3	Discussion	200
5.1.4	Conclusions.....	201
5.2	Electrical Properties of Wafer-Bonded p ⁺ -Ge/p-Si Isotype Heterostructures.....	202
5.2.1	Experimental Procedure.....	203
5.2.2	Results and Analysis.....	204
5.2.2.1	Anticipated Energy Band Diagram for Wafer-Bonded p ⁺ -Ge/p-Si Heterostructures	204
5.2.2.2	p ⁺ -Ge/p-Si Wafer-Bonded Heterostructure Current-Voltage Data	204

5.2.2.3	Current-Voltage Model for a Leaky Shottky-Diode-Like Heterojunction	207
5.2.3	Discussion	212
5.2.3.1	Anneal-Dependent Evolution of the Electrical Properties of the Wafer-Bonded Interface	212
5.2.3.1.1	Electrical Properties of the As-Bonded p^+ -Ge/p-Si Heterostructure	213
5.2.3.1.2	Evolution of the Bonded Interface upon Annealing	217
5.2.3.2	Twist-Dependent Electrical Properties of the Wafer-Bonded Interface	220
5.2.3.3	Comparison of Present Results to Theoretical and Experimental Results in the Literature	223
5.2.4	Conclusions	225
5.3	Summary	226
5.4	References	228
Chapter 6: Demonstration of Epitaxial Growth on Wafer-Bonded Templates		231
6.1	Epitaxy on Ge/Si Heterostructures	231
6.1.1	Growth Surface	231
6.1.2	Epitaxially Grown Structures	234
6.1.2.1	Triple-Junction Solar Cell Structures	234
6.1.2.2	Ge Homoepitaxy	238
6.1.3	Conclusions	241
6.2	Epitaxy on InP/Si Heterostructures	242
6.2.1	Growth Surface	243
6.2.1.1	As-Transferred InP/Si Surface	243
6.2.1.2	Surface Modification for Epitaxy	243

6.2.2	Epitaxial Growth of InGaAs Double-Heterostructures.....	245
6.2.3	Conclusions.....	249
6.3	Summary.....	249
6.4	References	250
Appendix:	MatLab Code for Detailed Balance Calculation	261

List of Figures

Chapter 1

- Figure 1.1** Production forecast of all hydrocarbons indicating that peak total hydrocarbon production will occur near the year 2015. 2
- Figure 1.2** Historical milestones in peak solar cell efficiency, showing the efficiency records and their holders as a by technology type. Note the rapid increase in efficiency for single-crystal silicon and III-V compound semiconductor multi-junction solar cells. 5
- Figure 1.3** The learning curve relating cost per watt of installed power to the cumulative production volume of the photovoltaic industry. 6
- Figure 1.4** Fundamental loss mechanisms in a photovoltaic device illustrating loss of power due to sub-bandgap photons and thermalization of excess photon energy along with absorption of a photon with energy E_G resulting in a band-to-band absorption event and thus no loss of power. The plot on the left illustrates the photon flux as a function of photon energy for actual solar spectra as well as for black body radiation. 8
- Figure 1.5** Bandgap energy as a function of lattice constant for common III-V semiconductors suitable for photovoltaic applications illustrating the limitations due to the interdependence of these two critical parameters. 12

Figure 1.6	Schematic of a two- or three-junction solar cell fabricated on a Ge/Si wafer bonded virtual substrate. In the three-junction cell the Ge transferred layer is p-type and grown to a sufficient thickness to serve as an active layer of the cell structure, while in the two-junction cell the Ge transferred layer is thin and n-type, serving only as an epitaxial template for the growth of the GaAs and GaInP subcell structures.....	23
Figure 1.7	Schematic of a proposed four-junction wafer bonding enabled solar cell fabricated on a InP/Si wafer bonded virtual substrate with a wafer bonded heteroepitaxial template of Ge (or GaAs) integrated with the bottom two subcell structure by wafer bonding and layer transfer.	26

Chapter 2

Figure 2.1	The AM1.5 solar spectrum used in the calculation of the detailed balance efficiency.	38
Figure 2.2	The detailed balance efficiency as a function of temperature for one-sun AM1.5 illumination for (a) a thin-film single-junction solar cell on a thick semiconductor substrate, (b) a thin-film single-junction solar cell on a low-index substrate, and (c) a thin-film single-junction solar cell on a reflective surface.	43
Figure 2.3	The detailed balance fill factor as a function of temperature for a concentration of 1 sun for (a) a thin-film single-junction solar cell on a thick semiconductor substrate, (b) a thin-film single-junction solar cell on a low-index substrate, and (c) a thin-film single-junction solar cell on a reflective surface.	44
Figure 2.4	The detailed balance efficiency as a function of solar concentration for a temperature of 300 K for (a) a thin-film single-junction solar cell on a thick	

semiconductor substrate, **(b)** a thin-film single-junction solar cell on a low-index substrate, and **(c)** a thin-film single-junction solar cell on a reflective surface. .. 45

Figure 2.5 The detailed-balance fill-factor as a function of solar concentration for a temperature of 300 K for **(a)** a thin-film single-junction solar cell on a thick semiconductor substrate, **(b)** a thin-film single-junction solar cell on a low-index substrate, and **(c)** a thin-film single-junction solar cell on a reflective surface. .. 47

Figure 2.6 **(a)** Iso-efficiency curve for a two-junction parallel connected solar cell operated at 300 K and 100 suns concentration as a function of the top and bottom subcell bandgaps (E_1 and E_2 respectively). **(b)** Iso-efficiency curve for a two-junction series connected solar cell operated at 300 K and 100 suns concentration. The maximum efficiency for a single junction solar cell operating on a thick substrate in these conditions is marked by the dashed line. 53

Figure 2.7 **(a)** Iso-efficiency curve for a three-junction parallel connected solar cell operated at 300 K and 100 suns concentration as a function of the top and middle subcell bandgaps (E_1 and E_2 respectively) operating on a bottom subcell with the Ge bandgap of 0.67 eV. **(b)** Iso-efficiency curve for a two-junction series connected solar cell operated at 300 K and 100 suns concentration. The maximum efficiency for a single junction solar cell operating on a thick substrate in these conditions is marked by the dashed line. 54

Figure 2.8 The iso-efficiency plot for the variation of the top two subcell band gaps in a triple-junction solar cell fabricated on a wafer bonded Ge/Si substrate with an active Si subcell operated under 100 sun AM1.5 illumination at 300 K. The dashed line at $\eta = 0.476$ represents the limiting efficiency for an optimal dual-junction solar cell operated under the same conditions. 58

- Figure 2.9** (a) Iso-efficiency curve for a three-junction series-connected wafer-bonded solar cell operated at 300 K under one sun AM0 illumination as a function of the top and middle subcell bandgaps (E_1 and E_2 respectively) operating on a bottom subcell with the Si band gap of 1.12 eV. (b) Iso-efficiency curve for a three-junction series-connected solar cell operated under the same conditions with a Ge bottom subcell band gap of 0.67 eV. 60
- Figure 2.10** Iso-efficiency plots for a three-junction series-connected solar cell with a Ge bottom subcell (0.67 eV bandgap) operated under AM0 1 sun concentration at (a) 200 K, (b) 300 K and (c) 400 K, and iso-efficiency plots for the same cell geometry and operating conditions consisting of a Si bottom subcell (1.12 eV bandgap) operated at (d) 200 K, (e) 300 K and (f) 400 K..... 61
- Figure 2.11** Efficiency curves as a function of top subcell bandgap for a three junction solar cell with a 1.42 eV center subcell with either Ge or Si bottom subcells operated at various temperatures under a 1 sun AM0 illumination..... 62
- Figure 2.12** Variation of efficiency of an optimal 100 sun AM1.5 series-connected four-junction solar cell with changes of each subcell bandgap. Each cell is subcell is varied independently maintaining the other subcells at their optimum bandgap of 2.00, 1.49, 1.12, and 0.72 eV respectively..... 65
- Figure 2.13** The iso-efficiency plot for the variation of the bottom two subcell bandgaps in a four-junction solar cell operated under 100 sun AM1.5 illumination at 300 K... 67
- Figure 2.14** Schematic of a four-junction solar cell fabricated by bonding and transferring a GaAs epitaxial template to an active Si subcell and subsequently growing an AlGaInP/InGaAsP tandem structure via MOCVD. Following growth, a bonding process is used to integrate a thin Ge subcell to the back surface of the structure..... 68

- Figure 2.15** The iso-efficiency plot for the variation of the top two subcell bandgaps in a four-junction solar cell operated under 100 sun AM1.5 illumination at 300 K. The bottom two subcells consist of an active Si support substrate and a Ge subcell wafer bonded to the back surface of the structure. The band gaps are 1.12 and 0.67 eV respectively. The two dashed lines at 46.3% and 51.2% efficiency mark the predicted efficiencies of a GaInP/GaAs/Ge triple-junction cell and a band gap optimized triple-junction cell with an active Si subcell, respectively..... 69
- Figure 2.16** Efficiency variation of an optimal 100 sun AM1.5 parallel-connected five-junction solar cell with independent variation of each subcell band gap from its optimum bandgap of 2.50, 1.93, 1.53, 1.13 and 0.70 eV, respectively..... 71

Chapter 3

- Figure 3.1** Particle-induced void radius as a function of the particle radius, h , and the bond energy, γ , for a 300 μm Ge substrate wafer bonded to a 200 μm Si substrate. The white region is for particles below the critical radius, causing the particle-induced void to be approximately the same radius as the particle itself, and thus tolerable for most applications..... 82
- Figure 3.2** The model-predicted effect of surface roughness and asperity geometry on the bondability of Ge/Si substrates. The three surface adhesion energies, w , displayed correspond to H-passivated (10 mJ m^{-2}), oxide passivated(100 mJ m^{-2}), and plasma treated (500 mJ m^{-2}), bonding surfaces..... 84
- Figure 3.3** The coefficient of thermal expansion for Si, Ge, GaAs and InP over the range of interest for wafer bonding, fabrication, and operation of wafer-bonded multi-junction solar cells. The data points labeled fit are estimated either using a reported model for α as is the case for the high temperature data reported for Ge,

or the data is extracted from reported data on the lattice parameter by fitting the lattice parameter over the range and taking the derivative of the fitting function, as is the case for InP. 86

Figure 3.4 Calculated radius of curvature for a Ge/Si and an InP/Si with a 300 μm thick device substrate and a 140 μm thick Si handle substrate. The radius of curvature goes to infinity as the bond temperature approaches the process temperature. ... 88

Figure 3.5 Calculated elastic strain energy for Ge/Si and an InP/Si bulk-bonded substrates with a 300 μm thick device substrate and a 140 μm thick Si handle substrate under thermal processing. 89

Figure 3.6 Predicted wafer bow for 100 mm virtual substrates consisting of a 140 μm thick substrate suitable for space photovoltaic systems with a 0.5 μm thick device film. The vertical dashed lines mark the boundaries on the temperature ranges of interest for device growth by MOCVD at temperatures above 850 K and operation of the solar cell device structure in a space power system below 400 K. 92

Figure 3.7 Predicted substrate bow for a 6 μm GaAs-like multi-junction solar cell on a 0.5 μm Ge film on a 140 μm Si substrate. The impact of the bond temperature and cell growth temperature are illustrated. The dashed lines indicate that the model predicts the bow beyond the critical stress for substrate shape bifurcation. 93

Figure 3.8 Wafer bonding apparatus designed to exert uni-axial, pressure through the application of a controlled torque, to the lead screw at the top of the bonder during anneals up to 350°C. 97

Figure 3.9 Generalized process for the fabrication of wafer-bonded alternative substrates showing: 1. H-implantation of the device substrate; 2. surface cleaning and

- passivation; 3. bond initiation; 4. film exfoliation by annealing; and, 5. removal of implant damage and exfoliation-induced surface roughness..... 98
- Figure 3.10** (a) Hydrophilically wafer bonded Ge/Si structures fabricated by wet chemical passivation followed by ozone cleaning prior to bonding. (b) Typical trapped gas microstructure for hydrophobically and hydrophilically wafer bonded Ge/Si structures. (c) A Ge/Si wafer bonded structure formed by hydrophilically wafer bonding – as described in (a) – Ge to a Si sample with a recessed grid pattern lithographically defined. This enables the release of trapped and evolved gas at the bonded interface. (d) Optical microscopy view of a grid-bonded sample as described in (c) showing the large, defect-free field of Ge between the grid lines and regions of Ge over the grid lines that have formed bubbles either through trapped gas or thermally-induced buckling..... 99
- Figure 3.11** A 100 mm Ge/Si wafer bonded and layer transferred structure fabricated by use of plasma activation and annealing. The pin-holes are caused by blisters and untransferred regions of Ge. The important result is that through the use of improved surface cleaning and activation along with better tooling, substantial advancements can be made in the fraction and quality of transferred material. 102
- Figure 3.12** An AFM scan of an as-transferred Ge/Si surface with a roughness of ~10 nm. The sample was made by transferring a film from an on-axis (100)Ge substrate to a Si handle wafer..... 103
- Figure 3.13** Measured surface roughness for Ge/Si films transferred from bulk Ge substrates with 9° and 15° miscut angles as a function of the AFM measurement area. The individual data points represent different samples. The error bars are defined as ±one standard deviation based on three measurements. 104
- Figure 3.14** (a) A schematic representation of the distribution of micro-cracks that ripn during the H-induced exfoliation of an on-axis (100) semiconductor. (b) A

	schematic of the same distribution of micro-cracks in a H-implanted semiconductor substrate miscut by an angle θ	105
Figure 3.15	InP/Si wafer bonded structure formed by wet chemical passivation of the bonding surfaces.	106
Figure 3.16	50 mm InP/Si wafer bonded structures fabricated by use of plasma activation and annealing showing: (a) the presence of particle-induced voids; (b) a void-free InP/Si bonded structure achieved by superior particle removal prior to bonding; and, (c) the use of the crack-opening method to estimate the bond strength of a given plasma condition by the insertion of a 50 μm thick blade between the bonded substrates.	108
 Chapter 4		
Figure 4.1	(a) MIT-FTIR sample holder showing the sample location and configuration of the incoming IR beam and the beam path to the detector. (b) A schematic of the sample geometry for the MIT-FTIR sampling system showing the orientation of the s- and p-polarization directions and their contribution parallel (x- and y-axis) and perpendicular (z-axis) fields in the sample.	118
Figure 4.2	Sensitivity factor for radiation in an MIT-FTIR geometry sample as a function of the normalized distance of the layer from the outer surface, d/λ . [Chabal]	121
Figure 4.3	TRIM simulation of the H implantation profile (a) and the damage distribution (b) in the near surface region of a Ge substrate implanted at an angle of 7° with H^+ at 80 keV.....	123
Figure 4.4	(a) Cross-sectional TEM image of Ge as-implanted with 80 keV H^+ to a dose of $1 \times 10^{17} \text{ cm}^{-2}$ on a gas cooled stage revealing the broad damage distribution structure of Ge implanted under these conditions. (b) High-resolution image of	

	the heavily damaged region near the peak range of the implant showing a large concentration of (100) platelet defect structures and a smaller concentration of (111) platelets.	124
Figure 4.5	(a) Cross-sectional TEM image of Ge implanted with 80 keV H ⁺ to a dose of 1x10 ¹⁷ cm ⁻² without active cooling following an anneal to 250°C for 10 minutes. (b) High-resolution of the nano-crack region under the same conditions presence of (100) and (111) hydrogen platelets and nano-cracks just beginning to form in the material.	126
Figure 4.6	High-resolution cross-sectional TEM image of Ge implanted with 80 keV H ⁺ to a dose of 1x10 ¹⁷ cm ⁻² without active cooling following an anneal to 250°C for 10 minutes under close magnification showing the coalescence of nanocracks into microcracks that eventually lead to exfoliation.	127
Figure 4.7	(a) Contact-mode AFM image of an H-implanted Ge surface following an anneal to 250°C for 10 min. for an 80 keV H ⁺ dose of 1x10 ¹⁷ cm ⁻² without active cooling. (b) Contact-mode AFM image of the same surface following an anneal to 300°C for 10 min.	129
Figure 4.8	MIT-FTIR spectra of unannealed H-implanted samples of 2x10 ¹⁶ cm ⁻² , 52x10 ¹⁶ cm ⁻² and 1x10 ¹⁷ cm ⁻² showing the discrete Ge-H defect modes seen in this study. The top panel shows the s-polarized spectra and the bottom panel shows the p-polarized spectra.	132
Figure 4.9	S-polarized MIT-FTIR spectra for 2x10 ¹⁶ cm ⁻² implanted Ge as a function of the isochronal annealing temperature.	133
Figure 4.10	P-polarized MIT-FTIR spectra for 2x10 ¹⁶ cm ⁻² implanted Ge as a function of the isochronal annealing temperature.	137

- Figure 4.11** S-polarized MIT-FTIR spectra for $1 \times 10^{17} \text{ cm}^{-2}$ implanted Ge as a function of the isochronal annealing temperature. The spectrum for 399°C is taken following exfoliation of the implanted Ge layer. 138
- Figure 4.12** P-polarized MIT-FTIR spectra for $1 \times 10^{17} \text{ cm}^{-2}$ implanted Ge as a function of the isochronal annealing temperature. The spectrum for 399°C is taken following exfoliation of the implanted Ge layer. 139
- Figure 4.13** S-polarized MIT-FTIR spectra for $5 \times 10^{16} \text{ cm}^{-2}$ implanted Ge as a function of the isochronal annealing temperature. 141
- Figure 4.14** P-polarized MIT-FTIR spectra for $5 \times 10^{16} \text{ cm}^{-2}$ implanted Ge as a function of the isochronal annealing temperature. 142
- Figure 4.15** Spectral evolution of the Ge-H states in Ge with He-implantation-induced voids. This is a model system for the interaction of H with internal surfaces and discrete defect states in (100)Ge that should lack strong signals from the defect structures that directly precede blister opening in the exfoliation process. [Stein] 144
- Figure 4.16** Temperature resolved comparison of normalized p- and s-polarized spectra for Ge implanted with 80 keV H^+ to a dose of $2 \times 10^{16} \text{ cm}^{-2}$. The dashed spectra in red indicate p-polarized spectra in which strong enhancement is observed suggesting their critical role in the exfoliation process..... 149
- Figure 4.17** Temperature resolved comparison of normalized p- and s-polarized spectra for Ge implanted with 80 keV H^+ to a dose of $5 \times 10^{16} \text{ cm}^{-2}$. The dashed spectra in red indicate p-polarized spectra in which strong enhancement is observed suggesting their critical role in the exfoliation process..... 150
- Figure 4.18** Temperature resolved comparison of normalized p- and s-polarized spectra for Ge implanted with 80 keV H^+ to a dose of $1 \times 10^{17} \text{ cm}^{-2}$. The dashed spectra in red indicate p-polarized spectra in which strong enhancement is observed suggesting their critical role in the exfoliation process..... 151

Figure 4.19	Peak position comparison for dominant peaks in the 2000 to 2050 cm^{-1} range for all implant conditions as a function of temperature.	158
Figure 4.20	(a) The in situ resistive heater used for performing 45° incidence transmission-mode FTIR spectroscopy measurements of InP. (b) The controlled atmosphere sample holder installed in a Thermo-Nicolet mass spectrometer, enabling in situ sample annealing in an inert N_2 environment.	164
Figure 4.21	A cross-sectional TEM micrograph of H-implanted InP annealed to 350°C, showing cleavage parallel to the implanted surface.	165
Figure 4.22	Transmission-mode FTIR spectral evolution of In-H modes at 1600 cm^{-1} and 1705 cm^{-1} , corresponding to In-H and adsorbed water modes, overlapping with the H-O-H scissor mode of adsorbed water. The peak overlap associated with adsorbed water is lost upon annealing.	167
Figure 4.23	Transmission-mode FTIR spectra showing the loss of absorption at 3500 cm^{-1} associated with the H-O-H stretch mode upon annealing to 292°C, further confirming the loss of water from the surface seen in Fig. 4.22.	168
Figure 4.24	Transmission-mode FTIR spectra showing the evolution of P-H modes found in the 2100 to 2450 cm^{-1} range. Upon annealing, lower wavenumber modes associated with discrete defects are preferentially lost, while modes at higher wavenumbers associated with extended defect structures grow as they sequester mobile hydrogen that diffuses through the lattice during anneal steps.	170
Figure 4.25	The interference effects of local field intensities for MIT-mode FTIR spectroscopy measured near the outer surface of the InP prism. The intensities shown are qualitative in nature, as they do not incorporate the predicted effect of evanescent enhancement for absorption in the buried layer.	174

- Figure 4.26** The temperature-dependent evolution of \bar{s} -polarized MIT-mode FTIR spectra showing the growth of higher wavenumber modes associated with extended defects upon annealing..... 176
- Figure 4.27** The temperature-dependent evolution of \bar{p} -polarized MIT-mode FTIR spectra showing the growth of higher wavenumber modes associated with extended defects upon annealing..... 177
- Chapter 5**
- Figure 5.1** Band energy diagrams for Ge/Si isotype heterostructures suitable for tunneling between degenerately doped Ge and Si substrates based upon the ideal heterojunction band offsets showing the anticipated band diagram of **(a)** p^+ -Ge/ p^+ -Si and **(b)** n^+ -Ge/ n^+ -Si structures..... 188
- Figure 5.2** Band energy diagrams for Ge/Si heterostructures suitable for tunneling between degenerately doped Ge and Si substrates based upon the ideal heterojunction band offsets showing the anticipated band diagram of **(a)** n^+ -Ge/ p^+ -Si and **(b)** p^+ -Ge/ n^+ -Si structures..... 189
- Figure 5.3** Modified goniometer stage used for precision control of the azimuthal twist angle to within $\pm 0.1^\circ$ in bonded samples showing **(a)** the complete device with reflective surfaces for laser alignment, **(b)** the rotating stage with knife-edges for {100} alignment, and **(c)** the top sliding sample holder with vacuum port and knife-edges for {100} alignment 191
- Figure 5.4** Sample measurement configuration for measuring the current-voltage behavior of a wafer bonded structure..... 192
- Figure 5.5** Current-voltage measurements of heavily-doped wafer-bonded Ge/Si heterostructures showing ohmic, low-resistance electrical contact. 193

Figure 5.6	Band energy diagrams for Ge/Si wafer bonded heterostructures based upon the Anderson model of heterojunction band offsets using the doping levels described in §5.1.1.2.1 showing the anticipated band structure of (a) p ⁺ -Ge/p ⁺ -Si and (b) p ⁺ -Ge/n ⁺ -Si.....	194
Figure 5.7	Current-voltage measurements of heavily-doped wafer-bonded InP/Si heterostructures showing ohmic, low-resistance electrical contact.	197
Figure 5.8	MIT-FTIR spectra of hydrophobically-bonded InP/Si heterostructures as a function of anneal time, showing the loss of between seven and 11 monolayers of adsorbed water upon annealing at 350°C.....	199
Figure 5.9	Cross-sectional TEM micrograph of an annealed wafer-bonded InP/Si interface showing the presence of a thick amorphous material determined by FTIR spectra to be primarily InPO _x with some SiO ₂ present.	200
Figure 5.10	Band energy diagrams for InP/Si wafer bonded heterostructures based upon ideal heterojunction band offsets using the doping levels described in §5.1.1.2.1 showing the anticipated band structure of (a) n ⁺ -InP/n ⁺ -Si and (b) n ⁺ -InP/p ⁺ -Si.....	201
Figure 5.11	Band energy diagram for wafer-bonded p ⁺ -Ge/p-Si heterostructures based upon the ideal heterojunction band offsets showing (a) the full band bending and (b) a magnification of the interface region.....	204
Figure 5.12	Current-voltage characteristics of p ⁺ -Ge/p-Si as a function of (a) annealing time at 400°C for wafer-bonded p ⁺ -Ge/p-Si heterostructures bonded with a 5° azimuthal twist angle between the substrates and (b) azimuthal twist angle for an anneal of four hours at 400°C.....	206
Figure 5.13	Circuit diagram for a wafer-bonded p ⁺ -Ge/p-Si heterostructure modeled by a leaky Schottky diode featuring a thermionic diode structure in parallel with a shunt resistance, R_{sb} , and in series with a parasitic resistance, R_s	208

- Figure 5.14** Fitting of the current-voltage curve for the sample annealed to 400°C for one hour curve to estimate the parasitic series resistance in the leaky Schottky diode model. 210
- Figure 5.15** The optimized leaky Schottky diode curve fits for wafer-bonded p⁺-Ge/p-Si heterostructures showing the model (solid curves) and data (open circles) for **(a)** the anneal-time-dependent *J-V* behavior at 400°C for heterostructures with a 5° azimuthal twist angle and **(b)** the twist-angle dependent *J-V* behavior for heterostructures annealed at 400°C for four hours..... 211
- Figure 5.16** The effective barrier heights given as a function of both anneal time and azimuthal twist angle. The solid squares show the optimized fit, and the open triangles show the estimated values based on the linear analysis of the forward and reverse bias *J-V* behavior. The dashed arrow points out two conditions that should be reasonably well matched – the 5° sample annealed for two hours (black) and the 5° sample annealed for four hours (red). These values are not identical, but are within the estimated error bars. 213
- Figure 5.17** The shunt resistance given as a function of both anneal time and azimuthal twist angle. The solid squares show the optimized fit, and the open triangles show the estimated values based on the linear analysis of the forward and reverse bias *J-V* behavior. The dashed arrow points out two conditions that should be reasonably well matched – the 5° sample annealed for two hours (black) and the 5° sample annealed for four hours (red). 214
- Figure 5.18** The *J-V* curves for 5° twisted as-bonded p⁺-Ge/p-Si heterostructures showing the impact of the time delay between voltage steps. The inlaid plot shows the estimated effective barrier height as a function of the scan time delay. 215
- Figure 5.19** The transient response for an as-bonded p⁺-Ge/p-Si illustrating the long lifetime of defect states at the bonded interface. The sample was first allowed to come to

steady state under 3 V forward bias. The bias was reversed to -0.4 V and the current was monitored as the interface states discharged. The transient response of the effective barrier height is shown in the inset plot..... 216

Figure 5.20 Transmission-mode FTIR spectra of wafer-bonded Ge/Si heterostructures at 10, 45, and 60° transmission angles. The different colors refer to different bonding conditions and reference spectra. In the black curve, the effects of annealing a hydrophobically-bonded sample following an anneal to 300°C referenced to an as-bonded sample. The red curve shows an as-bonded hydrophilically-bonded sample referenced to an as-bonded hydrophobically-bonded sample. And, the green curve shows an as-bonded hydrophilically-bonded sample referenced to a hydrophobically-bonded sample that has been annealed to 300°C..... 218

Figure 5.21 Change in barrier height at an anneal time of two hours at 400°C for Ge/Si bonded interfaces as a function of $\sin(\theta_{twist}/2)$, the argument of the expected change in the twist interfacial dislocation density, as expressed in total dislocation length per cm^{-2} . The sub-linear behavior is consistent with the suppression of defect decoration due to Coulombic repulsion in closely spaced defects..... 222

Figure 5.22 Change in shunt conductivity at an anneal time of two hours at 400°C for Ge/Si bonded interfaces as a function of $\sin(\theta_{twist}/2)$, the argument of the expected change in the twist interfacial dislocation density, as expressed in total dislocation length per cm^{-2} . The approximately linear behavior is consistent with the expectation that defect states that are transiently occupied during conduction through the interface are not sensitive to the occupation level. 223

Figure 5.23 Band energy diagram for wafer-bonded p^+ -Ge/p-Si heterostructures illustrating the conceptual model for thermionic and tunneling conduction mechanisms as

they relate to the anneal-dependent interface states and barrier height in **(a)** an as-bonded unannealed heterostructure featuring slow defect states in a surface passivation interfacial layer and **(b)** an annealed sample having lost the passivation layer but replaced it with a network of twist and anneal dependent interfacial misfit dislocation defect states that lead to shunt conductivity and barrier height reduction..... 226

Chapter 6

- Figure 6.1** A cross-sectional view of the AFM-measured surface morphology for one of the lines in the scan direction of the AFM image shown in Fig. 3.12. The derivative of the scan has been converted into a local miscut angle value, assuming that there is no miscut in the direction of the scan. For directions offset by ϕ from the miscut direction, the local miscut has an angle of $|\theta_{miscut} \cos \phi|$ added to the local miscut..... 233
- Figure 6.2** A cross-sectional SEM image of a triple-junction solar cell structure fabricated on an as-transferred Ge/Si wafer-bonded epitaxial template (left) and a bulk Ge substrate (right), showing the transferred Ge film, the GaAs buffer layer, the GaAs and GaInP subcells, and the GaAs cap layer, as well as the intervening tunnel junctions..... 234
- Figure 6.3** Representative PL spectra from the GaAs capping layer of a triple-junction solar cell structure grown on a Ge/Si wafer-bonded epitaxial template and a bulk Ge substrate, showing comparable intensity between the two structures..... 236
- Figure 6.4** TRPL data for the best measured photoluminescence decay for the GaAs capping layer in a triple-junction solar cell structure grown on both a Ge/Si wafer-bonded epitaxial template and a bulk Ge control. 237

- Figure 6.5** Representative PL spectra from the GaInP subcell of a triple-junction solar cell structure grown on a Ge/Si wafer-bonded epitaxial template and a bulk Ge substrate, showing comparable intensity between the two structures, but with a significant red shift of the peak position for the GaInP layer grown on a Ge/Si 238
- Figure 6.6** The post-growth RHEED pattern of a 250 nm thick Ge homoepitaxial layer grown at 450°C on a Ge/Si substrate at 0.1 nm s⁻¹. The primary RHEED pattern is formed by diffraction from the Ge transferred film, while the offset RHEED pattern is formed by diffraction from Ge grown epitaxially on the Si handle wafer. The offset is attributed to the slight twist between the substrates..... 240
- Figure 6.7** AFM images of the surface of a 250 nm thick Ge homoepitaxial buffer layer grown on a Ge/Si wafer-bonded structure at a growth rate of 0.1 nm s⁻¹ and a growth temperature of 450°C. 241
- Figure 6.8** XTEM image of a ~500 nm thick Ge homoepitaxial film grown at a temperature of 500°C and a growth rate of 0.1 nm s⁻¹ on a Ge/Si wafer-bonded epitaxial template, showing the origin of threading dislocations at the interface between the transferred film and the homoepitaxial layer. 242
- Figure 6.9** InP/Si surface roughness as a function of etch time and dilution ratio for a HCl:H₃PO₄:H₂O₂ wet etch, showing up to an 80% reduction in roughness. Also shown is the post-polish roughness (shown in blue) of an InP/Si wafer-bonded heterostructure following a CMP process, with error bars illustrated by dashed lines..... 244
- Figure 6.10** PL spectra from InP/In_{0.53}Ga_{0.47}As/InP DHs grown on bulk InP and InP/Si wafer-bonded epitaxial templates both unprocessed and processed with chemical etching with 1:2:2 and 1:2:4 ratios of the HCl: H₃PO₄: H₂O₂ etch or CMP with a sodium hypochlorite slurry. 246

List of Tables

Chapter 2

Table 2.1	Summarized results for the detailed balance efficiency of a single-junction thin-film solar cell in AM1.5 illumination as a function of film geometry, operating temperature and operating concentration.....	48
Table 2.2	Summarized results for the efficiency of the detailed balance model of two- and three junction tandem solar cell structures in both independent and series connected device geometries operated at 300 K under a concentration of 100 sun AM1.5 radiation.....	55
Table 2.3	The summarized detailed-balance efficiency calculations for wafer-bonding enabled solar cell designs under 100 sun AM1.5 illumination at a cell temperature of 300 K.....	73

Chapter 3

Table 3.1	Coefficient of thermal expansion model parameters for the empirical α -model, $\alpha(T) = C_1 \{1 - \exp[a(T - T_0)]\} + C_2 T$, for Si, Ge, InP, and GaAs. The model has been fit for data reported from 200 to 1000 K and is suitable for that range.....	87
------------------	--	----

Chapter 4

Table 4.1	Literature reported values for discrete defect and extended surface modes of hydrogen in Ge.....	131
Table 4.2	Peak location as a function of temperature for peaks in the 1900 – 2100 cm^{-1} for 2×10^{16} , 5×10^{16} , and 1×10^{17} cm^{-2} . The p-polarized peaks in red signify peaks where strong enhancement is observed. The s-polarized peaks that are thought to be associated with those enhanced peaks are also highlighted in red.....	148

Chapter 5

Table 5.1	Summarized barrier heights for the present study and previously reported theoretical and experimental estimates of the valence band offsets at Ge/Si heterojunctions. The literature values highlighted in bold correspond to those conditions that most closely correspond to the measurement conditions of the present work.....	224
------------------	--	-----

Chapter 6

Table 6.1	The $\text{In}_{0.53}\text{Ga}_{0.47}\text{As}$ PL emission peak position and intensity relative to a control DH grown on bulk epi-ready InP for all of the surface conditions tested.....	248
------------------	--	-----

Chapter 1: Introduction

1.1 Photovoltaic Devices

Photovoltaics allow conversion of light to electrical power and are an integral component of a renewable energy alternative to our present non-renewable energy economy. The following section describes the motivation for making a transition away from a hydrocarbon-based energy economy to a renewable-energy economy based in part on photovoltaic power generation. Additionally, the fundamental operating principle of photovoltaic devices is described along with efficiency limitations for solar energy conversion.

1.1.1 Photovoltaics as a Critical Step toward a Sustainable Energy Economy

Ever diminishing supplies of fossil fuels and recent geo-political events emphasize the importance of photovoltaic devices in our national energy policy. The eventual depletion of fossil fuel reserves was first pointed out and projected by the geologist M. King Hubbert. Hubbert made the logical assumption that the rate of replacement of fossil fuels is essentially zero and that the rate of oil usage increases in lockstep with the rate of oil discovery. However, given the finite, and as yet unknown, quantity of fossil fuels in the ground, it was unclear when the rate of production would peak and begin to decline. By studying the historical rate of discovery for the lower 48 states, Hubbert projected in 1956, that the rate of oil production would peak at around 1970. Applying this technique to global production rates, the peak rate of production, known as

the “Hubbert peak” is generally anticipated to occur during the present decade.^{1,2} A representative projection of the general peak shape is given in Fig. 1.1 where the peak rate of discovery is anticipated to occur around 2015.³ One of the most important premises of the Hubbert interpretation of oil reserves is that the negative effects of the finite nature of fossil fuel energy reserves does not start upon pumping the last drop of oil or mining the last lump of coal, but rather when we reach the half-way point. At that time a steady, unstoppable decline in the rate of oil extraction will begin, and the ensuing rise in energy costs will throw the global economy into shock.

Estimates on oil reserves vary, but what is indisputable is that these reserves are being depleted while global demand for energy is increasing. At some point in the future the world will be forced to turn the corner and pursue new sources of power for everything from lighting to transportation to industrial production. There is merit in acknowledging this now and fostering research and industry to address this indisputable need for alternative, renewable energy sources.

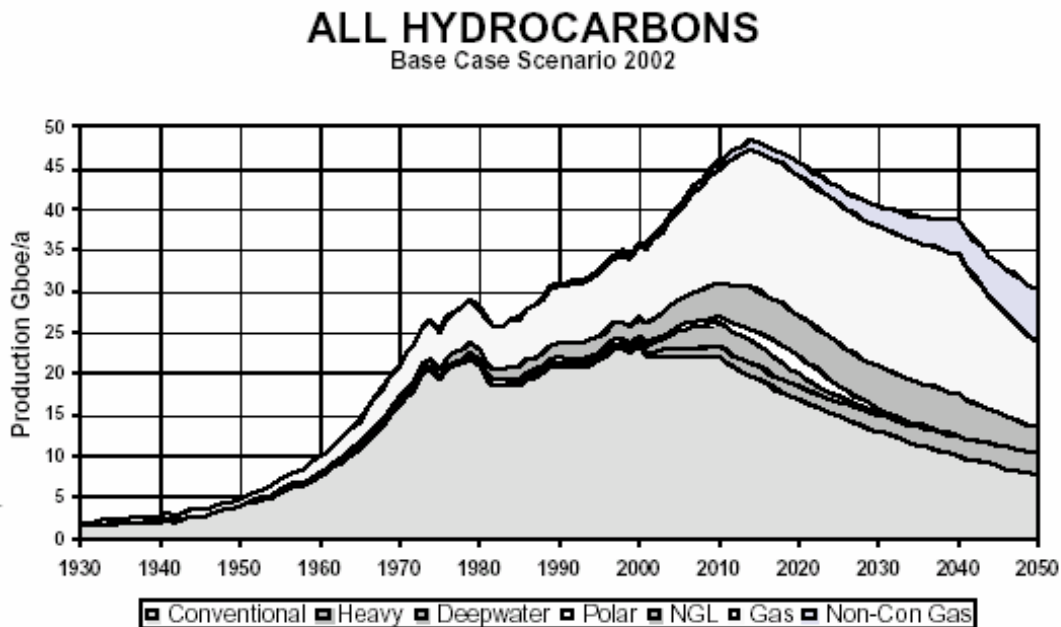


Figure 1.1 Production forecast of all hydrocarbons indicating that peak total hydrocarbon production will occur near the year 2015.³

While the risk of global warming that accompanies heavy reliance on fossil fuels is a subject of some debate, it is generally acknowledged that the release of large quantities of carbon dioxide through the combustion of fossil fuels will affect the global climate. Most models for climate change associated with the release of greenhouse gases predict temperature rises on the order of 1.5 to four°C over the next century.⁴

Irrespective of political persuasion, the reliance of the industrialized world on fossil fuels impacts the need for and nature of our relationships with governments in geo-political hotspots. It would be inappropriate to advocate for the development of a renewable power base to facilitate the disengagement and isolation of the industrialized world from such troubled locations. However, decreasing the reliance of developed nations on fossil fuels would change the nature of the interaction with these parts of the developing world, enabling the United States and other economically developed countries to aid and counsel countries in these regions without a conflict of interest that might lead to bad advice, or worse still, corruption.

In addition to the need for improvement of photovoltaic devices to serve as one component of a renewable energy program, solar cells have long been an essential component of the United States space program. Space power systems for satellites based on solar cell technology have driven the development of high performance photovoltaic systems. The primary reason for this performance push is the key figure of merit for space power systems, watts per kilogram, also known as specific power. Higher specific power translates directly into a lower launch cost for a satellite. One of the most straightforward ways to accomplish this is through the improvement of cell efficiency. It is the push to increase the specific power of space power systems that motivates the work of this thesis. However, as know how improves, costs for high performance photovoltaics will naturally decline, enabling these devices to be implemented in terrestrial systems. Thus, through pursuing the development of high-performance photovoltaic devices for space power systems, an essential step is made toward sustainable energy independence.

1.1.2 A Performance and Economic History of Photovoltaic Devices

A review of the performance and economic history of photovoltaic systems gives reason to believe that future progress in photovoltaic systems will enable these technologies to become competitive with conventional power generation. Several recent texts broadly review the field of photovoltaics and provide excellent descriptions of the history and progress of photovoltaics.^{5,6} The key moments in the history of photovoltaics are well summarized in both texts.

In Fig. 1.2 the record efficiency as a function of year is plotted for various photovoltaic technologies. The general trend is promising for all of the technologies reported, but considering the balance of systems cost of installed modules, only photovoltaic devices with efficiency in excess of approximately 20% are likely to become promising long-term alternatives to hydrocarbon-based power. Only multi-junction III-V compound semiconductor and single-crystal silicon solar cells exceed this practical threshold of efficiency. Fortunately, both technologies show promising performance trends.

The improvement of efficiency depicted in Fig. 1.2 is the natural result of intensive research and growth of the volume of photovoltaic production. The learning curve shown in Fig. 1.3 illustrates the coincidental reduction of photovoltaic cost with increasing production volume. In other words, photovoltaics, like most other commodities, benefit from economies of scale. While the curves in Figs. 1.2 and 1.3 are promising, inevitably disruptive innovation is required to continue the performance enhancement trend shown in Fig. 1.2. However, to make a practical impact and fall on the curve in Fig. 1.3, such an innovation should provide both performance advantages and enable that performance advantage at a competitive cost. As will be described below, wafer-bonding enabled solar cell designs meet these requirements, especially when operated under concentrated sunlight to reduce the cell cost as a fraction of the total installed module cost.

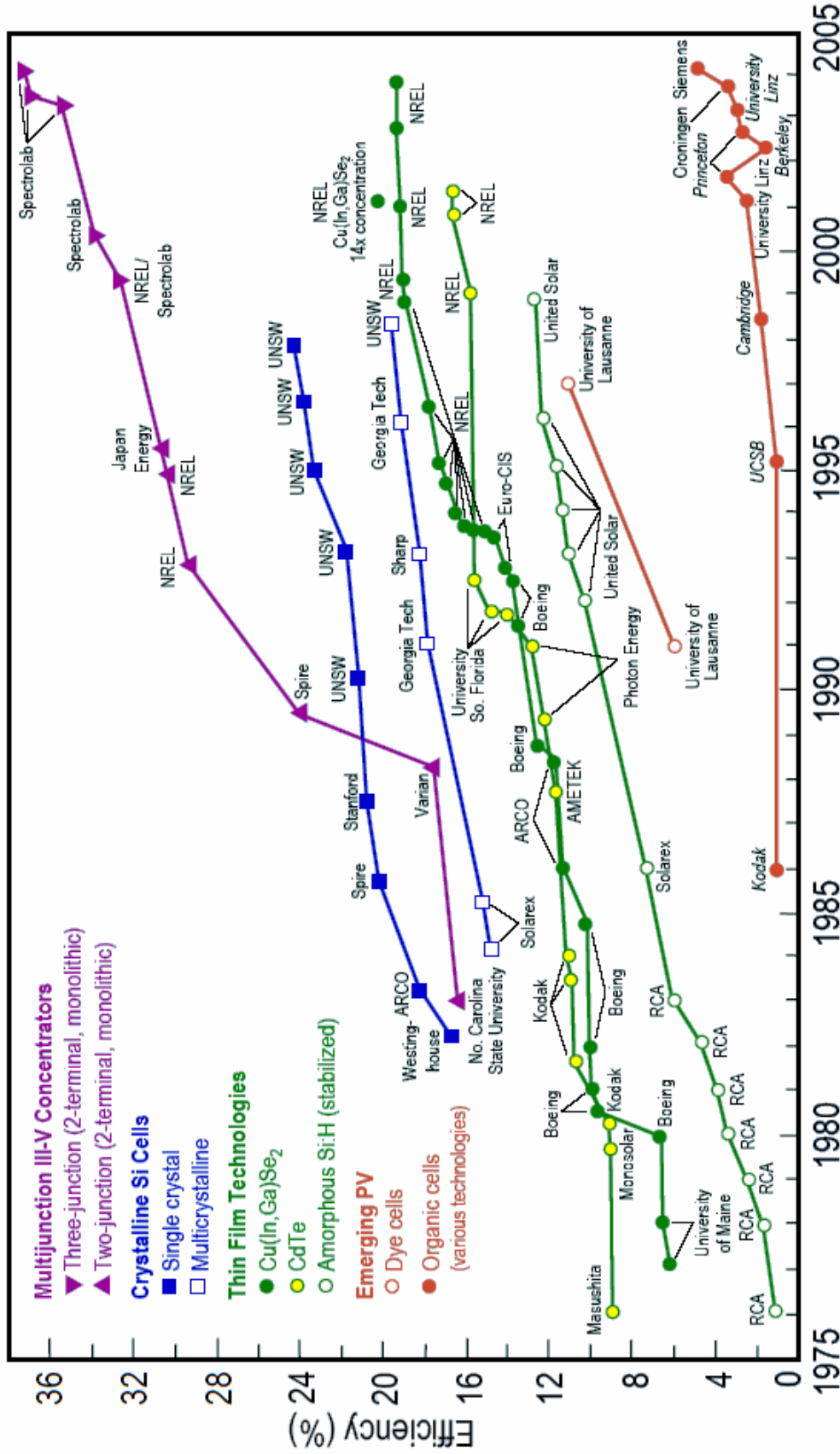


Figure 1.2 Historical milestones in peak solar cell efficiency, showing the efficiency records and their holders as a by technology type. Note the rapid increase in efficiency for single-crystal silicon and III-V compound semiconductor multi-junction solar cells.

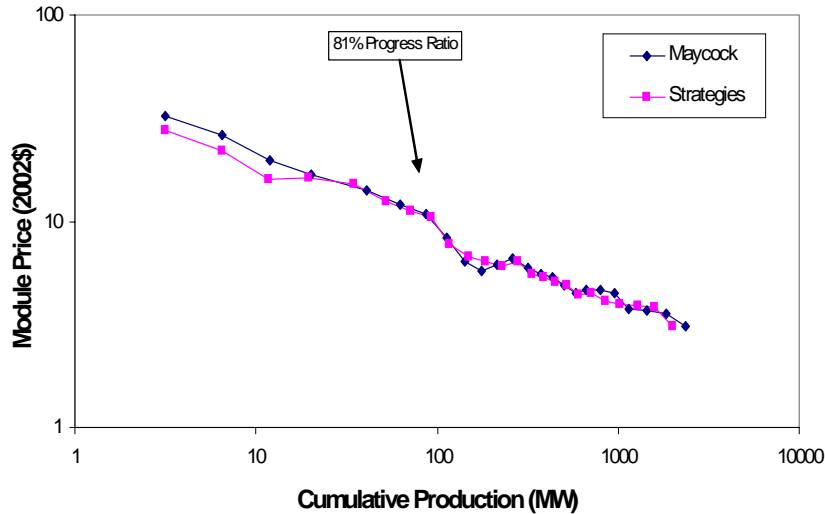


Figure 1.3 The learning curve relating cost per watt of installed power to the cumulative production volume of the photovoltaic industry.

1.1.3 Photovoltaic Operating Principle

At a high level of description, solar cells convert photons to electrical power by a transition from a photon's energy to an excited state in a material. The energy stored in this excited state is then removed from the cell to produce useful electric power. To achieve this solar cells broadly consist of:

- An absorber material that converts photon energy into an excited state. This is generally done by semiconductors, which absorb photons with energy above their band gap to form an electron-hole pair.
- A means of carrier separation. In semiconductors this is done by forming a doped junction that forms a built-in field in the device. This field causes photo-generated carriers that are created in the field or reach the field by diffusion to be separated by drift. Additionally, the built-in voltage of the junction sets an upper limit for the potential of the generated carriers.

- A means of carrier extraction from the semiconductor to an external circuit. This is generally accomplished by metal-semiconductor contacts.

In a real device, such as a silicon solar cell, these components are the silicon itself, which serves as photon absorber, a formed p-n junction, which serves to separate carriers and impart a potential on the carriers, and metal contacts, which serve to extract carriers at some potential to an outside circuit. When considering the potential of solar cells in the global energy infrastructure and various special applications, such as space power systems, it is useful to consider the fundamental and practical limits of photovoltaic devices.

1.1.4 Fundamental and Practical Limits to Photovoltaic Efficiency

1.1.4.1 Fundamental Limits to Photovoltaic Efficiency

In space the integrated power of the solar spectrum is 1353 W m^{-2} with a broad spectrum, while on the surface of the earth the integrated spectral power is lower with absorption bands of varying intensity depending on the inclination of the sun relative to the solar cell and the elevation of the cell. In both instances the spectrum is broad, leading to fundamental performance limitations for a single absorber material. That is, the loss of efficiency due to the inability of the material to absorb sub-bandgap photons, while photons with energy above the bandgap generally lead to the formation of hot carriers (Fig 1.4).⁷ These hot carriers have excess energy that is quickly lost due to interaction of the photons with the crystal lattice and the loss of the excess energy to heat. Thus, photon energy in excess of the cell operating point is lost, further limiting efficiency.

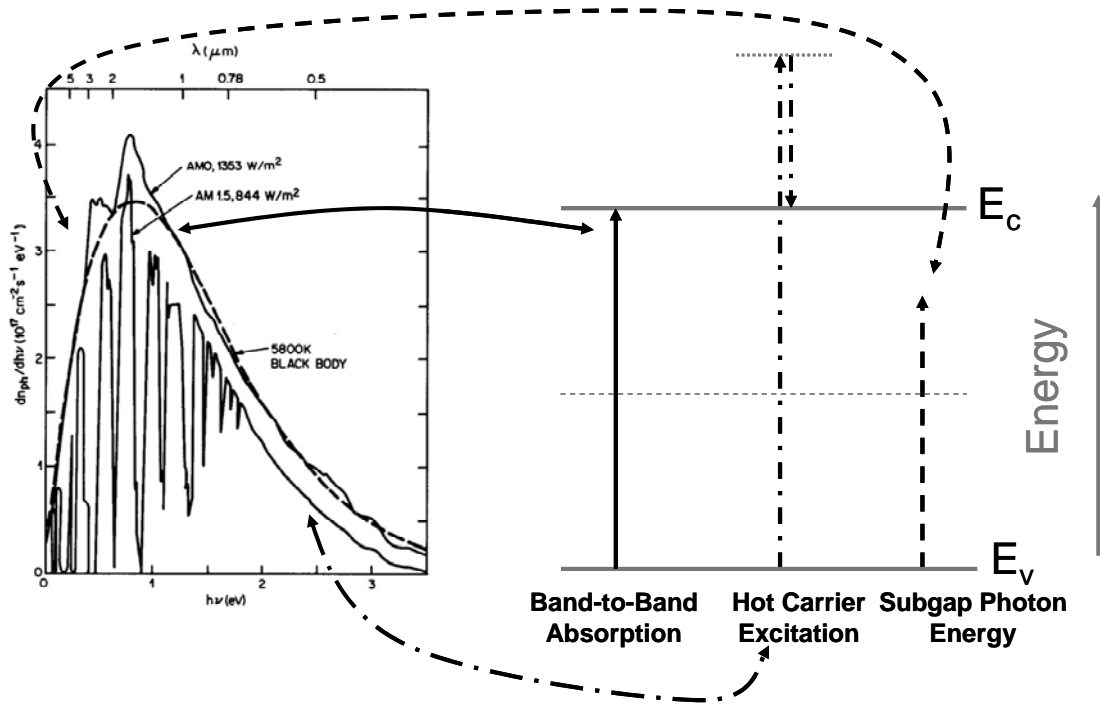


Figure 1.4 Fundamental loss mechanisms in a photovoltaic device illustrating loss of power due to sub-bandgap photons and thermalization of excess photon energy along with absorption of a photon with energy E_G resulting in a band-to-band absorption event and thus no loss of power. The plot on the left illustrates the photon flux as a function of photon energy for actual solar spectra as well as for black body radiation.⁵

Additionally, thermodynamics places an upper limit on the performance of a solar cell due to the statistics of radiative recombination in a two-level photon gas, the statistical approximation of bandgap-containing medium, such as a semiconductor. Generally, current loss due to radiative recombination increases exponentially as the potential, i.e., quasi-Fermi level separation or cell operating voltage, of carriers in the bandgap medium approaches the bandgap energy of the medium. This is independent of the anticipated performance of the real materials that constitute the cell. The radiation of carriers from the cell then defines the tradeoff between the operating voltage and the extracted photo-current. This concept is developed in Chapter 2 for solar cells in general and for novel multi-junction solar cells in particular.

1.1.4.2 Practical Limitations to Photovoltaic Efficiency

The fundamental limitations described above apply to ideal materials and real materials alike. However, in the case of real materials the efficiency of a cell is often limited by carrier recombination that results from defects that are formed during growth of the material. Additionally, the act of doping a semiconductor to form a junction impacts carrier mobilities and recombination adversely. Additionally, the increased majority carriers on each side of the junction lead to increased free-carrier absorption, a process that leads to loss of photon energy to heat. However, without these doped structures photo-generated carriers can not be extracted.

For these reasons the performance of real solar cells is tied to the device design and means of fabrication. As the absorber materials of construction become better characterized and their growth becomes better understood, the overall performance of cells fabricated with these materials improves. Thus, it is essential that the materials of construction for solar cells be selected from a well-characterized group with well-developed growth techniques.

1.1.4.3 Solar Cell Designs for Improved Limiting Efficiency

By sustaining improvements in design and fabrication, single-junction solar cells can be improved to asymptotically approach the thermodynamic limiting efficiency associated with their absorber bandgap. For instance, PERL silicon solar cells fabricated by the University of New South Wales have reported efficiencies in excess of 24%.⁸ However, the design modifications in such refined structures do not address the fundamental limits of photovoltaic efficiency outlined in §1.1.4.1. Most attempts to address the fundamental loss mechanisms of solar cells rely on the concept of spectrum splitting. In spectrum splitting solar cells the solar spectrum is discretized in such a way that the loss of power due to sub-bandgap and super-bandgap photons is minimized.

Several designs have been proposed to accomplish spectrum splitting. An excellent review of spectrum splitting cell designs and their thermodynamic limiting efficiency can be found in Martin Green's *Third Generation Photovoltaics: Advanced Solar Energy Conversion*.⁹ One

spectrum splitting solar design, the quantum well solar cell, seeks, through the use of quantum well structures, to collect sub-bandgap photons by creating a structure that has engineered separations of energy states in the quantum wells of tailored bandgap within the intrinsic region of a p-i-n cell structure. However, this design has yet to show improvement over the best single-junction cell designs.¹⁰⁻¹² More radical designs focus on the conversion of a portion of the spectrum to photons that closely match the bandgap energy of a single absorber. Two such designs are photon up-converters and photon down-converters.¹³⁻¹⁵ In the up-converter the absorber collects photons above the bandgap energy, and an up-converting material located on the opposite side of the absorber from the radiation source converts sub-bandgap photons to super-bandgap photons by absorbing two photons through an intermediate state and emitting a photon upon transition from the excited to ground state.¹⁴ Theoretical calculations indicate that both up-converters and down-converters could deliver substantial improvements to the limiting efficiency of solar cells.^{14,15} This approach to efficiency improvement is relatively new. Consequently, the materials used for photon energy conversion are poorly developed and characterized. At present the use of an up-converting doped vitroc ceramic has been shown to add 2.5% absolute efficiency to the operation of a GaAs solar cell.¹⁶

The best developed and most promising means of spectrum splitting is the tandem multi-junction solar cell.¹⁷⁻²¹ Such a multi-junction solar cell design uses stacked subcells of successively decreasing energy to perform spectrum splitting to improve cell efficiency. In such a design the lower cutoff energy is determined by the smallest bandgap subcell. Additionally, because each subcell collects a smaller quantity of photons, the photon energy lost to hot carrier thermalization is reduced. Due to excessive fabrication cost, these cells have been limited to space applications where improved performance leads to a net savings due to reduced array size and mass and thus launch costs. These multi-junction solar cells generally consist of GaInP, GaAs and Ge subcells for triple-junction cells or GaInP and GaAs subcells for dual-junction cells. The March 2005 world record for a triple-junction solar cell held by Spectrolab is over 37.3% under

AM1.5 global illumination at a cell temperature of 25 °C at a concentration of 66.3 suns.²² The selection of the GaInP/GaAs/Ge material system is necessitated by nature. For a multi-junction two-terminal solar cell to produce efficiency gains the photo-current generated by each subcell must be closely matched as Kirchoff's Law implies that the complete cell will operate at a current roughly equivalent to the photo-current generated in the subcell with the smallest photo-current. Control of the subcell band gaps is limited by the preferable fabrication method of heteroepitaxy, which requires that the subcell materials have lattice mismatches under 1.0% to avoid the formation of dislocations during growth. Fortuitously, the GaInP/GaAs/Ge system meets these criteria.

The path to further improvement in the limiting efficiency of multi-junction solar cells relies on the addition of more subcells, and the optimization of the bandgaps and material properties of the subcells making the multi-junction structure. However, no lattice-matched system of well-developed materials exists to enable the fabrication of a solar cell with four or more junctions by heteroepitaxy. This problem is illustrated by studying the lattice constant of well-developed ternary III-V semiconductors illustrated in Fig. 1.5. To enable these new structures, a new material integration process is required that is independent of the lattice constant of the integrated materials.

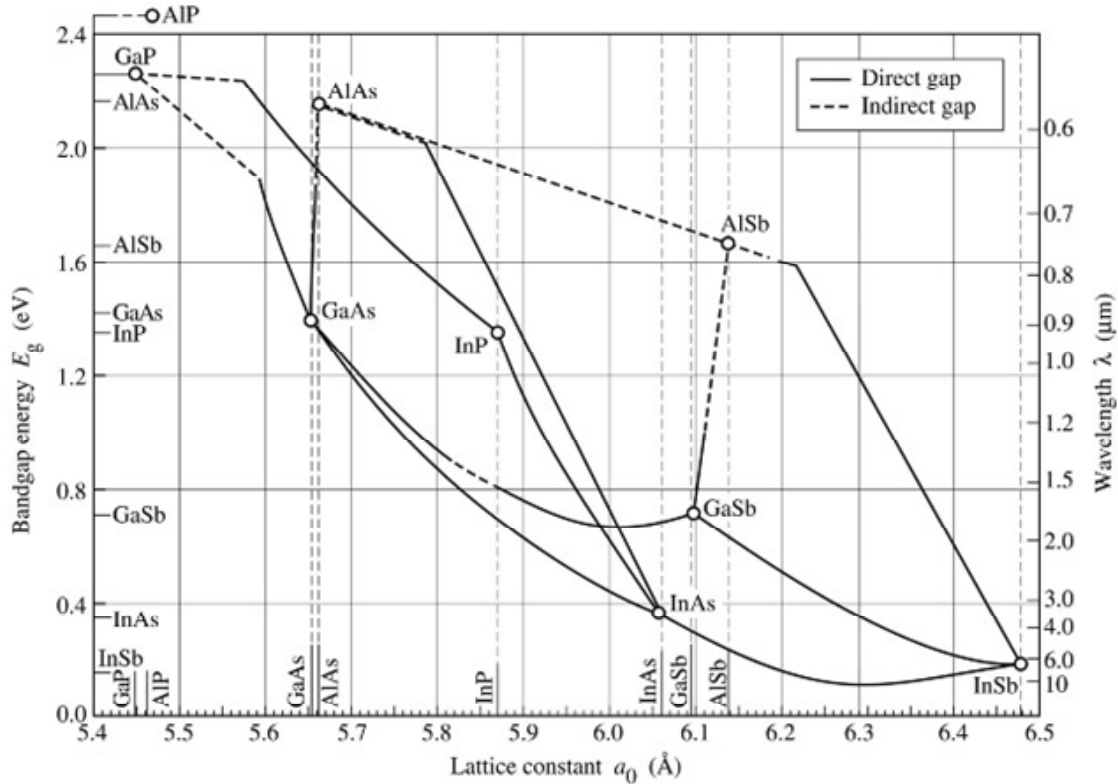


Figure 1.5 Bandgap as a function of lattice constant for common III-V semiconductors suitable for photovoltaic applications illustrating the limitations due to the interdependence of these two critical parameters.

1.2 Materials Integration

1.2.1 Traditional Epitaxial Strategies

In the microelectronics industry epitaxy, chemical vapor deposition (CVD), sputter deposition and high-temperature growth are the dominant methods for the integration of differing materials. Strictly speaking, only epitaxy leads to the deposition of an electronic quality, single-crystal semiconductor, although CVD deposition can lead to poly-crystalline films. When the deposited semiconductor differs from the substrate upon which it is grown the process is referred to as heteroepitaxy. Substantial effort has been placed on the application of heteroepitaxy to integration of differing semiconductors to confer new properties on a finished device that normally are

unachievable by a single material. For instance, integration of optical emitters and detectors requiring a direct bandgap semiconductor such as GaAs with logic components typically based on Si complementary metal oxide semiconductor (CMOS) devices. This is not a task for which heteroepitaxy is well suited. The limitations associated with heteroepitaxial growth of non-lattice-matched semiconductors are described below along with some progress on various materials.

1.2.1.1 Fundamental Limits of Heteroepitaxy

In heteroepitaxial growth there are two primary limitations that have limited the applications for which this integration technique can be used. These limitations are lattice matching of the differing materials and nucleation of the epitaxial film.

The lattice constant of the epitaxial film can deviate only slightly from the lattice constant of the underlying substrate before misfit-induced strain causes the formation of dislocations, which allow the relaxation of that strain.²³ In particular, when growing coherently strained epitaxial layers on a foreign substrate, there is an associated critical thickness, at which the strain energy of the film makes the formation of structures that lead to the reduction of that strain energy. These strain energy reducing structures can include threading dislocations, surface undulations, or even island growth. For heavily strained (>1%) epitaxially grown semiconductors of interest to photovoltaic devices, the films are sufficiently thick, on the order of several microns, that the formation of threading dislocations is the dominant form of stress relaxation. These dislocations are electrically active, leading to decreased minority carrier lifetimes and mobilities and therefore diminished cell performance. For this reason, lattice matching is important in the selection and growth of device structures and materials for photovoltaics.

In addition to the lattice-matching requirement for heteroepitaxy, nucleation of the epitaxial film is of importance when growing polar on non-polar substrates as will be described below in §1.2.1.3.1. Numerous attempts have been made to integrate semiconductors on foreign but

substantially non-lattice-matched substrates through heteroepitaxy. Some examples of importance to photovoltaics applications are described in the subsequent sections.

1.2.1.2 Heteroepitaxial Ge/Si Integration

Direct heteroepitaxy of Ge on Si is one of the dominant methods for the formation of Ge quantum dot structures. For epitaxy of Ge on Si, the critical film thickness is reached within a few monolayers, depending on the growth conditions. Upon reaching this critical thickness, a random distribution of Ge islands forms to relieve the strain energy in the growing film.²⁴⁻²⁶ Of course, if thin coherently-strained layers are grown under the critical thickness for island formation, the value of these layers for integration of additional materials closely lattice matched to Ge, such as GaAs, is essentially nonexistent, because the lattice constant of bulk Ge has not been conferred on the thin strained film. After growth of sufficiently thick Ge layers, the island structures are overgrown and the thicker Ge film relaxes to have the lattice constant of bulk Ge, but in the process of relaxation, an unacceptable number of threading dislocations are formed.

To solve the problem of epitaxially integrating low defect density Ge with Si substrates, compositionally graded epitaxy has been used to create substrates with Ge/Ge_xSi_{1-x}/Si structures. This has been accomplished by growing films of Ge_xSi_{1-x} approximately one μm thick starting with a Ge fraction of 0.1 and ending with a pure Ge film. These structures have been shown to be suitable for use as heteroepitaxial templates for GaAs growth enabling the integration of GaAs with Si substrates.²⁷⁻²⁹ These layers have been shown to have hole minority carrier lifetimes in GaAs test structures of 7.7 ns, a value comparable to such structures grown on bulk GaAs substrates.³⁰ Feasibility has been demonstrated for use of these structures in GaAs-based solar cells,³¹ Ge-photodiodes,³² and 885 nm continuous wave edge-emitting lasers based on GaAs/AlGaAs and InGaAs/GaAs/AlGaAs structures grown on Ge/Ge_xSi_{1-x}/Si substrates.³³ However, all of these structures suffer from limitations. The buffer layer structure through which strain is relaxed and resulting threading dislocations are overgrown is in excess of 10 μm thick.

This leads to problems with device cracking due to thermo-mechanical strain energy of thick structure. Depending on the growth temperature of the GaAs-based device structure, the critical thickness for cracking of the device upon cool down is between two and 3.5 μm , while the critical thickness for GaAs grown directly on Si is five to seven μm for the same growth conditions.³⁴ This critical thickness for crack formation precludes the use of these structures in integrating traditional triple-junction solar cell structures with Si substrates, because these solar cell structures generally are on the order of 10 μm or more in thickness. Even two-junction structures, which use Ge only as an epitaxial template, are too thick to be integrated on Si using this technique, requiring a total thickness in excess of five μm .

1.2.1.3 Heteroepitaxial III-V/Si Integration

The excessive cost of III-V semiconductor substrates has driven efforts to develop and perfect heteroepitaxial growth of this class of materials on Si for more than 20 years. Heteroepitaxial growth of III-V semiconductors on Si presents two problems: first, the growth of polar on non-polar semiconductors presents unique challenges that are not present for the growth of Ge on Si, and, second, there is substantial mismatch between most III-V semiconductors and Si.

1.2.1.3.1 Polar on Non-Polar Heteroepitaxy

The primary challenge in polar on non-polar epitaxy arises from the polarity of the epitaxial layer. In particular, the ordering of the anion and cation sublattices in the grown film must be contiguous throughout the grown film to avoid degradation of the electrical performance of the film. During nucleation the film does not nucleate at a single point and spread laterally in the first monolayer. Nor does the film nucleate spontaneously across the entire substrate. Rather the growing film nucleates spontaneously at multiple, closely spaced points on the non-polar substrate surface. Depending on the type of nucleating species – cation or anion – and the terracing (both single monolayer and double monolayer surface steps can form) of the non-polar

substrate surface, there exists the possibility of forming (100) monolayers that have compositional discontinuities where independently nucleated islands meet. In the early stages of growth these discontinuities would result in an extended monolayer of anions in one region switching to an extended monolayer of cations. Upon growth, this boundary propagates through the film in what is known as an anti-phase domain boundary. These anti-phase domain boundaries (APD's) are electrically active and deleterious to the electrical properties of III-V semiconductor thin films.^{35,36}

If the non-polar substrate could be made to be perfectly smooth, that is no atomic steps are present on the reconstructed surface of the non-polar substrate. And, the nucleation species was controlled to be comprised entirely of cations, or, as is usually the case, entirely of anions. Then one would expect there to be no APD's formed upon the intersection of nucleated islands. However, such a step-free surface is essentially impossible to generate. Fortunately, vicinal non-polar substrates, intentionally miscut off of the (100) surface by several degrees, reconstruct with double-step edges, which are energetically preferable for these surfaces. Thus, by nucleating the polar semiconductor growth by initiating growth with the anion on a miscut substrate, the formation of APB's can be completely suppressed. This general form of growth is the basis for the metal-organic chemical vapor deposition growth of dual- and triple-junction solar cells on Ge substrates.³⁷⁻³⁹

1.2.1.3.2 Heteroepitaxial GaAs/Si and InP/Si Integration

GaAs and InP and their lattice matched family of ternary and quaternary III-V semiconductors are of particular interest in existing high-performance triple-junction solar cells and novel next-generation high-performance solar cell designs, respectively. For this reason, we focus on results for the integration of these materials with Si by heteroepitaxy.

The lattice mismatch between InP and Si is 8.1%. This excessive lattice mismatch leads to large dislocation densities upon growth reported to be in excess of 10^7 cm^{-2} .⁴⁰ The dislocation

density has been reduced to less than 10^5 cm^{-2} for InP epitaxy on Si through the use of conformal growth.⁴¹ However, this growth process only produces small regions of low-defect-density InP.

For growth of GaAs on Si the lattice mismatch is only 4.2%. Thus, the interest and activity around heteroepitaxy of GaAs on Si is higher. In fact, this epitaxy challenge spurred much of the initial thinking on growth of polar semiconductors on non-polar substrates. Nevertheless, the results are still less than desirable. Recent results have shown threading dislocation density less than $3 \times 10^6 \text{ cm}^{-2}$ in GaAs grown on Si(100) offcut 4° in the [110] direction by growth of a low-temperature monolithic epitaxial layer and a subsequent high-temperature thick GaAs film all using molecular beam epitaxy (MBE).⁴² On the other hand, the use of MBE for the growth of this layer substantially limits the scalability of this process for the commercial fabrication of dual-junction solar cells on Si. Additionally, the material quality is still below that of GaAs grown on Ge.

1.2.2 Materials Integration by Wafer Bonding and Layer Transfer

By wafer bonding, materials integration can be achieved for crystalline semiconductors on amorphous substrates. Additionally, and more importantly, wafer bonding enables the integration of non-lattice-matched semiconductors in such a way that misfit dislocations that would degrade the material quality in heteroepitaxy are isolated at the bonded interface. Thus, materials that are not suitable for heteroepitaxy can be integrated with bulk quality semiconductor behavior. By incorporating a means of layer transfer with wafer bonding, thin films of a desirable device material can be bonded to mechanically or economically desirable handle substrates. Several good reviews and texts are available on the subject of wafer bonding and layer transfer⁴³⁻⁴⁵ along with historical perspectives on the art of wafer bonding.⁴⁶ The basic principles and history of wafer bonding and layer transfer are introduced below.

1.2.2.1 General Principle of Wafer Bonding

The interaction between flat surfaces now utilized in wafer bonding was first observed and systematically studied by Lord Rayleigh in 1936 with smooth glass surfaces that interact strongly to form a surface-to-surface bond.⁴⁷ The bonding of surfaces in direct wafer bonding occurs due to the interaction of surface terminating species via van der Waals interactions. In this context van der Waals interactions include dipole-dipole, dipole-induced dipole, and dispersion forces between surface terminating groups controlled by the passivation process on the substrates of interest. Van der Waals interactions between molecules in free space decrease with distance as⁴⁸

$$F_v \propto d^{-7} \quad (1.1)$$

Fortunately, forces between molecules forming a plane of surface terminating species interact as⁴⁹

$$F_v \propto d^{-3} \quad (1.2)$$

This power of four difference in the force-distance interaction greatly improves the collective interaction of surface terminating species on a smooth flat surface. Thus, to ensure strong room-temperature bonding the following conditions are necessary:

- Surfaces with desired chemical passivation to maximize the force of interaction between the surfaces,
- Minimal surface micro-roughness,
- Particle-free surfaces to allow intimate contact of surfaces.

In the process of wafer bonding, samples are annealed to enhance the force of interaction and thus strengthen the bond between the materials by means of chemical reactions and rearrangement of atoms at the bonded interface leading to covalent bond formation between the two materials.

1.2.2.2 Processes for Layer Thinning

In most applications it is not desirable to join two full substrates, but rather to bond a thin layer of some device material to a thicker mechanical handle substrate. The thinning of the device layer

has been achieved by many techniques, including epitaxial layer liftoff in which a selective etch layer is epitaxially grown into the device substrate allowing this layer to be slowly etched away following bonding by a lateral etching process that undercuts the bonded film.^{50,51} Unfortunately, the epitaxial layer liftoff technique is by its nature a slow process due to transport limitations of the wet chemical etch, thus placing a practical limit on the size of device region that can be transferred by this process. One way to overcome this limitation in using etch stop layers to define the thickness of a device film is to use bond-and-etch-back techniques. In the bond-and-etch-back process an etch-stop layer is defined beneath the device film. Following bonding the entire device substrate is removed by a combination of grinding and wet chemical etching, stopping just before reaching the device layer by the etch-stop layer.^{52,53} This solves the transport limitations of using an etch-stop layer, but in this case the entire device substrate is consumed, making this thinning technique an undesirable option for many devices because of the economics of sacrificing an entire substrate during the transfer process.

The process of H-induced exfoliation allows a device substrate implanted with hydrogen, or co-implanted with hydrogen and a light gas such as helium, to exfoliate a thin film upon annealing. If that film is made rigid by wafer bonding, then the exfoliation process transfers an intact thin film of extremely uniform thickness. This process was first developed for Si in the fabrication of silicon-on-insulator (SOI) substrates.⁵⁴ Subsequently, it has been developed for most crystalline semiconductors, including Ge⁵⁵ and InP,⁵⁶ the materials of interest in the present thesis. The advantage of using wafer bonding with H-induced exfoliation of the device film to fabricate Ge/Si and InP/Si heteroepitaxial templates is the ability to reuse the device substrate following exfoliation. Chemical mechanical polishing (CMP) can be used to remove the rough damaged layer from the surface of the device substrate following exfoliation. Following CMP the reclaimed device substrate is implanted with hydrogen. The reclaimed substrate is then bonded to a new handle substrate and another layer is exfoliated following upon annealing. In this way, many Ge/Si or InP/Si substrates can be fabricated from a single Ge or InP “donor” substrate.

1.3 Application of Materials Integration by Wafer Bonding and Layer Transfer to Photovoltaics

The processes of wafer bonding and layer transfer described above can be used to fabricate what are commonly referred to as “virtual substrates.” The term virtual substrate was coined to refer to a substrate consisting of a thin film of a foreign material deposited on or bonded to a supporting substrate. The substrate then has the epitaxial and, in the near-surface region, the electrical and lattice properties of the thin device film. At the same time, the virtual substrate has the mechanical, thermal and economic properties of the underlying handle substrate upon which the film is supported. Two applications of wafer bonded virtual substrates to photovoltaic devices are the motivation for this thesis. The virtual substrates are Ge/Si and InP/Si; the applications are alternative substrates for dual- and triple-junction solar cells and a base substrate for a proposed four-junction cell design respectively. The potential advantages of these wafer bonded virtual substrates, as well as the material requirements for their use in these photovoltaic devices are described below.

1.3.1 Ge/Si Wafer Bonded Substrates for Dual- and Triple-Junction Solar Cells

As was described in §1.1.4.3, triple-junction solar cells consist of GaInP, GaAs and Ge active subcells separated by tunnel junctions to allow the efficient conduction of current between cells. As was described above, the optimum cell performance requires current matching between the cells, and in this serendipitous system of Ge and GaAs-related materials this requirement is satisfactorily met in a lattice-matched material group. Despite the level of development and success of the triple-junction cell, there is still strong demand for improvement of cell efficiencies.

Using Ge substrates as mechanical supports and epitaxial templates for the fabrication of triple-junction solar cells confers negative attributes on the cells that can be improved

substantially by using wafer bonded Ge/Si heteroepitaxial templates. Limitations of the conventional triple-junction solar cell design on bulk Ge substrates that are alleviated by fabricating these cells on Ge/Si virtual substrates include:

- The germanium substrates are expensive, constituting nearly 50% of the cost of an uninstalled solar cell. This is one of the factors that limit the use of triple-junction solar cells to space power systems, where savings due competitive specific power and smaller solar cell area offset the added device cost. By fabricating in excess of 10 Ge/Si substrates from a single Ge device substrate, the cell cost can potentially be reduced by 10 to 25%, depending on the costs associated with the added processing steps in the fabrication of Ge/Si substrates. This provides savings for space power applications, and moves triple-junction solar cells toward a cost-competitive price for terrestrial applications.
- Because triple-junction solar cells are used in space power applications, the minimization of weight is an important consideration in selection of space power systems, as was pointed out in §1.1.3.3. The cost of launching a satellite into low earth orbit (LEO) as of 2002 ranged from \$3,000 to \$14,000 per kg, while launching a satellite into geosynchronous orbit (GEO) cost between \$11,500 and \$50,500 (on the Space Shuttle, a rather inefficient vehicle for satellite launches) per kg.⁵⁷ A typical triple junction solar cell is grown on a 140 μm thick Ge substrate. The density of Ge is 5.32 g cm^{-3} ; the density of Si is 2.33 g cm^{-3} .⁵⁸ The absolute mass savings for launching triple-junction cells on Ge/Si wafer bonded substrates rather than Ge is 0.4186 kg m^{-2} . The efficiency of Emcore's Advanced Triple-Junction solar cells is 27.5% at the beginning of life,⁵⁹ providing 372 W m^{-2} power to the satellite. Thus, the potential gain in specific power using wafer bonded Ge/Si substrates to fabricate Emcore's Advanced Triple-Junction solar cells is 890 W kg^{-1} . With satellite power demands ranging up to 10,000 W, the

potential savings per satellite launched could range from \$33,600 to \$157,000 for LEO launches and \$129,000 to \$566,000 for GEO launches. Thus, transferring triple-junction cells to Ge/Si substrate technology can provide considerable savings in space power applications, above and beyond simply reducing substrate costs.

- The mechanical and thermal properties of Ge substrates are less than desirable. Use of thin Ge substrates to minimize weight, necessarily leads to increased yield loss in substrate manufacture, cell fabrication, and panel assembly. The present thickness of 140 μm is presumably a cost-optimized thickness. By switching to Ge/Si wafer bonded substrates, this thickness could be maintained or reduced leading to greater launch cost savings than those estimated above, while simultaneously increasing yield at all processing steps. Additionally, the thermal conductivity of Si is $1,300 \text{ W m}^{-1} \text{ K}^{-1}$ compared to $580 \text{ W m}^{-1} \text{ K}^{-1}$ for Ge.⁵⁸ This difference can lead to lower operating temperatures for triple-junction solar cells under concentration. This in turn would result in higher efficiency and longer lifetime for such cells fabricated on Ge/Si wafer bonded substrates. The improved operation under concentration is of importance for new concentrator designs being considered for space power and for terrestrial installations where concentration is essential to minimize the solar cell cost component of produced power.

The limitations of triple-junction solar cells and associated wafer-bonding-based improvements provided by Ge/Si substrates described above motivate the development of such a cell as shown in Fig. 1.6. The fabrication of a bottom Ge subcell adds considerable technical challenge to the finished device structure in a solar cell fabricated on Ge/Si substrates, while adding only roughly two absolute percent additional efficiency. For this reason, fabrication of GaInP/GaAs two-junction tandem solar cells on Ge/Si substrates is a desirable first step in the development of this technology. Also, because of the minimal sacrificed efficiency and the considerable economic advantages associated with using Ge/Si replacement substrates, dual-

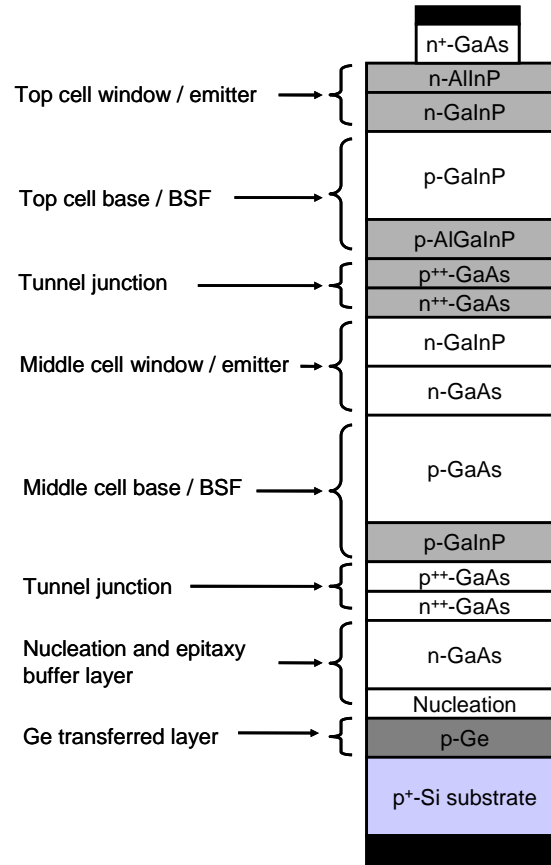


Figure 1.6 Schematic of a two- or three-junction solar cell fabricated on a Ge/Si wafer bonded virtual substrate. In the three-junction cell the Ge transferred layer is p-type and grown to a sufficient thickness to serve as an active layer of the cell structure, while in the two-junction cell the Ge transferred layer is thin and n-type, serving only as an epitaxial template for the growth of the GaAs and GaInP subcell structures.

junction solar cells fabricated on Ge/Si offer a cost performance improvement over traditional triple-junction cells fabricated on Ge substrates.

1.3.2 InP/Si Wafer Bonded Substrates for a Proposed Four-Junction Solar Cell

The transitioning of triple-junction solar cells to Ge/Si wafer bonded substrates described above offers considerable improvement of these devices from an economic standpoint. However, such a triple-junction solar cell on Ge/Si is not anticipated to improve the thermodynamic limiting solar cell efficiency. As was briefly described in §1.1.4.1, photovoltaic efficiency is limited by loss of

power from the solar spectrum due to sub-bandgap photons and thermalization of energy in excess of the bandgap. To minimize this effect, finer discretization of the solar spectrum by spectrum splitting with a multi-junction cell design comprised of more than three subcells can improve the overall cell efficiency, provided that the materials selected for the subcells are of sufficient quality to not limit the overall device. In such a device the requirements are:

- Reasonable current matching of the subcells to prevent limitation of the overall cell operating current,
- Reasonable material quality to prevent loss of power due to increased dark current and thus decreased operating voltage associated with electrically active defects,
- Means of integrating the various constituent materials.

It is difficult to design and construct a four-junction device that meets all of these requirements using heteroepitaxy. One approach that has been pursued to add a fourth, or perhaps even a fifth, subcell to improve the performance of a heteroepitaxially grown, monolithically integrated multi-junction solar cell is the development of a lattice matched InGaAsN subcell with a bandgap near 1.0 eV. The addition of two percent nitrogen to InGaAs to create $\text{In}_x\text{Ga}_{1-x}\text{As}_{0.98}\text{N}_{0.02}$ material is done to shrink the lattice constant of this subcell to closely match that of Ge and GaAs. Unfortunately, defects associated with the poor incorporation of nitrogen in the $\text{In}_x\text{Ga}_{1-x}\text{As}_{0.98}\text{N}_{0.02}$ film have prevented this subcell from achieving reasonable photo-currents. Thus, all four-junction solar cells fabricated in this way have actually led to efficiency loss relative to a triple-junction solar cell.⁶⁰ This highlights the difficulty of integrating more subcells by developing new lattice-matched epitaxial material.

A more desirable approach would be to select four subcell materials from well-developed binary and ternary III-V semiconductors shown in Fig. 1.5. However, no such lattice-matched group exists. As was mentioned in §1.2.2, wafer bonding and layer transfer enables the integration of non-lattice-matched materials, while isolating associated misfit dislocations at the bonded interface. Thus, if one does not make the bonded interface of the materials an active

region of the device, then wafer bonding enables optimal selection of the subcell materials with little concern for the lattice constant of those materials. A four-junction solar cell design based on this principle was first described by Sharps *et al.* using an epitaxially grown bottom two subcells of InGaAsP and InGaAs grown on an InP substrate. This bottom subcell pair was then bonded using a metallic bonding layer to a top subcell structure consisting of a conventional dual-junction structure of GaInP and GaAs grown on a thin GaAs substrate.⁶¹ Of course, there are some obvious sources of efficiency loss in such a design, primarily the reflection and attenuation of the solar spectrum at the metallic interfacial bond. Additionally, the presence of the relatively thick GaAs substrate in the bonded structure presents an undesirable tradeoff. Either the series resistance from the GaAs leads to efficiency loss or heavier doping to minimize electrical resistance leads to increased attenuation of the spectrum seen by the bottom two subcells due to free carrier absorption in the GaAs substrate.

An alternative version of this wafer bonding enabled four-junction solar cell has been proposed and is shown in Fig. 1.7.⁶² In this device, several improvements are proposed over the Sharps *et al.* design. First, the InP substrate is replaced with a lower cost and lower mass InP/Si wafer bonded heteroepitaxial template. Additionally, the metallic bonded interface is replaced by a direct hydrophobic bonded interface that leads to ohmic electric contact with significantly less reflectance and absorption loss. Also, in this proposed structure a thin exfoliated film of thin Ge or GaAs bonded to the bottom InGaAsP/InGaAs/InP/Si structure is proposed to serve as the heteroepitaxial template for the subsequent growth the GaInP/GaAs two subcell structure. This innovation saves considerable mass in the finished cell structure. The anticipated practical efficiency of this four-junction wafer bonded solar cell design is predicted to be 35.4% under one sun AM0 radiation (operation in outer space with no atmospheric absorption). This practical efficiency estimate is a rough calculation based upon the known performance of the constituent subcells and the anticipated solar spectrum reaching the subcells. An analysis of the

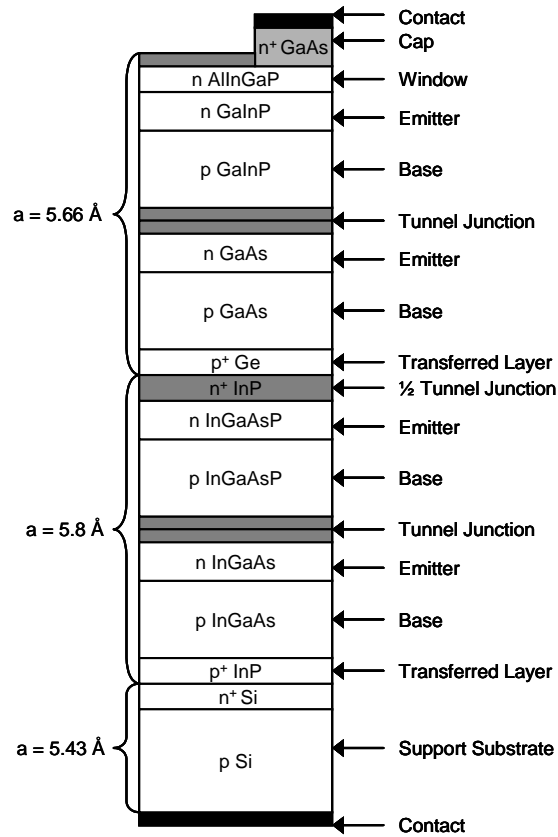


Figure 1.7 Schematic of a proposed four-junction wafer bonding enabled solar cell fabricated on a InP/Si wafer bonded virtual substrate with a wafer bonded heteroepitaxial template of Ge (or GaAs) integrated with the bottom two subcell structure by wafer bonding and layer transfer.⁵⁵

thermodynamic limiting efficiency of this four-junction cell design is more thoroughly described in Chapter 2.

1.3.3 Photovoltaic Device Requirements for Virtual Substrates Fabricated by Wafer Bonding and Layer Transfer

The potential for photovoltaic device improvement by wafer bonding and layer transfer for the integration of non-lattice-matched semiconductors is substantial. The requirements for implementing the use of wafer bonding and layer transfer serve as the motivation for most of the work in this thesis and are as follows:

- A robust process for fabricating Ge/Si and InP/Si wafer bonded heteroepitaxial templates is the essential first step in developing solar cells that rely on this integration capability.

- Conventional multi-junction and single-junction cells all rely upon back-surface electrical contact for extraction of power from the device. This is done to minimize the processing necessary to fabricate solar cells and thereby minimize construction costs. Additionally, making contacts to the back of a thin-film solar cell by an etch process from the front surface of the cell also causes loss of the total area for light absorption causing unnecessary efficiency loss. For these reasons, it is necessary to form an electrically conductive interface with ohmic, low-resistance properties. It is preferable to do this without resorting to a metallic bonding layer, because of contamination of the device regions of the cells with transition-metal contaminants in subsequent processing.
- Perhaps the most challenging step in the development of wafer bonding enabled solar cell designs is the preparation of a suitable epitaxial surface. The optimization of Ge and InP surfaces for nucleation and growth of III-V semiconductors has been the focus of years of research in the solar power, optoelectronic, and heterojunction bipolar transistor industries. When preparing the growth surface of Ge/Si and InP/Si wafer bonded heteroepitaxial templates, it is first necessary to reduce the surface roughness and remove damage in the near surface region of the transferred layer incurred during implantation and fracture processes involved in the H-induced exfoliation process. Additionally, growth on a heterogeneously integrated thin film on a foreign substrate presents unique challenges pertaining to thermo-mechanical strain and stress in the thin film, which change the film surface properties relative to a free-standing substrate of the same material.

1.4 *Organization of Thesis*

The technological requirements for wafer bonding enabled photovoltaic devices highlighted in the previous section provide an organizing structure to the contents of this thesis. The chapter-by-chapter content of the thesis is as follows:

Chapter 2 provides a description of the thermodynamic limits of photovoltaic devices in general and to wafer bonding enabled solar cell designs in particular. Using the detailed balance calculation of photovoltaic limiting efficiency, the importance of device geometry, operating temperature, and subcell bandgap selection to wafer bonding enabled cell designs are discussed in detail.

Chapter 3 provides a more detailed background of some of the fundamental issues in designing a fabrication process for wafer bonded substrates. These issues are discussed for the material combinations of Ge/Si and InP/Si are discussed in particular. Additionally, successful processes for wafer bonding and layer transfer are described.

Chapter 4 summarizes the first known study of the role of hydrogen in the exfoliation process of Ge and InP. In this analysis atomic force microscopy (AFM), transmission electron microscopy (TEM), thermal desorption mass spectroscopy and Fourier transform infrared (FTIR) spectroscopy are used to study the physical structure of these materials along with the chemical state of implanted hydrogen during the exfoliation process.

In Chapter 5 the electrical properties of hydrophobically wafer bonded interfaces are studied for both Ge/Si and InP/Si. Ohmic, low-resistance electrical contact is demonstrated using heavily doped substrates to form wafer-bonded heterojunctions with narrow depletion regions. Additionally, the evolution Ge/Si Schottky-diode-like p^+ -Ge/p-Si wafer bonded structures are used to study the dependence of the electrical properties of wafer bonded interfaces as a function of annealing and azimuthal twist angle between the bonded substrates. This enables the impact of chemical and defect states at the bonded interface on the electrical properties of the bonded structures.

In Chapter 6 preliminary results for the epitaxial growth of III-V semiconductors on Ge/Si and InP/Si substrates are discussed. Additionally, results for surface improvement processes, including chemical etching and chemical mechanical polishing are discussed and correlated to improved optical properties of InGaAs grown on InP/Si heteroepitaxial templates.

In Chapter 7 the content of this thesis is summarized and further work relating to the project objectives is proposed.

1.5 *References*

- ¹ D. L. Goodstein, *Out of Gas* (W. W. Norton, New York, 2004).
- ² K. S. Deffeyes, *Hubbert's Peak: the Impending World Oil Shortage* (Princeton University Press, Princeton, 2001).
- ³ C. J. Campbell, "Forecasting Global Oil Supply 2000-2050," Report No. M. King Hubbert Center for Petroleum Supply Studies Newsletter #2002/3 (2002).
- ⁴ A. J. McMichael, *Planetary Overload: Global Environmental Change and the Health of the Human Species* (Cambridge University Press, Cambridge, 1993).
- ⁵ *Handbook of Photovoltaic Science and Engineering; Vol.*, edited by A. Luque and S. Hegedus (John Wiley & Sons, West Sussex, England, 2003).
- ⁶ *Clean Electricity from Photovoltaics; Vol.*, edited by M. D. Archer and R. Hill (Imperial College Press, London, 2001).
- ⁷ S. M. Sze, *Physics of Semiconductor Devices*, 2nd ed. (John Wiley & Sons, New York, 1981).
- ⁸ J. Zhao, A. Wang, and M. A. Green, *Progress in Photovoltaics: Research and Applications* **7**, 471-474 (1999).
- ⁹ M. A. Green, *Third Generation Photovoltaics: Advanced Solar Energy Conversion* (Springer, New York, 2003).
- ¹⁰ K. W. J. Barnham, I. Ballard, J. Barnes, J. G. Connolly, P. Griffin, B. G. Klugtinger, J. Nelson, E. Tsui, and A. Zachariou, *Applied Surface Science* **113/114**, 722-733 (1997).

- ¹¹ K. W. J. Barnham, I. Ballard, J. G. Connolly, N. Ekins-Daukes, B. G. Klugtinger, J. Nelson, J. Rohr, and M. Mazzer, *Journal of Materials Science - Materials in Electronics* **11**, 531-536 (2000).
- ¹² J. Nelson, in *Clean Electricity from Photovoltaics; Vol. 1*, edited by M. D. Archer and R. Hill (Imperial College Press, London, 2001).
- ¹³ A. S. Brown and M. A. Green, *Journal of Applied Physics* **94**, 6150-6158 (2003).
- ¹⁴ T. Trupke, M. A. Green, and P. Würfel, *Journal of Applied Physics* **92**, 4117-4122 (2002).
- ¹⁵ T. Trupke, M. A. Green, and P. Würfel, *Journal of Applied Physics* **92**, 1668-1674 (2002).
- ¹⁶ P. Gibart, F. Auzel, J.-C. Guillaume, and K. Zahraman, *Japanese Journal of Applied Physics* **35**, 4401-4402 (1996).
- ¹⁷ N. H. Karam, R. R. King, M. Haddad, J. H. Ermer, H. Yoon, H. L. Cotal, R. Sudharsanan, J. W. Eldredge, K. M. Edmondson, D. E. Joslin, D. D. Krut, M. Takahashi, W. Nishikawa, M. Gillanders, J. Granata, P. Hebert, B. T. Cavicchi, and D. R. Lillington, *Solar Energy Materials & Solar Cells* **66**, 453-466 (2001).
- ¹⁸ K. A. Bertness, S. R. Kurtz, D. J. Friedman, A. E. Kibbler, C. Kramer, and J. M. Olson, *Applied Physics Letters* **65**, 989-991 (1994).
- ¹⁹ C. M. Fetzer, R. R. King, P. C. Colter, K. M. Edmondson, D. C. Law, A. P. Stravides, H. Yoon, J. H. Ermer, M. J. Romero, and N. H. Karam, *Journal of Crystal Growth* **261**, 341-348 (2004).
- ²⁰ M. Yamaguchi, *Semiconductors* **33**, 961-964 (1999).
- ²¹ M. Yamaguchi, in *Clean Electricity from Photovoltaics; Vol. 1*, edited by M. D. Archer and R. Hill (Imperial College Press, London, 2001), p. 347-375.
- ²² R. R. King, C. M. Fetzer, P. C. Colter, K. M. Edmondson, D. C. Law, A. P. Stravides, H. Yoon, G. S. Kinsey, H. L. Cotal, J. H. Ermer, R. A. Sherif, and N. H. Karam, in *Lattice-matched and metamorphic GaInP/GaInAs/Ge concentrator solar cells*, Osaka, 2003.

- 23 J. Y. Tsao, *Materials Fundamentals of Molecular Beam Epitaxy* (Academic Press, Boston, 1993).
- 24 J. Tersoff, *Physical Review B* **43**, 9377-9380 (1991).
- 25 H. Sunamura, N. Usami, Y. Shiraki, and S. Fukatsu, *Applied Physics Letters* **66**, 3024-3026 (1995).
- 26 D. J. Eaglesham and M. Cerrulo, *Physical Review Letters* **64**, 1943-1946 (1990).
- 27 C. L. Andre, J. J. Boeckl, C. W. Leitz, M. T. Currie, T. A. Langdo, E. A. Fitzgerald, and S. A. Ringel, *Journal of Applied Physics* **94**, 4980-4985 (2003).
- 28 M. T. Currie, S. B. Samavedam, T. A. Langdo, C. W. Leitz, and E. A. Fitzgerald, *Applied Physics Letters* **72**, 1718-1720 (1998).
- 29 R. M. Sieg, S. A. Ringel, S. M. Ting, S. B. Samavedam, M. T. Currie, T. A. Langdo, and E. A. Fitzgerald, *Journal of Vacuum Science and Technology B* **16**, 1471-1474 (1998).
- 30 R. M. Sieg, J. A. Carlin, J. J. Boeckl, S. A. Ringel, M. T. Currie, S. M. Ting, T. A. Langdo, G. Taraschi, E. A. Fitzgerald, and B. M. Keyes, *Applied Physics Letters* **73**, 3111-3113 (1998).
- 31 J. A. Carlin, S. A. Ringel, E. A. Fitzgerald, and M. Bulsara, *Progress in Photovoltaics: Research and Applications* **8**, 323-332 (2000).
- 32 S. B. Samavedam, M. T. Currie, T. A. Langdo, and E. A. Fitzgerald, *Applied Physics Letters* **73**, 2125-2127 (1998).
- 33 M. E. Groenert, A. J. Pitera, R. J. Ram, and E. A. Fitzgerald, *Journal of Vacuum Science and Technology B* **21**, 1064-1069 (2003).
- 34 V. K. Yang, M. E. Groenert, C. W. Leitz, A. J. Pitera, M. T. Currie, and E. A. Fitzgerald, *Journal of Applied Physics* **93**, 3859-3865 (2003).
- 35 H. Kroemer, T.-Y. Liu, and P. M. Petroff, *Journal of Crystal Growth* **95**, 96-102 (1989).
- 36 W. A. Harrison, E. A. Kraut, J. R. Waldrop, and R. W. Grant, *Physical Review B* **18**, 4402-4410 (1978).

- 37 R. M. Sieg, S. A. Ringel, S. M. Ting, E. A. Fitzgerald, and R. N. Sacks, *Journal of Electronic Materials* **27**, 900-907 (1998).
- 38 S. M. Ting, E. A. Fitzgerald, R. M. Sieg, and S. A. Ringel, *Journal of Electronic Materials* **27**, 451-461 (1998).
- 39 Q. Xu, J. W. P. Hsu, S. M. Ting, E. A. Fitzgerald, R. M. Sieg, and S. A. Ringel, *Journal of Electronic Materials* **27**, 1010-1016 (1998).
- 40 M. Sugo, Y. Takanashi, M. M. Al-Jassim, and M. Yamaguchi, *Journal of Applied Physics* **68**, 540-547 (1990).
- 41 O. Parilloud, E. GilLafon, B. Gerard, P. Etienne, and D. Pribat, *Applied Physics Letters* **68**, 2654-2656 (1996).
- 42 P. J. Taylor, W. A. Jesser, J. D. Benson, M. Martinka, J. H. Dinan, J. Bradshaw, M. Lara-Taysing, R. P. Leavitt, G. Simonis, W. Chang, W. W. Clark III, and K. A. Bertness, *Journal of Applied Physics* **89**, 4365-4375 (2001).
- 43 U. Gosele and Q.-Y. Tong, *Annual Review of Materials Science* **28**, 215-241 (1998).
- 44 Q.-Y. Tong and U. Gosele, *Semiconductor Wafer Bonding: Science and Technology* (John Wiley & Sons, New York, 1999).
- 45 Q.-Y. Tong and U. Gosele, *Materials Chemistry and Physics* **37**, 101-127 (1994).
- 46 J. Haisma and G. A. C. M. Spierings, *Materials Science and Engineering R* **37**, 1-60 (2002).
- 47 L. Rayleigh, *Proceedings of the Physical Society* **40**, 326 (1936).
- 48 C. Kittel, *Introduction to Solid State Physics*, 2nd ed. (John Wiley and Sons, New York, 1986).
- 49 R. Horn, *Journal of the American Ceramics Society* **73**, 1117 (1990).
- 50 A. Ersen, I. Schnitzer, E. Yablonovitch, and T. Gmitter, *Solid State Electronics* **36**, 1731-1739 (1993).

- 51 C. C. Cheng, A. Scherer, R. C. Tyan, Y. Fainman, G. Witzgall, and E. Yablonovitch,
Journal of Vacuum Science and Technology B **15**, 2764-2767 (1997).
- 52 K. Mori, K. Tokutome, and S. Sugou, Electronics Letters **31**, 284 (1995).
- 53 T. Yonehara, K. Sakaguchi, and N. Sato, Applied Physics Letters **64**, 2108 (1994).
- 54 M. Bruel, Electronics Letters **31**, 1201 (1995).
- 55 Q.-Y. Tong, K. Gutjahr, S. Hopfe, U. Gosele, and T.-H. Lee, Applied Physics Letters **70**,
1390-1392 (1997).
- 56 B. Aspar, H. Moriceau, E. Jalaguier, C. Lagahe, A. Soubie, B. Biasse, A. Papon, A.
Claverie, J. Grisolia, G. Benassayag, F. Letertre, O. Rayssac, T. Barge, C. Maleville, and
B. Ghyselen, Journal of Electronic Materials **30**, 834-840 (2001).
- 57 www.futuron.com.
- 58 www.ioffe.ru/SVA/NSM/Semicond/.
- 59 www.emcore.com.
- 60 S. R. Kurtz, A. A. Allerman, C. H. Seager, R. M. Sieg, and E. D. Jones, Applied Physics
Letters **77**, 400-402 (2000).
- 61 P. Sharps, M. Timmons, J. Hills, and J. Gray, in *Wafer bonding for use in mechanically
stacked multi-bandgap cells*, Anaheim, CA, 1997 (IEEE Press), p. 895-898.
- 62 J. M. Zahler, A. Fontcuberta i Morral, C.-G. Ahn, H. A. Atwater, M. W. Wanlass, C.
Chu, and P. A. Iles, in *Wafer bonding and layer transfer processes for 4-junction high
efficiency solar cells*, New Orleans, 2002.

Chapter 2: Detailed Balance Calculation of the Thermodynamic Limiting Efficiency of Wafer-Bonding Enabled Solar Cells

When considering a new device design to achieve greater photovoltaic efficiency, it is instructive to consider the thermodynamic limiting efficiency for the proposed structure to determine if there is sufficient opportunity for efficiency improvements over existing devices. Additionally, the thermodynamic limiting efficiency of photovoltaic devices provides an excellent illustration of the fundamental limits of efficiency in photovoltaic energy conversion described in §1.1.3.1. This thermodynamic limiting efficiency is determined by the detailed-balance model originally developed by Shockley and Quiesser, and described in the following section.¹

2.1 The Detailed-Balance Theory of Photovoltaic Efficiency

There are many models and analyses based upon the performance of photovoltaic materials available for device construction.²⁻⁴ These models, which take measured material parameters such as minority carrier lifetime, diffusivity, surface recombination velocity and spectral absorption as inputs into the governing equations of p-n junction device. The governing equations are then solved numerically or analytically subject to limiting assumptions. Such materials-based models are excellent tools for determining the suitability of various real materials in new and existing photovoltaic devices. Additionally, these models are generally excellent tools for the determination of break-even performance parameters for materials, and for determining the effect

of certain aspects of geometric design on the achievable efficiency for a solar cell design. However, these models do not address the fundamental limits of efficiency that thermodynamics places on a solar cell. This limiting efficiency defines the asymptotic limit of efficiency improvement as the materials of construction and cell design of a given solar cell structure are perfected.

The detailed-balance theory of the fundamental thermodynamic model of the limiting efficiency of an absorber illuminated by a given spectrum has been described and reviewed in multiple publications.^{1,5-8} The detailed-balance theory of thermodynamic limiting efficiency is an excellent tool for gauging the promise of wholly new designs without regard to the impact of constraints arising from the actual available materials for constructing the system. Detailed-balance calculations are also valuable as a means of assessing the opportunity for further optimization of a given cell design. Presumably, as one asymptotically approaches the thermodynamic limiting efficiency for a cell, the return on invested time and money in research is significantly diminished. Finally, in the present case the detailed-balance model provides an excellent illustration of both the promise and the design constraints of multi-junction solar cell structures, particularly new multi-junction solar cells enabled by wafer bonding and layer transfer.

2.1.1 Formulation of the Detailed-Balance Theory for a Single-Junction Solar Cell

The efficiency of a solar cell is calculated by simply dividing the power extracted from the cell by the integrated power of the solar spectrum incident on the cell.

$$\eta = \frac{J(V) \cdot V}{P} \quad (2.1)$$

Where, $J(V)$ is the current density generated by the solar cell as a function of operating voltage.

It is in the estimation of the generated current at a given cell potential that the detailed-balance

model is applied. First proposed by Shockley and Quiesser in 1960,¹ the detailed-balance model makes the following basic assumptions about an ideal solar cell:

- All photons of energy greater than the band gap of the cell are absorbed by the cell to form electron hole pairs.
- All recombination of carriers occurs radiatively. That is, there are no recombination centers which reduce the lifetime and hence the collection efficiency of carriers that are a common feature of the materials that make real cells. Essentially, this and the previous point mean that the absorber is a perfect defect-free material.
- The radiation is non-thermal with a chemical potential equal to the separation of the electron and hole quasi-Fermi levels, i.e., the operating potential of the cell, V .⁹ This is a modification of the original Shockley and Quiesser formulation of the detailed-balance model which has been adopted by recent analyses of proposed photon-conversion next-generation solar cells by Martin Green *et al.*¹⁰⁻¹³ The basis for using this radiation model is described by Würfel as an extension of Planck's law for non-thermal radiation from a two-level photon gas at a chemical potential, μ .¹⁴
- Finally, the detailed-balance model makes the assumption that the number of photons absorbed by the cell must be equivalent to the number of photons reemitted through radiative recombination plus the number of electron-hole pairs extracted at the cell chemical potential by the contacts.

For the present work, the measured solar spectra for AM1.5 and AM0 radiation, as measured by the National Renewable Energy Laboratory will be used (Fig. 2.1) rather than the black body spectrum frequently used in the literature.¹⁵ The use of black body radiation eases the calculation, especially if approximations are made for the non-thermal radiation from the cell. These approximations taken together give an analytical set of equations that can be used to quickly estimate the detailed-balance efficiency of a given cell. However, in using an approximated

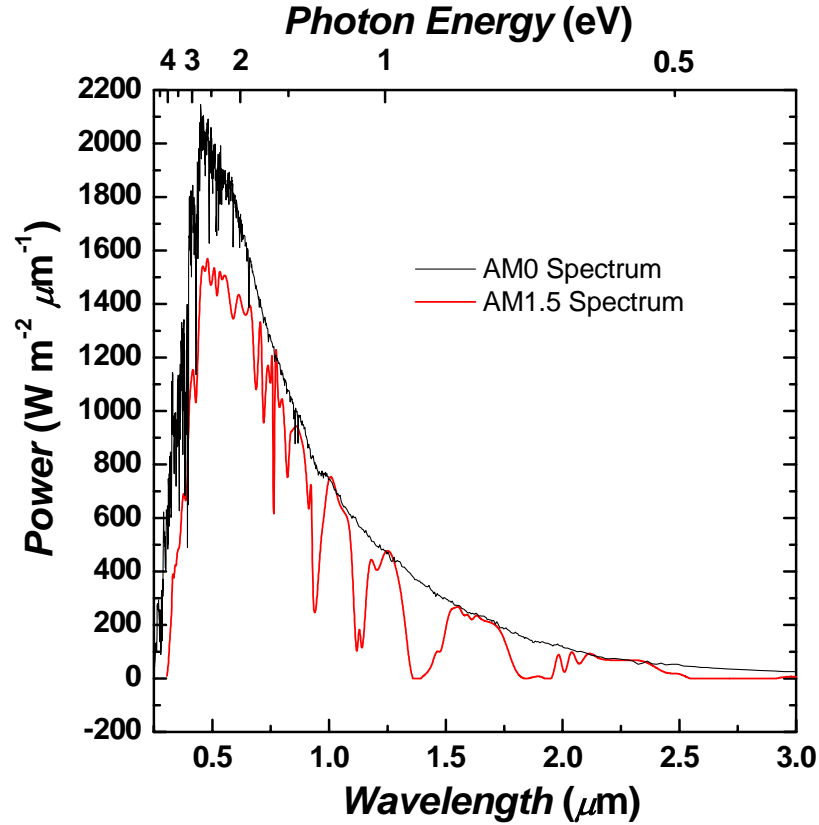


Figure 2.1 The AM1.5 solar spectrum used in the calculation of the detailed balance efficiency.

spectrum to represent the actual solar spectrum, the results of the analysis do not pertain to the real radiation environment in which all cells must operate. For this reason, the AM1.5 spectrum will be the spectrum used for comparison of the performance of various cell designs. For certain structures it is necessary to assess the performance of the device under AM0 illumination to illustrate the advantages of the design. From these spectra the number of photons arriving in the cell can be determined as a function of energy. Thus, the number of carriers generated by solar illumination is given by

$${}^{sol} N(E_G, \infty, C) = C \sum_{E=E_G}^{\infty} \rho(E) \Delta E \quad (2.2)$$

where,

E_G = the cell band gap,

C = the concentration of the incident solar radiation,

$\rho(E)$ = the number of photons per unit energy in the AM1.5 solar spectrum.

As mentioned above, the number of carriers lost due to radiative recombination is given by the generalization of Kirchoff's law for selective photon emission recently used by Green *et al.*^{11,14}

$${}^{rad}N(E_G, \infty, T, V, \varepsilon) = \frac{\varepsilon}{4\pi^3 \hbar^3 c^2} \int_{E_G}^{\infty} \left\{ (\hbar\omega)^2 \left[\exp\left(\frac{\hbar\omega - qV}{kT}\right) - 1 \right]^{-1} \right\} d\hbar\omega \quad (2.3)$$

where,

T = the cell operating temperature.

V = the cell operating voltage, equal to the chemical potential of radiation.

$\varepsilon = \pi n^2 \sin^2(\theta_c)$, the étendue.

θ_c = the critical angle for emission to a medium of a different refractive index.

The étendue of the emitter is a geometrical factor representing the degree of coupling of emission from a radiating body into the surrounding material. For radiative emission from the front surface of a cell into air or space the étendue, ε_{em} , is equal to π . This is based on the assumption that the surface of the cell has been modified by some combination of texturing and coatings to minimize reflection from the front surface. The étendue of internal surfaces is a function of the design and materials involved in the cell.

2.1.2 Detailed-Balance Efficiency Calculation for a Single-Junction Solar Cell

In a single-junction solar cell the thermodynamic limiting efficiency is a function of four key parameters: the absorber band gap, the solar concentration, the cell operating temperature, and the cell geometry. The formulation of the detailed-balance described in the previous section has been

applied to illustrate the effect of these parameters as well as the inherent limitation of a single-cell solar cell.

The operating current of a single-junction cell is calculated by a simple current balance defined as

$$\frac{J}{q} = {}^{AM1.5}N(E_G, \infty, C) - {}^{rad}N(E_G, \infty, T, V, \varepsilon_{em}) \quad (2.4)$$

where,

${}^{AM1.5}N(E_G, \infty, C)$ = the integrated flux of photons above the band gap arriving at the cell in the AM1.5 solar spectrum at a concentration C ,

${}^{rad}N(E_G, \infty, T, V, \varepsilon_{em})$ = the reemitted photons lost by non-thermal radiation above the band gap, at an operating voltage V .

A single-junction solar cell can be designed in many geometrical forms which impacts the detailed-balance limiting efficiency of the cell structure. Three basic geometries that will be considered here are:

- **A thin single-junction on a thick substrate.** In this geometry the separation of carriers is considered to occur in the near surface region of the cell with absorption of carriers in the thick substrate below the near-surface region not contributing to the current generated by the cell. Thus, all photons above the band gap are absorbed in the active cell structure, but reemitted photons can either be lost through the front surface of the cell or into the thick substrate. In either emission process, the photons are no longer able to contribute to the photo-current of the cell. As stated in the previous section the étendue of the cell for radiation from the front surface is π . However, for emission of radiation into the substrate below the cell, the étendue has a value of $\varepsilon_m = \pi n_i^2$. Where n_i refers to the refractive index of the semiconductor in question. For the purpose of simplifying the calculations, the refractive index is not adjusted as a function of wavelength or

semiconductor material and is assigned a constant value of 3.5, consistent with semiconductors commonly employed in photovoltaic applications. Thus, for a solar cell on a thick substrate, $\varepsilon_{in} = 12.25\pi$ into the support substrate. For this geometry the total étendue for the structure is 13.25π .

- **A thin single-junction on a low-index support substrate.** In this geometry the emission from the back surface into the cell below is altered by the critical angle for emission into the support material. The refractive index for this geometry is taken to be equal to the average value for sapphire, 1.85. The étendue for the back surface is thus given by $\varepsilon_{in} = \pi n_i^2 \sin^2 \theta_C = \pi n_o^2 = 3.4225\pi$. Thus, the loss of current due to radiative reemission at the back surface is significantly reduced. For this geometry the total étendue is 4.4225π . This geometry pertains to a thin film device transferred to a low-index substrate, such as Sapphire or glass.
- **A thin single-junction on a reflective surface contact.** In this geometry the use of a complete metal back surface contact acts as a mirror to reflect the back surface emission back into the cell. Thus, the étendue of the back surface is zero, and the total étendue for the structure is π .

The effect of cell operating temperature as a function of band gap for one-sun AM1.5 radiation is shown in Fig. 2.2 for all three geometries. The local maxima are attributed to the atmospheric absorption peaks in the AM1.5 spectrum. The three plots clearly illustrate the point that even when considering the maximum thermodynamic efficiency of a cell structure, the operating parameters selected for the cell have a strong effect on performance. The limit of efficiency as the temperature approaches absolute zero is referred to as the ultimate efficiency, and is the achievable efficiency under the assumption that no radiative emission occurs.¹⁶ The theoretical operation of a cell at absolute zero allows the cell to be operated at a voltage equal E_G/q while collecting all photo-generated carriers. As can also be seen, the cell temperature has a

greater impact on the performance of narrow band gap solar cells. This is consistent with equation 2.3. The maximum radiative emission occurs for photons close to the band gap. The expression in the exponential of equation 2.3 is the difference between the photon energy – equal to the band gap energy for non-thermal emission – and the operating voltage. Thus, when the band gap is small, there is little room for the potential to operate below the band gap energy. This effect is strong enough to lead to a prediction of zero conversion efficiency for narrow band gap materials above a temperature of 500 K. The impact of the cell geometry is less obvious, but can still be seen to contribute to the efficiency on the order of ~1% absolute. Simply put, the higher the étendue, the greater the loss component associated with radiative reemission of photons into the surroundings.

The effects of the étendue of the three thin-film geometries for the single-junction cell are also illustrated by Fig. 2.3, which shows the fill-factor for the three geometries as a function of temperature of operation. The fill-factor is a figure of merit for solar cells that indicates the quality of the current-voltage curve for the operating conditions of the cell. To be exact, the fill-factor is the ratio of the power produced by the cell operating at its maximum power point divided by the power defined by the product of the open-circuit voltage of the cell and the short-circuit current of the cell.

$$FF = \frac{P_m}{J_{sc} V_{oc}} \quad (2.5)$$

The fill-factor as a function of temperature, band gap and cell geometry shows that cells that emit more efficiently into their surroundings are more sensitive to the operating temperature of the cell.

Figure 2.4 shows the effect of concentration of incident AM1.5 radiation on the cell efficiency for all three cell geometries operating at 300 K. When concentration is used to decrease

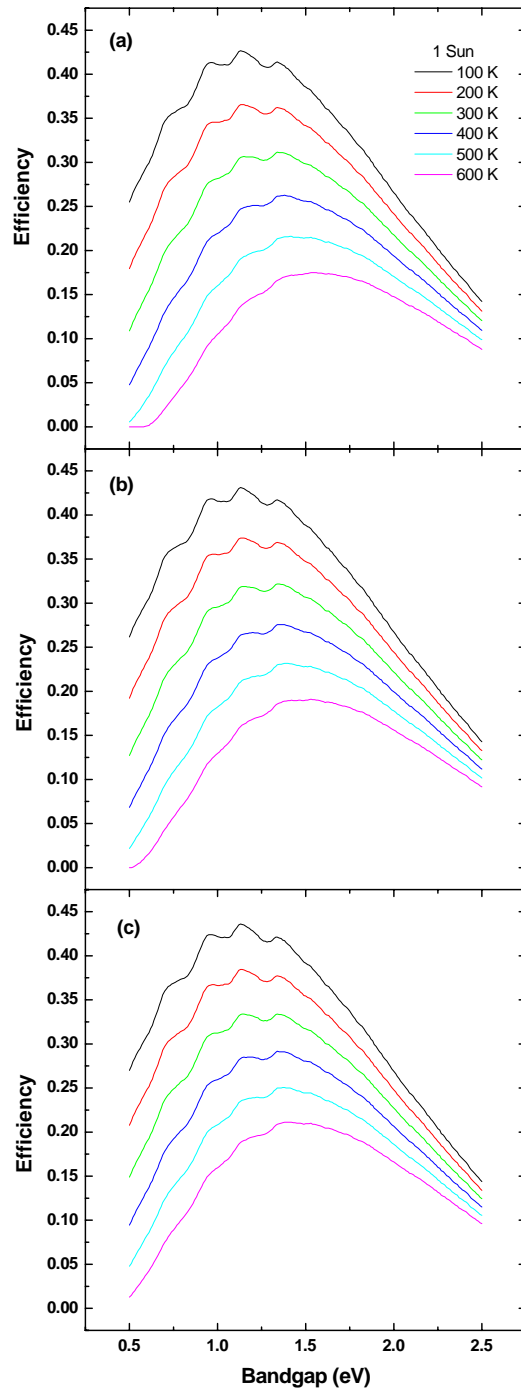


Figure 2.2 The detailed balance efficiency as a function of temperature for one-sun AM1.5 illumination for (a) a thin-film single-junction solar cell on a thick semiconductor substrate, (b) a thin-film single-junction solar cell on a low-index substrate, and (c) a thin-film single-junction solar cell on a reflective surface.

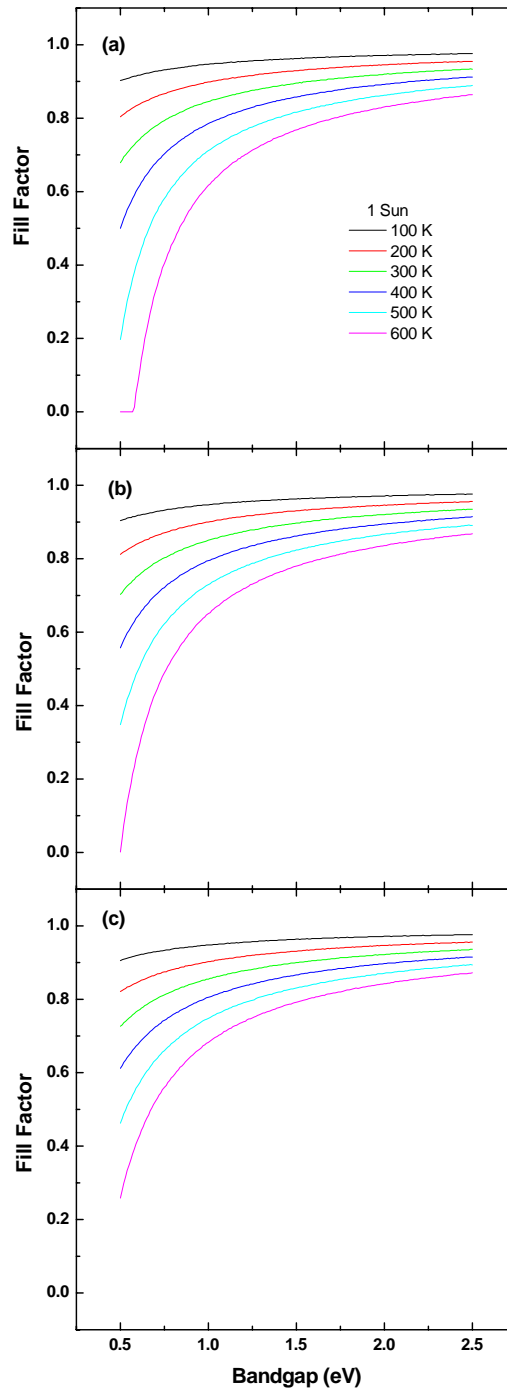


Figure 2.3 The detailed balance fill factor as a function of temperature for a concentration of 1 sun for (a) a thin-film single-junction solar cell on a thick semiconductor substrate, (b) a thin-film single-junction solar cell on a low-index substrate, and (c) a thin-film single-junction solar cell on a reflective surface.

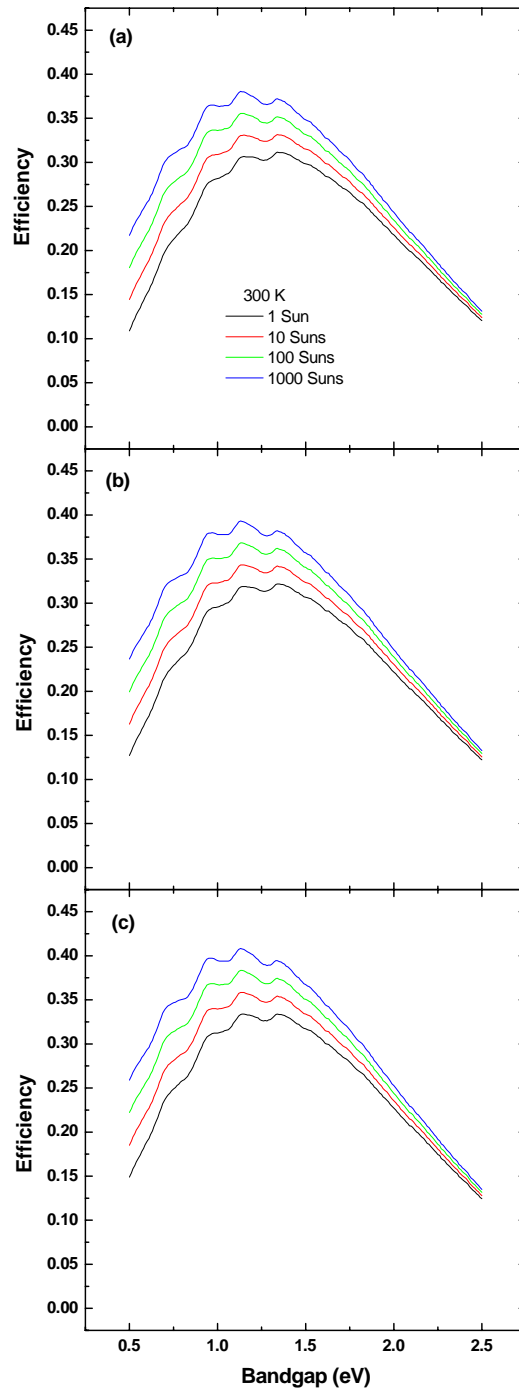


Figure 2.4 The detailed balance efficiency as a function of solar concentration for a temperature of 300 K for (a) a thin-film single-junction solar cell on a thick semiconductor substrate, (b) a thin-film single-junction solar cell on a low-index substrate, and (c) a thin-film single-junction solar cell on a reflective surface.

the device area necessary for collecting a large area of illumination, the resulting photo-current is increased. When operated under concentration, a cell can thus operate at a higher potential, because the accompanying rise in radiative reemission represents a less significant fraction of the concentration-enhanced photo-current. This effect is once again strongest for narrow band gap absorbers where the separation between the operating potential and the band gap energy is a larger fraction of the band gap energy. Additionally, cell designs that are most prone to reemission to the surroundings benefit the most from concentration. The fill-factor versus the concentration is shown in Fig. 2.5. The effect of concentration on the fill-factor is less dramatic than the effect of temperature. The preferential fill-factor improvement at lower band gaps follows the same logic as above. (It is important to note that there is a serious technological challenge in operating a real device at both high concentration and low temperature.) The results of this analysis are captured in Tab. 2.1. The maximum efficiency and associated band gap are reported for all of the conditions mentioned above. Additionally, the results of previous detailed balance analyses reported in the literature are summarized for comparison. Based on these literature values the present single-junction detailed-balance analysis appears consistent with previously reported values.

2.2 Detailed-Balance Efficiency of Multi-Junction Solar Cell Structures

As can be seen in Fig. 2.1 the distribution of power in the solar spectrum is a broad distribution that can not be efficiently harnessed by utilizing a single band gap semiconductor. As was described in §1.1.3.1 and illustrated in Fig. 1.3, the two dominant sources of loss are photons with energies below the band gap and photons with energies in excess of the band gap. Photons with energies below the gap are not collected by the absorber. While photons with energies above the gap are absorbed, photon energy in excess of the band gap energy generates hot carriers that

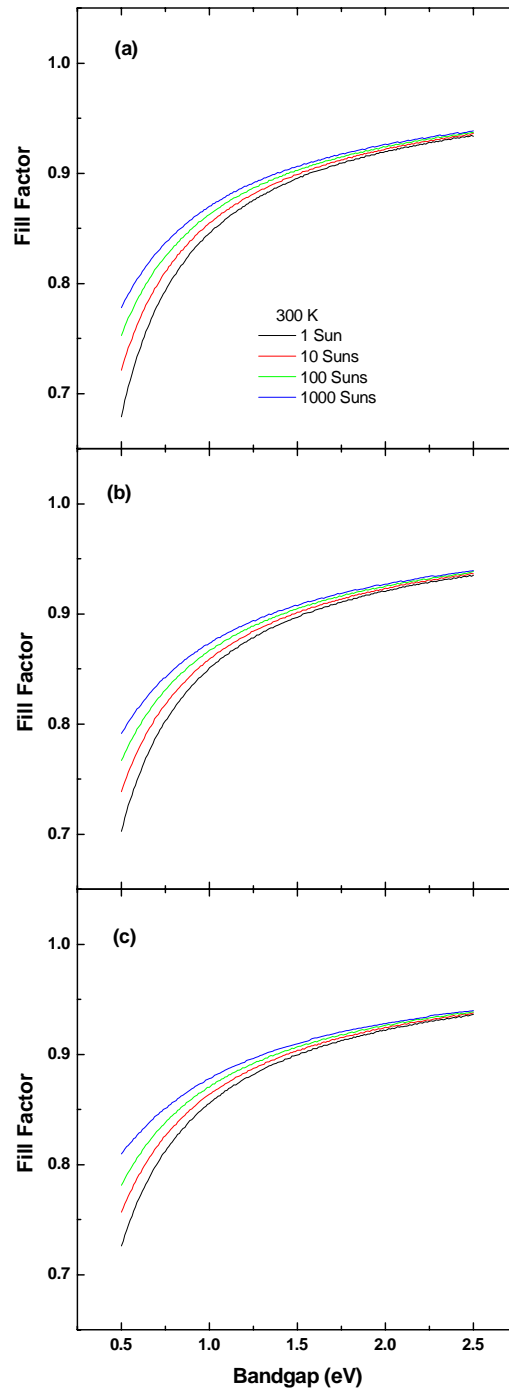


Figure 2.5 The detailed balance fill factor as a function of solar concentration for a temperature of 300 K for (a) a thin-film single-junction solar cell on a thick semiconductor substrate, (b) a thin-film single-junction solar cell on a low-index substrate, and (c) a thin-film single-junction solar cell on a reflective surface.

Table 2.1 Summarized results for the detailed balance efficiency of a single-junction thin-film solar cell in AM1.5 illumination as a function of film geometry, operating temperature and operating concentration.

			Maximum Power Condition		
			Bandgap (eV)	Fill Factor	Efficiency
Thin-Film cell on a thick semiconductor substrate ($\epsilon = 13.25\pi$)	Constant Concentration (1 Sun)	100 K	1.13	0.953	0.427
		200 K	1.14	0.910	0.366
		300 K	1.34	0.883	0.311
		400 K	1.38	0.846	0.263
		500 K	1.41	0.803	0.216
		600 K	1.42	0.753	0.172
	Constant Temp. (300 K)	1 Sun	1.15	0.865	0.307
		10 Suns	1.15	0.872	0.331
		100 Suns	1.14	0.877	0.355
		1000 Suns	1.13	0.882	0.380
Thin-Film cell on a low-index substrate ($\epsilon = 4.225\pi$)	Constant Concentration (1 Sun)	100 K	1.13	0.952	0.431
		200 K	1.14	0.912	0.374
		300 K	1.34	0.886	0.311
		400 K	1.38	0.851	0.276
		500 K	1.38	0.808	0.232
		600 K	1.42	0.766	0.190
	Constant Temp. (300 K)	1 Sun	1.34	0.886	0.311
		10 Suns	1.34	0.888	0.332
		100 Suns	1.34	0.893	0.352
		1000 Suns	1.34	0.897	0.372
Thin-Film cell with a reflective back surface ($\epsilon = \pi$)	Constant Concentration (1 Sun)	100 K	1.13	0.953	0.436
		200 K	1.13	0.912	0.384
		300 K	1.34	0.889	0.334
		400 K	1.34	0.852	0.291
		500 K	1.38	0.817	0.251
		600 K	1.41	0.778	0.211
	Constant Temp. (300 K)	1 Sun	1.34	0.889	0.334
		10 Suns	1.34	0.893	0.354
		100 Suns	1.34	0.898	0.374
		1000 Suns	1.34	0.902	0.395

Previously reported single-junction detailed-balance efficiencies				
Illumination Conditions	Temp. (K)	Band Gap (eV)	Efficiency	Investigator
1 sun 6000 K BB	300	1.10	0.300	Shockley and Queisser ¹
1 sun AM1.5	300	1.40	0.310	Henry ⁷
1000 suns AM1.5	300	1.40	0.370	Henry ⁷
1 sun 5759 K BB	300	1.26	0.305	Araújo and Martí ⁵

quickly lose this excess energy to phonon generation in the absorber. By utilizing multiple absorbers to achieve spectrum splitting, the solar spectrum is more efficiently converted to electric power by minimizing the effect of these two loss mechanisms. This is typically accomplished by epitaxial fabrication of tandem, multi-junction solar cells, which consist of multiple subcells at successively decreasing band gap energies to enable energy binning of the incident photons. In a multi-junction solar cell, one of the key factors in the design freedom for selection of absorber materials for the subcells is the electrical connectivity of the subcell structures described below.

2.2.1 Multi-Junction Solar Cell Electrical Connectivity

Tandem multi-junction solar cell structures can generally be configured in two wiring geometries – independently-connected and series-connected. When cells are connected independently, the current generated in each subcell can be collected independently. On the other hand, in a series connected cell, the larger cell structure is subject to the operating constraint imposed by Kirchoff's law that each subcell must operate at the same current. Thus, the subcell with the least current contribution will limit the performance of the entire structure. This current-matching requirement in turn places stringent requirements upon the band gaps of the subcells that form the multi-junction solar cell.

Thus, it is obvious that the independent connectivity is desirable, but the advantageous design freedom of the independently-connected structure is offset by the added cost and difficulty of fabricating and assembling in a solar cell module a independently-connected, multi-junction solar cell structure. (Additionally, the independently-connected system has its own challenges. Each of the independently-connected cells will operate at a different voltage. However, if the independently-connected subcells are to be connected back into a single circuit for power inversion – conversion to alternating current – the voltage of each of the independently-connected circuits must be closely matched, or there will be associated power losses due to current and

voltage adjustments in the independently-connected circuits necessary to set a single operating voltage for the entire independently-connected structure.) For these reasons, it is important to consider how the subcell current matching design constraint affects the selection of materials and design of the cell structure.

In the following results for the detailed-balance method applied to multi-junction structures, both wiring geometries are considered, but because this is strictly a thermodynamic assessment of the cell efficiency, the technical challenge of wiring a independently-connected structure into a larger module are not taken into account when setting the limiting solar cell efficiency.

2.2.2 Detailed-Balance Efficiency Formulation for Tandem, Multi-Junction Solar Cells

The same general principles used in the detailed-balance analysis of the single-junction solar cell apply to the case of a tandem, multi-junction solar cell. However, the optics and current contributions are slightly different for the multi-junction case. The subcells of a multi-junction structure behave like a single-junction thin-film cell operated on a thick semiconductor substrate considered in the single-junction analysis. This is because the subcells above a given cell are transparent for the overwhelming majority of photons emitted out the front of that cell. Thus, the contribution of front surface emission to the total étendue of the subcell is equal to π . This is due to the fact that these photons eventually have to be emitted from the front surface of the solar cell structure, or they will be reflected back into the structure and reabsorbed by the cell that originally emitted them in what is known as photon recycling. Thus, these photons experience an étendue equal to the étendue for the front surface of the structure. Photons emitted from the back of a subcell, however, are emitted into a nearly index matched material and are perfectly absorbed by the cell below. Thus, the total étendue for any subcell in a multi-junction structure is

$$\varepsilon_{tot} = \pi + \pi n_i^2 = 13.25\pi .$$

To account for all of the sources of current in the subcells, one must consider the full structure. Each subcell below the top subcell has the following current contributions:

- **Photo-current.** Each photon from the solar spectrum above the band gap of the subcell under consideration but below the band gap of the subcell above is absorbed to generate an electron-hole pair.
- **Radiative recombination from the subcell above.** Radiative recombination of electron-hole pairs in the subcell above the subcell under consideration consists entirely of photons in excess of the band gap energy of the subcell under consideration. Thus, the fraction of that energy that is reemitted into the subcell under consideration is perfectly absorbed.
- **Radiative recombination from the subcell below.** This radiation is almost entirely below the band gap of the cell under consideration, and for this reason it is ignored in this analysis. This approximation would break down, if one were to estimate the efficiency of a many-band-gap multi-junction solar cell. In particular, as the difference in adjacent subcell energies approaches kT the approximation is no longer valid. However, because of the technological infeasibility of such structures, they are not considered here.

Based on these sources of current generation plus the loss of current due to the radiative recombination of carriers in each subcell the following set of equations for the current of a subcell in the tandem solar cell is derived.

$$\frac{J_1}{q} = AM^{1.5} N((E_G)_1, \infty, C) - {}^{rad} N((E_G)_1, \infty, T, V_1, (\varepsilon_{em} + \varepsilon_{in})) \quad (2.6)$$

$$\frac{J_n}{q} = AM^{1.5} N((E_G)_n, (E_G)_{n-1}, C) + {}^{rad} N((E_G)_{n-1}, \infty, T, V_{n-1}, \varepsilon_{in}) - {}^{rad} N((E_G)_n, \infty, T, V_n, (\varepsilon_{em} + \varepsilon_{in})) \quad (2.7)$$

$$\frac{J_N}{q} = {}^{AM1.5}N\left((E_G)_N, (E_G)_{N-1}, C\right) + {}^{rad}N\left((E_G)_{N-1}, \infty, T, V_{N-1}, \varepsilon_{in}\right) - {}^{rad}N\left((E_G)_N, \infty, T, V_N, (\varepsilon_{em} + \varepsilon_{in})\right) \quad (2.8)$$

Here the subscripts 1, n , and N refer to top subcell, the n^{th} subcell in the center of the stack, and the bottom N^{th} subcell of the solar cell structure, respectively. For the case of a series-connected cell the current for the entire cell is set as the minimum current at the maximum power current-voltage condition among the subcells in the stack. This is actually an estimate of the optimal current for a series-connected, multi-junction solar cell structure, because as the operating point of the surrounding cells is adjusted to match the operating current of the limiting subcell, the radiative reemission of the surrounding cells changes affecting the operation of the entire structure and the limiting subcell in particular. However, because this is a second order effect and also because the present analysis relies on the numerical approximation of the integrated absorbed radiation from the AM1.5 spectrum and the integrated radiative-recombination current loss, the effect of this coupling is neglected to avoid excessive calculation time necessary for an iterative solution of the coupled equations. Thus, the operating voltages of the remaining subcells are adjusted to set the operating current of those subcells equal to the limiting current of the entire cell structure.

2.2.3 Detailed-Balance Efficiency Calculation of Tandem, Dual- and Triple-Junction Solar Cells

The most illustrative example of how the connectivity of a tandem multi-junction solar cell affects the theoretical limiting efficiency– and, consequently, the actual efficiency – is the dual-junction system where the effect of each junction can be fully visualized by an iso-efficiency contour plot. Such a plot is shown for both the independently- and series-connected geometries of a dual-junction cell structure operating at a temperature of 300 K under 100 sun concentration of

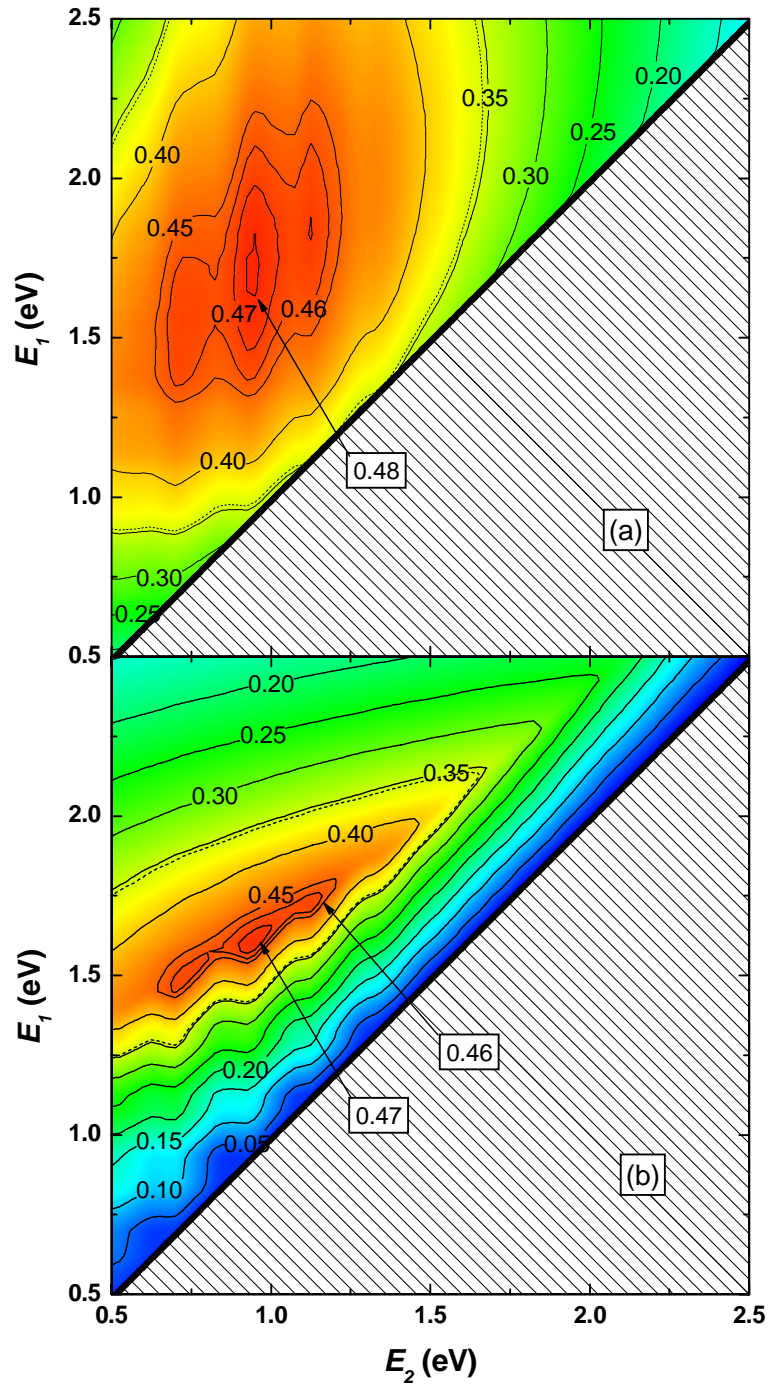


Figure 2.6 (a) Iso-efficiency curve for a two-junction independently-connected solar cell operated at 300 K and 100 suns concentration as a function of the top and bottom subcell bandgaps (E_1 and E_2 respectively). (b) Iso-efficiency curve for a two-junction series connected solar cell operated at 300 K and 100 suns concentration. The maximum efficiency for a single junction solar cell operating on a thick substrate in these conditions is marked by the dashed line.

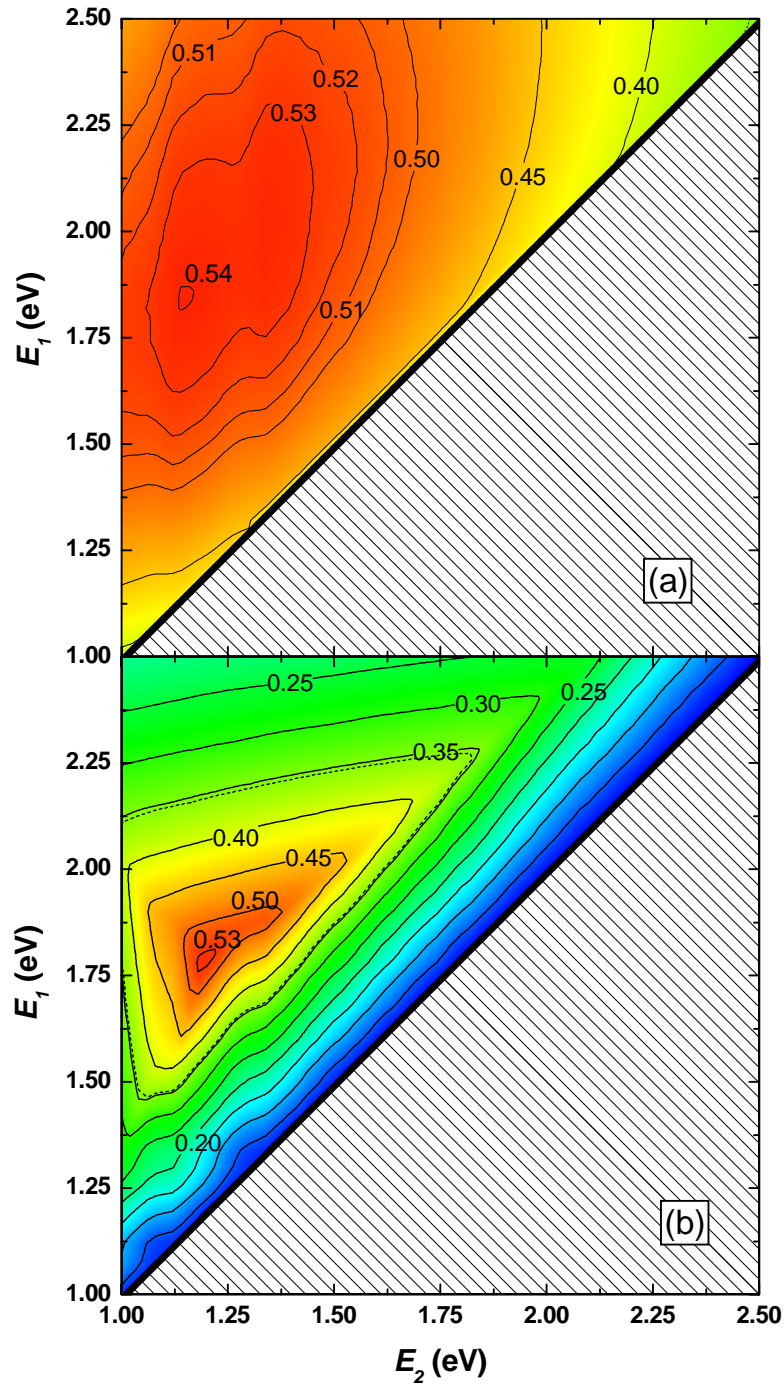


Figure 2.7 (a) Iso-efficiency curve for a three-junction independently-connected solar cell operated at 300 K and 100 suns concentration as a function of the top and middle subcell bandgaps (E_1 and E_2 respectively) operating on a bottom subcell with the Ge bandgap of 0.67 eV. (b) Iso-efficiency curve for a two-junction series connected solar cell operated at 300 K and 100 suns concentration. The maximum efficiency for a single junction solar cell operating on a thick substrate in these conditions is marked by the dashed line.

AM1.5 spectrum in Fig. 2.6. The iso-efficiency curves for the dual-junction tandem cell illustrate the relatively wide degree of freedom in selecting the band gaps of the subcells in a independently-connected, as opposed to a series-connected, tandem solar cell structure. As with the single-junction case, this figure shows the effect of atmospheric absorption on the efficiency as indicated by the undulating edges of the iso-efficiency curves.

Figure 2.7 shows the iso-efficiency plots of a triple-junction tandem solar cell in both wiring geometries operating at a temperature of 300 K under 100 sun concentration of AM1.5 spectrum. However, in this case the parameter space is large enough that it is now difficult to illustrate the impact of all parameters. For this reason, the impact of the top two subcells is shown for a bottom subcell consisting of Ge with a band gap of 0.67 eV. This is of practical importance, because triple-junction cells that dominate the space photovoltaic market are heteroepitaxially grown on a Ge substrate. The top two subcells generally consist of $\text{Ga}_x\text{In}_{1-x}\text{P}$ and GaAs.

The detailed-balance results for dual- and triple-junction tandem structures are summarized for both series- and independently-connected geometries in Tab. 2.2. The present state of the art for this cell structure is 35.2% for a concentrated 66 sun AM1.5 spectrum at a cell temperature of 298 K.¹⁷ This is well below the peak efficiency calculated here of 53.6% under 100 sun AM1.5 illumination at 300 K. The theoretical limiting efficiency of 53.6% corresponds to a cell with

Table 2.2 Summarized results for the efficiency of the detailed balance model of two- and three junction tandem solar cell structures in both independent and series connected device geometries operated at 300 K under a concentration of 100 sun AM1.5 radiation.

			Independent	Series	
			Maximum	Maximum	$\text{Ga}_{0.5}\text{In}_{0.5}\text{P} / \text{GaAs} / \text{Ge}$
Two-junction Tandem	Bandgap (eV)	Cell 1	1.60	1.625	---
		Cell 2	0.95	0.975	---
	Efficiency		0.479	0.476	---
Three-junction Tandem	Bandgap (eV)	Cell 1	1.82	1.78	1.90
		Cell 2	1.14	1.20	1.42
		Cell 3 (Ge)	0.67	0.67	0.67
	Efficiency		0.540	0.536	0.463

1.78, 1.20 and 0.67 eV band gap subcells. As is illustrated by the plot of band gap versus lattice constant for the ternary III-V semiconductors in Fig. 1.4, this combination of band gaps cannot be achieved in a lattice-matched ternary III-V semiconductor system. The lattice-matched structure of a 1.80 to 1.90 eV $\text{Ga}_{0.5}\text{In}_{0.5}\text{P}$, 1.42 eV GaAs, and 0.67 eV Ge tandem cell has a more modest predicted efficiency of 46.3% at 300 K under 100 sun AM1.5 illumination. Thus, there is still room for improvement, but with 35.2% efficiency already demonstrated the asymptotic part of the curve is being reached. To open up new avenues for rapid performance improvement, new designs are needed, many of which are enabled only by the development of a radical integration technique such as wafer bonding and layer transfer.

2.3 Detailed-Balance Efficiency Calculation of Wafer-Bonded, Multi-Junction Solar Cells

As was mentioned in Chapter 1, we propose that the use of wafer bonding in the fabrication of photovoltaic devices could become a powerful new tool to enable advanced device designs to be implemented. While one obvious application is the reduction in substrate costs for traditional triple-junction solar cells by replacement of the Ge substrate structure with a Ge/Si wafer-bonded virtual substrates, several more exciting device designs are readily available for fabrication, such as the four-junction cell described in §1.3.2. In this section the detailed-balance efficiency will be calculated for several wafer-bonding-enabled solar cell designs to assess the value in proceeding with their development.

The promise of wafer-bonding of photovoltaic device design is primarily the improved selection of cell band gap for a given subcell. Importantly, now a subcell can be selected to have both the desired band gap and well developed material properties, independent of the lattice constant of the cell. Utilizing this new freedom three promising wafer-bonded device designs are:

- **Triple-junction solar cell fabricated on a Si substrate.** As this device was previously described, the motivation was for the replacement of the expensive Ge substrate with

Si. However, this device structure also has the possibility of incorporating an active Si subcell with upper subcells grown on either a Ge or GaAs thin film bonded to the Si substrate.

- **Four-junction solar cell.** This design was described in §1.3.2. A detailed-balance analysis of the limiting efficiency will result in optimally selected subcell materials and an analysis of the potential gain in fabricating such a cell. Additionally, as with a wafer-bonded triple-junction solar cell, wafer-bonded four-junction solar cells can be designed such that an active Si substrate is incorporated in the design. Additionally, wafer bonding enables the integration of a Ge subcell with such a device.
- **Five-junction, independently-connected solar cell.** This cell design could reach theoretical efficiencies in excess of 60% under concentration. The practical challenge is in identifying a well-behaved wide band gap semiconductor to serve as the top subcell in this structure. However, the promise is fantastic, and the use of wafer bonding to achieve independent subcell connection would even further enhance the potential of such a wafer-bonded solar cell.

2.3.1 Detailed-Balance Efficiency Calculation of a Triple-Junction Wafer-Bonded Solar Cell Fabricated on an Active Si Subcell

While Ge/Si substrates are obviously desirable, due to fabrication limitations in making the Ge/Si substrate, any practical cell design would consist of less than one μm of Ge on a thicker substrate of Si. Because the Ge film is so thin, it would be difficult to utilize it in a traditional Ge subcell geometry without performing an epitaxial growth of a thicker Ge subcell on the transferred Ge film. For this reason, it may be necessary to grow a thicker Ge film during the MOCVD growth of the top two subcells. Alternatively, this substrate offers the opportunity to use an extremely thin Ge film (or perhaps a thin GaAs film) on a Si substrate that also serves as an active Si subcell. The operating voltage of such a subcell would certainly increase the cell operating

voltage. Provided that the photo-current-voltage tradeoff is not too extreme, incorporation of a Si subcell into a Ge/Si substrate might be a viable technological alternative to the use of such a substrate to support a conventional triple-junction solar cell. This has been explored by the detailed-balance model and the iso-efficiency plot for 100 sun AM1.5 illumination at 300 K is shown in Fig. 2.8. The maximum efficiency under these conditions is 51.2% for subcell band gaps of 2.00, 1.49 and 1.12 eV. This is slightly below the maximum calculated for the optimal triple-junction on Ge of 53.6% for the same operating conditions. However, for terrestrial operation, such a solar cell offers the practical advantage of being incorporated on a Si substrate. This dramatically improves the thermal conductivity of the structure, and should enable operation

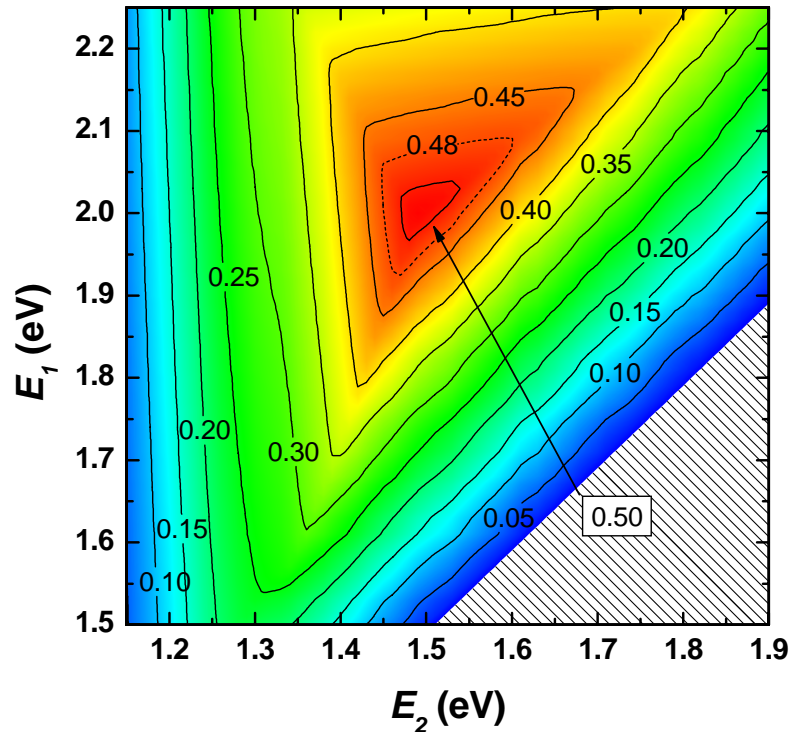


Figure 2.8 The iso-efficiency plot for the variation of the top two subcell band gaps in a series-connected triple-junction solar cell fabricated on a wafer bonded Ge/Si substrate with an active Si subcell operated under 100 sun AM1.5 illumination at 300 K. The dashed line at $\eta = 0.476$ represents the limiting efficiency for an optimal dual-junction solar cell operated under the same conditions.

at lower temperatures under concentration. This effect could be large enough to offset the slightly lower limiting efficiency of the structure.

The most immediate application for a triple-junction solar cell fabricated on a Ge/Si virtual substrate with an active Si subcell, would be increasing the specific power of a space power photovoltaic system. To explore the performance of such a cell structure relative to conventional GaInP/GaAs/Ge triple-junction cells, detailed-balance calculations were made for both GaInP/GaAs/Si and GaInP/GaAs/Ge triple-junction solar cells operated under one sun AM0 illumination at a temperature of 300 K. The iso-efficiency plots from this analysis are shown in Fig. 2.9. As with operation under AM1.5 illumination, the wider band gap of the bottom subcell forces the maximum operation point to a wider band gaps for the upper subcells of the structure. It also creates a steeper iso-efficiency surface for the top two subcells. Additionally, the limiting efficiency for an optimum three-junction cell with an active Si subcell is 43.1% at subcell band gaps of 2.08, 1.52, and 1.12 eV, versus a limiting efficiency for an optimum three-junction cell with an active Ge subcell of 44.6% at subcell bandgaps of 1.76, 1.12, and 0.67 eV. In light of such a small difference, the Si subcell triple-junction is shown to be a viable alternative to the conventional Ge subcell triple-junction, and the presence of active Si can be used to increase the total system efficiency over a two-junction cell.

The present cell design for triple-junction solar cells in space applications uses a GaInP/GaAs/Ge cell structure. This limits the range of band gaps for the top- and middle-subcells to 1.70 to 1.90 eV and 1.35 to 1.45 eV, respectively. To investigate this more realistic device design, detailed-balance efficiency calculations were made with these constraints on the upper and middle subcell band gaps. The resulting iso-efficiency curves are plotted in Fig. 2.10. It is worthy to note that the predicted efficiencies are very similar for both cell designs. Another important observation is that the cell utilizing a Si subcell has both a flatter efficiency in this region of parameter space and has a reduced dependence on the operating temperature because of

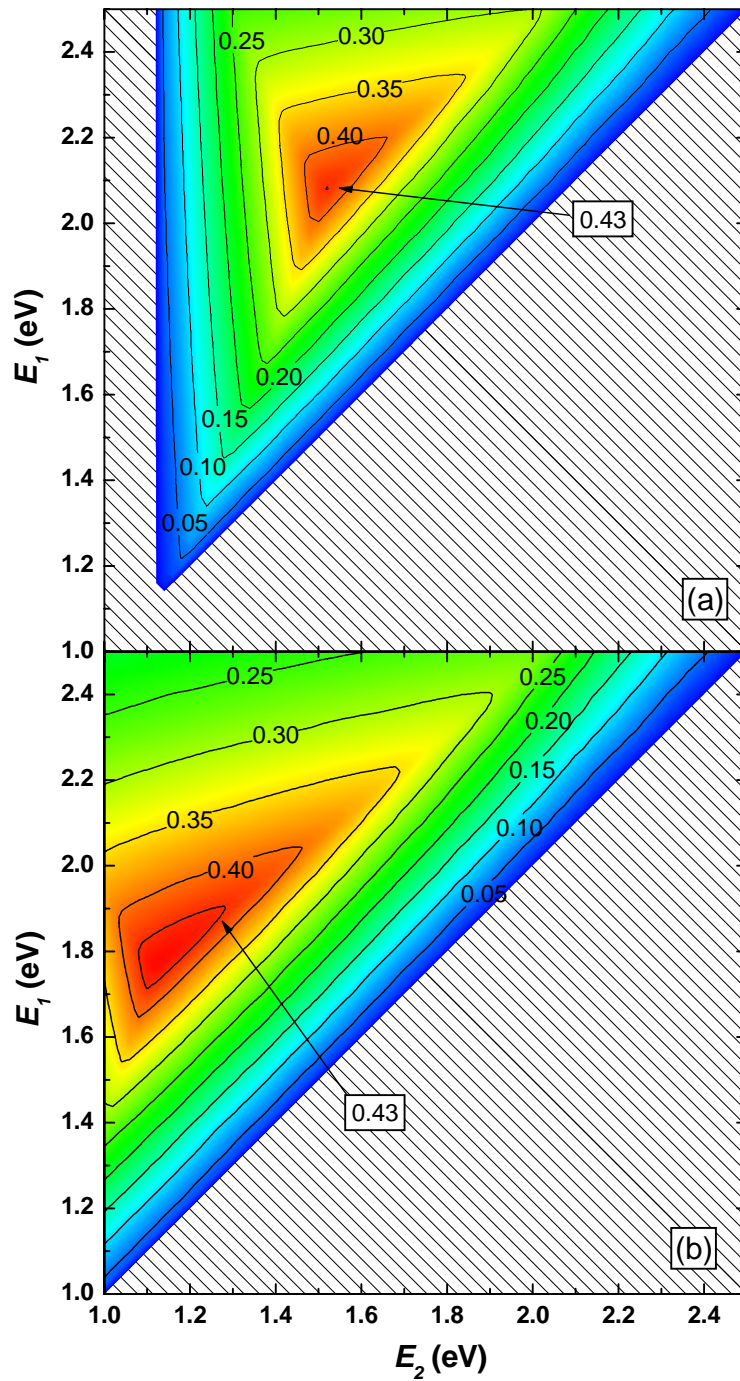


Figure 2.9 (a) Iso-efficiency curve for a three-junction series-connected wafer-bonded solar cell operated at 300 K under one sun AMO illumination as a function of the top and middle subcell bandgaps (E_1 and E_2 respectively) operating on a bottom subcell with the Si band gap of 1.12 eV. (b) Iso-efficiency curve for a three-junction series-connected solar cell operated under the same conditions with a Ge bottom subcell band gap of 0.67 eV.

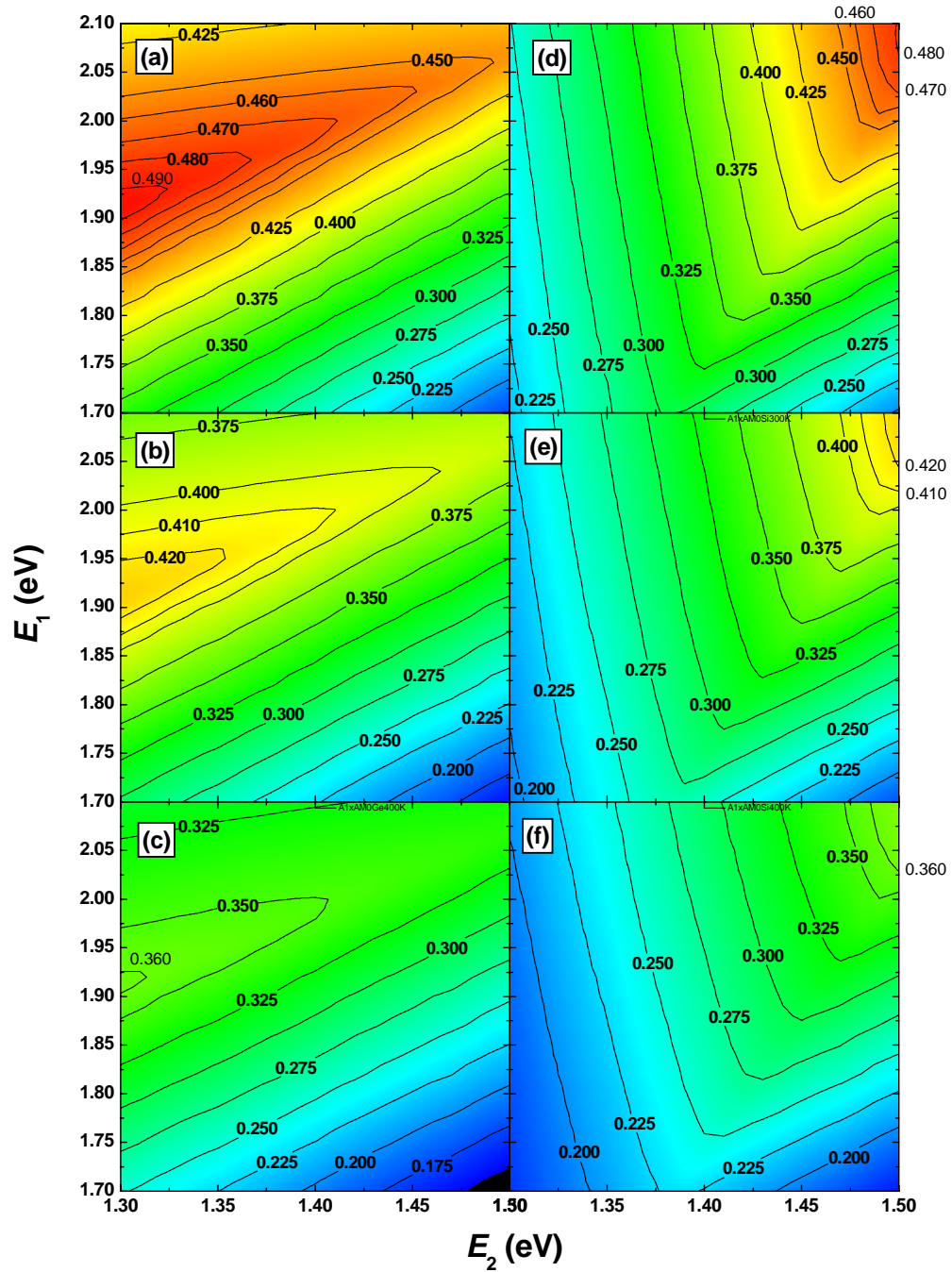


Figure 2.10 Iso-efficiency plots for a three-junction series-connected solar cell with a Ge bottom subcell (0.67 eV bandgap) operated under AM0 1 sun concentration at (a) 200 K, (b) 300 K and (c) 400 K, and iso-efficiency plots for the same cell geometry and operating conditions consisting of a Si bottom subcell (1.12 eV bandgap) operated at (d) 200 K, (e) 300 K and (f) 400 K.

its wider bottom cell band gap. The efficiencies for a typical GaAs middle subcell (1.42 eV band gap) are plotted in Fig. 2.11. These yet again illustrate the comparable efficiencies in such a structure. Taken with the reduced mass and improved thermal and mechanical properties, the use of an active Si subcell in a Ge/Si wafer bonded substrate offers comparable power conversion efficiency and improved economic performance of triple-junctions solar cells for use in space applications relative to conventional GaInP/GaAs/Ge cells.

2.3.1 Detailed-Balance Efficiency Calculation of a Four-Junction Wafer-Bonded Solar Cell

A more creative application of wafer bonding and layer transfer is to realize novel photovoltaic

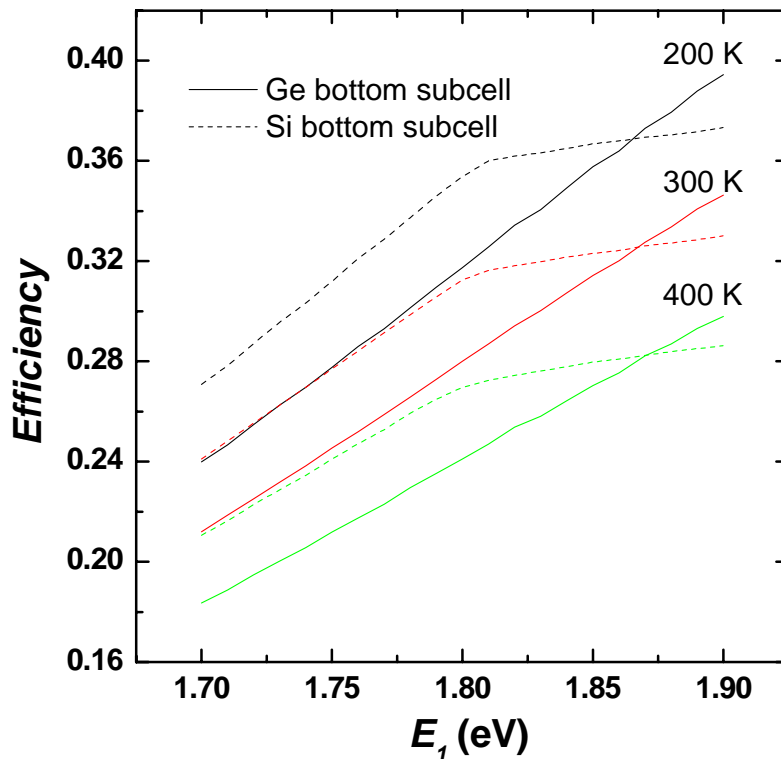


Figure 2.11 Efficiency curves as a function of top subcell bandgap for a three junction solar cell with a 1.42 eV center subcell with either Ge or Si bottom subcells operated at various temperatures under a 1 sun AM0 illumination.

devices that are difficult to build by traditional fabrication with heteroepitaxy because of the requirement of using nearly-lattice-matched materials for the constituent subcells. As was previously described, series-connected multi-junction solar cells are current limited by the least performing subcell. For this reason, there is little flexibility in selecting the band gaps of the constituent cells as was illustrated in §2.2.3, and the flexibility in subcell band gap selection becomes even more restricted when the number of subcells increases. The design requirement is even further complicated by the fact that the well-characterized III-V semiconductors that cover the spectrum necessary for photovoltaic power conversion are not sufficiently lattice-matched to be integrated into a monolithic heteroepitaxially grown structure. For this reason there is an ongoing effort to develop new direct band gap semiconductors with a band gap near 1.0 eV that are lattice-matched to the GaAs system. As was mentioned in §1.3.2, the most developed of these materials is $\text{In}_x\text{Ga}_{1-x}\text{As}_y\text{N}_{1-y}$. However, defects caused by the difficulty of incorporating the relatively small nitrogen atom into the anion sub-lattice have prevented this material from achieving the quality necessary for photovoltaic applications.¹⁸ By utilizing wafer bonding and layer transfer, one can integrate well-developed semiconductors such as $\text{In}_x\text{Ga}_{1-x}\text{As}$ and $\text{In}_x\text{Ga}_{1-x}\text{As}_y\text{P}_{1-y}$ with other well-developed III-V semiconductors such as those in the GaAs system, like GaAs, GaInP, and AlGaInP. As with the wafer-bonded triple-junction solar cell described in §2.3.1, the support substrate – such as Si or Ge – in a wafer-bonded solar cell structure can also serve as an active subcell of the finished structure. Such a structure could reduce fabrication costs for the finished device by cutting one subcell growth from the epitaxial process. Additionally, Si solar cell technology is very well developed with efficiencies in excess of 24%.¹⁹ In all proposed four-junction wafer-bonded solar cell designs, wafer bonding enables monolithic integration of the cell structure, while isolating the associated misfit dislocations to the bonded interface. Provided that the bonded interface is a passive component of the device (i.e., the wafer bonded junction is not used to separate carriers to contribute to photo-current) then well-developed materials can be integrated independent of their lattice constant to form a new solar cell structure.

2.3.2.1 Detailed-Balance Efficiency Calculation of an Ideal Wafer-Bonded Four-Junction Solar Cell

The detailed-balance model was used to calculate the efficiency of a series-connected four-junction solar cell structure under 100 sun AM1.5 illumination operating at a cell temperature of 300 K. Because the parameter space has now moved into four dimensions, the iso-efficiency curves of this type of solar cell can no longer be shown as before. Instead, an iterative process was used to converge on the optimal subcell band gaps for a four-junction solar cell operating under these conditions. It was found that a maximum efficiency of 57.9% could be expected for a cell consisting of subcells with energies: $E_1 = 2.00$ eV, $E_2 = 1.49$ eV, $E_3 = 1.12$ eV, and $E_4 = 0.72$ eV. In Fig. 2.12 the impact of independently varying the subcell band gaps around their optimized values is shown. Thus, the shape of the parameter space can be viewed in one dimension to illustrate the dependence of efficiency on the band gaps of the various subcells. The efficiency of the structure falls off rather quickly by varying the top subcell band gap either above or below the ideal value. For the second and third subcells in the stack the effect is even stronger, and some undulations in the efficiency appear due to intensity fluctuations in the AM1.5 spectrum caused by the absorption of the solar spectrum by gas constituents in the atmosphere. Decreasing the bottom subcell in the stack has little effect on the efficiency of the structure, because the voltage supplied to the entire structure by this subcell is minimal. By decreasing the band gap, the photo-current of the bottom subcell does not become limiting, but rather increases. However, increasing the bottom subcell band gap causes a reduction in the subcell operating current, thus limiting the current for the entire cell leading to a sharper decrease in efficiency with independently increasing the bottom subcell band gap.

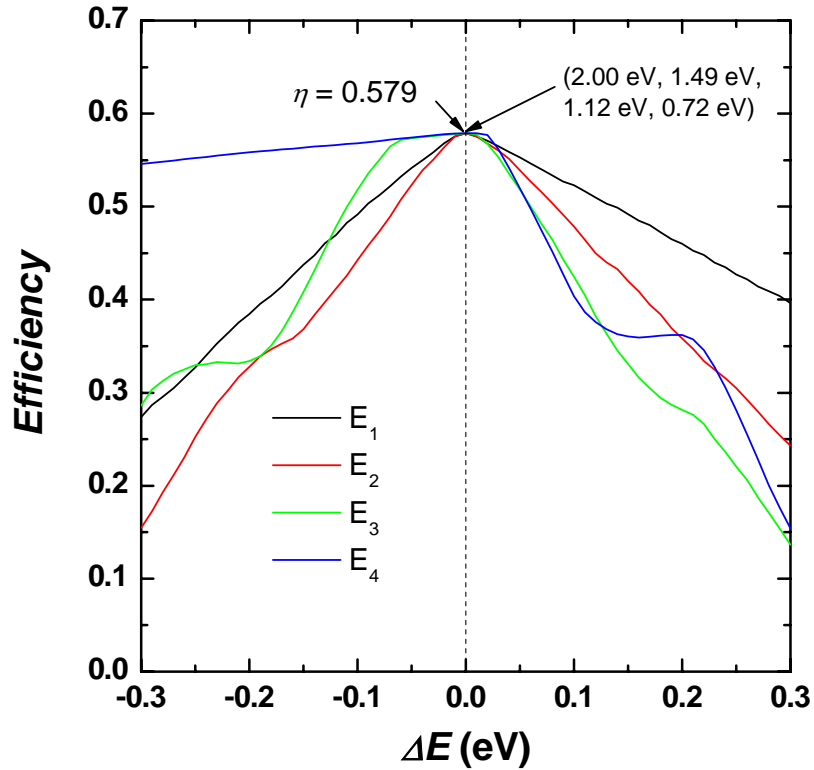


Figure 2.12 Variation of efficiency of an optimal 100 sun AM1.5 series-connected four-junction solar cell with changes of each subcell bandgap. Each cell is subcell is varied independently maintaining the other subcells at their optimum bandgap of 2.00, 1.49, 1.12, and 0.72 eV respectively.

2.3.2.2 Detailed-Balance Efficiency Calculation of a Wafer-Bonded Four-Junction GaInP/GaAs/InGaAsP/InGaAs Solar Cell

To approach this thermodynamic limiting efficiency for a four-junction solar cell, one must still work with real materials. For this reason, the proposed wafer-bonded four-junction solar cell structure that will be pursued consists of a top and second cell consisting of $\text{Ga}_{0.5}\text{In}_{0.5}\text{P}$ and GaAs respectively. This essentially sets the top two band gaps at 1.90 eV and 1.42 eV (with some small opportunity to vary these subcell band gaps). Detailed-balance calculations for the same operating conditions, but with the constraint that the top two subcells operate at these fixed band gaps, have been made to determine the optimum band gaps of the bottom two subcells. The results of this

simulation are represented by the iso-efficiency plot in Fig. 2.13. The optimum band gaps for a four-junction cell utilizing lattice matched $\text{Ga}_{0.5}\text{In}_{0.5}\text{P}$ and GaAs for the top two subcells are $E_1 = 1.90$ eV, $E_2 = 1.42$ eV, $E_3 = 1.02$ eV, and $E_4 = 0.60$ eV. The calculated thermodynamic limit for this structure is 54.9%. This design offers substantial improvement over the limiting efficiency of a conventional GaInP/GaAs/Ge triple-junction solar cell structure, which is limited to an efficiency of 46.3% when operated under these conditions. However, the four-junction cell consisting of GaInP and GaAs top subcells only marginally outperforms the optimum triple-junction cell operated under these conditions, which has a limiting efficiency of 53.6%. Figure 2.13 gives insight to the design of the bottom tandem. For instance, as was illustrated in Fig. 2.12, decreasing the bottom cell band gap, E_4 , has relatively little impact on the cell efficiency. This is because the bottom subcell contributes relatively little to the operating voltage of the cell structure, and moving to a lower than optimal band gap leads to an increase in photo-current that does not impact the cell operation and causes only a slight decrease in the cell operating voltage. Also, the increase in the number of photo-generated carriers in the bottom subcell when it is operated at a band gap below the optimal value of 0.60 eV allows the potential of the subcell to operate at a potential closer to the band gap energy, because the increased photo-current allows greater radiative reemission to be tolerated. It should be noted that these effects may be hard to achieve in a real cell where the maximum operating voltage is limited by the separation of the electron and hole quasi-Fermi levels, which are in turn a function of the doping levels of the p-n junctions of the subcells.

The iso-efficiency plot of Fig. 2.13 also indicates that as the bottom subcell band gap is reduced below the optimum value of 0.60 eV that the efficiency surface is relatively flat from about 0.90 to 1.04 eV for the third subcell. Thus, the performance of a four-junction cell structure can be better controlled for fluctuations in the band gaps of these subcells by fabricating the cell in such a way that deviations from the optimal bottom subcell band gap are toward lower energies than 0.60 eV. In short, this information shows solar cell designers where there are opportunities to

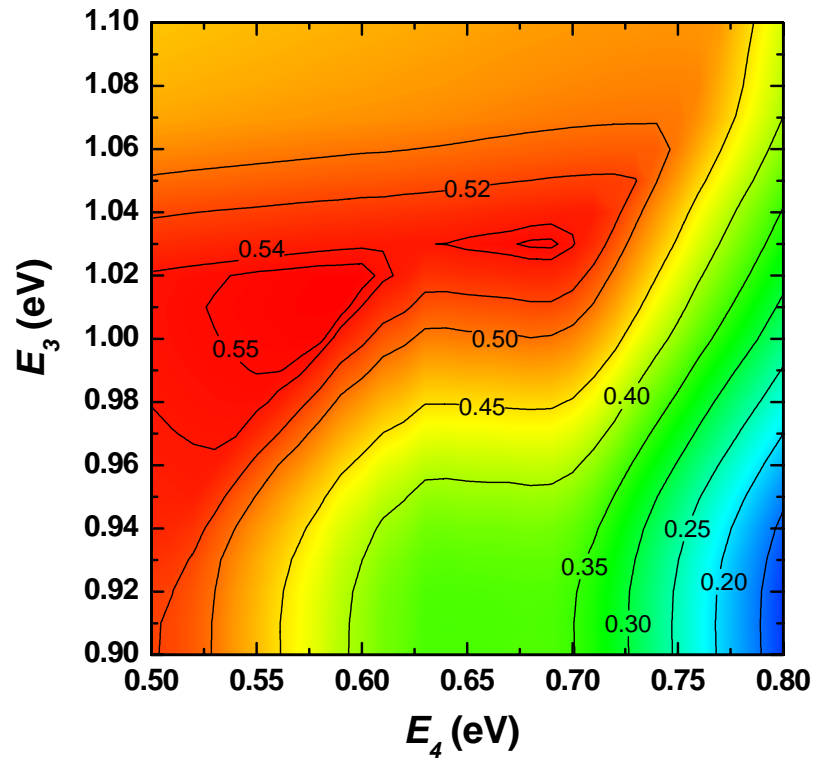


Figure 2.13 The iso-efficiency plot for the variation of the bottom two subcell bandgaps in a four-junction solar cell operated under 100 sun AM1.5 illumination at 300 K.

improve the robustness of the fabrication process for next-generation high efficiency photovoltaic devices.

2.3.2.3 Detailed-Balance Efficiency Calculation of a Wafer-Bonded Four-Junction GaInP/GaAs/Si/Ge Solar Cell

In §2.3.2.1 it was shown that for an ideal four-junction wafer-bonded solar cell, the ideal bottom two subcells for operation in AM1.5 illumination at 100 suns and 300 K have band gaps of 1.12 and 0.72 eV. These values are very close to the band gaps of Si and Ge, 1.12 and 0.67 eV respectively. Additionally, both of these materials have demonstrated excellent photovoltaic

performance, especially Si, which has achieved single-junction efficiencies in excess of 24%.¹⁹ Wafer bonding makes possible the growth of ternary and quaternary III-V alloys on a GaAs epitaxial template wafer bonded to an active Si subcell that serves as a mechanical support for the structure. Following growth of the AlGaInP/GaInAsP/Si top three subcells, wafer bonding can be used to integrate a thin Ge subcell on the back surface of the Si substrate. Such a device is shown in Fig. 2.14. In this cell design, there are only two subcell band gaps that can be optimized in the detailed-balance analysis of the limiting efficiency. The iso-efficiency plot in Fig. 2.15 shows the dependence of the limiting efficiency on the top and second subcell structures at 300 K under 100 sun AM1.5 illumination. In this design, the optimum efficiency is predicted to be 57.4% with subcell band gaps of 2.00 and 1.49 eV for the top two subcells respectively. It is also important to

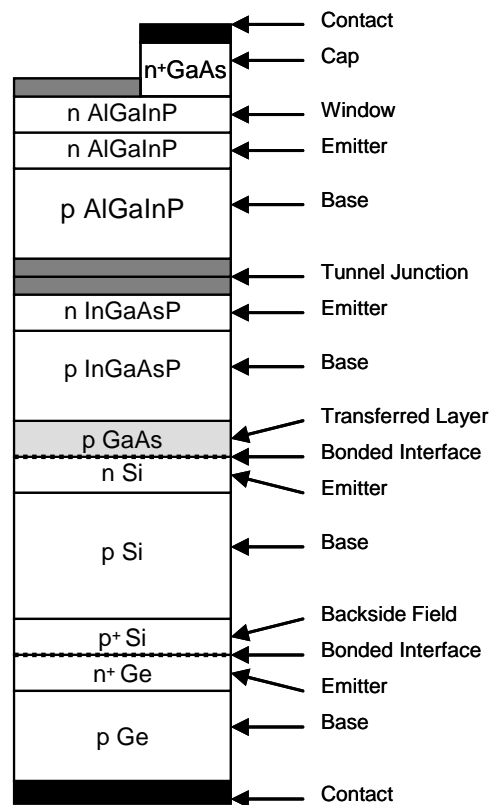


Figure 2.14 Schematic of a four-junction solar cell fabricated by bonding and transferring a GaAs epitaxial template to an active Si subcell and subsequently growing an AlGaInP/InGaAsP tandem structure via MOCVD. Following growth, a bonding process is used to integrate a thin Ge subcell to the back surface of the structure.

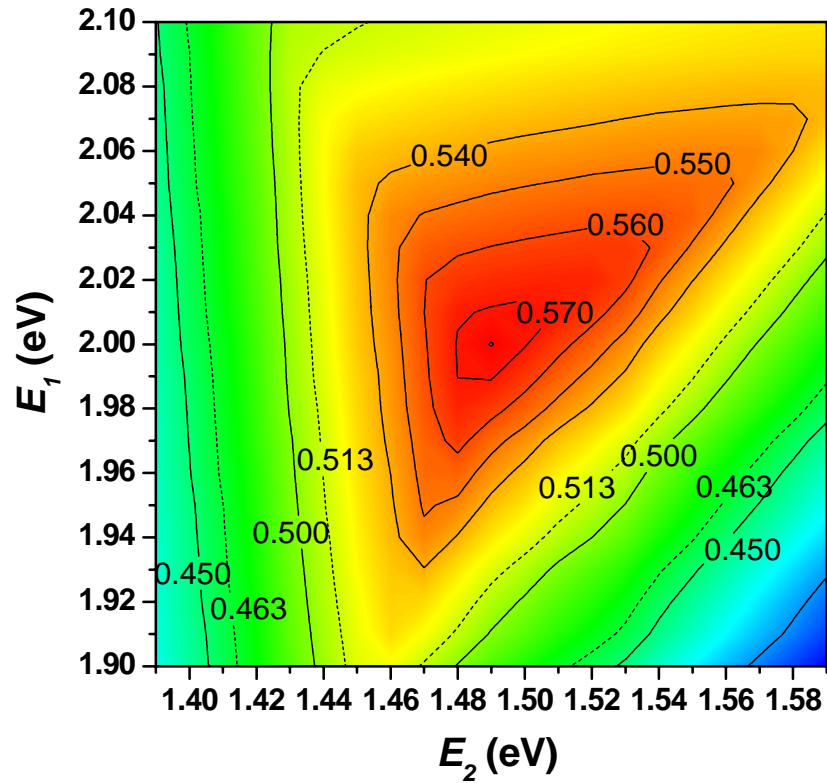


Figure 2.15 The iso-efficiency plot for the variation of the top two subcell bandgaps in a four-junction solar cell operated under 100 sun AM1.5 illumination at 300 K. The bottom two subcells consist of an active Si support substrate and a Ge subcell wafer bonded to the back surface of the structure. The band gaps are 1.12 and 0.67 eV respectively. The two dashed lines at 46.3% and 51.2% efficiency mark the predicted efficiencies of a GaInP/GaAs/Ge triple-junction cell and a band gap optimized triple-junction cell with an active Si subcell, respectively.

note how large the range of band gaps is that leads to efficiency above the optimal triple-junction on an active Si subcell with a limiting efficiency of 51.3%. Thus, it is clear that there is great promise for implementing this cell design.

2.3.3 Detailed-Balance Efficiency Calculation of a Five-Junction, Independently-Connected Solar Cell Enabled by Wafer Bonding

The most ambitious application of wafer bonding to enable high-efficiency solar cells is in the joining of many materials to optimize spectrum splitting in multi-junction cell designs. When using this technique, multiple advantages are conferred. First, one can tailor the cell design by selecting well-developed materials systems at the optimal band gaps. Additionally, one can utilize foreign substrates with desirable mechanical, thermal, optical and economic properties as a support for the solar cell. Finally, when joining many materials for a cell consisting of five or more subcells, the use of an insulating layer between cells enables the convenient manufacture of Independently-connected solar cell structures. This is admittedly an expensive cell design, but by integrating such a cell into concentrator system a small high-performance five-junction cell can be used to collect power over a wide area offsetting the high cost of cell fabrication.

One possible structure uses multiple wafer-bonding steps to integrate subcells with sapphire support substrates. As was described in §2.1.2, the use of a low-index substrate improves the optical properties of these films by decreasing the coupling of radiatively emitted light from the subcell into the surrounding media, i.e., the sapphire substrate. This results in an étendue of 6.845π for a thin-film device sandwiched between two low-index materials. Thus, one can imagine a five-junction solar cell fabricated by bonding five epitaxial templates to sapphire substrates. The templates would then be used to grow high-performance III-V semiconductor subcells. These independent subcells would then be integrated into a monolithic structure by wafer bonding. Grid contact could be accomplished during the integration step. The use of such a structure under concentration would serve to offset the obvious cost incurred in fabricating the cell itself. The module would then be assembled to meet the voltage-matching requirements for such a structure. For such a complex device with five band gaps to vary, the iterative approach to

band gap optimization used for determining the optimal subcell band gaps of the four-junction cell in §2.3.2 would be prohibitively slow. For that reason, a different approach is taken.

Using the approximation to the detailed balance model proposed by C. H. Henry, simulations of the optimum five-junction solar cell structure for 300 sun AM1.5 and an operating temperature of 353 K were performed.⁷ The optimum subcell band gaps for this structure are 2.50, 1.93, 1.53, 1.13, and 0.70 eV. Using these band gaps as inputs, the rigorous detailed-balance model was used to investigate the impact of independently varying the band gap energies of the subcells as shown in Fig. 2.16. In this analysis the operating conditions were adjusted to be consistent with the previous devices – 100 suns AM1.5 radiation with a cell temperature of 300 K. In Fig. 2.16, the peak can be seen to be slightly shifted relative to the Henry analysis. The peak efficiency is

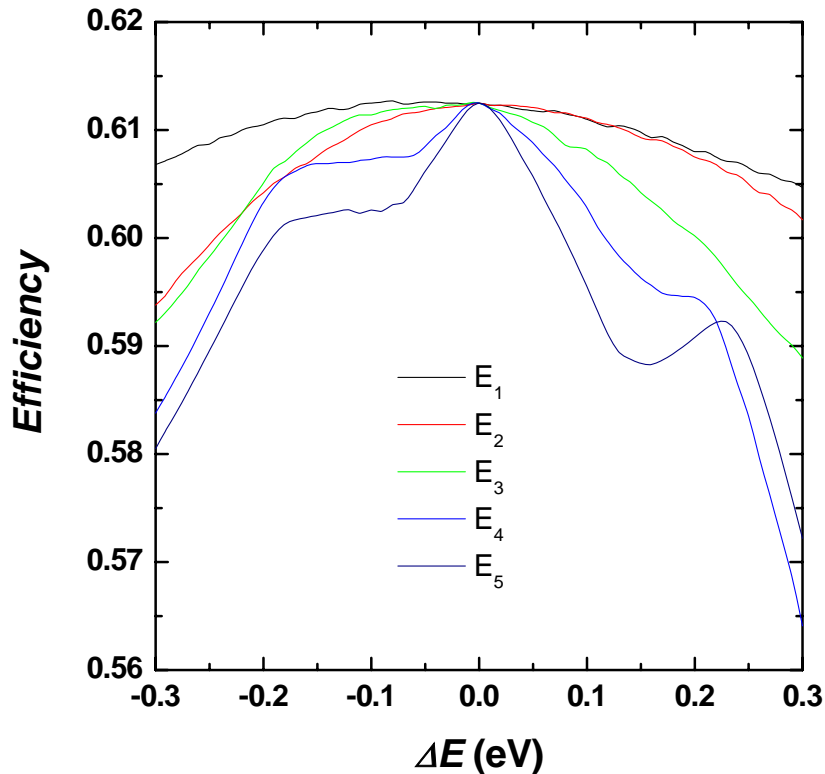


Figure 2.16 Efficiency variation of an optimal 100 sun AM1.5 parallel-connected five-junction solar cell with independent variation of each subcell band gap from its optimum bandgap of 2.50, 1.93, 1.53, 1.13 and 0.70 eV, respectively.

approximately 61.2% with a broad peak for the top three subcells. The bottom two subcells indicate that the exact selection of these cells leads to a relatively substantial change in the total efficiency of the structure. This is likely due to the fact that these subcells have band gap energies that are in the region of strong atmospheric absorption of the AM1.5 spectrum. This interpretation is supported by the undulations of the efficiency as the band gap moves away from the optimum value. However, it is important to note that the scale in Fig. 2.16 only spans 6% absolute efficiency. Thus, this structure is very robust with respect to variations in the subcell band gaps. The variation of subcell band gaps due to process control during the fabrication of the structure is of greater concern when wiring and assembling the overall independently connected solar panel, where the voltages of the independently circuits must be closely matched.

2.4 *Summary*

In the preceding analysis, the fundamental limitations of photovoltaic efficiency were explored using the detailed-balance method. The detailed-balance analysis for single-junction solar cells illustrates the effects of temperature, concentration and optical geometry on the performance of the cell. Generally speaking, it is desirable to operate a solar cell at low temperatures under extreme concentration. Additionally, it is desirable to operate the cell in such a way that the loss of photons is minimized by affecting the geometry of the back surface of the cell. In addition to the single-junction cell, conventional dual- and triple-junction cells were evaluated to assess the performance improvements that are achievable in these devices, and to check the accuracy of the model by comparison to values reported in the literature.

The limiting efficiency for several wafer-bonding enabled solar cell designs were explored with the detailed-balance model. The calculated efficiency of these cell designs, along with the preferred band gaps of their constituent subcells, are cataloged in Tab. 2.3. These calculated efficiencies show the merit of pursuing the development of these devices. The use of an active Si subcell in a replacement Ge/Si substrate for a triple-junction solar cell was shown to improve

Table 2.3 The summarized detailed-balance efficiency calculations for wafer-bonding enabled solar cell designs under 100 sun AM1.5 illumination at a cell temperature of 300 K.

Series-connected triple-junction on a Si subcell	Band gap (eV)	Subcell 1	2.00
		Subcell 2	1.49
Subcell 3		1.12	
	Efficiency		0.512
Optimum series-connected four-junction	Band gap (eV)	Subcell 1	2.00
		Subcell 2	1.49
		Subcell 3	1.12
		Subcell 4	0.72 (GaSb)
	Efficiency		0.579
Series-connected GaInP/GaAs/InGaAsP/InGaAs four-junction	Band gap (eV)	Subcell 1	1.90
		Subcell 2	1.42
		Subcell 3	1.02
		Subcell 4	0.60
	Efficiency		0.549
Series-connected four-junction with Si and Ge subcells	Band gap (eV)	Subcell 1	2.00
		Subcell 2	1.49
Subcell 3		1.12	
Subcell 4		0.67	
	Efficiency		0.574
Independently-connected five-junction	Band gap (eV)	Subcell 1	2.50
		Subcell 2	1.93
		Subcell 3	1.53
		Subcell 4	1.13
		Subcell 5	0.70
	Efficiency		0.612

performance relative to a dual-junction solar cell. Despite this gain in efficiency, an active-Si wafer-bonded triple-junction solar cell still underperforms a conventional triple-junction solar cell. However, the added benefits of higher specific power and better thermal conductivity of the handle substrate offset these slight efficiency performance losses. Additionally, wafer-bonding enabled four-junction designs were proposed that would enable record-setting efficiencies. Of particular promise is the idea of using a Si-based substrate that doubles as a subcell and incorporates a Ge subcell on the back surface to fabricate a cell that very nearly matches the subcell band gaps of an optimal four-junction cell. Finally, the promise of a five-junction solar cell consisting of independently-connected subcells wafer bonded in a mechanical stack that

separates the subcells with a low refractive index material such as sapphire was demonstrated, and a limiting efficiency in excess of 60% was predicted.

2.5 *References*

- ¹ W. Shockley and H. J. Queisser, *Journal of Applied Physics* **32**, 510-519 (1961).
- ² M. E. Nell and A. M. Barnett, *IEEE Transactions on Electron Devices* **ED-34**, 257-266 (1987).
- ³ M. W. Wanlass, K. A. Emery, T. A. Gessert, G. S. Horner, C. R. Osterwald, and T. J. Coutts, *Solar Cells* **27**, 191-204 (1989).
- ⁴ P. A. Basore and D. A. Clugson, in *PCID version 4 for Windows: from analysis to design*, Washington, D. C., 1996 (IEEE Press).
- ⁵ G. L. Araujo and A. Marti, *Solar Energy Materials & Solar Cells* **33**, 213-239 (1994).
- ⁶ S. P. Bremner, R. Corkish, and C. B. Honsberg, *IEEE Transactions on Electron Devices* **46**, 1932-1939 (1999).
- ⁷ C. H. Henry, *Journal of Applied Physics* **51**, 4494-5000 (1980).
- ⁸ P. T. Landsberg, A. De Vos, and P. Baruch, *Journal of Physics C: Condensed Matter* **3**, 6415-6424 (1991).
- ⁹ M. Green, J. Zhao, A. Wang, P. Reece, and M. Gal, *Nature* **412**, 805-808 (2001).
- ¹⁰ T. Trupke, M. A. Green, and P. Würfel, *Journal of Applied Physics* **92**, 1668-1674 (2002).
- ¹¹ T. Trupke, M. A. Green, and P. Würfel, *Journal of Applied Physics* **92**, 4117-4122 (2002).

- ¹² M. A. Green, *Third Generation Photovoltaics: Advanced Solar Energy Conversion* (Springer, New York, 2003).
- ¹³ A. S. Brown and M. A. Green, *Journal of Applied Physics* **94**, 6150-6158 (2003).
- ¹⁴ P. Würfel, *Journal of Physics C: Solid State Physics* **15**, 3967-3985 (1982).
- ¹⁵ www.nrel.gov.
- ¹⁶ W. Shockley and H. Queisser, *Journal of Applied Physics* **32**, 510-519 (1961).
- ¹⁷ R. R. King, C. M. Fetzer, P. C. Colter, K. M. Edmondson, D. C. Law, A. P. Stravides, H. Yoon, G. S. Kinsey, H. L. Cotal, J. H. Ermer, R. A. Sherif, and N. H. Karam, in *Lattice-matched and metamorphic GaInP/GaInAs/Ge concentrator solar cells*, Osaka, 2003.
- ¹⁸ S. R. Kurtz, A. A. Allerman, C. H. Seager, R. M. Sieg, and E. D. Jones, *Applied Physics Letters* **77**, 400-402 (2000).
- ¹⁹ J. Zhao, A. Wang, and M. A. Green, *Progress in Photovoltaics: Research and Applications* **7**, 471-474 (1999).

Chapter 3: Materials Integration by Wafer Bonding and Layer Transfer

In Chapters 1 and 2 the basics of photovoltaics and the importance of wafer bonding for device improvement are described. Additionally, Chapter 1 lays out the basics of wafer bonding and layer transfer by H-induced exfoliation for materials integration of non-lattice-matched semiconductors. In this chapter, general processes for wafer-bonded integration of Ge/Si and InP/Si are described. In this chapter it is shown that through hydrophobic, hydrophilic, and plasma-activated wafer bonding, Ge and InP layers can be transferred to Si handle substrates. The characterization of these structures fabricated by the methods described in the present chapter forms the basis for the remaining chapters of this thesis.

3.1 Challenges of Wafer Bonding and Layer Transfer

The general concept of wafer bonding was described in §1.2.2. Additionally, wafer bonding and layer transfer have been described in review texts¹⁻³ and review articles.⁴⁻⁷ Briefly stated, wafer bonding is driven by the surface energy minimization of interacting surfaces requiring that these surfaces are flat, smooth, and particle-free. Thus, the following considerations are important in the development of a generalized wafer bonding process for materials integration:

- surface activation,
- surface morphology,

- layer thinning, if necessary (This is accomplished by H-induced layer exfoliation in the present study.),
- thermal processing issues in bonding dissimilar materials.

These process considerations are summarized in the subsequent sections. In §3.2 a generalized wafer bonding process for integrating Ge/Si and InP/Si structures is described and key results for both materials are summarized.

3.1.1 Surface Activation

One of the least defined, but most important, considerations in wafer bonding is the nature of the interaction between the bonded substrates both at bond initiation and subsequent to annealing at elevated temperatures. The nature of the surface-surface interaction is governed by the surface terminating species of the two bonded substrates. The surface-surface interactions can be categorized by the process employed to activate the surfaces. These surface activation processes generally fall into the following categories:

- Wet chemical activation⁸⁻¹²
- Gas-phase radical activation¹³
- Plasma activation¹⁴⁻¹⁹
- Deposited bonding material activation²⁰⁻²²
- Vacuum activation^{13,23,24} by surface reconstruction, sputtering, or film growth

The surface energy, γ , of surfaces activated by these techniques is correlated with the bond energy, w , of wafer bonded structures formed by bonding substrates featuring surfaces activated by the processes described above. Maximizing w with respect to material constraints dictated by the ultimate application – in this thesis conductive interfaces to facilitate current collection from the back surface of the wafer-bonded structure – increases the robustness of the wafer bonding process.

Broadly speaking, surfaces activated by wet chemical processing for wafer bonding are grouped into two categories – hydrophilic and hydrophobic. By the literal definition, hydrophobic surfaces are “water fearing,” and hydrophilic surfaces are “water loving.” The nature of the intermolecular forces leading to hydrophobicity and hydrophilicity impacts the bond strength: hydrophobicity arises from relatively weak dispersion forces and hydrophilicity arises from relatively strong dipole-dipole interactions between the facing surfaces. Hydrophobically-passivated surfaces are generally un-reconstructed hydrogenated surfaces consisting of mono-, di-, and tri-hydride surface species. Hydrophilically-passivated surfaces are generally passivated with a hydroxyl termination. The hydroxyl groups passivate an underlying oxide whose thickness is dependent on the way in which it was grown.

Gas phase radical activation generates surface species by exposing the substrate to a radical gas source in a controlled atmosphere at a controlled pressure. This process is much the same as wet chemical passivation, but at room temperature the risks of etching and thus roughening the surface are reduced. Additionally, the exposure of the surface to passivating species can be more precisely controlled in this mode of surface activation.

Plasma activation is similar to gas-phase radical activation, but there is an additional high energy ion component to the activating gas species. This causes surface damage while altering the passivation of the bonding surface. A limited amount of surface damage can cause dangling bonds that greatly increase the surface energy and increase the bond strength in wafer bonded structures. However, too much exposure, or excessive plasma power, can lead to sputtering that roughens the surface, decreasing the bond strength in wafer bonded structures by forming an unfavorable surface morphology that prevents intimate contact between the surfaces. Plasma surface activation can be conducted in a number of regimes. Recently, the use of atmospheric pressure plasma systems has gained interest for industrial processes because of ease of use and improved throughput relative to traditional rarified gas plasmas. Also, the atmospheric pressure operation regime leads to increased ion scattering, reduced mean free path, and thus lower energy

collisions of ions with the surface, causing bond breakage but reducing the likelihood of sputtering or plasma etching that leads to roughening of the surface.

By depositing a thin film of a foreign material on a bonding surface, the surface terminating groups can be changed, and the surface morphology can be changed. For instance, a spin-on glass can both terminate with hydroxyl groups and smooth the bonding surface. Additional properties can be conferred on the bond such as compliance of the deposited layer to accommodate thermo-mechanical stress. Most importantly, the interface between the device semiconductor and the bonding material can be precisely controlled to minimize contamination or undesirable passivation species. Thus, the bonded interface that is more difficult to control can be engineered to avoid interfaces between less compatible materials.

Finally, the bonding surface can be modified in ultra-high vacuum by deposition of a sputtered bonding film, or by the vacuum annealing and reconstruction of a semiconductor bonding surface. This highly idealized case of bonding sputtered or reconstructed surfaces in vacuum is valuable when studying wafer bonding at a fundamental level, but it is relatively impractical in bonding materials for industrial applications.

In this chapter, results for wafer bonding of Ge/Si and InP/Si wafer pairs are presented. Generally hydrophobic wet chemical activation was used to prepare the bonding surfaces. However, some results from gas-phase radical and plasma surface activation processes are given. The processes described are not optimized in any industrial sense.

3.1.2 Surface Morphology: Particles and Surface Roughness

As described in the previous section, wafer bonding is driven by the minimization of the surface energy of activated surfaces. This minimization can only occur when the facing surfaces are in sufficiently close proximity to interact and thereby reduce their collective surface energy by satisfying dipoles and dangling bonds. This surface energy minimization drives the accommodation of asperities such as roughness, particles, and substrate non-uniformities such as

substrate warpage and total thickness variation through substrate deformation. The increase in the system energy due to strain the energy required to accommodate these morphological non-idealities must be offset by a greater reduction in the surface energy, or wafer bonding is inhibited.

For most substrates of reasonable thickness with technologically well-developed materials such as Si, Ge, and InP, the warpage and thickness variation is easily accommodated in the bonding process and presents no difficulty to wafer bonding. On the other hand, surface roughness and the presence of particles are both very problematic to wafer bonding.

The presence of particles on a surface inhibits contact between the wafers in the region surrounding the particle. If the coverage of particles is sufficiently high, wafer bonding will be completely inhibited. Tong and Gösele summarize a solid mechanics analysis of the void radius surrounding a particle based on the assumption that the particle is incompressible.¹ The following relationship for the particle-induced void radius is determined.¹

$$R = \left[\frac{1.3E'_1 t_{w1}^3 E'_2 t_{w2}^3}{w(E'_1 t_{w1}^3 + E'_2 t_{w2}^3)} \right]^{1/4} h^{1/2} \quad (3.1)$$

Where, $E' = E/(1-\nu^2)$ and E is the Young's modulus and ν is the Poisson ratio. The particle radius is h and the bond energy is w . t_{w1} and t_{w2} refer to the thicknesses of wafers 1 and 2, respectively. As the particle becomes smaller, there eventually is a condition at which the strain energy associated with deforming the bonding substrates to completely envelop the particle is sufficiently low that there is no extended void due to the presence of such a particle. This occurs when $R \leq (t_{w1} + t_{w2})$.¹ The challenge presented by particulate contamination is illustrated in Fig. 3.1, which shows the void radius as a function of both the particle radius and bond energy for a 300 μm thick Ge substrate wafer bonded to a 200 μm thick Si substrate. Clearly, particulate contamination control is essential for any robust commercial process, as very few applications

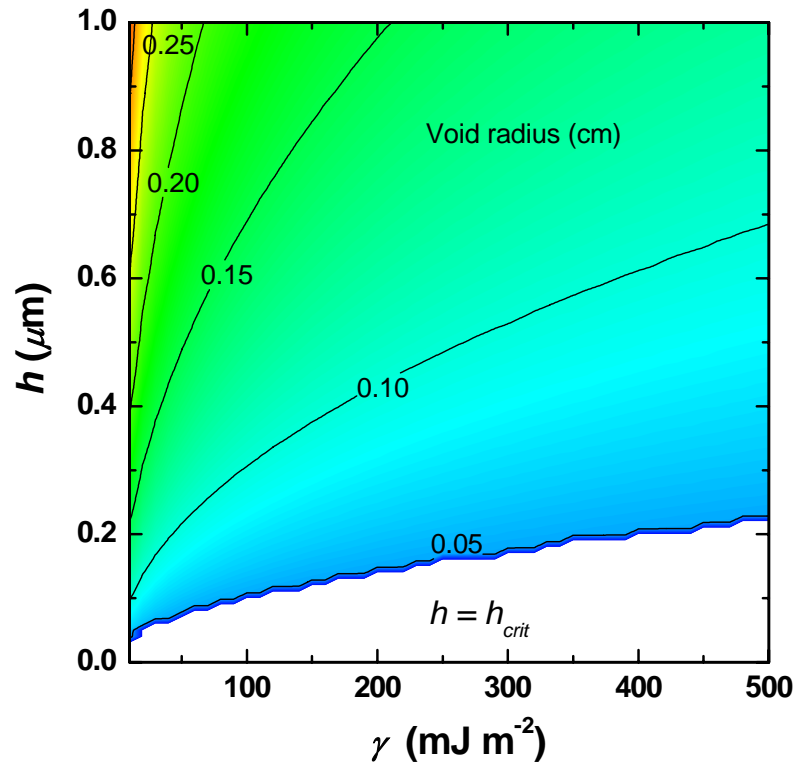


Figure 3.1 Particle-induced void radius as a function of the particle radius, h , and the bond energy, γ , for a $300 \mu\text{m}$ Ge substrate wafer bonded to a $200 \mu\text{m}$ Si substrate. The white region is for particles below the critical radius, causing the particle-induced void to be approximately the same radius as the particle itself, and thus tolerable for most applications.

can tolerate voids due to the presence of particles at the bonded interface. Furthermore, these voids become a problem for particles greater than the $\sim 0.1 \mu\text{m}$ radius.

The impact of surface roughness on the bond energy of wafer bonded pairs is more complicated. Generally, it is accepted that a surface micro-roughness of less than 1 nm is required to allow sufficiently intimate contact for wafer bonding to occur.¹ However, this “requirement” oversimplifies the mechanism by which roughness inhibits wafer bonding. The accommodation of surface roughness is made possible by the deformation of these asperities to enable intimate contact between the two wafers. In an interesting experimental and fundamental analysis of the impact of surface roughness on wafer bonding by Gui *et al.*, surface roughness asperities are

modeled as elastic spheres. Based on this assumption, a dimensionless “surface adhesion parameter” is derived.²⁵

$$\theta = \frac{E^*}{\gamma} \left(\frac{\sigma^3}{R} \right)^{1/2} \quad (3.2)$$

Where, $E^* = \frac{4}{3} \left[\frac{E}{(1-\nu^2)} \right]$. σ is a parameter closely related to the rms roughness of the bonding surface, R is the radius of the spherical caps of the asperities, and γ is the surface energy of the activated bonding surfaces. A more convenient way to monitor and model surface morphology is to measure the correlation length, ξ , through the use of a height-height analysis of an AFM surface scan.^{26,27} Based on a simple geometric assumption that the asperity edge is at a distance of $\xi/2$ from the asperity peak, equation 3.2 is modified to be a function of easily measured surface parameters.

$$\theta = 2\sqrt{2} \frac{E^*}{\gamma} \frac{\sigma^2}{\xi} \quad (3.3)$$

Gui *et al.* experimentally determined that spontaneous and strong bonding is observed for values of θ less than one.²⁵ With this as a guide, the relationship between the surface energy and the vertical and lateral components or roughness is shown in Fig. 3.2 for Ge and Si, where the value of E^* is an average value for the two materials. This figure illustrates the importance of surface roughness control in wafer bonding. More importantly, this figure indicates that the in-plane periodicity of surface roughness is of importance in wafer bonding, and should be controlled along with the out-of-plane rms roughness.

3.1.3 Layer Thinning

It is essential in thin film exfoliation that the bond strength be as high as is reasonably possible at the time of exfoliation. This is due to the violent nature of the fracture process that leads to H-induced layer transfer. Furthermore, the exfoliation mechanism of ripening of extended defect

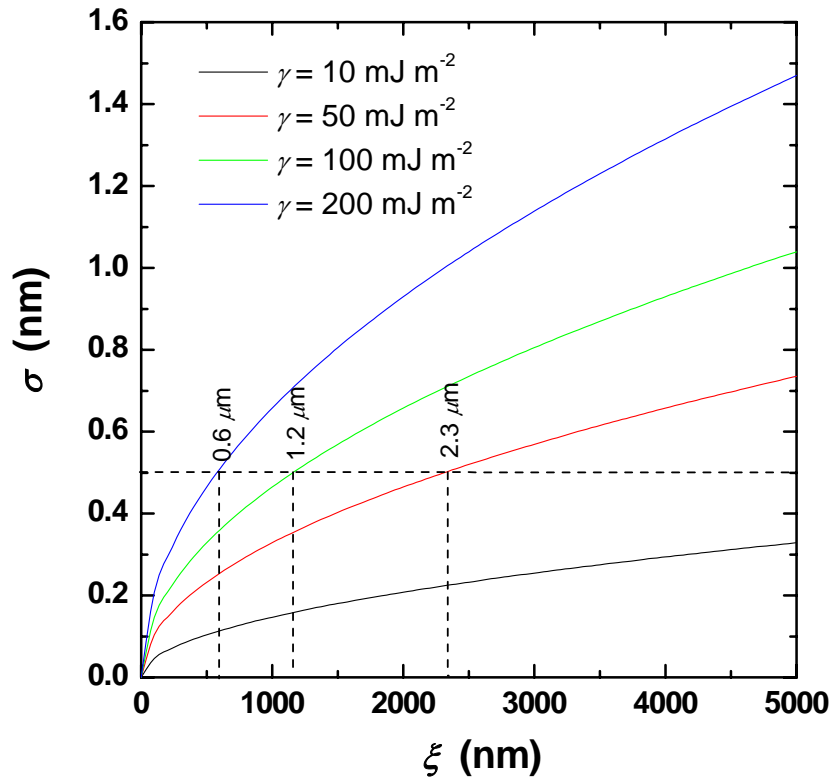


Figure 3.2 The model-predicted effect of surface roughness and asperity geometry on the bondability of Ge/Si substrates. The three surface adhesion energies, w , displayed correspond to H-passivated (10 mJ m^{-2}), oxide passivated (100 mJ m^{-2}), and plasma treated (500 mJ m^{-2}), bonding surfaces.

structures to form microcracks that serve as nucleation sites for H_2 ^{28,29} – described in Chapter 4 for Ge and InP – can occur at the bonded interface if the bond strength is not sufficiently high as increased temperatures begin to cause the hydrogen to be mobilized. The risk of blister formation at the bonded interface is exaggerated in the case of hydrophobic bonding where the interface structure may look similar to a (100) hydrogen platelet at temperatures sufficient to mobilize the hydrogen in the Ge.

3.1.4 Thermal Processing Issues for Wafer Bonding Integration of Dissimilar Materials

While the challenges discussed in §§3.1.2 and 3.1.3 apply to all wafer bonding processes, including SOI and MEMS, there are unique challenges associated with the bonding and layer transfer of different materials. The different coefficients of thermal expansion between the two materials can lead to stress in the wafers prior to exfoliation and in the thin film following exfoliation.

3.1.4.1 Coefficients of Thermal Expansion the Group IV and III-V Semiconductors of Interest

The coefficients of thermal expansion, α , for Si, Ge, InP, and GaAs have been measured and collected by various authors.³⁰⁻³⁴ The best curve fit for the available values of α in the technologically relevant range for photovoltaic devices used in space power systems – 200 to 1000 K – is given by the following empirical fit.³³

$$\alpha(T) = C_1 \left\{ 1 - \exp \left[a(T - T_0) \right] \right\} + C_2 T \quad (3.4)$$

The reported data and the functional fit to the data are shown in Fig. 3.3 for Si, Ge, InP, and GaAs. Table 3.1 lists the empirical model parameters for equation 3.4 for these materials.

The substantial differences in α for the materials of interest present challenges for both pre-exfoliation processing and subsequent processing of the wafer bonded heterostructures and for operations in space where 200°C temperature swings can be expected between illuminated and dark conditions.

3.1.4.2 Thermally-Induced Stress in Bulk-Bonded Structures

In using H-induced exfoliation as the thinning technique for wafer bonding and layer transfer integration of dissimilar materials, the dissimilar coefficients of thermal expansion place constraints on thermal processing of bulk wafer-bonded structures prior to layer transfer. It is

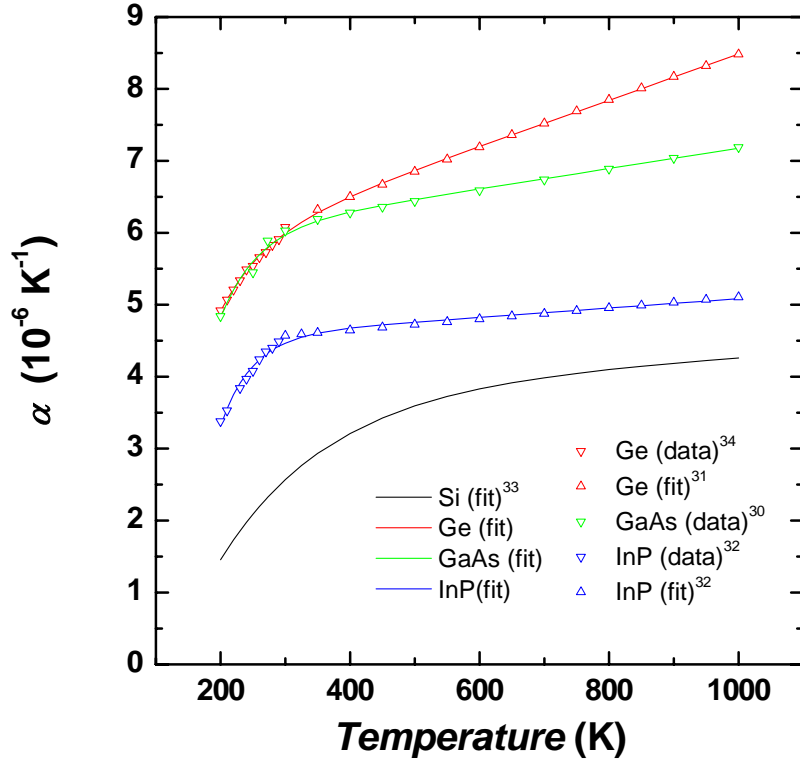


Figure 3.3 The coefficient of thermal expansion for Si, Ge, GaAs and InP over the range of interest for wafer bonding, fabrication, and operation of wafer-bonded multi-junction solar cells. The data points labeled fit are estimated either using a reported model for α as is the case for the high temperature data reported for Ge, or the data is extracted from reported data on the lattice parameter by fitting the lattice parameter over the range and taking the derivative of the fitting function, as is the case for InP.

preferable that the integrated elastic strain energy of the bulk wafer-bonded structure is less than the interfacial bond energy. In Tong and Gösele the integrated elastic strain energy is given by the following equation.¹

$$E_{el} = \int_0^{t_{w1}} \frac{\sigma_1^2(y)}{2E'_1} dy + \int_{-t_{w2}}^0 \frac{\sigma_2^2(y)}{2E'_2} dy \quad (3.5)$$

Where, $\sigma(y)$ is the vertical distribution of the normal stress due to the thermal expansion mismatch of the substrates under consideration.³⁵

Table 3.1 Coefficient of thermal expansion model parameters for the empirical α -model, $\alpha(T) = C_1 \{1 - \exp[a(T - T_0)]\} + C_2 T$, for Si, Ge, InP, and GaAs. The model has been fit for data reported from 200 to 1000 K and is suitable for that range.

	$C_1 (10^{-6} \text{ K}^{-1})$	$C_2 (10^{-9} \text{ K}^{-2})$	$a (10^{-3} \text{ K}^{-1})$	$T_0 (\text{K})$
Si ³³	3.725	55.48	-5.88	124
Ge	5.279	3.204	-14.1	82.8
InP	5.759	1.417	-17.4	111
GaAs	4.434	64.90	-20.45	138

$$\sigma_1(y) = \frac{1}{\rho} \left[\left(y - \frac{t_{w1}}{2} \right) E'_1 - \frac{2}{t_{w1}(t_{w1} + t_{w2})} \left(\frac{E'_1 t_{w1}^3 + E'_2 t_{w2}^3}{12} \right) \right] \quad (3.6)$$

$$\sigma_2(y) = \frac{1}{\rho} \left[\left(y + \frac{t_{w2}}{2} \right) E'_2 + \frac{2}{t_{w2}(t_{w1} + t_{w2})} \left(\frac{E'_1 t_{w1}^3 + E'_2 t_{w2}^3}{12} \right) \right] \quad (3.7)$$

Where, ρ is the radius of curvature for the bonded pair given by the following expression.³⁵

$$\rho = \frac{(t_{w1} + t_{w2}) \left[\left(1 + \frac{t_{w1}}{t_{w2}} \right)^2 + \left(1 + \frac{t_{w1} E'_1}{t_{w2} E'_2} \right) \left(\frac{t_{w1}^2}{t_{w2}^2} + \frac{t_{w2} E'_2}{t_{w1} E'_1} \right) \right]}{6 \left(1 + \frac{t_{w1}}{t_{w2}} \right)^2 \varepsilon_m} \quad (3.8)$$

The quantity ε_m is the thermally-induced strain caused by the difference in the coefficients of thermal expansion between the device material and the substrate and is given by the following expression.

$$\varepsilon_m = \int_{T_0}^T \Delta\alpha(T') dT' \quad (3.9)$$

Where, $\Delta\alpha(T) = \alpha_{w1}(T) - \alpha_{w2}(T)$. Using equation 3.4 to estimate $\Delta\alpha(T)$, Fig. 3.4 shows the substrate radius of curvature as a function of bond temperature and process temperature.

From these equations the elastic strain energy of dissimilar materials is given by

$$E_{el} = \frac{E'_1}{2\rho^2} \left(\frac{t_{w1}^3}{3} - C_1 t_{w1}^2 + C_1^2 t_{w1} \right) + \frac{E'_2}{2\rho^2} \left(\frac{t_{w2}^3}{3} - C_2 t_{w2}^2 + C_2^2 t_{w2} \right) \quad (3.10)$$

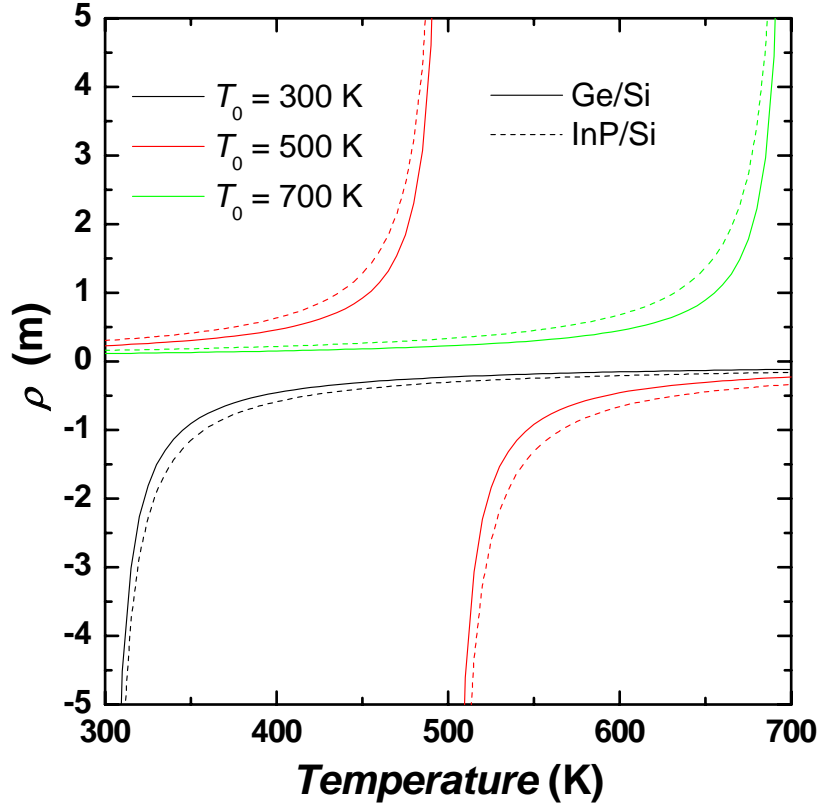


Figure 3.4 Calculated radius of curvature for a Ge/Si and an InP/Si with a 300 μm thick device substrate and a 140 μm thick Si handle substrate. The radius of curvature goes to infinity as the bond temperature approaches the process temperature.

Where,

$$C_1 = \frac{t_{w1}}{2} + \frac{2}{t_{w1}(t_{w1} + t_{w2})} \left(\frac{E'_1 t_{w1}^3 + E'_2 t_{w2}^3}{12E'_1} \right) \quad (3.11)$$

$$C_2 = \frac{t_{w2}}{2} + \frac{2}{t_{w2}(t_{w1} + t_{w2})} \left(\frac{E'_1 t_{w1}^3 + E'_2 t_{w2}^3}{12E'_2} \right) \quad (3.12)$$

Figure 3.5 shows the integrated elastic strain energy for a 300 μm thick Ge or InP substrate wafer bonded to a 140 μm thick Si substrate as a function of the process temperature of the bulk wafer-bonded substrate pair for bond initiation temperatures of 300, 500, and 700 K. When interpreting the results of this calculation, it is important to note that as the temperature of the

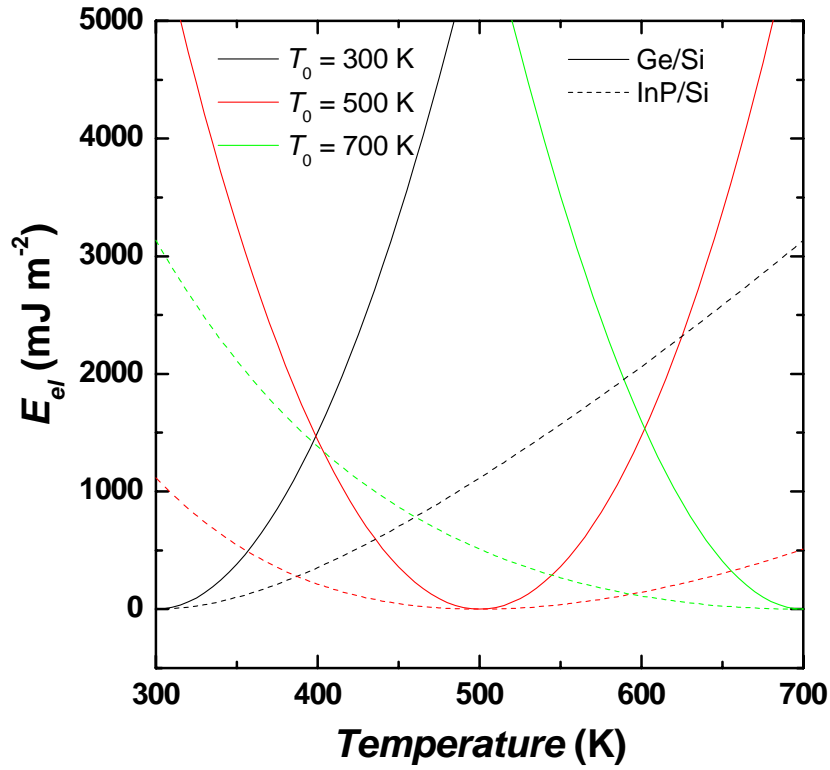


Figure 3.5 Calculated elastic strain energy for Ge/Si and an InP/Si bulk-bonded substrates with a $300 \mu\text{m}$ thick device substrate and a $140 \mu\text{m}$ thick Si handle substrate under thermal processing.

wafer bonded pair increases, the bond energy increases. However, it can also be expected that the increased normal and peeling stresses in the wafer bonded substrate due to the coefficient of thermal expansion mismatch inhibit this process relative to un-stressed wafers.

3.1.4.3 Stress and Substrate Morphology during Thermal Processing of Thin-Film Wafer-Bonded Heterostructures

Following layer transfer from the implanted device substrate, the behavior of the wafer-bonded heterostructure during thermal cycles is still of concern for the fabrication and operation of photovoltaic devices on these structures. The three primary concerns for subsequent thermal processes are

- film strain and substrate deformation in MOCVD growth of photovoltaic structures;

- film strain and substrate deformation following cool down following MOCVD;
- and, stability and fracture of thick, heavily-strained thin film device structures in operation.

These concerns are addressed in the following sections.

3.1.4.3.1 Substrate Shape during MOCVD

The substrate shape during MOCVD growth of ternary and quaternary III-V semiconductor materials is of concern in the stoichiometry control of the material. This is due to temperature non-uniformities attributed to the lack of thermal contact with the susceptor. Temperature non-uniformities during growth of ternary or quaternary III-V semiconductors can impact the incorporation of cations due to thermodynamic solubility changes and can impact the incorporation of anions due to changes in the precursor cracking kinetics.

The key figure of merit for substrate shape during MOCVD growth is wafer bow, which is the vertical displacement at the edge of the substrate relative to the center zero position, assuming axially symmetric deformation of the substrate. For substrates of constant curvature the substrate bow is related to the curvature of the substrate by the following geometrical relationship.

$$b = \frac{\kappa R^2}{2} \quad (3.13)$$

Where b is the wafer bow, κ is the substrate curvature, and R is the substrate radius. In the case of thin films under limited strain, the curvature is related to the strain in the thin film by Stoney's equation.³¹

$$\kappa = \frac{6\varepsilon_m M_f h_f}{M_s h_s^2} \quad (3.14)$$

Where ε_m is the thermal strain of the thin film given by equation 3.9, M is the biaxial elastic modulus of the substrate or thin film, and h is the thickness of the substrate or thin film.

A correction to the relationship between strain-induced stress and curvature is represented by the dimensionless stress, S , and curvature, K , variables.³⁶

$$S = K \left[1 + (1 - \nu) K^2 \right] \quad (3.15)$$

Where,

$$S = \frac{3\varepsilon_m R^2 h_f M_f}{2h_s^3 M_s} \quad (3.16)$$

$$K = \frac{R^2 \kappa}{4h_s} \quad (3.17)$$

The predicted curvature and corresponding bow of the substrate departs from the linear Stoney region for values of S greater than 0.3.³⁶ For the range $0.3 < S < 1.4$ the curvature of the substrate is axially symmetric, but the curvature varies along the radius, so that the substrate does not bow in a spherical shape, but rather with a flat-bottom bowl morphology with more exaggerated bowing at the edge of the substrate. The predicted curvature from equation 3.7 is the average curvature, and can still be used to approximate the bow of a wafer bonded bi-material substrate. Figure 3.6 shows the bow predicted by equation 3.7 for Ge/Si, InP/Si, and GaAs/Si wafer bonded virtual substrates consisting of $0.5 \mu\text{m}$ thick device film on a $140 \mu\text{m}$ thick Si substrate, the same thickness as substrates used for space power system photovoltaics. The substrate diameter is 100 mm. The black family of curves shows the predicted bow for substrates in which the bonding temperature, and thus the zero-stress temperature, is 300 K. The red family of curves shows the predicted substrate bow for wafer-bonded substrates bonded at 500K, the highest bond initiation temperature considered practical with the process presently being studied. The decreasing rate of bow at higher temperature excursions from the bond initiation temperature is attributed to the non-linear portion of the stress-curvature relationship. For sufficiently high values of film stress, the equilibrium substrate shape is no longer axially symmetric, and the curvature bifurcates into a saddle-shape with orthogonal directions of minimum and maximum curvature. Bifurcation of the

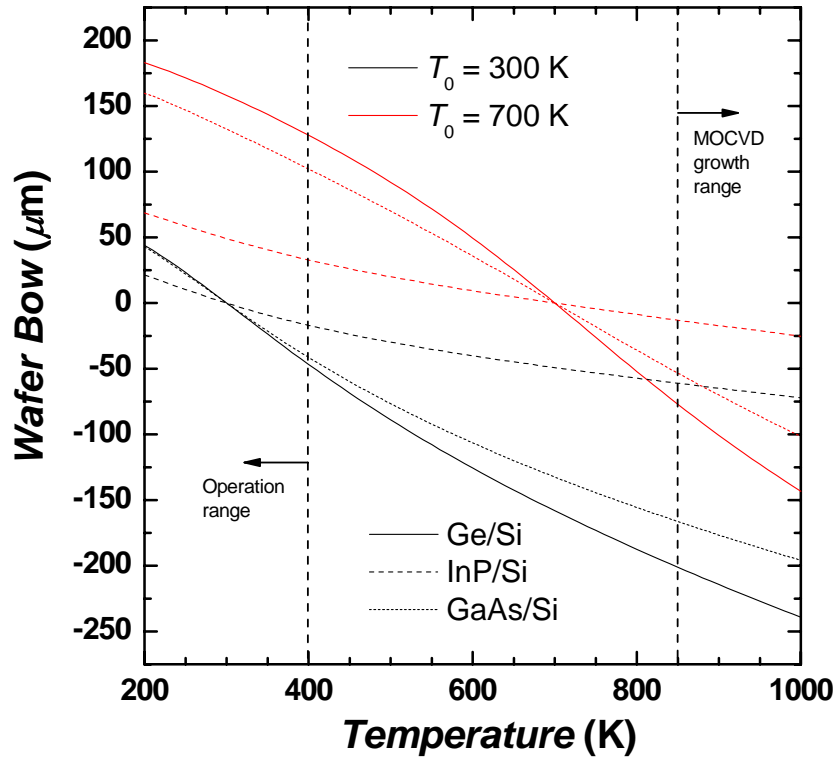


Figure 3.6 Predicted wafer bow for 100 mm virtual substrates consisting of a 140 μm thick substrate suitable for space photovoltaic systems with a 0.5 μm thick device film. The vertical dashed lines mark the boundaries on the temperature ranges of interest for device growth by MOCVD at temperatures above 850 K and operation of the solar cell device structure in a space power system below 400 K.

substrate curvature is shown to occur for $S > 1.43$.³⁶ This is not predicted to occur prior to device film growth for the substrates under consideration in the present work. However, as the subsequent section shows, the predicted film stress surpasses the curvature bifurcation critical value for thick epitaxial films that are relaxed at the growth temperature.

3.1.4.3.2 Substrate Deformation and Stress Following Photovoltaic Device Growth

The growth of thick relaxed films on Ge/Si and InP/Si at elevated temperatures further increases the likelihood of substrate deformation during cool down, presenting challenges for subsequent processing such as lithography, cover-glass interconnection, and module assembly. Based upon

equation 3.7, the predicted substrate bow is shown in Fig. 3.7 for a $6 \mu\text{m}$ thick GaAs-like material – a material with the same value of α as bulk GaAs – grown at an elevated temperature on a Ge/Si wafer-bonded substrate consisting of a $0.5 \mu\text{m}$ film of Ge on a $140 \mu\text{m}$ thick Si handle substrate. The predicted bow is plotted as a function of temperature for a number of bonding and growth temperatures. It is clear that regardless of actions taken in bonding and growth temperature selection, bifurcation of the substrate curvature is anticipated, illustrated in Fig. 3.7 by dashed horizontal lines. The predicted bow and substrate geometry past the bifurcation point is difficult to model. The value predicted in Fig. 3.7 for substrate bow beyond the bifurcation point is correct for four radial positions on the substrate, and is essentially an average of the bow for the

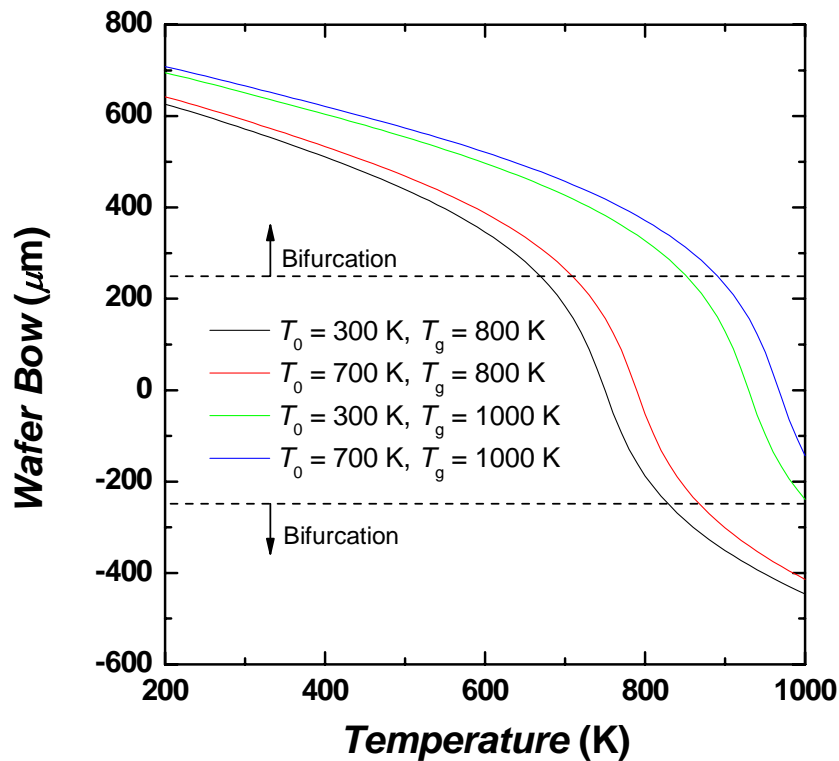


Figure 3.7 Predicted substrate bow for a $6 \mu\text{m}$ GaAs-like multi-junction solar cell on a $0.5 \mu\text{m}$ Ge film on a $140 \mu\text{m}$ Si substrate. The impact of the bond temperature and cell growth temperature are illustrated. The dashed lines indicate that the model predicts the bow beyond the critical stress for substrate shape bifurcation.

bifurcated shape. Thus, the maximum edge displacement is much greater than the predicted bow in this regime, and the minimum edge displacement is much less. Either way, this is a serious challenge for subsequent processing that is not addressed in the present thesis, due to the developmental nature of process research on device fabrication and integration topics such as the impact of substrate shape on subsequent processing and operation.

3.1.4.3.3 Photovoltaic Device Film Stability in Operation from 200 to 400 K

Following device fabrication and packaging, the high levels of stress and elastic strain energy in the thin film device are of concern for long-term reliability. Previous work on compositionally graded Ge/Si³⁷⁻³⁹ structures used as templates for dual-junction GaInP/GaAs solar cells studied the cracking of GaAs/Si structures at temperatures well below the growth temperature. It was shown that for a temperature 650°C less than the growth temperature of the GaAs film, the onset of cracking occurs for thicknesses greater than 5 μm .⁴⁰ Thus, 5 μm thick device structures fabricated on a 0.5 μm thick Ge thin film on Si will be resilient with regard to thin film cracking, especially in light of the lower value of α for GaInP ($5.3 \times 10^{-6} \text{ K}^{-1}$ at 300 K) relative to GaAs ($5.7 \times 10^{-6} \text{ K}^{-1}$ at 300 K).³⁴

3.2 Wafer Bonding Process and Results

The preceding section describes some of the guiding principles in designing a wafer bonding process. The optimization of such a process is an endeavor that is better suited for industry with its larger research budget and need for process perfection. However, the generalized wafer bonding process described below for both Ge/Si and InP/Si wafer bonding has been successfully implemented to fabricate structures to characterize the electrical properties of the bonded interface and to perform initial testing of the feasibility of these materials for use as epitaxial templates in the MOCVD growth of III-V semiconductors.

3.2.1 Generalized Wafer Bonding Process for Ge/Si and InP/Si Wafer Bonding

As was mentioned in the previous sections, it is critical for wafer bonding in general to use clean and smooth surfaces. Additionally, when bonding dissimilar materials it is desirable to target a low H-induced exfoliation temperature to prevent the buildup of excessive strain energy in the wafer bonded pair prior to exfoliation. To meet these challenges the following general wafer bonding and layer transfer process has been generated for the materials under consideration.

1. **H-implantation** – H⁺ at an energy of 80 keV was generally employed with a beam current of approximately 100 μA over a 52 cm² area. Multiple doses were tested, but generally it was shown that 1×10^{17} cm⁻² was satisfactory for Ge exfoliation, and 1.5×10^{17} to 2.0×10^{17} cm⁻² was satisfactory for InP exfoliation.
2. **Surface Protection** – Due to the cost of Ge and InP substrates, it was necessary to experiment with smaller sample sizes. To protect the substrate surfaces during cleaving, several methods were employed, including cleaving in an acetone bath, as is described in Chapter 5 for the fabrication of *J-V* test structures. However, the most effective and commonly used method was to spin coat the substrates with Shipley 1813 photoresist using a 3000 rpm spin for one minute. The substrates were then cleaved into the desired size, typically about 1 cm². The same process was employed for cleaving small Si samples.
3. **Organic Cleaning and Particle Removal** – Organic solvents were used to clean the small samples for wafer bonding to remove the photoresist and any adsorbed hydrocarbons. Additionally, the use of ultrasonic baths during some of these cleaning steps improved particle removal and prevented particles trapped in the protective photoresist coat from being deposited onto the substrate surface. The process steps were:
 - a. **Boiling Acetone** – Typically on a 100°C hot plate for five minutes or longer.

- b. Acetone Ultrasonic Bath** – This was first applied to the boiled acetone bath after step a followed by a second ultrasonic acetone bath in a new, clean beaker using new acetone for at least five minutes.
 - c. Methanol Ultrasonic Bath** – A five minute ultrasonic methanol bath was used as a final organic cleaning step. Methanol serves as an efficient solvent of any adsorbed acetone and is easily solvated during the final deionized water rinse.
 - d. De-ionized Water Rinse** – This step allows the substrate to be dried without concern for contamination residue from the organic cleaning steps remaining on the surface. For Ge cleaning, water etches the Ge surface by dissolving germanium oxide. Thus, it is critical that the duration of the de-ionized water rinse be kept short (less than one minute) to prevent roughening of the Ge surface.
4. **Oxide Etching** – To ensure intimate contact between the bonded substrates with minimal electrical resistance, it is necessary to etch any native oxide on the Ge or InP and Si. This is generally accomplished with a dilute HF dip, typically 30 seconds or less in a 5% or less HF solution. This process is followed by a final rinse in de-ionized water with the same restriction for Ge that is described in process step 3d.
5. **Bond Initiation** – Many bond initiation schemes were attempted, but generally these consist of carefully placing the samples face-to-face in a clean environment, and initiating bonding by slight pressure in the center of the sample. Upon initiation, if the bond energy is sufficiently high, then the remaining gas between the substrates is extruded as the bonding front propagates to further minimize the surface energy of the two samples.
6. **Annealing** – By annealing the substrates, the H-induced exfoliation process is activated (see Chapter 4), and the electrical properties of the wafer-bonded interface are improved (see Chapter 5). Samples were generally annealed under an applied uni-axial pressure



Figure 3.8 Wafer bonding apparatus designed to exert uni-axial, pressure through the application of a controlled torque, to the lead screw at the top of the bonder during anneals up to 350°C.

ranging from one to 10 MPa while annealing to a temperature of approximately 325°C in the apparatus shown in Fig. 3.8. This was sufficient to cause the exfoliation of the thin device film for the implant conditions described in step 1 above. In certain experiments, annealing was performed in the absence of applied pressure to temperatures of up to 400°C (see Chapter 5).

This generalized process is depicted in Fig. 3.9. Key results and observations from the Ge/Si and InP/Si wafer bonding process are summarized in §3.2.2 and §3.2.3, respectively.

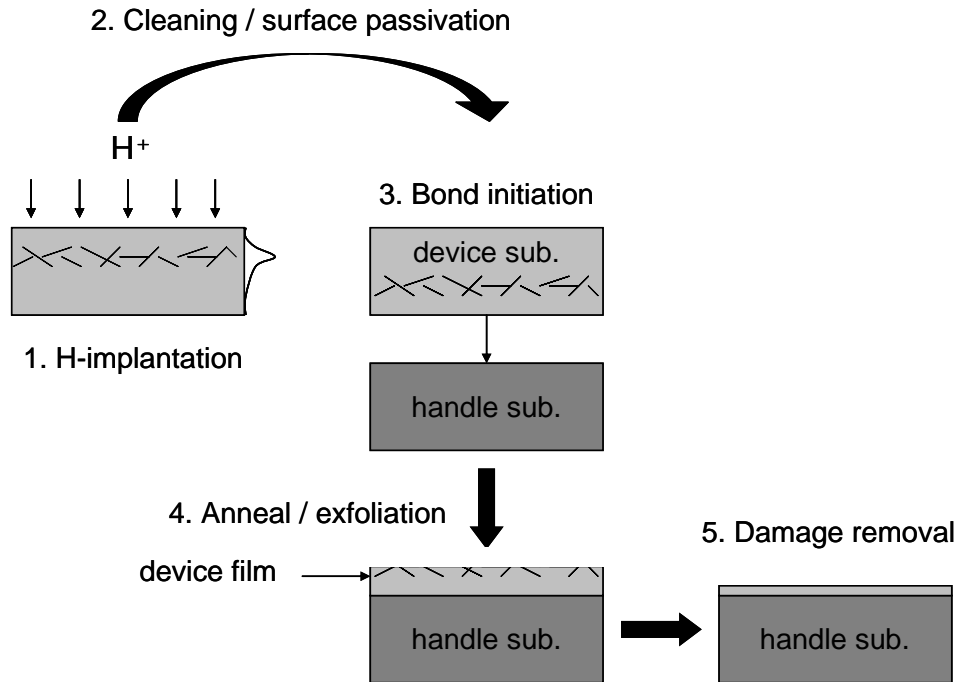


Figure 3.9 Generalized process for the fabrication of wafer-bonded alternative substrates showing: 1. H-implantation of the device substrate; 2. surface cleaning and passivation; 3. bond initiation; 4. film exfoliation by annealing; and, 5. removal of implant damage and exfoliation-induced surface roughness.

3.2.2 Ge/Si Wafer Bonding Process and Results

The process conditions for wafer bonding have been permuted to a much greater extent in Ge/Si wafer bonding, relative to the work on InP/Si wafer bonding to be presented in §3.2.3. The summary here is not intended as a report of all conditions attempted, but rather to show the results from a generalized process that works sufficiently well to provide a proof of concept. Ge/Si wafer bonding has been demonstrated by the following process permutations.

- **Method I: Hydrophobic Bonding** – The process of §3.2.1, where the wafer bonding forces are predominantly dispersion forces that are dominant in hydrophobically passivated surfaces.
- **Method II: Hydrophilic Bonding** – The process of §3.2.1 with an additional step of treating the Ge and Si samples with a 10 minute exposure to ultraviolet ozone. This

process creates thin surface oxides with hydrophilic hydroxyl termination groups. The presence of these hydroxyl groups has been shown to increase the bond strength of the bonded structure. Additionally, ozone cleaning is commonly used as a means of removing hydrocarbons adsorbed to surfaces. The presence of hydrocarbons at the bonded interface has been shown to decrease the thermal stability of bonded structures.⁴¹

Optical images of representative bonded structures are presented in Figs. 3.10(a) and (b) for hydrophilic and hydrophobic wafer bonding, respectively. Fig. 3.10(a) shows that an area on the

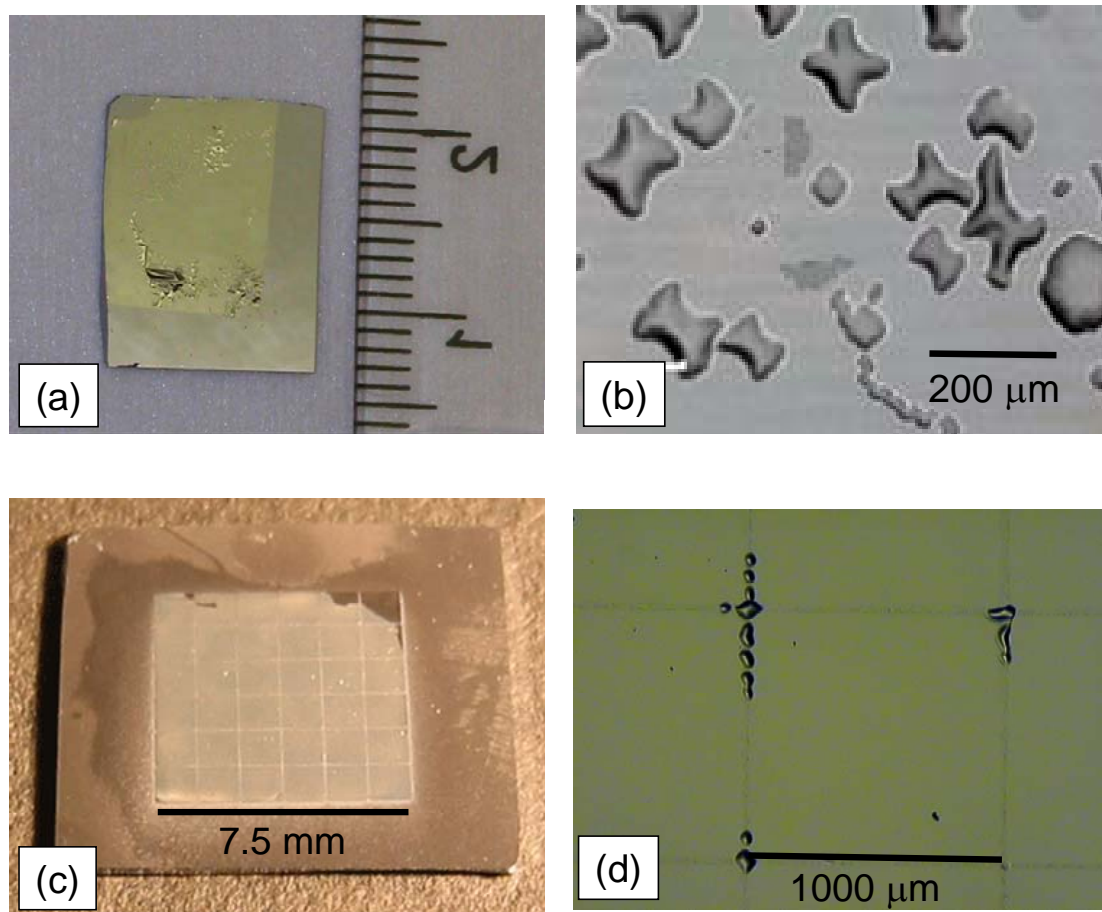


Figure 3.10 (a) Hydrophilically wafer bonded Ge/Si structures fabricated by wet chemical passivation followed by ozone cleaning prior to bonding. (b) Typical trapped gas microstructure for hydrophobically and hydrophilically wafer bonded Ge/Si structures. (c) A Ge/Si wafer bonded structure formed by hydrophilically wafer bonding – as described in (a) – Ge to a Si sample with a recessed grid pattern lithographically defined. This enables the release of trapped and evolved gas at the bonded interface. (d) Optical microscopy view of a grid-bonded sample as described in (c) showing the large, defect-free field of Ge between the grid lines and regions of Ge over the grid lines that have formed bubbles either through trapped gas or thermally-induced buckling.

order of one cm^2 can be transferred by hydrophilic bonding in a bench top experiment using the technique illustrated in Fig. 3.9 and the uniaxial pressure annealing equipment shown in Fig. 3.8. Figure 3.10(b) shows that this process can be extended to surfaces that have been rendered largely oxide and hydroxyl free by dipping them in a 5% HF bath. However, it also shows an attendant problem with bonding substrates in this way, the formation of bubbles consisting of trapped gas at the bonded interface. This is thought to be formed by adsorbed species trapped at the bonded interface at room temperature and subsequently evolved by thermal processing. As was previously mentioned, these have been speculated to be related to several contamination sources: desorbed hydrogen from the hydride passivation layer, desorbed water molecules present on the surfaces at room temperature, and decomposition of hydrocarbon contamination into hydrogen gas and smaller gas-phase contaminants such as CH_x .

To improve on the results presented above, additional permutations, described below, of the generalized bonding process have been attempted. These wafer bonding process variations have been shown to enable wafer bonding and layer transfer. Except in the case of plasma surface activation, insufficient data exists to demonstrate that these techniques improve the wafer bonding process. However, they are potentially beneficial for solving some of the fundamental problems confronted in Ge/Si wafer bonding.

- **Method III: Surrogate Layer Bonding** – In this permutation of the process described in §3.2.1, a thin amorphous film of Si is deposited on the Ge bonding surface using molecular beam deposition. The presence of the amorphous Si enables the use of traditional Si cleaning methods that are too harsh for Ge. Additionally, the formation of a Si/Si interface allows techniques developed for wafer bonding of Si/Si structures to be extended to bonding Ge/Si substrates. This technique was demonstrated for both hydrophobic and hydrophilic wafer bonding of Ge on which a 4.0 nm amorphous Si film was deposited. Both of these bonding conditions demonstrated bonding areas on the order of one mm^2 .

- **Method IV: Bonding to Grid Patterned Substrates** – In this permutation of Methods I and II, lithography is used to define a square grid of trenches approximately 20 μm wide and 1 μm deep. These trenches were spaced at several different pitches. Representative optical images are given in Figs. 3.10(c) and (d). In Fig. 3.10(c) a full-field image of a Ge film hydrophobically bonded to a grid with a 1.25 mm pitch and transferred from a Ge device substrate implanted with H^+ at 25 keV to a dose of $1.0 \times 10^{17} \text{ cm}^{-2}$ shows the relative sample perfection achievable by this method. The magnified view in Fig. 3.10(d) of a film hydrophilically bonded and transferred from a Ge device substrate implanted with H^+ at 80 keV to a dose of $1.0 \times 10^{17} \text{ cm}^{-2}$ illustrates the lack of trapped gas at the bonded interface. Interestingly, the device film extends from one edge of the trench to the other for this thicker film transferred from the 80 keV H^+ implanted sample.
- **Method V: Plasma Assisted Bonding** – As was mentioned in §3.1.1, plasma surface activation has been demonstrated as a means of improving bond strength for wafer bonding of several materials. Using plasma surface activation by an atmospheric pressure N_2 parallel plate plasma source that couples to the bonding surface, large area layer transfer has been demonstrated as shown in Fig. 3.11. This image in the infrared of a 50 mm substrate shows defective regions (light colored splotches) in the transferred film where the presence of trapped gas changes the transmission of the IR light. The ring at the center is caused by a reflection of the camera image off of the surface of the transferred film.

While there is much technical work left to move from this proof of concept demonstration of hydrophobic and hydrophilic wafer bonding and layer transfer fabrication of Ge/Si substrates, the present results show the feasibility of Ge/Si integration for GaAs-based device integration with Si. Furthermore, these structures and the wafer bonding process described in this chapter serve as the basis for subsequent testing of the electrical properties of the wafer bonded interface and the

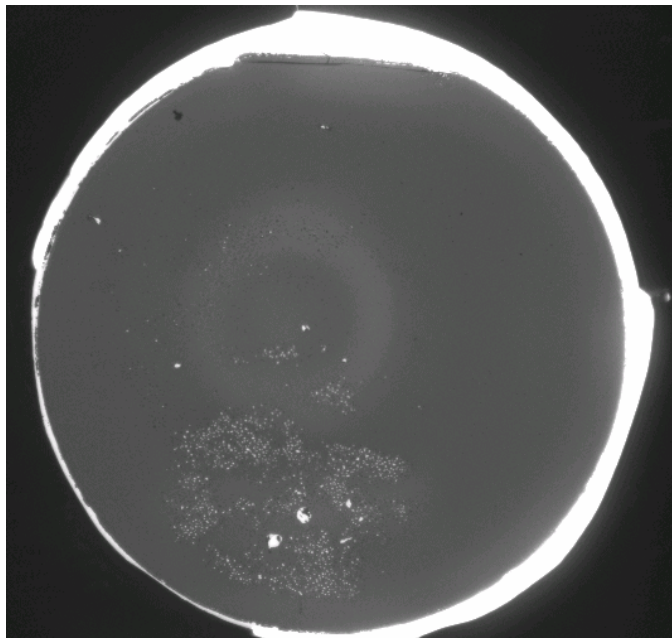


Figure 3.11 A 100 mm Ge/Si wafer bonded and layer transferred structure fabricated by use of plasma activation and annealing. The pin-holes are caused by blisters and un-transferred regions of Ge. The important result is that through the use of improved surface cleaning and activation along with better tooling, substantial advancements can be made in the fraction and quality of transferred material.

suitability of these structures for the epitaxial growth of GaAs on Ge/Si wafer bonded heterostructures using metal-organic chemical vapor deposition (MOCVD).

3.2.1.1 AFM Characterization of Wafer Bonded Heterostructures

The as-transferred Ge surface morphology in Ge/Si wafer bonded heterostructures has been studied using atomic force microscopy (AFM). AFM indicates that the surface of an as-transferred Ge film has a roughness between 10 and 20 nm rms. An AFM image of a typical Ge transferred film is shown in Fig. 3.12. The suitability of as-transferred Ge/Si heterostructures for MBE growth of Ge films and MOCVD growth of GaAs and triple-junction solar cell structures is investigated in Chapter 6.

As was mentioned in §1.2.1.3.1, it is common to intentionally miscut Ge substrates intended for GaAs heteroepitaxy. AFM analysis of Ge films transferred from Ge substrates of 9° and 15° miscut angles and (100) on-axis substrates showed that the roughness of the as-transferred surface is dependent upon the miscut angle. The angle dependence of the transferred Ge surface

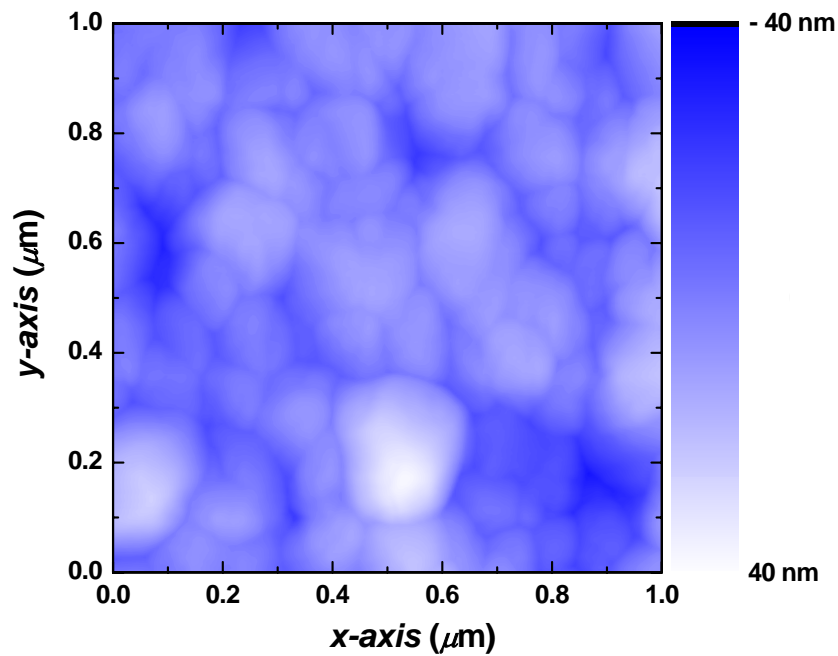


Figure 3.12 An AFM scan of an as-transferred Ge/Si surface with a roughness of ~ 10 nm. The sample was made by transferring a film from an on-axis (100)Ge substrate to a Si handle wafer.

roughness is shown in Fig. 3.13. As will be further discussed in Chapter 4, the physical mechanism that leads to the exfoliation of thin films is associated with the formation of (100) micro-cracks in the Ge substrate. The extension of cracks along the (100) plane proceeds by the ripening of many micro-cracks at varying depths through the peak range of the H-implantation zone. This ripening process is shown by TEM evidence to proceed by “jumping” of the crack between (100) micro-cracks at differing depths. The observation that the roughness of the exfoliated surface is correlated with the miscut of the Ge substrate is consistent with this view. Figure 3.14 shows a simplified schematic of the depth distribution of micro-cracks. Figure 3.14(a) is a representation of the distribution of micro-cracks in an on-axis crystal. In this orientation, the

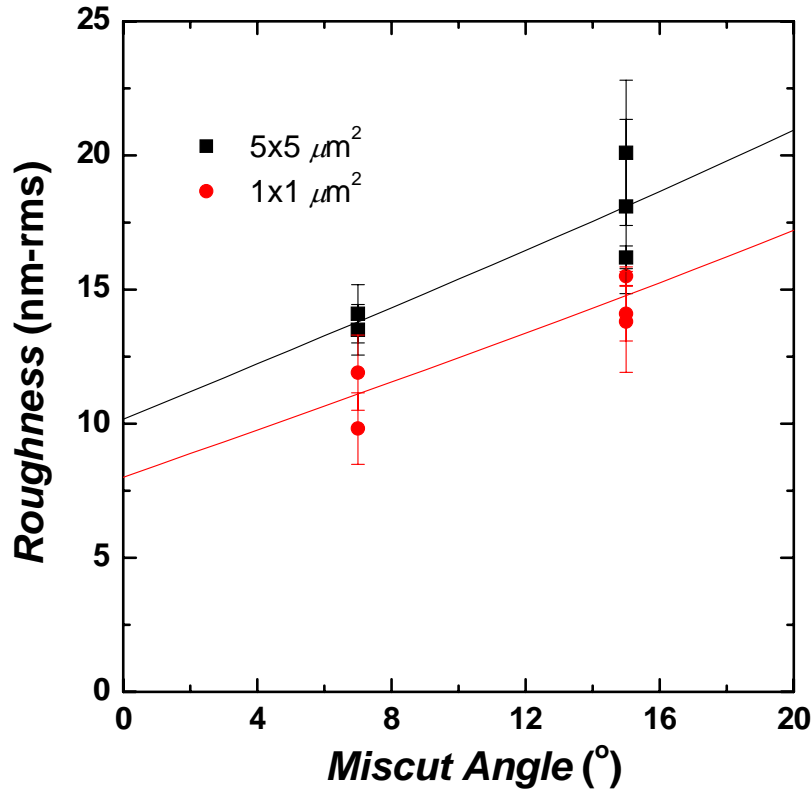


Figure 3.13 Measured surface roughness for Ge/Si films transferred from bulk Ge substrates with 9° and 15° miscut angles as a function of the AFM measurement area. The individual data points represent different samples. The error bars are defined as \pm one standard deviation based on three measurements.

micro-crack distribution is characterized by two key parameters: $\langle \delta \rangle$, the mean separation in depth between adjacent micro-cracks; and, $\langle L \rangle$, the mean micro-crack lateral extension just prior to ripening with an adjacent micro-crack to form an extended crack structure. It is assumed that the rms roughness of an on-axis exfoliated surface is proportional to $\langle \delta \rangle$. In Fig. 3.14(b), the same network of dislocations is shown for a substrate with a miscut angle of θ . It is assumed that the average depth of the ensemble of micro-cracks that lead to exfoliation is unaltered by the change in the substrate orientation in the miscut substrates. Thus, $\langle \delta \rangle$ is also assumed to be

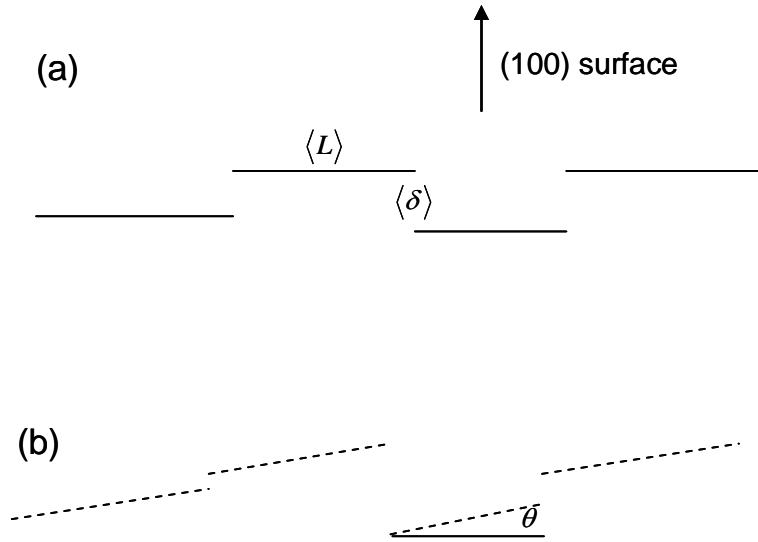


Figure 3.14 (a) A schematic representation of the distribution of micro-cracks that ripn during the H-induced exfoliation of an on-axis (100) semiconductor. (b) A schematic of the same distribution of micro-cracks in a H-implanted semiconductor substrate miscut by an angle θ .

unchanged. A simple standard deviation calculation based on these assumptions gives the following relationship between rms roughness, σ , $\langle L \rangle$, and θ .

$$\sigma_{\theta} = \sigma_{(100)} + \langle L \rangle \tan \theta \quad (3.9)$$

In Fig. 3.13 the lines on the plot show the best fit of the data for the $1 \mu\text{m} \times 1 \mu\text{m}$ and $5 \mu\text{m} \times 5 \mu\text{m}$ scan areas. Based upon these fits, the value of $\langle L \rangle$ is estimated for 24.8 nm and 29.6 nm for the $1 \mu\text{m} \times 1 \mu\text{m}$ and $5 \mu\text{m} \times 5 \mu\text{m}$ scan areas, respectively. These values should be scan area independent. However, these numbers are reasonably close given the error bars and scatter in the reported roughness data. Additionally, hysteresis and line-to-line variations during AFM measurements may cause scan area dependent variation in roughness. Also, as the scan area increases, surface features of longer length scale are included in the surface measurement, such as surface undulations related to flatness of the underlying Si substrate.

3.2.2 InP/Si Wafer Bonding Process and Results

As mentioned in the previous section, fewer process permutations were attempted in the bonding of InP/Si structures. The process described in §3.2.1 and categorized as Method I in §3.2.2 was applied to InP to enable hydrophobic wafer bonding and layer transfer. In the transfer of InP thin films to Si it was observed that the application of uniform pressure during annealing is essential. Additionally, as will be presented in greater detail in §5.1.3, the use of HF treatment of InP substrates prior to wafer bonding does not lead to the formation of an oxide-free bonding interface. This is thought to enable stronger bond strength in the as-bonded structures, as the existence of an oxide at the bonded interface suggests that hydroxyl groups and adsorbed water are present at bonding, forming a hydrophilic bonding structure that allows the bonding surfaces to interact by dipole-dipole structures. Figure 3.15 shows the large area layer transfer of InP to Si using the technique described above.

In addition to the bonding method described above, a plasma activated bonding method

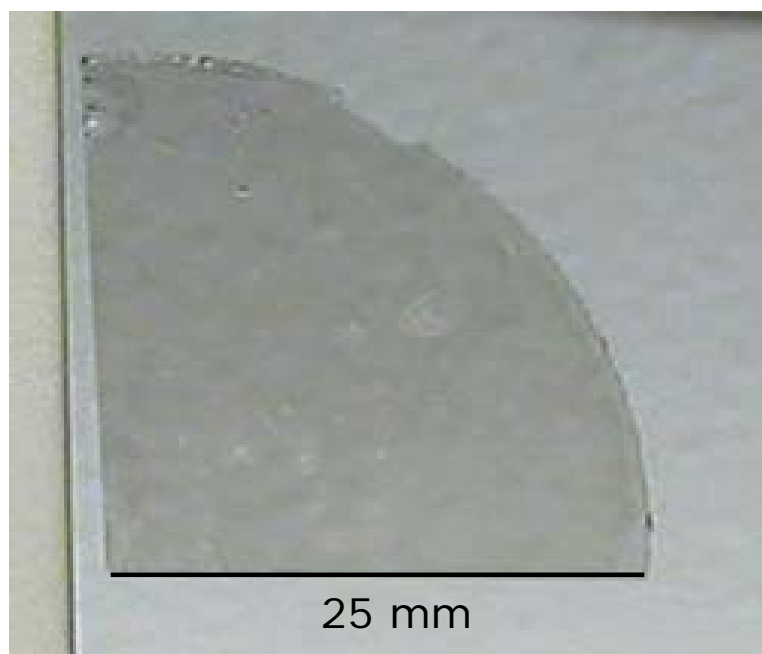


Figure 3.15 InP/Si wafer bonded structure formed by wet chemical passivation of the bonding surfaces.

similar to Method V in §3.2.2 was applied to the bonding of InP/Si structures. In this work, process equipment from Suss MicroTec, including the NP12 atmospheric plasma tool, the CL200 megasonic DI water particle removal system, and the SB6e wafer bonding tool were used to reduce particle contamination. Figure 3.16(a) shows an infrared transmission image of an InP/Si bonded interface with voids due to particulate contamination present during bonding. By optimizing the particle removal process, Fig. 3.16(b) shows that bonded interfaces can be achieved without the presence of particulate contamination. Figure 3.16(c) illustrates the use of crack length testing to determine the bond strength of an InP/Si pair. This work is ongoing, but preliminary results show that with the correct selection of plasma surface activation parameters and surface cleaning, bond strengths six times greater than those achievable by Method I described in the previous chapter are possible.

3.2.2.1 AFM Characterization of Wafer Bonded Heterostructures

AFM measurements of the as-transferred InP/Si structure indicate that the surface roughness of the transferred film is comparable to that observed in Ge/Si. In particular, the surface roughness of InP transferred layers, generally ranged from eight to 12 nm rms for on-axis films. This is the same as the measured value of 10 nm rms for the surface roughness of as-transferred on-axis Ge/Si structures.

3.3 *Summary*

In the previous section a generalized wafer bonding process was described for the fabrication of Ge/Si and InP/Si virtual substrates. This method and several variations on the method were shown to enable transfer of thin Ge and InP films on the order of mm^2 to cm^2 to Si handle substrates. The surface morphology of these structures was shown to have a surface roughness of 10 to 20 nm rms. The degree of roughness was shown to be a function of the miscut angle in the material system. Additionally, the general challenges for wafer bonding were summarized as they

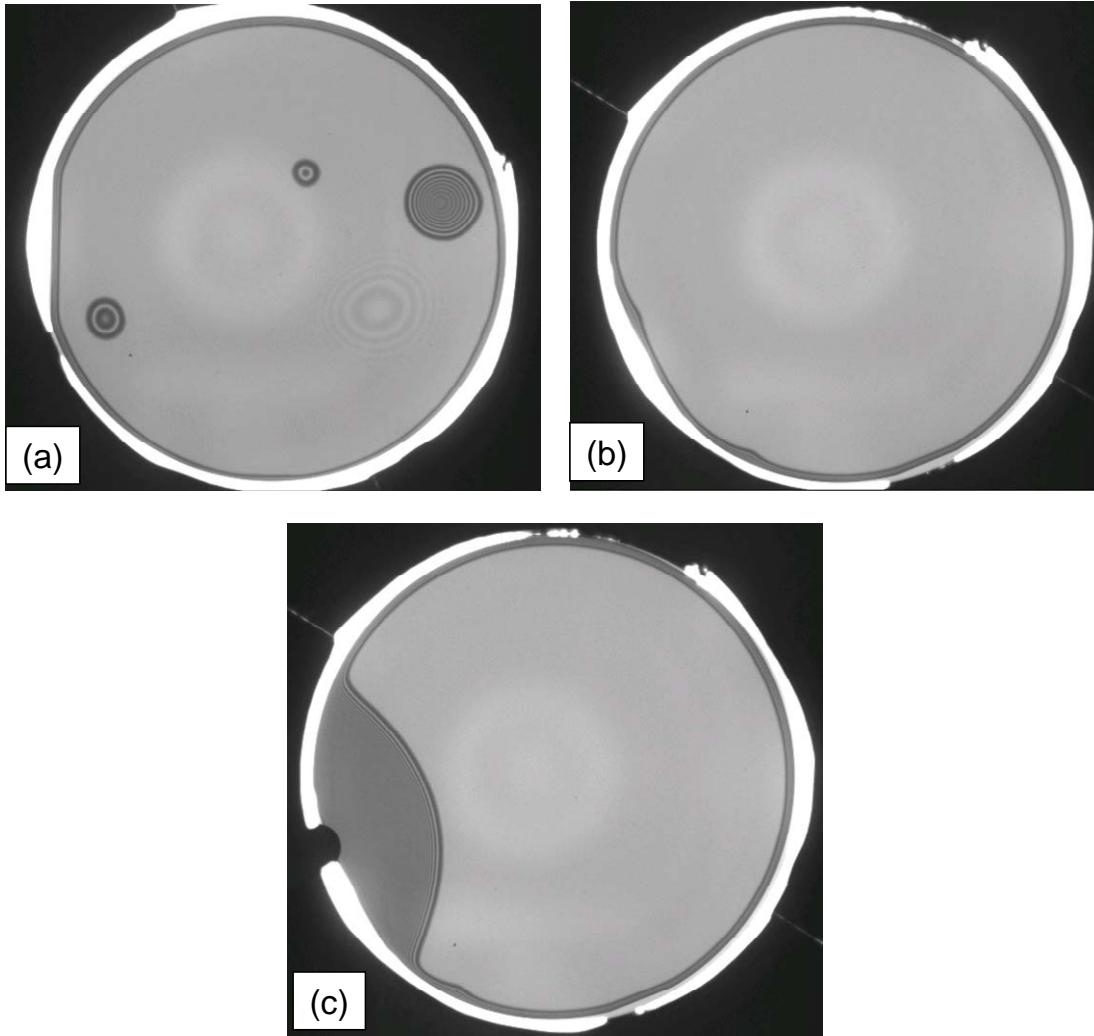


Figure 3.16 50 mm InP/Si wafer bonded structures fabricated by use of plasma activation and annealing showing: (a) the presence of particle-induced voids; (b) a void-free InP/Si bonded structure achieved by superior particle removal prior to bonding; and, (c) the use of the crack-opening method to estimate the bond strength of a given plasma condition by the insertion of a 50 μm thick blade between the bonded substrates.

apply to the Ge/Si and InP/Si materials systems, and specific challenges associated with the bonding of dissimilar materials are also evaluated for Ge/Si and InP/Si structures. Specifically, it was shown that not only must the bonding surface roughness be minimized, but also the lateral wavelength of surface roughness must be maximized to facilitate bonding. Additionally, particles with diameters in excess of 0.2 μm were shown to be unacceptable at the bonded interface. The coefficient of thermal expansion mismatch associated with wafer bonding of dissimilar materials

was especially problematic for the Ge/Si system, where temperature excursions of more than 150°C from the bond initiation temperature can not be tolerated in large area substrates.

In the subsequent chapters, the results here are further studied to better characterize the mechanism of the exfoliation process, the electrical properties of the wafer bonded interface, and the properties of Ge/Si and InP/Si structures for the MOCVD growth of III-V semiconductors.

3.4 *References*

- ¹ Q.-Y. Tong and U. Gosele, *Semiconductor Wafer Bonding: Science and Technology* (John Wiley & Sons, New York, 1999).
- ² *Wafer Bonding; Vol.*, edited by M. Alexe and U. Gosele (Springer-Verlag, New York, 2004).
- ³ S. Subramanian and A. Auberton-Herve, *Si Wafer Bonding Technology for VLSI and MEMS Applications* (INSPEC, The Institute of Electrical Engineers, London, 2002).
- ⁴ Q.-Y. Tong and U. Gosele, *Materials Chemistry and Physics* **37**, 101-127 (1994).
- ⁵ J. Haisma and G. A. C. M. Spierings, *Materials Science and Engineering R* **37**, 1-60 (2002).
- ⁶ U. Gosele and Q.-Y. Tong, *Annual Review of Materials Science* **28**, 215-241 (1998).
- ⁷ U. Gosele, Y. Bluhm, G. Kastner, P. Kopperschmidt, G. Krauter, R. Scholz, A. Schumacher, S. Senz, Q.-Y. Tong, L.-J. Huang, Y.-L. Chao, and T. Lee, *Journal of Vacuum Science and Technology A* **17**, 1145-1152 (1999).
- ⁸ J. M. Zahler, A. Fontcuberta i Morral, C.-G. Ahn, H. A. Atwater, M. W. Wanlass, C. Chu, and P. A. Iles, in *Wafer bonding and layer transfer processes for 4-junction high efficiency solar cells*, New Orleans, 2002.
- ⁹ A. Fontcuberta i Morral, J. M. Zahler, H. A. Atwater, M. M. Frank, Y. J. Chabal, P. Ahrenkiel, and M. W. Wanlass, in *Electrical and structural characterization of the interface of wafer bonded InP/Si*, San Francisco, 2003.

- ¹⁰ J. M. Zahler, C.-G. Ahn, S. Zaghi, H. A. Atwater, C. Chu, and P. A. Iles, *Thin Solid Films* **403-404**, 558-562 (2002).
- ¹¹ Q.-Y. Tong, E. Schmidt, U. Gosele, and M. Reiche, *Applied Physics Letters* **64**, 625-627 (1994).
- ¹² S. Farrens, C. Hunt, B. Roberds, and J. Smith, *Journal of the Electrochemical Society* **141**, 3225-3230 (1994).
- ¹³ T. Akatsu, A. Plossl, R. Schloz, H. Stenzel, and U. Gosele, *Journal of Applied Physics* **90**, 3856-3862 (2001).
- ¹⁴ M. Wiegand, M. Reiche, and U. Gosele, *Journal of the Electrochemical Society* **147**, 2734-2740 (2000).
- ¹⁵ D. Pasquariello, M. Camacho, K. Hjort, L. Dozsa, and B. Szentpali, *Materials Science and Engineering* **B80**, 134-137 (2001).
- ¹⁶ D. Pasquariello and K. Hjort, *IEEE Journal on Selected Topics in Quantum Electronics* **8**, 118-131 (2002).
- ¹⁷ P. Amirfeiz, S. Bengtsson, M. Bergh, E. Zanghellini, and L. Borjesson, *Journal of the Electrochemical Society* **147**, 2693-2698 (2000).
- ¹⁸ S. Farrens, J. Dekker, J. Smith, and B. Roberds, *Journal of the Electrochemical Society* **142**, 3949-3955 (1995).
- ¹⁹ Y. Li and R. Bower, *Japanese Journal of Applied Physics* **37**, 737-741 (1998).
- ²⁰ H. Lin, K. Chang, G. Pickrell, K. Hsieh, and K. Cheng, *Journal of Vacuum Science and Technology B* **20**, 752-754 (2002).
- ²¹ J. Folta, C. Hunt, and S. Farrens, *Journal of the Electrochemical Society* **141**, 2157-2160 (1994).
- ²² B. Roberds and S. Farrens, *Journal of the Electrochemical Society* **143**, 2365-2371 (1996).

- 23 H. Takagi, R. Maeda, T. Chung, N. Hosoda, and T. Suga, *Japanese Journal of Applied Physics* **37**, 4197-4203 (1998).
- 24 T. Kagawa and Y. Matsuoka, *Applied Physics Letters* **69**, 3057-3059 (1996).
- 25 C. Gui, M. Elwenspoek, N. Tas, and J. Gardeniers, *Journal of Applied Physics* **85**, 7448-7454 (1999).
- 26 V. Constantoudis, G. Patsis, A. Tserepi, and E. Gogolides, *Journal of Vacuum Science and Technology B* **21**, 1019-1026 (2003).
- 27 T.-M. Lu, H.-M. Yang, and G.-C. Wang, in *When interface gets rough...* Boston, 1995 (Materials Research Society), p. 283.
- 28 M. Weldon, M. Collot, Y. Chabal, V. Venezia, A. Agarwal, T. Haynes, D. Eaglesham, S. Christman, and E. Chaban, *Applied Physics Letters* **73**, 3721-3723 (1998).
- 29 M. Weldon, V. Marsico, Y. Chabal, A. Agarwal, D. Eaglesham, J. Sapjeta, W. Brown, D. Jacobson, Y. Caudano, S. Christman, and E. Chaban, *Journal of Vacuum Science and Technology B* **15**, 1065-1073 (1997).
- 30 *Properties of Gallium Arsenide; Vol.*, edited by M. Brozel and G. Stillman (INSPEC, London, 1996).
- 31 L. Freund and S. Suresh, *Thin Film Materials: Stress, Defect Formation and Surface Evolution* (Cambridge University Press, Cambridge, 2004).
- 32 INSPEC, *Properties of Indium Phosphide* (INSPEC, The Institute of Electrical Engineers, London, 1991).
- 33 *Semiconductors: Group IV Elements and III-V Compounds; Vol.*, edited by O. Madelung (Springer Verlag, New York, 1991).
- 34 www.ioffe.ru/SVA/NSM/Semicond/.
- 35 G. Cha, R. Gafiteanu, Q.-Y. Tong, and U. Gosele, in *Design considerations for wafer bonding of dissimilar materials*, Honolulu, HI, 1993 (The Electrochemical Society), p. 257-266.

- ³⁶ H. Lee, A. Rosakis, and L. Freund, *Journal of Applied Physics* **89**, 6116-6129 (2001).
- ³⁷ C. L. Andre, J. J. Boeckl, C. W. Leitz, M. T. Currie, T. A. Langdo, E. A. Fitzgerald, and S. A. Ringel, *Journal of Applied Physics* **94**, 4980-4985 (2003).
- ³⁸ M. T. Currie, S. B. Samavedam, T. A. Langdo, C. W. Leitz, and E. A. Fitzgerald, *Applied Physics Letters* **72**, 1718-1720 (1998).
- ³⁹ R. M. Sieg, S. A. Ringel, S. M. Ting, S. B. Samavedam, M. T. Currie, T. A. Langdo, and E. A. Fitzgerald, *Journal of Vacuum Science and Technology B* **16**, 1471-1474 (1998).
- ⁴⁰ V. K. Yang, M. E. Groenert, C. W. Leitz, A. J. Pitera, M. T. Currie, and E. A. Fitzgerald, *Journal of Applied Physics* **93**, 3859-3865 (2003).
- ⁴¹ K. Mitani, V. Lehmann, R. Stengl, D. Feijoo, U. Gosele, and H. Massoud, *Japanese Journal of Applied Physics* **30**, 615-622 (1991).

Chapter 4: The Role of H in the H-induced Layer Exfoliation of Ge and InP

In this chapter the role of hydrogen in the exfoliation of Ge and InP is studied. Using cross-sectional transmission electron microscopy (XTEM), atomic force microscopy (AFM), Fourier-transform infrared (FTIR) spectroscopy and thermal hydrogen desorption with mass spectroscopy, a qualitative model for the physical and chemical action of hydrogen in the exfoliation of these materials is obtained. H-implantation creates damage states that store hydrogen and create nucleation sites for the formation of micro-cracks. These micro-cracks are chemically stabilized by hydrogen passivation, and upon annealing serve as collection points for molecular hydrogen. Upon further heating the molecular hydrogen trapped in these cracks exerts pressure on the internal surfaces causing the cracks to extend and coalesce. When this process occurs in the presence of a handle substrate that provides rigidity to the thin film, the coalescence of these cracks leads to exfoliation.

In addition to providing insight into the mechanistic role of hydrogen in H-induced exfoliation of single-crystal thin films, the vibrational spectra studied here provide information into the states of hydrogen in heavily damaged Ge and InP. Furthermore, the information obtained from such a study has practical importance for the optimization of H-induced layer transfer as a technological tool for materials integration with these materials systems.

4.1 *H-induced Exfoliation of Ge*

The H-induced exfoliation mechanism of Ge is expected to be similar to this mechanism in Si, which has been extensively studied by researchers at Bell Labs.^{1,2} Using the methods employed in the present study – TEM, AFM, mass spectroscopy and FTIR spectroscopy – in addition to forward recoil scattering (FRS), a model was proposed for the role of hydrogen in the exfoliation of Si. It is worthwhile to summarize the assumptions and conclusions of the Bell Labs study briefly to provide background for the present work, as the conclusions regarding the distribution and role of H in the exfoliation of Si can, due to the structural and chemical similarity between Si and Ge, be extrapolated to the interpretation of the present experimental results.

4.1.1 **Summary of the Qualitative Model for the H-induced Exfoliation of Si**

In the pioneering work by Weldon *et al.* the following conclusions were substantiated:¹

- Implantation induced defects served to trap H within the Si substrate.
- A broad distribution of vacancy hydrogen defect structures was the main reservoir for hydrogen that contributed to the exfoliation process. In sub-critical doses of H the IR band contributed by these defects was significantly diminished.
- Agglomerated $VH_{3,4}$ defect structures were precursors to the formation of extended internal surfaces that served to accumulate H_2 and build internal pressure. Furthermore, it was asserted that (100) and (111) platelet structures observed in TEM served as nucleation points for the agglomeration of vacancy-hydrogen defect structures.
- The concentration of bound hydrogen was reduced upon annealing, as indicated by a decrease in the integrated intensity of the Si-H modes in FTIR. The majority of this un-bound hydrogen was shown by FRS to remain in the Si rather than to diffuse out of the semiconductor. Thus, the un-bound hydrogen was postulated to be confined to internal structures as molecular H_2 .

- The H₂ trapped in internal surfaces was shown by mass spectroscopy to have the physical role of pressurizing the micro-cracks to provide the energy necessary for their extension through the material.
- By studying bonded implanted samples along with free surfaces, it was shown that the presence of the handle substrate plays only a dynamic role as a stiffener during the internal pressurization of the micro-cracks. This induces lateral crack growth, but shows no spectroscopic difference from the free surface sample.

The final conclusion above regarding measurements of the evolution of hydrogen in bonded versus free surfaces indicates that we can make a relevant and informative study of the role of hydrogen in the exfoliation of other semiconductor materials using the much simpler experimental conditions of measurement of free surface exfoliation.

4.1.2 Experimental Procedure

Ge(100) substrates, As-doped to a resistivity of 10 Ω ·cm, were used for FTIR measurements in order to minimize free-carrier absorption during measurement. The substrates were double-side polished to avoid scattering loss of the infrared signal. A substrate thickness of 500 μ m was used to enable easy fabrication of prism samples for multiple internal-transmission (MIT)-FTIR spectroscopy, a special case of multiple internal reflection (MIR)-FTIR spectroscopy.

Samples were implanted on a back-side gas cooled stage to control the substrate temperature during implantation and thereby minimize the dynamic annealing of the substrates during the implantation process. The gas cooled stage passes low pressure gas across the back surface of the substrate during implantation to ensure uniform thermal contact during the implantation process. The maximum temperature observed during implantation was 30°C as measured with a thermocouple in contact with the back surface of the substrate. Substrates were implanted with 80 keV H⁺ at an incidence angle of 7° to doses of 2x10¹⁶, 5x10¹⁶, and 1x10¹⁷ cm⁻². These samples were then analyzed by cross-sectional TEM (XTEM), AFM and FTIR. XTEM images of the

implanted region were taken transmission electron microscope, in both bright and dark-field modes. The XTEM samples were prepared by dimpling followed by Ar-ion milling.

For FTIR analysis MIR samples were prepared measuring 15 mm by 40 mm to fit the apparatus shown in Fig 4.1(a). The MIR samples were then beveled at an angle of 45° on both ends to ensure efficient coupling of light in and out of the structure. All spectra were referenced to the spectrum measured for an un-implanted prism that was processed with the implanted prisms through all temperature steps. Any background from the absorbance spectra was

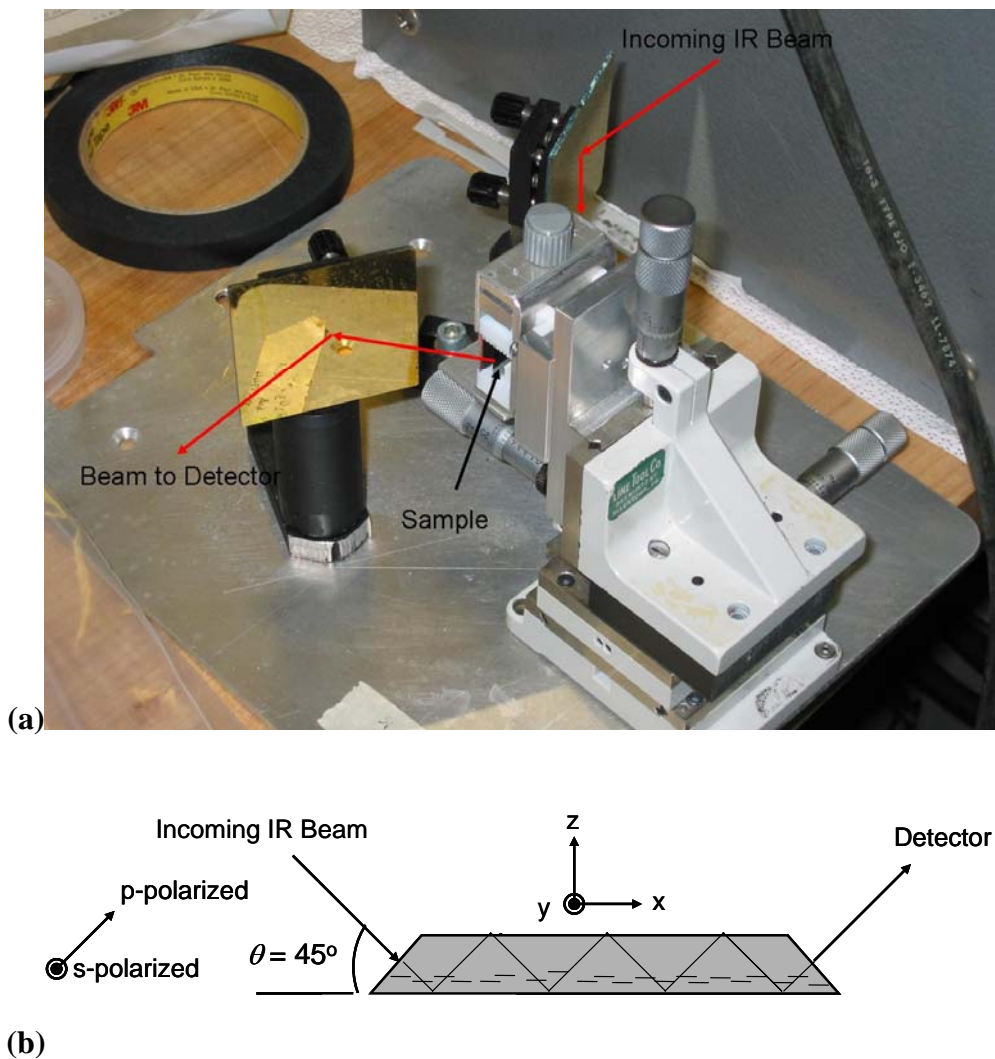


Figure 4.1 (a) MIT-FTIR sample holder showing the sample location and configuration of the incoming IR beam and the beam path to the detector. (b) A schematic of the sample geometry for the MIT-FTIR sampling system showing the orientation of the s- and p-polarization directions and their contribution parallel (x- and y-axis) and perpendicular (z-axis) fields in the sample.

subtracted after being fit to a high order polynomial. All spectra were collected with a Thermo-Nicolet spectrometer using a liquid-nitrogen cooled mercury cadmium telluride detector with a cutoff near 600 cm^{-1} . Spectra were acquired following approximately 15 minute isochronal annealing steps of 59, 131, 170, 221, 297, 339, 399 and 501°C to allow the evolution of the chemical state of Ge-H in the sample to be observed. The temperature of the sample during anneal steps was monitored with a Sensarray thermocouple-instrumented wafer, accurate to $\pm 0.1^{\circ}\text{C}$. Uncertainty in the duration of the anneal limit our ability to develop a quantitative model for the exfoliation process, but given the extreme complexity of the chemical states and associated spectra for Ge-H, a quantitative model would be challenging to deduce, even under ideal circumstances. Spectra were collected for both s- and p-polarized radiation. The s-polarization direction consists entirely of y-axis radiation parallel to the (100) surface, while the p-polarization direction consists of both z-axis and x-axis fields as illustrated in Fig. 4.1(b), perpendicular and parallel to the (100) surface, respectively. Assuming that the transmission through the sample occurs at a 45° angle, the expected number of passes through the implanted region of the sample is approximately 80. Thus, absorption enhancement of approximately 80 times over the single-pass absorption is anticipated.

In addition to the gain in signal due to multiple passes through the prism, MIT enhancement occurs when there is transmission through a buried interface of lower refractive index than the bulk of the material. This condition exists for ion implanted samples in which the ion implantation damage – H-decorated vacancies, interstitials and platelet structures – cause the refractive index of the material to be reduced. If the refractive index contrast is high enough, a situation exists in which the IR light at the interface between the high index bulk material and the low index damaged region is above the critical angle for total internal reflection at the bulk-damage interface. However, if the buried layer is much thinner than the wavelength of the radiation in question, the evanescent field of the IR photons penetrates the buried region and leads to evanescent tunneling of the photons to the opposite side of the implant damage. In this process,

confinement of the evanescent field between the two high-index regions of the material leads to enhancement of the e-field, especially for the z-axis component of the electric field perpendicular to the low-index plane. This enhancement is a function of the refractive index of the dielectric bulk material constituting the prism. The infrared refractive indices for Si, Ge, and InP are 3.43, 4.00, and 3.1, respectively.³ MIT-mode enhancement for interfaces far from the external surface of the prism is given by the following expression derived by Chabal.⁴

$$\left(\frac{MIT}{MIR}\right)_{parallel} = \frac{\cos^2 \theta}{I_x} \quad (4.1)$$

$$\left(\frac{MIT}{MIR}\right)_{perpendicular} = \left(\frac{n_1}{n_0}\right)^4 \frac{\sin^2 \theta}{I_z} \quad (4.2)$$

Where,

$$I_x = \frac{4n_1^2 \cos^2 \theta}{n_1^2 - n_0^2} \frac{(n_1/n_0)^2 \sin^2 \theta - 1}{\left[1 + (n_1/n_0)^2\right] \sin^2 \theta - 1} \quad (4.3)$$

$$I_z = \frac{4n_1^2 \cos^2 \theta}{n_1^2 - n_0^2} \frac{(n_1/n_0)^2 \sin^2 \theta}{\left[1 + (n_1/n_0)^2\right] \sin^2 \theta - 1} \quad (4.4)$$

Where, n_1 is the refractive index of the dielectric that forms the prism, n_0 is the refractive index of the surrounding medium, in this case 1.0, and θ is the angle of incidence for the light on the prism, taken as 45° in the present analysis. The predicted enhancements of dipoles oriented in the z-axis for Si, Ge, and InP are 29.0, 56.3, and 18.5, respectively. The predicted enhancement factor for dipoles oriented along the x- and y-directions is 0.25 for all three materials. Based on this analysis, it is anticipated that the greatest degree of enhancement will be observed for Ge. This is indeed what is found, as will be shown when the spectra are examined.

When the low-index buried layer is located near an external surface of the material being probed in MIT-FTIR spectroscopy, the phase-shifted reflected radiation from the surface causes interference at the buried interface. This effect can lead to either increased or decreased signal

enhancement depending on the wavelength of interest and the distance of the buried layer from the external surface. Based upon the calculations of Chabal⁴ (Fig. 4.2), assuming a buried layer depth of 460 to 660 nm based upon the TRIM⁵ simulation estimated implant range \pm the estimated implant straggle and a wavenumber range of 1900-2100 cm^{-1} for the Ge-H modes of interest, the single pass enhancement for the z-axis is expected to be between 65 and 115. For these conditions the parallel components have predicted enhancement factors of 0.0 to 0.3 for the x-axis and 0.0 to 1.0 for the y-axis. However, subsequent data will show that the enhancement must be above zero, as evidence of absorption is observed in the x- and y-axis components. This estimate is made assuming that near the surface, Ge behaves similarly to Si, which is the material for which the plot in Fig. 4.2 was constructed. Assuming that there is relatively little change in the phase of light at the external surface with the differing refractive index between Ge and Si,

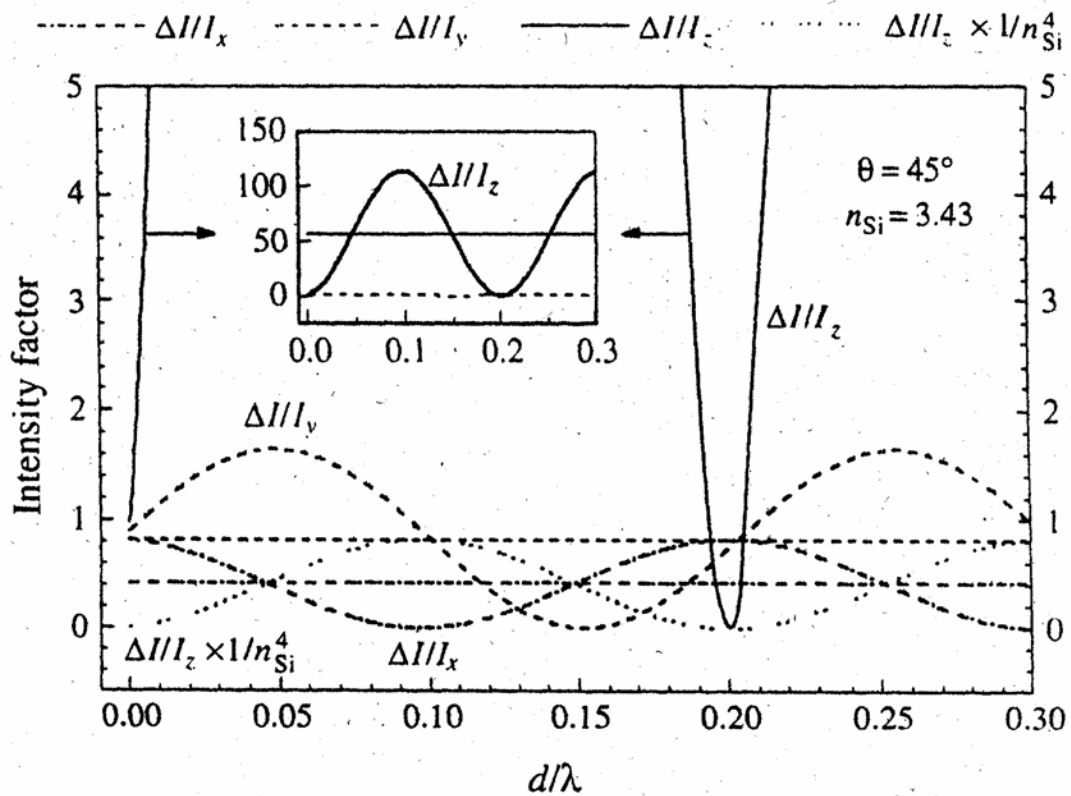


Figure 4.2 Sensitivity factor for radiation in a Si MIT-FTIR geometry sample as a function of the normalized distance of the layer from the outer surface, d/λ .⁴

this estimate is probably low and can, to the first order be scaled using the predicted enhancements calculated for buried layers deep in the bulk of the Si and Ge. Using this adjustment, the predicted z-axis enhancement in the implanted region of the Ge samples under consideration is between 126 and 223 per pass.

The MIT geometry offers special advantages for the study of the exfoliation of thin films in the manner under consideration. This is because the evanescent tunneling condition that leads to enhancement only exists in the presence of a well-defined buried layer in the material. The skewed normal distribution of the implanted species and implantation damage for an 80 keV H^+ is depicted by the TRIM simulation profile shown in Fig. 4.3. This simulation was performed for a 7° angle of incidence assuming a lattice displacement energy of 14 eV. Based on the TRIM simulation, the as-implanted damage and hydrogen distribution is broad with a gradual transition from minimally-damaged to heavily-damaged Ge only following the formation of a well-developed interface between the bulk Ge and the low-index region formed by the coalescence of well-defined internal defects that strong z-axis enhancement will be seen. Thus, we can identify the temperature at which the exfoliation process begins to occur.

4.1.3 Results and Interpretation

4.1.3.1 Transmission Electron Microscopy

The XTEM images in Fig. 4.4 show H-implanted Ge substrates in cross-section. This figure shows both low-magnification and high-resolution images of an as-implanted Ge sample implanted on a gas-cooled stage with H^+ at 80 keV to a total dose of $1 \times 10^{17} \text{ cm}^{-2}$. In Fig. 4.4(a) the broad distribution of the implant induced damage immediately following implant is clearly shown, and matches well with the predicted distribution of H within the Ge substrate. The predominant component of the damage in this dark-field image is attributed to H-platelet structures oriented along the (100) plane, with a significantly lower concentration of (111)

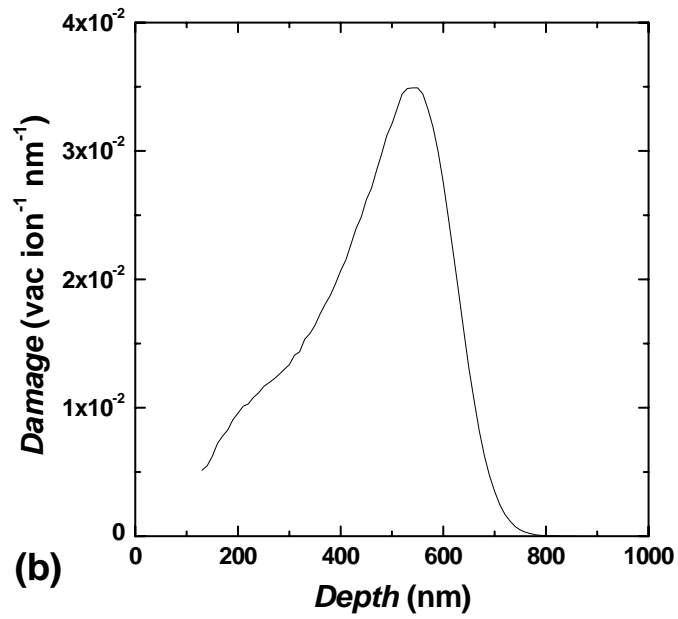
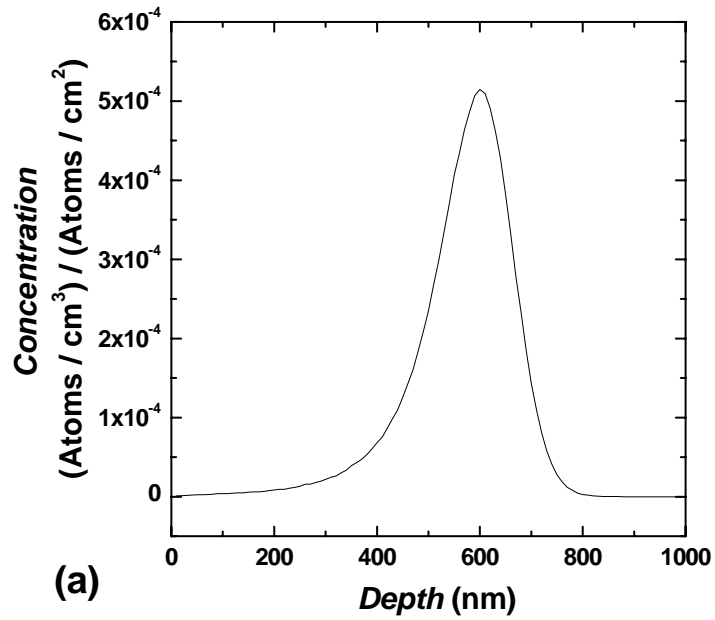


Figure 4.3 TRIM simulation of the H implantation profile (a) and the damage distribution (b) in the near surface region of a Ge substrate implanted at an angle of 7° with H^+ at 80 keV.

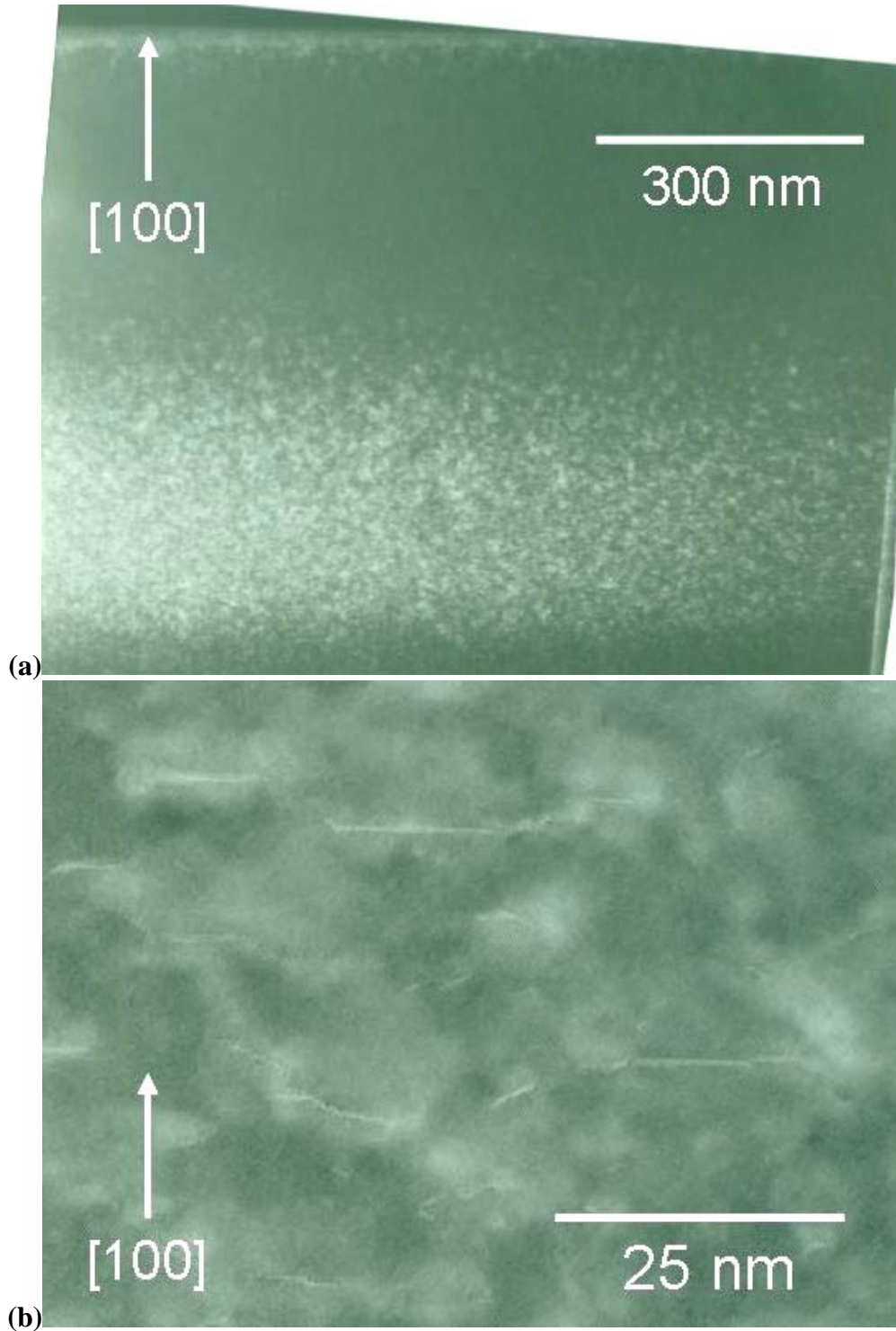


Figure 4.4 (a) Cross-sectional TEM image of Ge as-implanted with 80 keV H⁺ to a dose of $1 \times 10^{17} \text{ cm}^{-2}$ on a gas cooled stage revealing the broad damage distribution structure of Ge implanted under these conditions. (b) High-resolution image of the heavily damaged region near the peak range of the implant showing a large concentration of (100) platelet defect structures and a smaller concentration of (111) platelets.

platelets. These platelet structures are thought to be the nucleation points for the exfoliation process.¹ Figure 4.4(b) shows the platelets in high-resolution, revealing the presence of off-axis dislocation loops presumably caused by strain induced by the implantation process. In this image the platelet structures can be seen to be approximately five to 15 nm in length and oriented predominantly along the (100) plane.

Figure 4.5 shows the XTEM of a sample that was implanted with 80 keV H⁺ at a 7° angle to a dose of 1×10^{17} cm⁻² that has been annealed to 250°C for 10 minutes. Unlike the sample shown in Fig. 4.4, this sample was not actively cooled with backside gas, and FTIR spectra suggest that the sample may have reached temperatures as high as 150°C during the implant process. However, the general defect morphology of these structures is representative of that just prior to large area exfoliation. The variation in the implant conditions is thought only to affect the temperature at which these defects form in the Ge system. In Fig. 4.5(a) the dark-field image shows the defect structure throughout the thin film, and shows the initial stages of the formation of micro-cracks at the TRIM-predicted peak range of 560 nm. These cracks are referred to as micro-cracks in reference to the distribution of crack lengths from 25 to 100 nm. The high-resolution image in Fig. 4.5(b) shows the formation of the exfoliation crack structure. Further inspection of these images shows an increase in the number of (111) and (100) platelets following the 250°C anneal.

Finally, Fig. 4.6 captures the process by which the micro-cracks viewed in Fig. 4.5 coalesce by jumping between (100) micro-cracks at differing depths. This process is logically consistent with the physical model of (100) platelets opening at various implantation depths to form micro-cracks. These micro-cracks are distributed in depth in the film around the range of the implant. To complete the exfoliation process the micro-cracks ripen to form extended internal crack structures as illustrated in Fig. 4.5 by the joining of micro-cracks at various depths in the H-implanted region of the Ge substrate through crack-jumping along planes that would not preferentially form a cleavage plane.

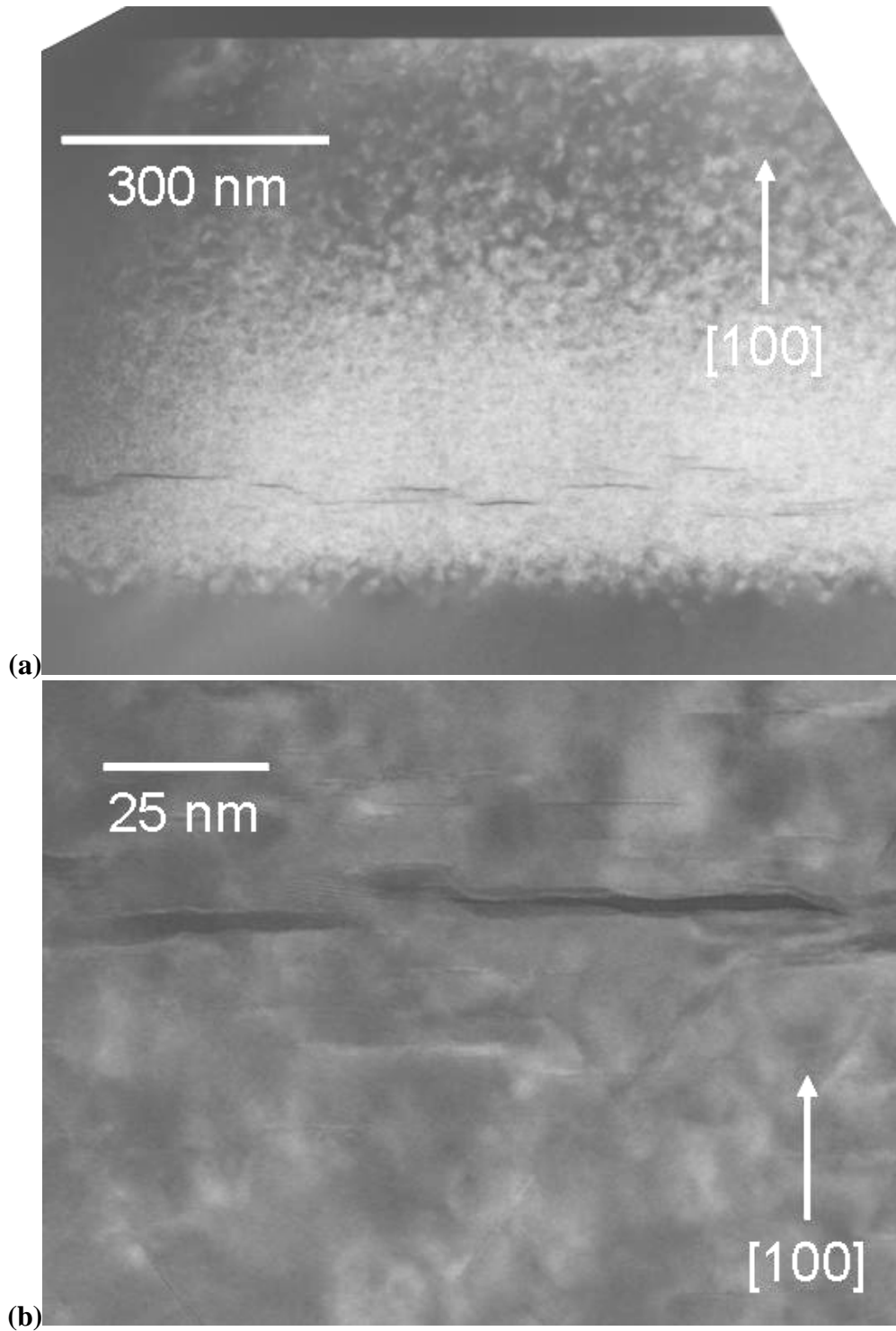


Figure 4.5 (a) Cross-sectional TEM image of Ge implanted with 80 keV H^+ to a dose of $1 \times 10^{17} \text{ cm}^{-2}$ without active cooling following an anneal to 250°C for 10 minutes. (b) High-resolution of the nano-crack region under the same conditions presence of (100) and (111) hydrogen platelets and nano-cracks just beginning to form in the material.

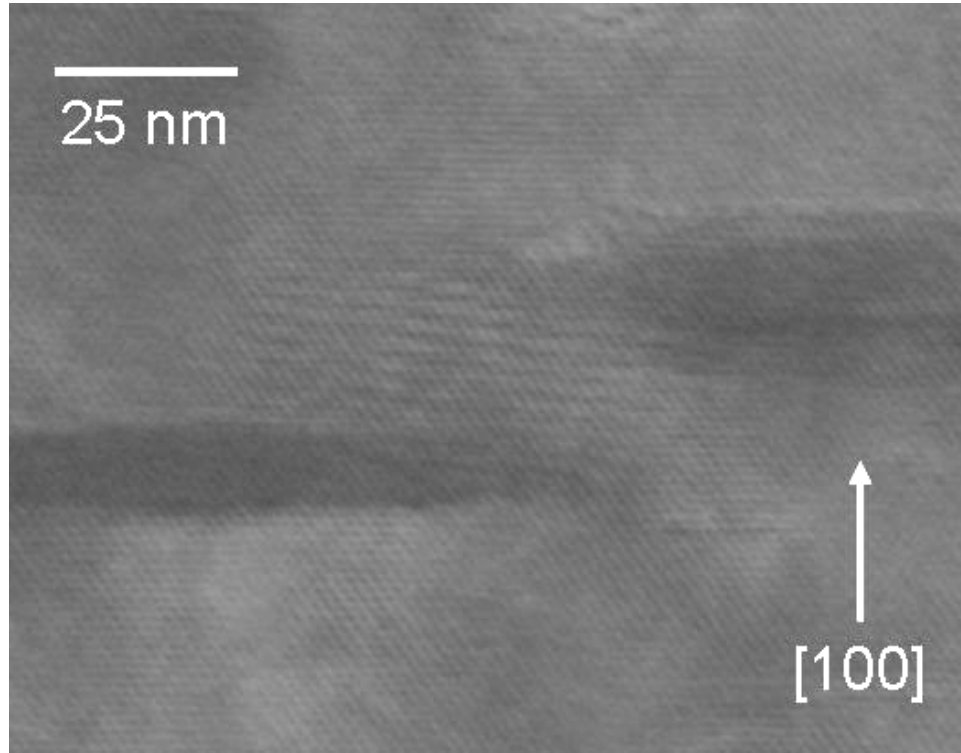


Figure 4.6 High-resolution cross-sectional TEM image of Ge implanted with 80 keV H^+ to a dose of $1 \times 10^{17} \text{ cm}^{-2}$ without active cooling following an anneal to 250°C for 10 minutes under close magnification showing the coalescence of nanocracks into microcracks that eventually lead to exfoliation..

4.1.3.2 Atomic Force Microscopy

The blistering process indicated by the XTEM images presented in the previous section was further corroborated by studying of the surface of Ge-H implanted substrates upon annealing. Figure 4.7 shows the development of blisters on the surface of a Ge substrate implanted with 80 keV H^+ to a dose of $1 \times 10^{17} \text{ cm}^{-2}$ without active cooling. In Fig. 4.7(a) an AFM image following a 10 minute 200°C anneal shows a dense coverage of small surface protrusions corresponding to blisters formed in the early stages of the exfoliation process. Following an additional 10 minute anneal at 300°C an AFM image shown in Fig. 4.7(b), the disperse blisters in Fig. 4.7(a) have ripened into larger blisters. This provides direct support for the physical picture suggested by the XTEM images from §4.1.3.1. That is, the exfoliation process is initiated with the formation of a dense network of micro-scale cracks around the peak range of the H-implant. Upon further

annealing, these micro-cracks ripen to form extended internal surfaces. In the H-implantation-induced exfoliation of Si, it has been previously shown that the hydrogen that is made mobile by annealing, and the attendant release of hydrogen from defect states, does not diffuse out of the substrate, but is trapped in internal features as H₂.¹ Upon the formation of a ripened micro-crack above a critical size, the internal pressure of the H₂ leads to the formation of a larger area blister that has a more three-dimensional morphology and can then rupture as seen by the crater-like structure found in Fig. 4.7(b).

4.1.3.3 Infrared Spectroscopy

TEM and AFM are clearly valuable for showing the physical phenomena that occur during the exfoliation and layer transfer of a Ge thin film in H-implantation-induced exfoliation. However, they are limited by their inability to reveal the chemical role of H in the exfoliation of thin films of this and other semiconductor materials. To understand the chemical state of H in the process, a spectroscopic technique is required. For this MIT-FTIR spectroscopy was employed with a polarizing filter to obtain rich spectroscopic data of the chemical state and dipole orientation of Ge-H modes in ion implanted Ge substrates during the exfoliation process. Additionally, as was previously described, signal enhancement in the \bar{p} -polarized spectra indicate critical steps in the exfoliation of Ge thin films due to the formation of a well-defined refractive index contrast between the regions with bulk-like properties – the underlying substrate and the near-surface film – and the internal surfaces that are precursors to exfoliation. This effect is most prevalent following the formation of internal micro-cracks that lead to the exfoliation process, which have a refractive index of very close to one.

The three implantation doses studied exhibit three essentially different physical behaviors: 1) 2×10^{16} – a sub-critical dose that does not blister upon annealing; 2) 5×10^{16} – an intermediate dose that exhibits retarded blistering at temperatures above 500°C; and, 3) 1×10^{17} – a high dose that leads to low-temperature blistering. Thus, they allow us to assess the importance of specific Ge-H

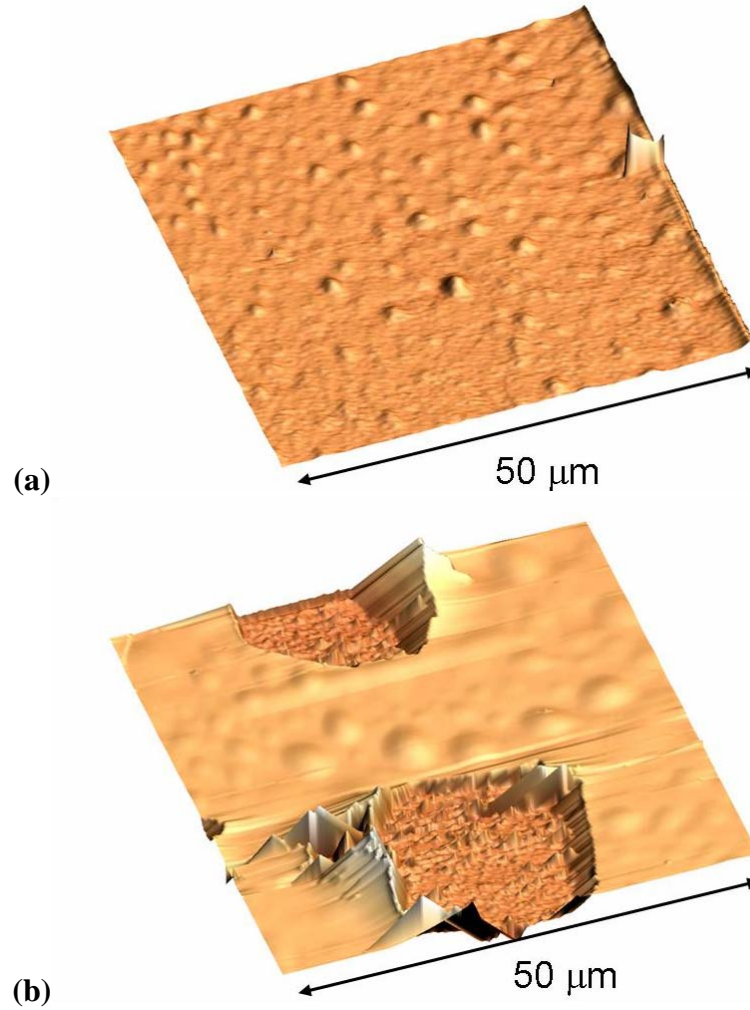


Figure 4.7 (a) Contact-mode AFM image of an H-implanted Ge surface following an anneal to 250°C for 10 min. for an 80 keV H^+ dose of $1 \times 10^{17} \text{ cm}^{-2}$ without active cooling. (b) Contact-mode AFM image of the same surface following an anneal to 300°C for 10 min.

chemical states in the exfoliation mechanism by comparing the temperature dependent evolution of features under conditions that lead to non-blistering and blistering behavior alike.

4.1.3.3.1 Identification of Discrete Defect Modes at Low Temperature

Table 4.1 lists values reported in the literature for well-studied defect structures in interstitial-hydrogen, vacancy-hydrogen and surface hydrogen defect structures for Ge. This catalog is useful in identifying discrete defects and extended surfaces observed in the present study. The spectra of all three implant conditions at room temperature following an implant at approximately 30°C are

shown in Fig. 4.8. In these spectra we can identify modes specifically assigned to discrete defect structures in previous studies. The \bar{s} -polarized spectra show much richer spectral detail, because the enhancement seen even at room temperature in the \bar{p} -polarized spectrum tends to overwhelm un-enhanced features that might be present. The selective enhancement of certain features in the \bar{p} -polarized spectrum may be due to the location of the un-enhanced, discrete defects outside of the low-index, heavily-damaged region that contributes to the observed enhancement. Additionally, any features with a strong z-axis-oriented dipole, such as extended surfaces, will contribute a very strong signal, obscuring the much smaller peaks of the discrete Ge-H defects. For this reason, the assignment of discrete defect modes at low temperature is done using the s-polarized spectra. The identification of discrete defect modes is made convincing only when the temperature-dependent stability of the defect is considered. The anneal-dependence of these modes is illustrated by the \bar{s} -polarized spectral evolution for the $2 \times 10^{16} \text{ cm}^{-2}$ dose shown in Fig. 4.9. The temperature dependence of the peaks attributed to discrete defects below is consistent for all three implant conditions.

The features located at 1763 cm^{-1} and 1979 cm^{-1} have been associated with the Ge-H_2^* defect structure. The feature at 1763 cm^{-1} exactly matches the frequency reported by Nielsen *et al.* for the Ge-H_2^* anti-bonding stretch mode. The frequency at 1979 cm^{-1} is slightly below the value reported in the same study of 1989 cm^{-1} for the Ge-H_2^* bond-centered stretch. However, both features show the same thermal stability as was reported by the Nielsen study, vanishing following an anneal step at 170°C , comparable to 165°C reported in the Nielsen study. Additional support for this assignment is the observation of a feature with the same anneal dependence at 763 cm^{-1} very close to the frequency of 765 cm^{-1} reported for the Ge-H_2^* bending mode.⁶ The discrepancies in the bond-centered stretching and bending modes relative to the values reported by Nielsen *et al.* can be attributed to perturbed bond centers caused by strain in the H-implantation-induced damage levels that are much higher for the doses used to study exfoliation,

Table 4.1 Literature reported values for discrete defect and extended surface modes of hydrogen in Ge.

ω (cm ⁻¹)	Temp. (°C)	Assignment	Author
765.0	<165	H ₂ [*] bend	Nielsen <i>et al.</i>
743.1 748.0	<240	IH ₂ bend	Nielsen <i>et al.</i>
1881.3 1883.5	<240	IH ₂ stretch	Nielsen <i>et al.</i>
1774.0	<165	H ₂ [*] AB stretch	Nielsen <i>et al.</i>
1971.0		(111) monohydride stretch	Stein <i>et al.</i>
1979.0		(100) monohydride asymmetric stretch	Chabal
1979.5	<130	VH ₂	Nielsen <i>et al.</i>
1989.0	<165	H ₂ [*] BC stretch	Nielsen <i>et al.</i>
1991.0		(100) monohydride asymmetric stretch	Chabal
1992.6	<130	VH ₂	Nielsen <i>et al.</i>
2014.9 2024.8	< 347	V ₂ H ₆	Nielsen <i>et al.</i>
2061.5	<317	VH ₄	Nielsen <i>et al.</i>

relative to the low dose implants used by Nielsen *et al.* to form discrete defects for a theoretical study.

In addition to the frequencies assigned to the H₂^{*} stretch modes, there are at least seven other modes in the range from 1700—2200 cm⁻¹. Of these the feature at 1870 cm⁻¹ is near the frequency of the stretch mode of the di-hydrogenated self-interstitial, IH₂, at 1880 cm⁻¹ reported by Nielsen *et al.* The temperature behavior of this defect also corroborates this assignment with the feature disappearing by 221°C, slightly below the literature reported value of 240°C.⁷

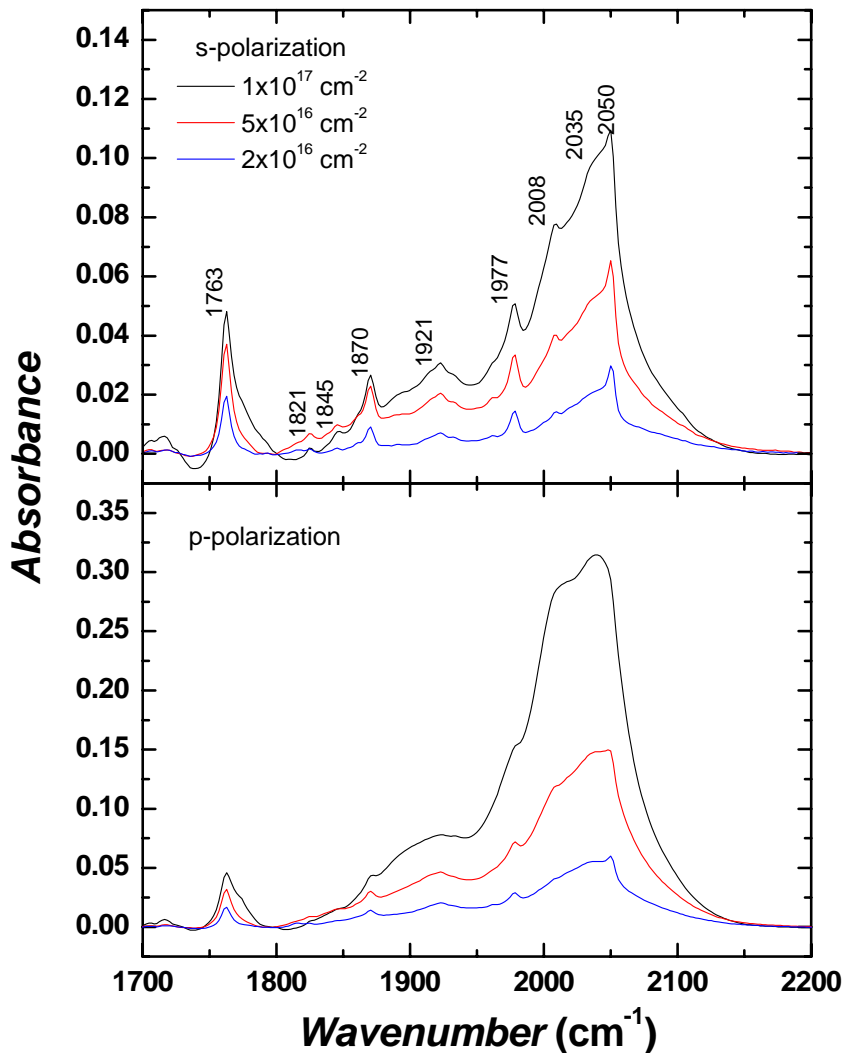


Figure 4.8 MIT-FTIR spectra of unannealed H-implanted samples of $2 \times 10^{16} \text{ cm}^{-2}$, $5.2 \times 10^{16} \text{ cm}^{-2}$ and $1 \times 10^{17} \text{ cm}^{-2}$ showing the discrete Ge-H defect modes seen in this study. The top panel shows the s-polarized spectra and the bottom panel shows the p-polarized spectra.

The strong feature located at 2050 cm^{-1} is near the reported value of the VH_4 defect at 2061.5 cm^{-1} . Additionally, this feature is seen to vanish between anneals of 297 and 339°C . In the report by Nielsen *et al.* the feature attributed to the VH_4 defect was seen to vanish at 317°C .⁸ As will be discussed later, this feature is very prominent in the temperature evolution of the spectra, and may be correlated with the formation of internal surfaces and subsequent micro-cracks.

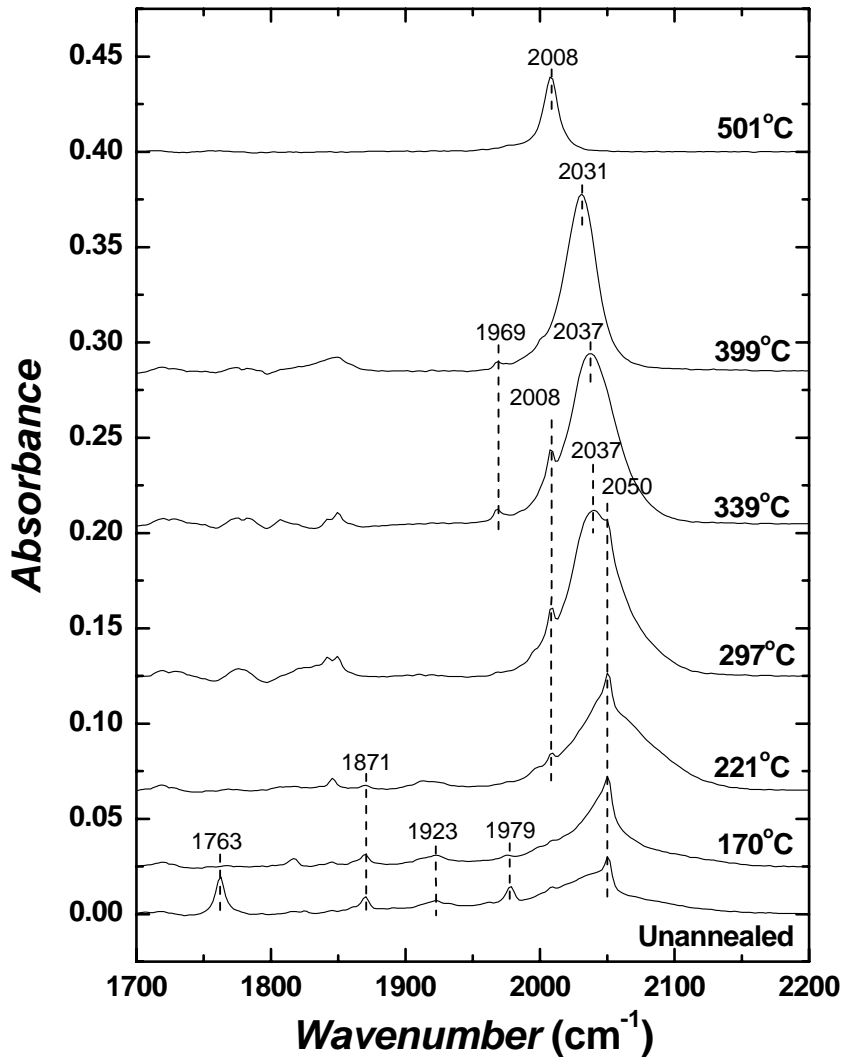


Figure 4.9 \bar{s} -polarized MIT-FTIR spectra for $2 \times 10^{16} \text{ cm}^{-2}$ implanted Ge as a function of the isochronal annealing temperature.

The mode at 2008 cm^{-1} is present at room temperature for all samples in s-polarization. This and its abrupt disappearance between 339 and 399°C suggests that this can be assigned to a discrete defect structure that contributes hydrogen to the exfoliation process and might form a precursor mode. One promising assignment is the V_2H_6 defect with a mode reported at 2014.9 cm^{-1} .⁸ This defect has been shown to be unstable above 347°C providing further support for this identification. While there is a secondary peak reported by Nielsen *et al.* for this defect structure

at 2024.8 cm^{-1} , its intensity is less than that of the 2014.9 cm^{-1} mode by a factor of more than five.⁸ Thus, it is not surprising that this secondary peak is not observed in the present study. Additionally, the

The remaining modes observed in the $1700\text{--}2200\text{ cm}^{-1}$ frequency range at room temperature do not correspond well to modes previously reported in the literature and are not assigned at present, but are assumed to correspond to hydrogen-decorated interstitials and vacancies induced during the implantation of the Ge substrate. Additionally, as was noted in the study of the exfoliation process in the Si-H system, there is a broad background in the Ge-H stretch region, although not as intense. The reduced intensity in the broad absorption background is perhaps due to differences in the methods used for the overall background subtraction in the Si-H study and the present study. As in the Si system this broad peak is attributed to the presence of a distribution of multi-vacancy defects of the form V_xH_y and hydrogenated self-interstitials of the form I_xH_y .¹ Another reasonable explanation of the difference between the background intensity in the present study and the Si-H study is the existence of less lattice damage following implant due to the larger mass of the Ge atom. However, TRIM simulations of implantation of Ge and Si with 80 keV H^+ at a 7° incidence angle, predict little difference between the number of vacancies produced per ion.

4.1.3.3.2 Spectral Evolution of the Sub-Critical $2 \times 10^{16}\text{ cm}^{-2}$ Dose

Figures 4.9 and 4.10 show the evolution of the s-polarized and p-polarized spectra as a function of isochronal anneal temperature for a sub-critical dose of $2 \times 10^{16}\text{ cm}^{-2}$. The s-polarized spectra show some of the more dominant discrete defect modes in the low temperature anneals. At temperatures above 170°C the dominant modes are all located in the $1950\text{--}2100\text{ cm}^{-1}$ range, which encompasses the vacancy-hydrogen defect modes as well as extended surfaces. The features seen in the $1700\text{--}1900\text{ cm}^{-1}$ range of the spectra at 297 , 339 and 399°C have been

attributed to contamination both in the anneal furnace and in the implantation process.¹ Large peaks attributed to the contamination have been subtracted for all samples in this region. However, residual peaks remain and are not attributed to any Ge-H structure reported in the literature, and are assumed to be due to contamination, and because of their expected proximity to the outer surface, are also not expected to interfere with the exfoliation process. Upon annealing, the features in the 1950—2100 cm^{-1} range sharpen and evolve losing the 2050 cm^{-1} mode and shifting down to a single peak with greatly reduced integrated intensity at 2008 cm^{-1} .

The \bar{p} -polarized spectra in Fig. 4.10 show the evolution of the peak enhancement. As was previously noted, the enhanced peak dominates the spectrum and makes it difficult to study unenhanced peaks attributed to Ge-H structures that reside outside of the internal structure or that have an x-axis dipole that does not experience enhancement, regardless of location within the sample. In Fig. 4.10 the \bar{p} -polarized spectrum for the unannealed sample shows minimal enhancement of the 2050 cm^{-1} mode tentatively attributed to the VH_4 defect.⁸ After annealing to 221°C the 2050 cm^{-1} peak is strengthened and broadened in the \bar{p} -polarized spectrum. However, at 297°C the peak at 2050 cm^{-1} is lost and there is a more strongly enhanced peak at 2035 cm^{-1} . This indicates that the low refractive index region of the implanted Ge is becoming better defined and that the feature being enhanced is a major constituent of that region with a strong z-axis dipole. For anneals of 339 and 399°C the enhanced feature shifts downward, and finally at 501°C

¹ Following implantation visual and spectroscopic evidence indicated the presence of surface oxidation due to increased base pressure near the sample in the gas cooled implantation stage. Following implantation, there is a large amount of absorption in the region where one would expect the O-H stretch of water to be observed. Additionally, absorption in the Ge-O region near 1000 cm^{-1} further corroborates the presence of a water saturated oxide. By etching the sample in 10% HF for approximately 30 minutes this contamination was removed and a subsequent spectrum shows little or no absorption in these regions. The contribution of contamination due to annealing was determined by the observation of peak growth in both the water and germanium oxide modes upon annealing.

the dominant feature is greatly reduced in intensity and is found at 2009 cm^{-1} . This spectral evolution is in good agreement with results previously obtained by Stein *et al.* for hydrogen implanted Ge in the absence of internal voids.⁹

4.1.3.3 Spectral Evolution of the Low-Temperature Blistering $1 \times 10^{17}\text{ cm}^{-2}$ Dose

The temperature evolved spectra for both \bar{s} - and \bar{p} -polarized MIT-FTIR spectroscopy measurements for the low-temperature-blistering condition $1 \times 10^{17}\text{ cm}^{-2}$ are shown in Figs. 4.11 and 4.12, respectively. The \bar{s} -polarization spectrum for the unannealed sample shows the dominant discrete features that were previously noted. As with the $2 \times 10^{16}\text{ cm}^{-2}$ sample the dominant peak in the \bar{s} -polarized spectra from as-bonded to 221°C is at 2050 cm^{-1} . However, unlike the $2 \times 10^{16}\text{ cm}^{-2}$ implantation dose there is a strong peak present in the unannealed spectrum at 2008 cm^{-1} attributed to V_2H_6 that continues to grow through 339°C . At 297°C a strong peak forms at 2032 cm^{-1} , while the peak at 2050 cm^{-1} is significantly diminished. Just prior to blistering, following an anneal to 339°C , the peak at 2032 cm^{-1} shifts to 2027 cm^{-1} while a peak at 1969 cm^{-1} appears in the spectrum. The final spectrum taken at 399°C is for an anneal condition in which the exfoliation process has occurred and the Ge-H modes in the spectrum are contributed by the hydrogen residing below the cleavage plane and in H-passivated free surfaces presumably created by the blister process. In the \bar{s} -polarized spectrum in Fig. 4.11 there is still a strong contribution at 2027 cm^{-1} . However, the contribution at 2008 cm^{-1} is no longer discernable. A peak at 1991 cm^{-1} has formed, which is near the value of 1979 cm^{-1} reported by Chabal for the asymmetric stretch-mode of Ge(100) monohydride, which should be observed in the s-polarized spectra due to the orientation of the dipole for this mode.¹⁰

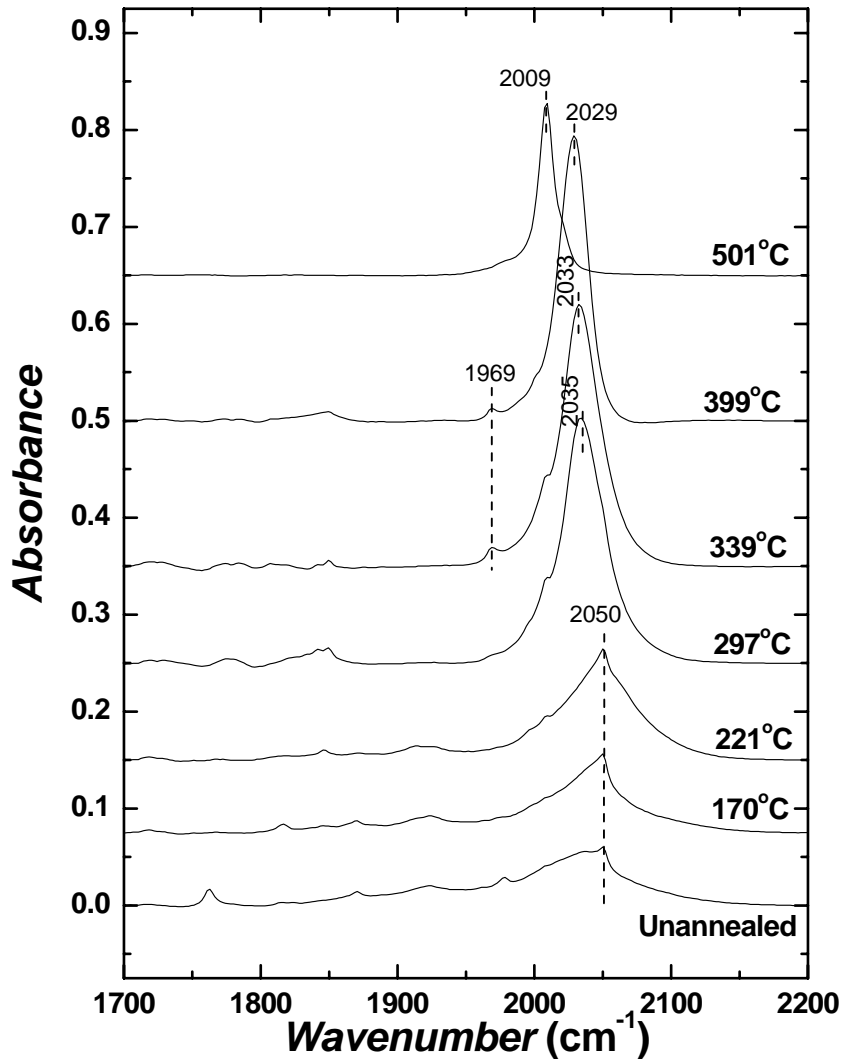


Figure 4.10 \bar{p} -polarized MIT-FTIR spectra for $2 \times 10^{16} \text{ cm}^{-2}$ implanted Ge as a function of the isochronal annealing temperature.

The \bar{p} -polarized unannealed spectrum of the $1 \times 10^{17} \text{ cm}^{-2}$ implant in Fig. 4.12 shows relatively little spectral detail due to the strong enhancement seen even prior to annealing. There is a slight shift of the dominant peak at 2046 cm^{-1} , relative to the dominant peak of 2050 cm^{-1} observed for samples implanted to 2×10^{16} and $5 \times 10^{16} \text{ cm}^{-2}$. Additionally, there is a broad shoulder toward lower frequencies that is suggestive of a peak near 2008 cm^{-1} as was observed for the

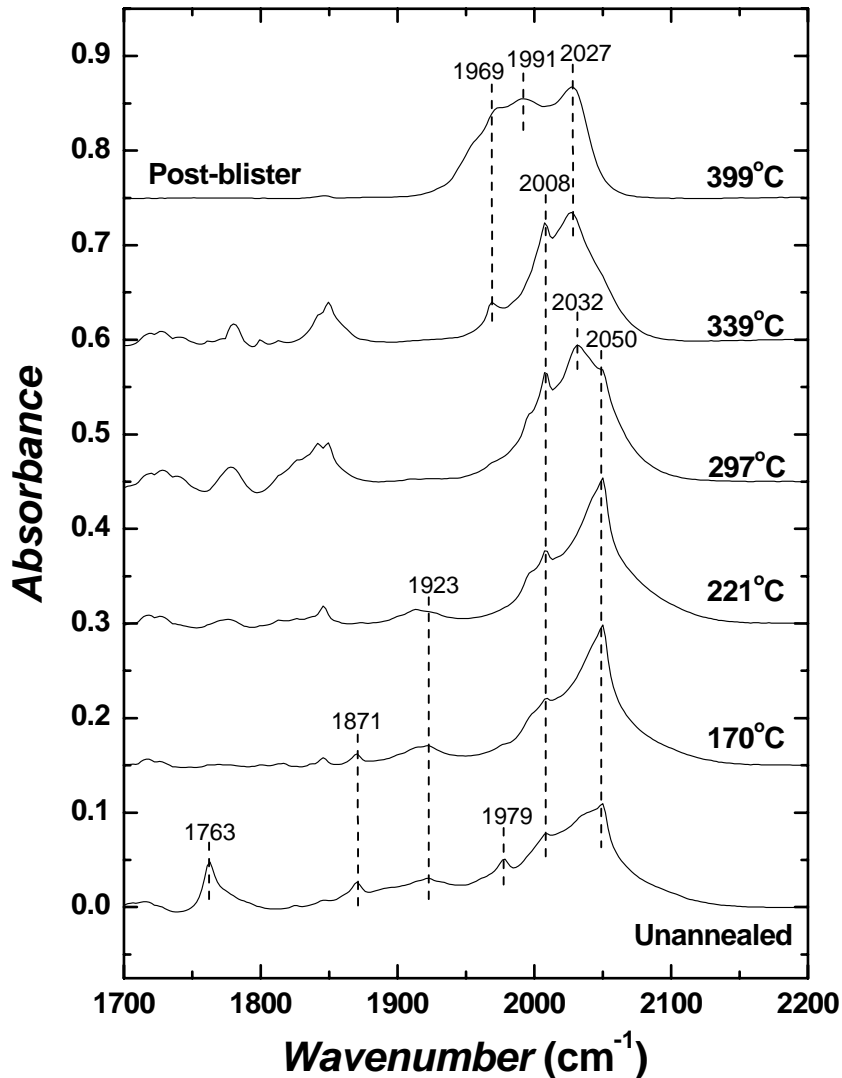


Figure 4.11 \bar{s} -polarized MIT-FTIR spectra for $1 \times 10^{17} \text{ cm}^{-2}$ implanted Ge as a function of the isochronal annealing temperature. The spectrum for 399°C is taken following exfoliation of the implanted Ge layer.

unannealed s -polarized spectrum. Annealing to 221°C causes only a slight change in the peak profile along with the loss of the Ge-H_2^* features at 1763 and 1979 cm^{-1} . Upon annealing to 297°C there is a dramatic increase in the enhancement indicating the onset of blistering accompanied by a shift of the dominant peak to 2031 cm^{-1} . The dominant peak must be present in the internal structure and must have a z -axis dipole component. Thus, we can conclude that this

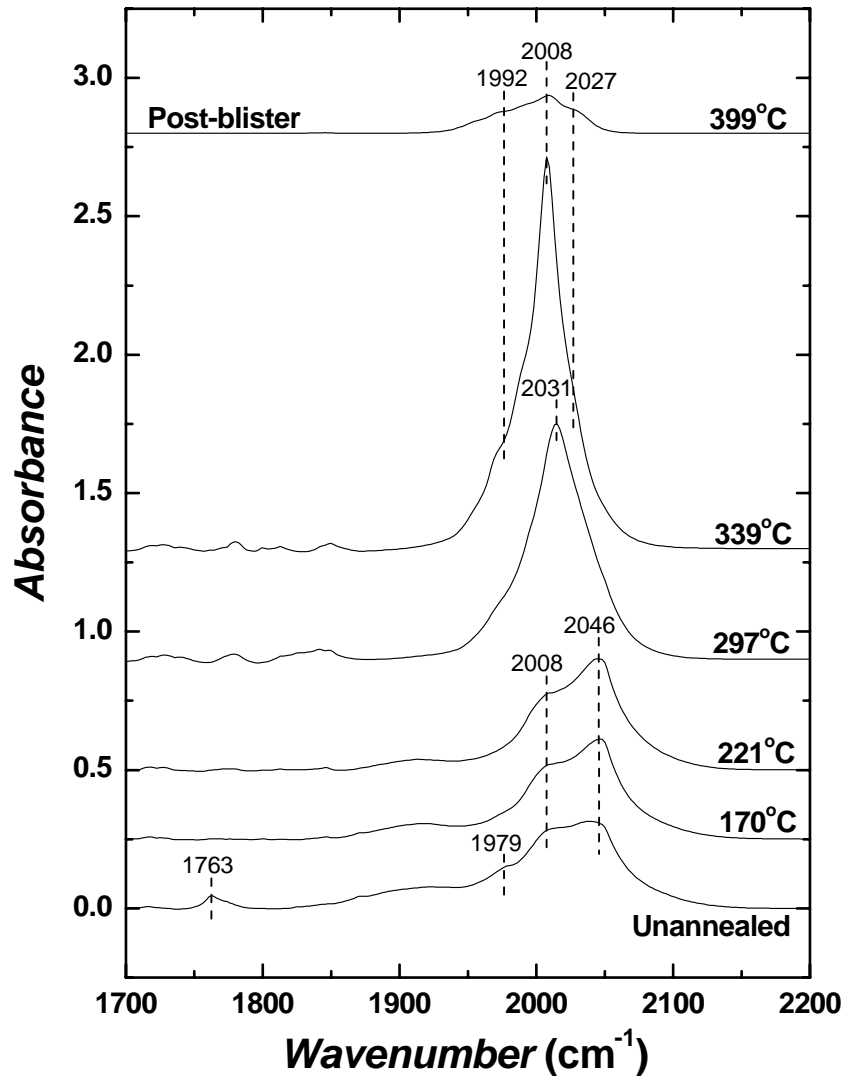


Figure 4.12 \bar{p} -polarized MIT-FTIR spectra for $1 \times 10^{17} \text{ cm}^{-2}$ implanted Ge as a function of the isochronal annealing temperature. The spectrum for 399°C is taken following exfoliation of the implanted Ge layer.

internal structure is clearly a precursor to the exfoliation of the thin film and also has a z-axis dipole component. Upon annealing to 339°C there is further enhancement and sharpening of the major peak, which has now shifted down to 2008 cm⁻¹. Finally, following a 399°C anneal, the film is exfoliated and, as one would expect, the enhancement of the spectrum is no longer observed. In addition to the now diminished peak at 2008 cm⁻¹, there are clearly distinguishable

shoulders at 1992 cm^{-1} and 2027 cm^{-1} that were likely present in the spectrum taken following the 339°C anneal but that were unobserved due to the peak enhancement at 2008 cm^{-1} . This suggests that these shoulders are associated with features that have a y-axis dipole as opposed to the feature at 2008 cm^{-1} that clearly has a z-axis component in its dipole.

4.1.3.3.4 Spectral Evolution of the Retarded-Blistering $5 \times 10^{16}\text{ cm}^{-2}$ Dose

To better understand the evolution of Ge-H chemical states in the exfoliation process, the use of an intermediate implant dose at $5 \times 10^{16}\text{ cm}^{-2}$ allows the process that was studied for a dose of $1 \times 10^{17}\text{ cm}^{-2}$ to be observed in a more gradual evolution of the Ge-H spectra. The spectra in Figs. 4.13 and 4.14 show the evolution of the \vec{s} - and \vec{p} -polarized spectra, respectively, for a $5 \times 10^{16}\text{ cm}^{-2}$ dose. The s-polarized spectra in Fig. 4.13 closely match the observations made for the s-polarized spectra of the $1 \times 10^{17}\text{ cm}^{-2}$ spectra shown in Fig. 4.11 through the 339°C anneal. Following an anneal to 399°C new features are observed due to the higher blistering temperature for this sample. In particular the dominant feature is now 2025 cm^{-1} . However, there are several modes at lower frequencies, including modes at 2000 , 1990 and 1969 cm^{-1} . The slight shoulder at 1990 cm^{-1} increases in intensity to become the dominant feature at 501°C . This is once again shifted by 10 cm^{-1} from the asymmetric stretch of the Ge(100) mono-hydride terminated surface reported by Chabal.¹⁰ Following the 501°C anneal there remains a slight shoulder extending to $\sim 1950\text{ cm}^{-1}$. This shoulder encompasses the reported values of 1978 cm^{-1} for the Ge(111) surface mono-hydride.⁹ Thus, these data provide evidence of the presence of (100) and (111) internal surfaces at 501°C .

In Fig. 4.14 critical steps in the evolution of the Ge-H structure necessary for exfoliation are again observed by the increase in the enhancement. As with the $1 \times 10^{17}\text{ cm}^{-2}$ sample, there is relatively little enhancement from the unannealed condition through 221°C . Upon annealing to 297°C there is an onset of enhancement with a strong peak at 2025 cm^{-1} . This is a slight shift to lower frequency from the peak observed in the $1 \times 10^{17}\text{ cm}^{-2}$ sample for this anneal condition.

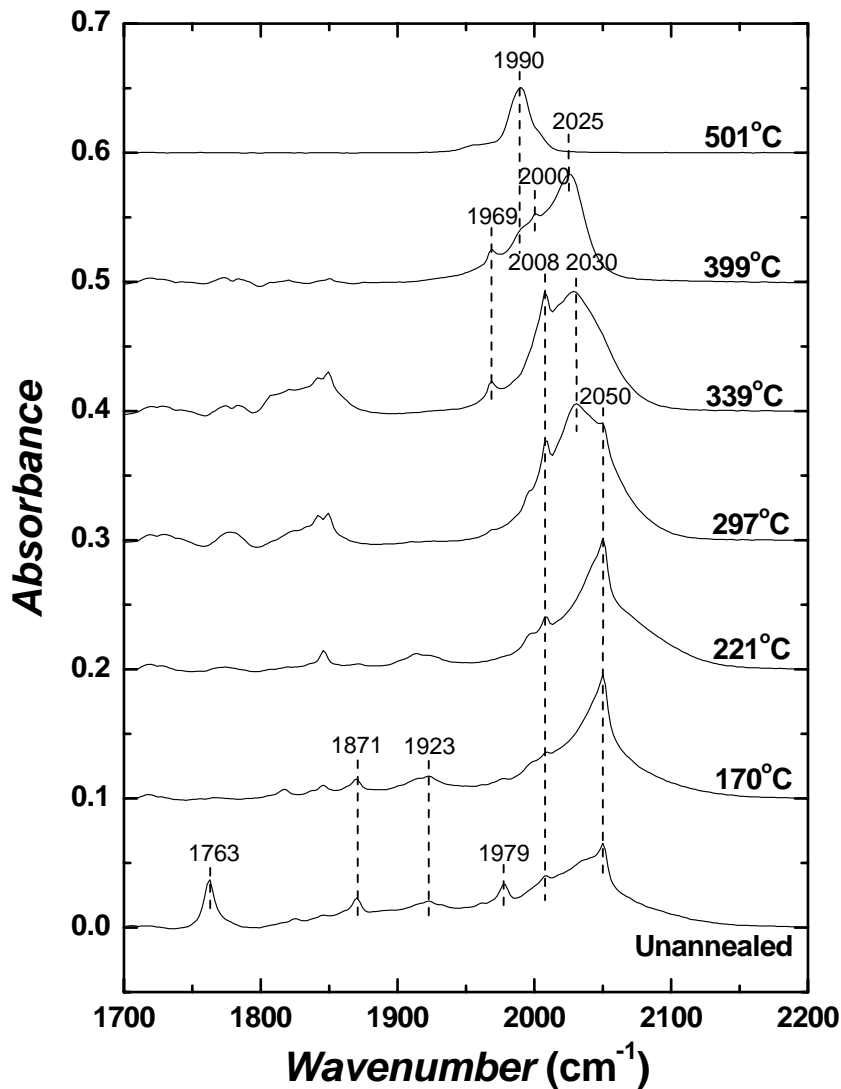


Figure 4.13 \bar{s} -polarized MIT-FTIR spectra for $5 \times 10^{16} \text{ cm}^{-2}$ implanted Ge as a function of the isochronal annealing temperature.

Following the 339°C anneal, the enhanced peak continues to shift downward to 2015 cm^{-1} , and there is now a shoulder at a slightly lower frequency that may be contributed by a feature observed at 1969 cm^{-1} in the \bar{s} -polarization spectrum. The relative weakness of this feature suggests that it either has a dipole in the plane of the sample and only contributes to the x-axis component of the \bar{p} -polarized spectrum or that the feature has a z-axis component but is of

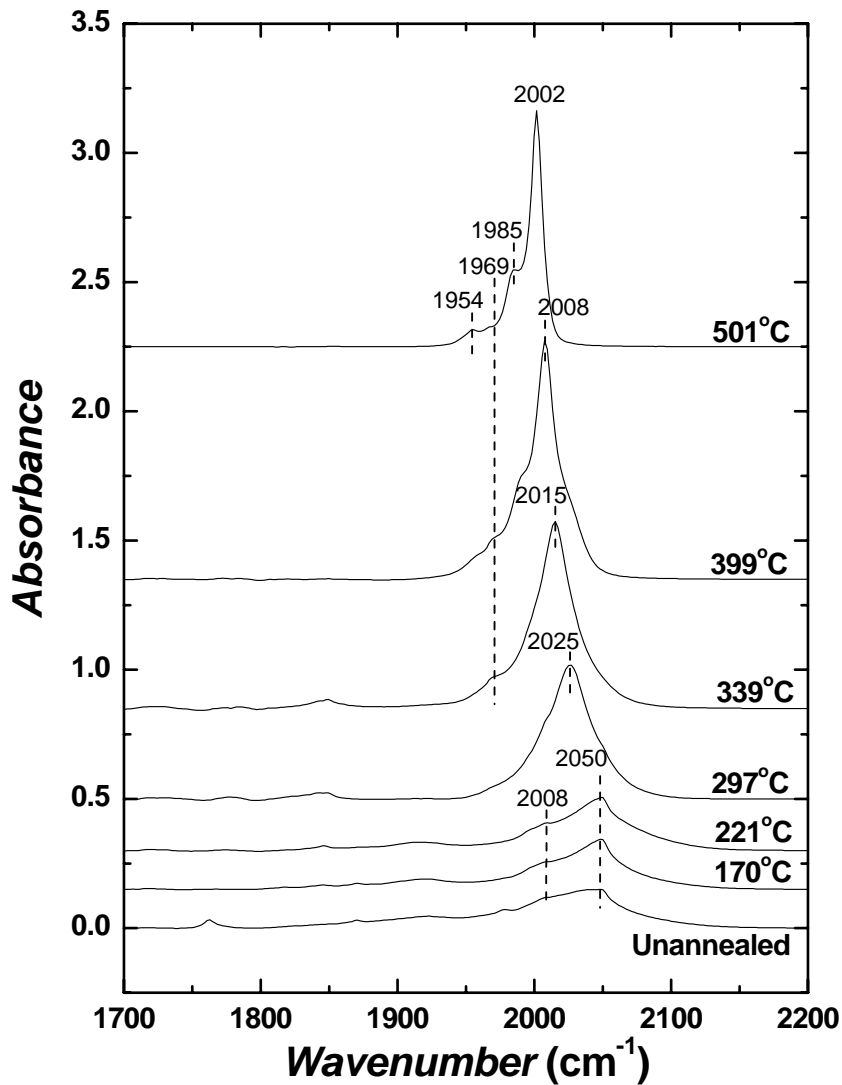


Figure 4.14 \vec{p} -polarized MIT-FTIR spectra for $5 \times 10^{16} \text{ cm}^{-2}$ implanted Ge as a function of the isochronal annealing temperature.

relatively low concentration in the sample or is not concentrated in the enhanced region of the sample. The sample annealed to 399°C shows a further shift in the dominant peak down to 2008 cm^{-1} accompanied by increased spectral detail in the low-frequency shoulder of this peak, which at this temperature appears to have contributions from modes at 1969 cm^{-1} and 2000 cm^{-1} . Both of these features were also observed in the s-polarization spectrum, suggesting that they are modes

with a parallel dipole. Finally, upon annealing to 500°C, a temperature at which the onset of blistering is observed but exfoliation has not yet occurred, the enhanced peak shifts further to 2002 cm⁻¹ and now has clearly distinguishable shoulder features at lower frequencies due to peaks estimated to be located at 1954, 1969 and 1985 cm⁻¹. The strong feature at 2002 cm⁻¹ is thought to be contributed by the symmetric stretch mode of the Ge(100) surface monohydride, which has a reported frequency of 1991 cm⁻¹.¹⁰ This is consistent with the \bar{s} -polarized spectrum in which there is a strong peak at 1990 cm⁻¹ that is tentatively assigned to the asymmetric stretch mode of the Ge(100) surface monohydride. The separation of these features and the polarization dependence supports this assignment. The shoulder at 1985 cm⁻¹ is near the Ge(111) surface monohydride value seen by Stein *et al.* of 1978 cm⁻¹. Furthermore, it is consistent with the physical picture of the ripening of micro-cracks into an extended crack structure by fractures along the higher index planes such as the (111) separating the micro-cracks that lie primarily on the Ge(100) plane.

4.1.4 Discussion

In §4.1.3 the observed spectra were described and some preliminary assignments were made, especially of discrete defect modes and hydrogenated extended surfaces. The 1900—2100 cm⁻¹ frequency range, where surface states thought to be critical to the exfoliation process are expected to be found are now studied in more detail to develop a thorough description of the evolution of hydrogen in the exfoliation process. To develop this description, the present results are first compared to previous work.

4.1.4.1 Comparison to Previous Work

4.1.4.1.1 Stein *et al.* H-implanted Ge

A previous study conducted by Stein *et al.* serves as an excellent guide to the interpretation of these spectra. In this study, Stein *et al.* used He-implantation and annealing to form void

structures in Ge. These samples were then implanted with H^+ to a dose of $1 \times 10^{16} \text{ cm}^{-2}$ as a novel means of studying the desorption kinetics of hydrogen from Ge (100) and (111) surfaces in the He-induced bubbles.⁹ Figure 4.15 shows the temperature evolution of the features in the spectral range from 1900 to 2100 cm^{-1} in the spectral evolution under isochronal annealing observed by

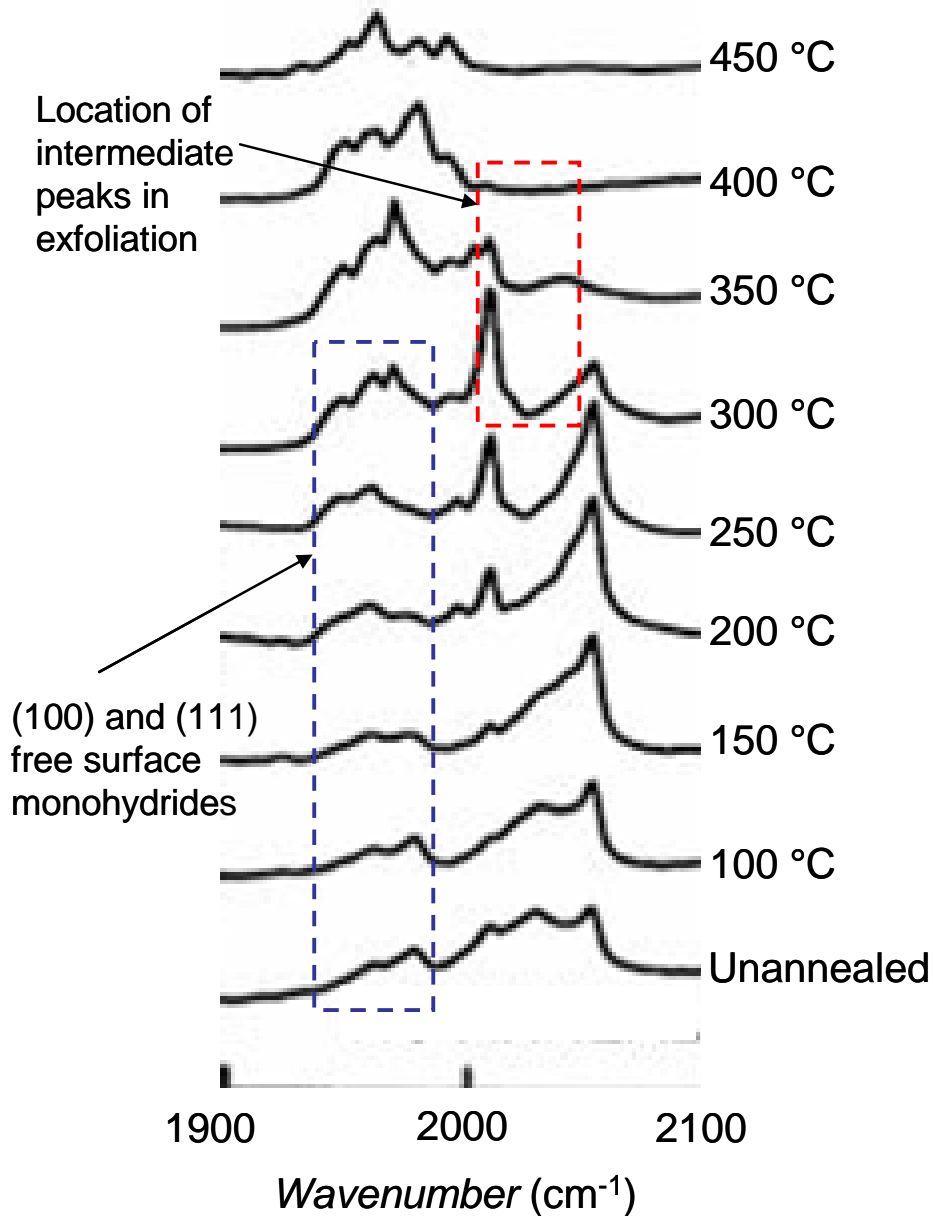


Figure 4.15 Spectral evolution of the Ge-H states in Ge with He-implantation-induced voids. This is a model system for the interaction of H with internal surfaces and discrete defect states in (100)Ge that should lack strong signals from the defect structures that directly precede blister opening in the exfoliation process.⁹

Stein *et al.* for hydrogen implanted in Ge with He-induced voids. In the blue box, the features attributed to internal surfaces at low temperatures are pointed out. In the present study, because of the lack of free internal surfaces immediately following implantation, these features are unobserved at low anneal temperatures. The red box highlights the region of the vibrational spectrum from 2000 to 2050 cm^{-1} in the temperature range of 300 to 400°C. These are the spectral and temperature ranges in which significant differences are observed between blistering and non-blistering samples in the present study. It is clearly seen that in this range in the Stein study there are no significant features present. This suggests that the modes here are both essential in the blister process, and are also not opportunistically formed upon implantation, but must form either by the capture of hydrogen freed from less stable discrete defects such as the Ge-H_2^* and VH_4 defects, which are observed at low temperature in both the present study and the Stein *et al.* work, or by the evolution of simple defect states that formed opportunistically during implantation into complex defects such as large vacancy-hydrogen defect structures.

In the Stein data, hydrogen released from discrete defect structures similar to those found at room temperature in the present study diffuses out of the Ge or is trapped in the He-induced voids, presumably a combination of both. The fact that spectral features observed as leading to the formation of internal structure in the present study are not observed in the Stein study indicates that mobile hydrogen preferentially segregates to free internal structures where it can exist as the more thermodynamically-favorable molecular H_2 . This further supports the notion that in the H-induced exfoliation of Ge, that as internal structures form, hydrogen reaching these structures preferentially segregates there providing internal pressure to further facilitate the exfoliation process. Thus, we can deduce that during annealing to a dose-dependent temperature, internal structure is being formed that can act to accumulate molecular hydrogen released from discrete defects. However, after a critical density of these structures is formed, subsequently released hydrogen is predominantly segregated in micro-cracks and other such internal structures.

The validity of the comparison above is supported by comparing the evolution of the sub-critical dose of $2 \times 10^{16} \text{ cm}^{-2}$ to the evolution of the spectra in a control sample in the work of Stein *et al.* The control sample in Stein *et al.* was not implanted with He^+ to form voids prior to implantation with H^+ to a dose of $1 \times 10^{16} \text{ cm}^{-2}$. However, blistering was not observed and the peaks that were noted between 2000 and 2050 cm^{-1} were not assigned to specific defects in the Stein *et al.* analysis likely because the Ge-H structures giving rise to these features are unique to the temperature evolution of H-implanted Ge.

4.1.4.1.2 Weldon *et al.* Study of H-induced Si Exfoliation

In addition to comparison with the Stein *et al.* work, the qualitative model proposed in the prior work on H-induced exfoliation of Si is consistent with the present data for Ge. That is, a broad background in the IR spectrum is correlated to a broad, thermally-unstable distribution of higher-order vacancy-hydrogen and interstitial-hydrogen defect structures.^{1,2} Upon annealing, this background is decreased, while, simultaneously, certain features in the spectra grow. Thus, we can conclude that the broad defect background observed for the blistering samples in the present study serves as a hydrogen source for the development of critical defect structures for the exfoliation process and also serves to provide internal pressure to the micro-cracks that precede exfoliation.

4.1.4.1.3 Summary of Comparison to Previous Work

Based upon these comparisons to previous work – both in H-implanted Ge and H-induced exfoliation of Si – the following points conclusions can be made:

- features forming in the 2000 to 2050 cm^{-1} range play a critical role in the formation of internal surface structures that lead to exfoliation,
- upon the formation of internal structure, hydrogen released from defect states by annealing preferentially segregates as molecular H_2 in internal structures such as voids,

- there must a critical concentration of such internal structures at which the formation of more internal structures or precursor defect structures is not favored, but hydrogen is more likely to be isolated in internal voids providing pressure necessary to extend surfaces,
- there is a broad distribution of discrete defects, including the Ge-H_2^* , VH_4 , V_2H_6 , IH_2 and other unidentified defects that serve as binding sites for hydrogen, that later contributes to the formation of internal structures and the development of internal pressure leading to cracks.

The conclusions drawn from these comparisons provide physical insight into the critical structures and steps of the exfoliation process.

4.1.4.2 Comparison of Blistering and Non-blistering Implant Conditions

Further insight into the exfoliation process is gained by comparison of the blistering and non-blistering implant conditions observed in the present study. To improve the visualization of the polarization information, plots have been prepared for each implant condition using spectra normalized by the maximum peak intensity. This allows the spectral detail to be easily compared as a function of polarization and anneal temperature for each of the implant conditions studied without loss of detail due to the enhanced p-polarized spectra dominating the s-polarized spectra. The spectra for $2 \times 10^{16} \text{ cm}^{-2}$, $5 \times 10^{16} \text{ cm}^{-2}$ and $1 \times 10^{17} \text{ cm}^{-2}$ are given in Figs. 4.16, 4.17 and 4.18, respectively. Additionally, Tab. 4.2 catalogs the dominant peaks observed in the different implant conditions as a function of temperature. By comparison of the position and polarization splitting of dominant peaks in this study between the blistering – 5×10^{16} and $1 \times 10^{17} \text{ cm}^{-2}$ – and the non-blistering – $2 \times 10^{16} \text{ cm}^{-2}$ – implant conditions, further information about the nature of the Ge-H defects leading to exfoliation can be deduced.

Table 4.2 Peak location as a function of temperature for peaks in the 1900 – 2100 cm^{-1} for 2×10^{16} , 5×10^{16} , and $1 \times 10^{17} \text{ cm}^{-2}$. The p-polarized peaks in red signify peaks where strong enhancement is observed. The s-polarized peaks that are thought to be associated with those enhanced peaks are also highlighted in red.

Temperature (°C)	Implant Dose (cm^{-2})					
	2×10^{16} – Sub-critical		5×10^{16}		1×10^{17}	
	S	P	S	P	S	P
Unannealed	1979 2008 2050	1979 2050	1979 2008 2050	1979 2008 2050	1979 2008 2050	2008 2038
170	2008 2050	2050	2008 2050	2050	1996 2008 2050	2046
221	2008 2050	2050	1996 2008 2050	2050	1996 2008 2050	2046
297	2008 2040 2050	2035	1996 2008 2030 2050	2027	1996 2008 2033 2050	2015
339	1969 2008 2038	2033	1969 1996 2029	2015	1969 2008 2027	2008
399	1969 2031	2029	1969 1990 2001 2025	2008	1972 1992 2027	1972 1992 2008 2027
501	2008	2008 2021	1962 1980 1990 2002	1957 1970 1986 2002		

4.1.4.2.1 Identification of Surface Modes Following Film Exfoliation

Following the blistering process in the $1 \times 10^{17} \text{ cm}^{-2}$ implant (Figs. 4.11, 4.12 and 4.17) there is a broad absorption band from 1950 to 2050 cm^{-1} in both the s- and p-polarizations. The dominant features in the s-polarized spectrum are at 1972, 1992 and 2027 cm^{-1} . The first two features are

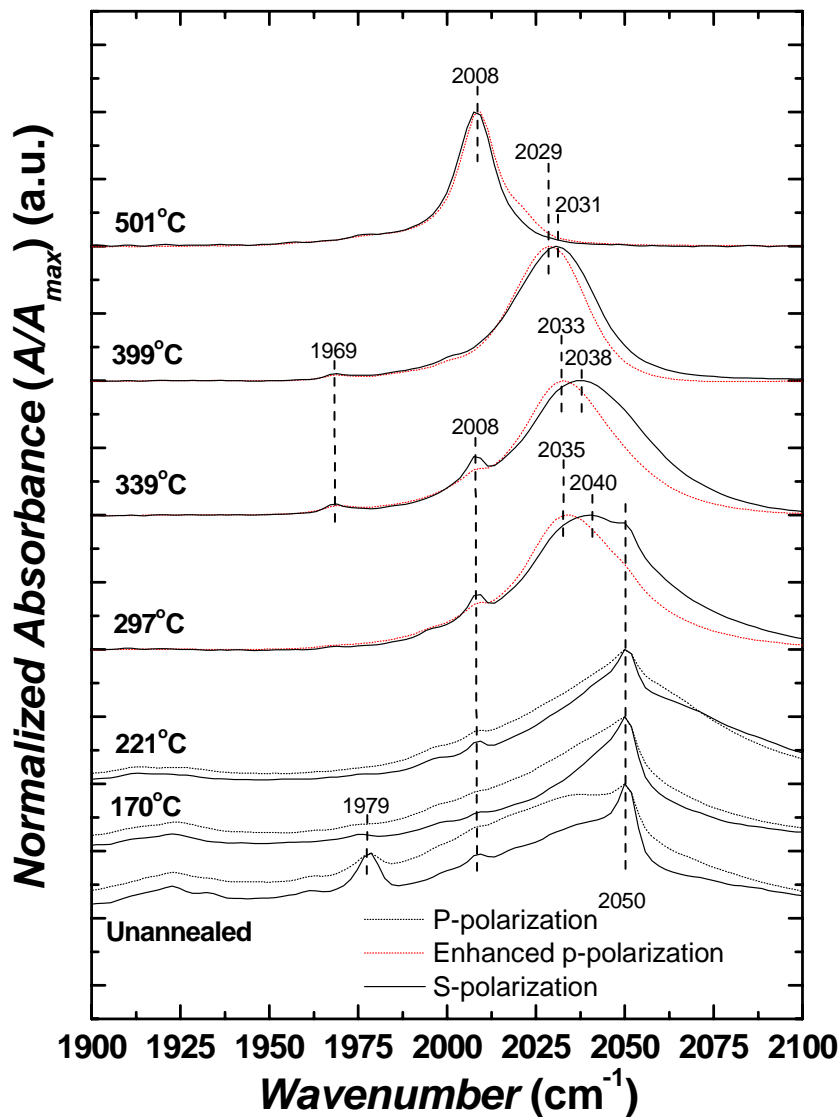


Figure 4.16 Temperature resolved comparison of normalized \bar{p} - and \bar{s} -polarized spectra for Ge implanted with 80 keV H^+ to a dose of $2 \times 10^{16} \text{ cm}^{-2}$. The dashed spectra in red indicate p-polarized spectra in which strong enhancement is observed suggesting their critical role in the exfoliation process.

consistent with (111) and (100) surface monohydride stretch modes, although they are shifted slightly from the reported values of 1971 and 1979 cm^{-1} , respectively.^{10,11} This peak shifting may be explained by the fact that the internal surfaces caused by the exfoliation process are rougher than ideal crystallographic surfaces, which has been shown to shift the mode position by up to 10

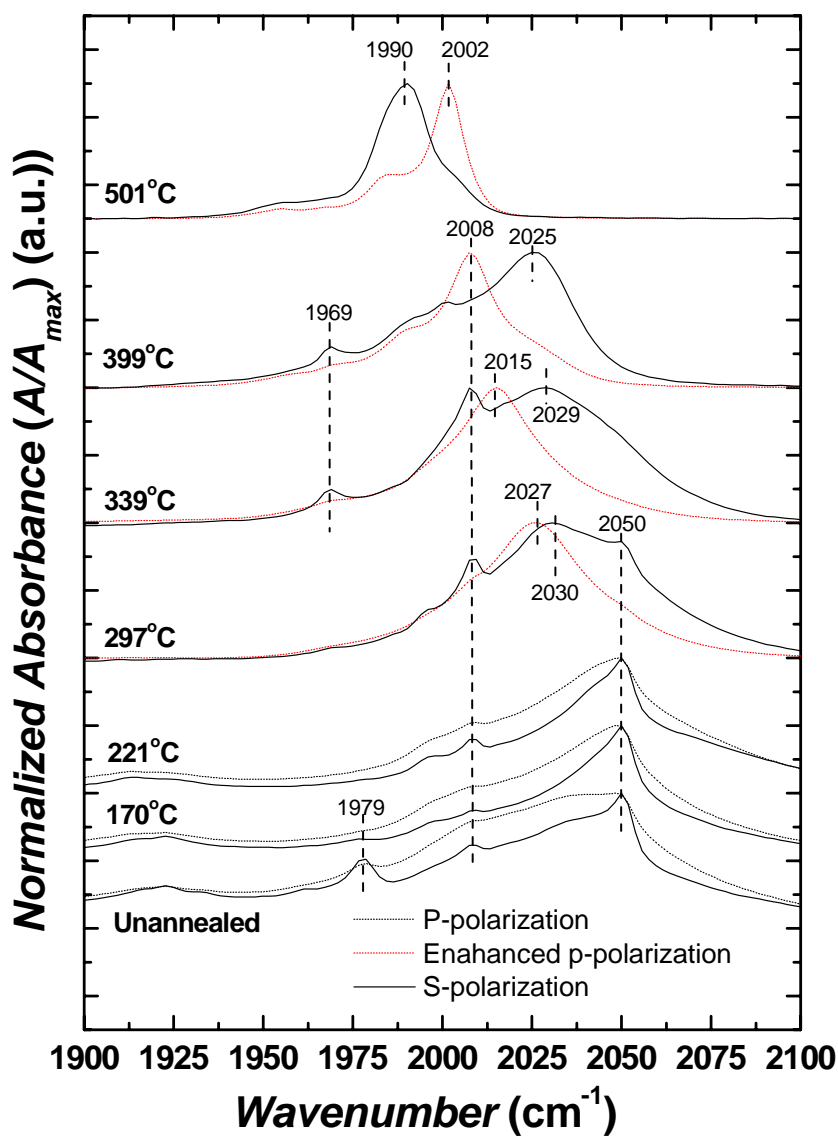


Figure 4.17 Temperature resolved comparison of normalized \vec{p} - and \vec{s} -polarized spectra for Ge implanted with 80 keV H^+ to a dose of $5 \times 10^{16} \text{ cm}^{-2}$. The dashed spectra in red indicate p-polarized spectra in which strong enhancement is observed suggesting their critical role in the exfoliation process.

cm^{-1} in Ge.¹² The feature at 2027 cm^{-1} is attributed to agglomerated defect structures that are precursors to blistering, as will be discussed below, and are still present in the substrate below the exfoliated region. The p-polarized spectrum has a strong peak at 2008 cm^{-1} that remains following exfoliation. This is assumed to be the z-axis spectral signature of the agglomerated defect

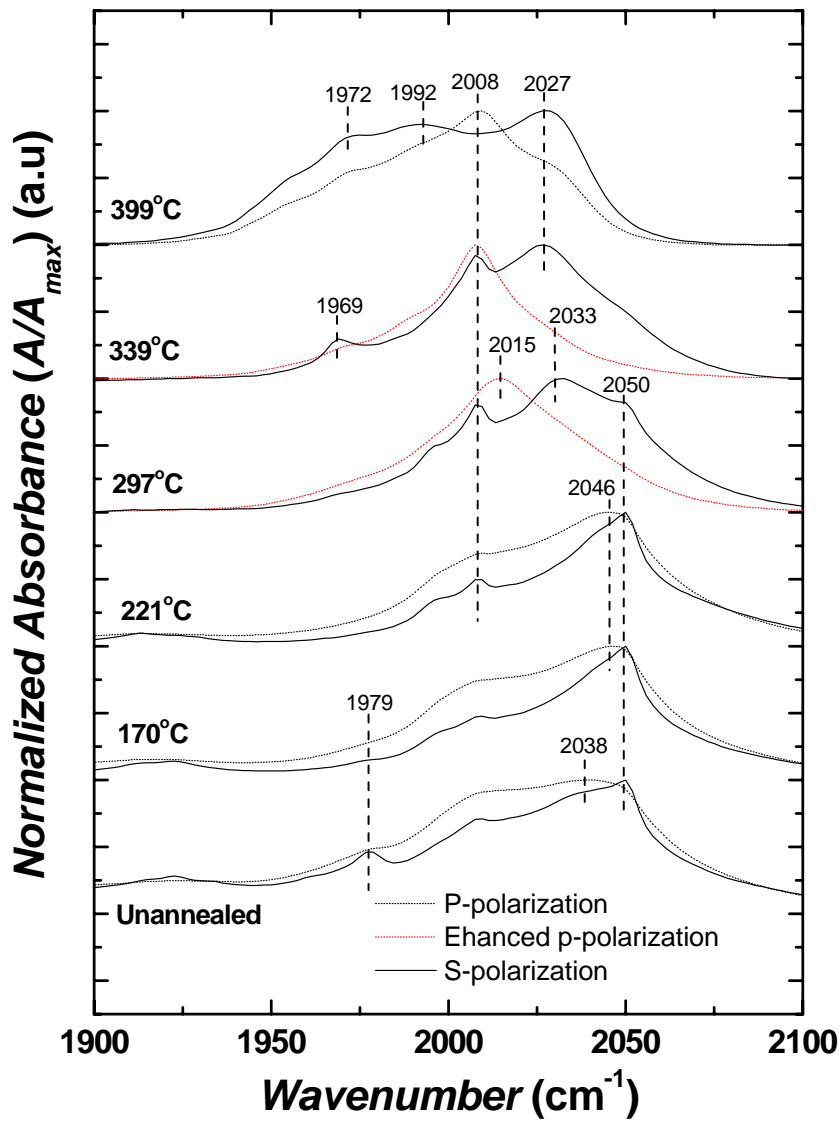


Figure 4.18 Temperature resolved comparison of normalized \bar{p} - and \bar{s} -polarized spectra for Ge implanted with 80 keV H^+ to a dose of $1 \times 10^{17} \text{ cm}^{-2}$. The dashed spectra in red indicate p-polarized spectra in which strong enhancement is observed suggesting their critical role in the exfoliation process.

structures leading to exfoliation. Additionally, following exfoliation at 399°C there is a more noticeable shoulder near 2027 cm^{-1} presumably due to the x-axis component of the p-polarized radiation. Following exfoliation at 399°C there is a broad tail toward 1950 cm^{-1} that is consistent with the presence of (111) surface monohydride modes.⁹ Also, there are likely contributions from

platelet structures that remain in the near surface region of blistered Ge. In fact, due to the temperature of the anneal as well as the slightly oxidizing ambient in the furnace, it is not clear that surface hydride modes are stable, and the surface monohydride signatures described above may be entirely contributed by structures that reside in the implant-damaged near-surface region of the sample.

4.1.4.2.2 Identification of Internal Surface Modes Prior to Exfoliation

Based on the study of the exfoliated surface of the $1 \times 10^{17} \text{ cm}^{-2}$ sample following an anneal to 399°C , it is clear that, as was expected, the exfoliation process leads to the formation of hydrogenated free-surfaces. For this reason, it is logical that the Ge-H structures immediately preceding the exfoliation of a film consist of internal-surface structures. The $5 \times 10^{16} \text{ cm}^{-2}$ dose sample corroborates this expectation due to its slower evolution of pre-exfoliation Ge-H microstructure allowing more finely discretized snapshots of the spectral evolution to be observed. In the $5 \times 10^{16} \text{ cm}^{-2}$ dose (Figs. 4.13, 4.14, and 4.17) the modes described below attributed to internal surfaces are observed prior to exfoliation, and are generally not observed for the sub-critical dose of $2 \times 10^{16} \text{ cm}^{-2}$ (Figs. 4.9, 4.10, and 4.16).

In the case of the intermediate dose of $5 \times 10^{16} \text{ cm}^{-2}$ evidence of the opening of micro-cracks begins to be observed at 501°C (Figs. 4.13, 4.14 and 4.16). Following an anneal to 501°C the p-polarized spectrum has a strong sharp peak centered at 2002 cm^{-1} with shoulders extending to lower frequencies. The s-polarized spectrum has a somewhat broader peak at 1990 cm^{-1} also with a shoulder extending down to 1950 cm^{-1} . These two features taken together are strongly suggestive of the presence of Ge(100) surface monohydrides in the interior of the substrate. The location of these surfaces in the interior of the substrate is proven by the strong enhancement of the mode at 2002 cm^{-1} in p-polarization indicating a well defined internal structure. The separation of the modes by 12 cm^{-1} is very close to that which is expected for the asymmetric (s-polarization) and symmetric (p-polarization) stretch modes of the Ge(100) surface monohydride.

There is even a strong shoulder around 1990 cm^{-1} in the p-polarized spectrum attributed to the x-axis radiation being absorbed by the asymmetric mode of the monohydride. The modes attributed to the Ge(100) surface monohydride stretch are shifted about 10 cm^{-1} higher in frequency than other values reported in the literature.¹⁰ However, the polarization behavior and XTEM evidence (Figs. 4.5 and 4.6) support the present assignment.

A possible explanation of the 10 cm^{-1} shift is the proximity of two opposing Ge(100) internal surfaces that reside on opposite sides of an opening micro-crack. It has been previously shown in the study of wafer bonding of Si(111) surfaces that the Si(111) surface monohydride stretch mode of two opposing closely interacting surfaces is perturbed by as much as 17 cm^{-1} when two such surfaces are in a proximity of 1-2 Å.^{1,13} However, in that study the perturbation was found to shift the free-surface vibration to lower frequencies, not higher. This does not rule this out as an explanation of the present observation, but it can not be verified as an explanation for the shift without theoretical calculations to verify this shift.

A second hypothesis is that the 10 cm^{-1} shift of the observed frequencies from free-surface Ge(100) frequencies could be attributed to a [100]-axis stress acting on the surfaces of the micro-crack. This would be due to the isotropic pressure induced by trapped H_2 in the crack. Over the extended surfaces far from the edge of the primarily two-dimensional micro-crack structure, any isotropic force would have a predominantly uniaxial component normal to the internal surfaces. As was previously mentioned, this gas is thought to be the driving force that provides the energy necessary to extend the cracks and break bonds in the Ge leading to blistering. The pressure of trapped gas in these structures can be estimated using the results of an analysis of the critical radius for blistering in Si performed by Gösele *et al.*¹⁴ In this analysis the critical radius for the formation of a popped-up blister is given by the following equation

$$r_{crit} = \left\{ 16\gamma_p E t^3 / \left[9\alpha (1 - \nu^2) \Delta p^2 \right] \right\}^{1/4} \quad (4.5)$$

So,

$$\Delta p = \frac{4t}{3r_{crit}^2} \left[\frac{\gamma_p Et}{\alpha(1-\nu^2)} \right]^{1/2} \quad (4.6)$$

Where,

Δp = the pressure differential between the internal and external pressures of the blister,

t = the thickness of the exfoliating film taken as the 561 nm, the estimated range from a TRIM simulation,

r_{crit} = the critical radius for blister formation taken as 1 μm ,

E = the Young's modulus of Ge,

α = a numerical calculation factor taken as 1,

ν = the Poisson's ratio,

γ_p = the surface energy associated with the interaction of hydrogen passivated internal surfaces that are forced out of contact by the action of the internal pressure of the blister.

The surface energy is presumably less than the cohesive energy of a (100)-plane in un-implanted material due to damage and hydrogenation of defect structures. In the Gösele *et al.* analysis this was taken as 0.5 J m⁻². For the present calculation the same number is used. Using these assumptions the estimated internal pressure in a popped-up blister is 120 MPa. In previous studies of discrete Ge-H defects, pressures of this magnitude were associated with a shift of approximately 1 cm⁻¹ to higher frequency for various defects.⁶⁻⁸ However, this estimate for the internal pressure may be low due to the value taken for several parameters such as the critical radius, the surface energy that is overcome in separating the material, and the assumed value of α . It is certainly possible that the internal pressure at the onset of blistering might be as high as 500 MPa which has been associated with frequency shifts as large as 4.5 cm⁻¹ in the VH₄ defect⁸ and by extension may result in an upward shift in frequency in the present case. It is reasonable to assume that a combined contribution of H₂-induced stress and interaction of internal Ge(100)

surfaces could explain the 10 cm^{-1} upward shift of Ge(100) surface monohydride peaks in the $5 \times 10^{16}\text{ cm}^{-2}$ dose following a 501°C anneal.

Following a 221°C anneal, a shoulder appears in s-polarization in the blistering implant conditions at approximately 1996 cm^{-1} . This is near the asymmetric mode for (100) surface monohydride, but it is shifted upward in frequency by 17 cm^{-1} . For this reason, it is hypothesized that this is associated with a (100) platelet structure that should have a (100) dihydride-like configuration. The Ge(100) surface dihydride has not, to our knowledge, been previously observed on a free Ge(100) surface. However, this assignment is supported by comparison to studies of hydrated Si surfaces that have attributed the dihydride asymmetric mode for a (100) surface to a mode at 2110 cm^{-1} . That is 23 cm^{-1} higher in frequency than the Si(100) surface monohydride asymmetric mode. It should be noted that bond-centered hydrogen in a (100) platelet structure would be expected to appear only in the presence of local out-of-plane strain in the crystal near the platelet, and that the bonds in the platelet are expected to be elongated and bent relative to their normal state. This presents complications when comparing (100) free-surfaces and (100) platelet structures in Si and Ge. However, the interpretation of the peak at 1996 cm^{-1} is not inconsistent with this caveat.

Above 300°C a feature that stands out when comparing the non-blistering to the blistering implant conditions is the presence of a strong feature at 1969 cm^{-1} in s-polarization for the blistering samples that is in close proximity to the reported value of 1971 cm^{-1} for the (111) surface monohydride stretch.⁹ This may be attributed to the increased presence of (111) platelet structures observed by TEM at elevated temperature in blistering samples, or it could be caused by small (111)-oriented cracks opening to form internal structures along (111) free surfaces. For the $5 \times 10^{16}\text{ cm}^{-2}$ dose the extension of a shoulder down to 1950 cm^{-1} can also be attributed to the presence of a Ge(111) surface monohydride in the sample.

Based on the observations in this and the previous section, it can be stated that the exfoliation process results in hydrogen-terminated free surfaces following exfoliation. Also, measured

spectra support the assertion that these hydrogen-terminated surface structures initially form as internal surfaces prior to exfoliation. What remains to be identified are the precursors and mechanisms that lead to the development of these internal surfaces.

4.1.4.2.3 Comparison of Exfoliation Precursor Modes from 2000 to 2050 cm^{-1}

As was pointed out by the comparison of the present results to the results of the Stein *et al.* study, the key to fully understanding the chemical mechanism behind the exfoliation of H-implanted Ge is to successfully identify the modes that arise from 2000 to 2050 cm^{-1} upon annealing above 297°C. The exact assignment of these modes is not possible in the present study, due to a lack of fundamental studies of complex extended defect structures in the literature. However, comparison of the features in this range for the blistering and non-blistering implant conditions, does allow one to draw important conclusions about the nature of these structures and critical steps that lead to exfoliation. In Tab. 4.2 the peaks that show strong enhancement in the \bar{p} -polarization are emphasized in red. These modes are thereby correlated with critical structures in the exfoliation process. The associated s-polarized peaks are also highlighted.

Following an anneal to 297°C all three implant doses begin to show major changes in the 2000 to 2050 cm^{-1} range. The spectra at this temperature are very similar in this range across all doses with the peak position in both polarizations being at lower frequencies for the $1 \times 10^{17} \text{ cm}^{-2}$ dose, indicating that the exfoliation process has proceeded further relative to the $5 \times 10^{16} \text{ cm}^{-2}$ dose. Also, there is more peak splitting observed between the s- and p-polarized spectra than for the other two spectra. Following further annealing to 339°C significant peak splitting is observed for both of the blistering doses, but no significant splitting is observed for the sub-critical dose. This behavior is characteristic of coupled modes on extended defect structures that have differing frequencies and polarization orientations depending on the manner of coupling, such as in the symmetric and anti-symmetric stretch modes on (100) surface monohydrides.¹⁰ In this case there is a clear splitting of the modes parallel and perpendicular to the (100)-plane suggesting that the

dipoles are associated with extended defects oriented along the (100)-plane. Another important observation about these exfoliation precursor modes is that they are rather broad by comparison to other vacancy-hydrogen modes that have been identified in the low-temperature spectra, such as those attributed to the VH_4 and V_2H_6 defects. This suggests that these modes are not well-defined structures, but are more likely agglomerated defects that have a somewhat random configuration and size resulting in broad peaks.

Upon annealing to 399°C the $1 \times 10^{17} \text{ cm}^{-2}$ dose has exfoliated, but the $5 \times 10^{16} \text{ cm}^{-2}$ dose has experienced further peak-splitting and definition of the peaks. Additionally, the first signs of internal surfaces have begun to appear at this temperature. However, the sub-critical dose of $2 \times 10^{16} \text{ cm}^{-2}$ is essentially featureless, and shows virtually no peak splitting.

After annealing to 501°C the mode observed for the exfoliation precursor at 2025 cm^{-1} is lost, suggesting that the defect structures associated with this band are not thermally stable at this temperature. At this point the formation of well-defined surfaces begins to be observed for the $5 \times 10^{16} \text{ cm}^{-2}$ dose, while the Ge-H modes for the $2 \times 10^{16} \text{ cm}^{-2}$ dose continue to diminish and do not develop indications of internal structure. The observation at this temperature is important for application of the spectral evolution knowledge to the development of a more robust exfoliation process. That is, the precursor structure for exfoliation is thermally unstable between 399 and 501°C and is therefore lost. Thus, one could potentially reach lower critical doses for exfoliation by performing a sustained anneal at a lower temperature near 399°C and enable the further development of the internal structure and defects necessary for exfoliation, prior to annealing to a temperature at which these defects are lost. Of course, there is clearly a minimum dose necessary to passivate two (100) monolayers and provide internal pressure to the passivated surfaces, but the kinetics of the process could still be aided to facilitate more efficient utilization of the implanted hydrogen.

The spectral evolution described above is graphically represented in Fig. 4.19, which shows the dominant peak position as a function of temperature for all three implant conditions and both

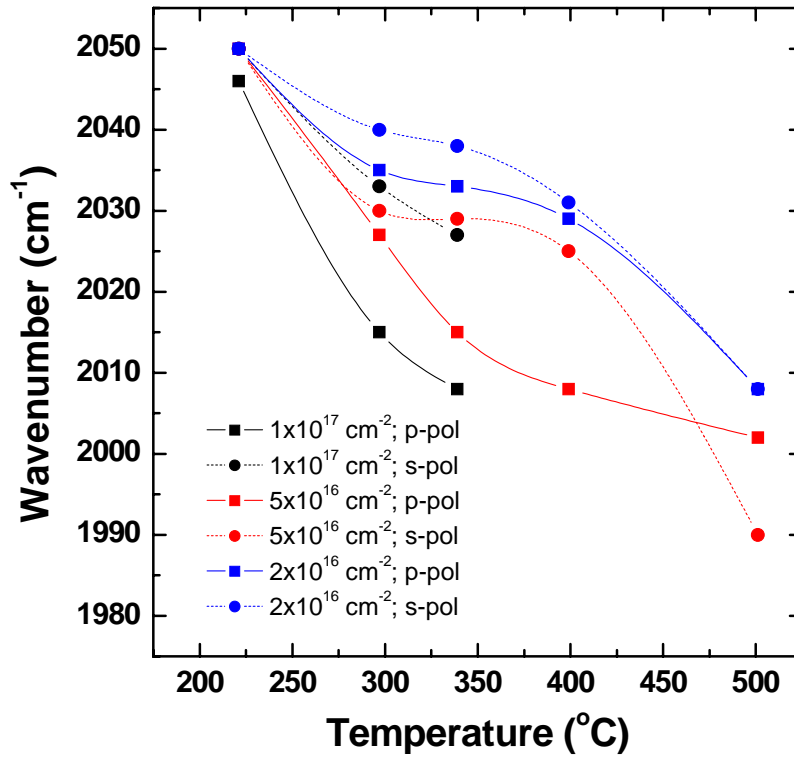


Figure 4.19 Peak position comparison for dominant peaks in the 2000 to 2050 cm^{-1} range for all implant conditions as a function of temperature.

polarizations. There are several physical interpretations consistent with this data. As was posited in the prior study of the exfoliation of Si by H-implantation, it is likely that the features between 2000 and 2050 cm^{-1} correspond to agglomerated vacancy-hydrogen defect structures. It was further suggested by that study that these structures agglomerated on (100) platelet structures.¹ This is consistent with the observation of (100) platelet structures in XTEM and with the polarization-dependent spectrum splitting described above. The notion of a critical size for the agglomerated structure is further suggested by the observed peak splitting in the p- and s-polarization spectra in the present study indicating that coupled modes between the hydrogen in the agglomerated structures gives rise to splitting of modes with well-oriented dipoles. Additionally, these modes are thermally stable at temperatures above those observed for discrete

vacancy-hydrogen defect structures in past studies. The manner in which these structures become stabilized may be due to the formation of void structures that trap thermally desorbed hydrogen as H_2 , preventing the loss of hydrogen from the vicinity of the defect structures. The pressure exerted by molecular H_2 in these structures would then provide the force necessary to extend the void size into micro-cracks, and would additionally prevent these structures from thermally healing in the event that high temperature annealing causes desorption of some of the hydrogen bonded to the defect structures.

4.1.4.2.4 Summary of Comparison of Blistering and Non-blistering Implant Conditions

Based upon the comparison of blistering and non-blistering conditions described above the following conclusions are reached:

- following exfoliation there is spectra evidence of Ge(100) and Ge(111) surface hydride states with Ge(100) being the dominant component,
- prior to exfoliation there is evidence of internally located Ge(100) surface monohydrides that are shifted 10 cm^{-1} higher in frequency than Ge(100) surface monohydrides on free surfaces,
- in blistering implant conditions there is a shoulder located around 1996 cm^{-1} that is indicative of a Ge(100) platelet structure observed by XTEM in Section 4.1.3.1 and having a chemical structure similar to a Ge(100) surface dihydride,
- at temperatures above 300°C a peak at 1969 cm^{-1} assigned to the Ge(111) surface monohydride is observed for blistering implant conditions,
- exfoliation precursors are observed in spectra from 297 to 399°C between 2000 and 2050 cm^{-1} and consist of broad peaks suggesting that these structures consist of agglomerated defects and have poorly defined size and configuration,

- the exfoliation precursors for doses leading to exfoliation undergo polarization-dependent splitting of approximately 15 cm^{-1} indicating that the agglomerated defects have coupled modes and are oriented along the (100) plane,
- these agglomerated exfoliation precursors probably nucleate on (100) platelet structures,
- the observation of polarization-dependent peak splitting in blistering samples only is suggestive of the notion of a critical agglomerated defect size.

4.1.5 Conclusions

Based upon the physical and chemical observations made by TEM, AFM, and MIT-FTIR, a qualitative understanding of the H-induced layer transfer process has been achieved. Upon H-implantation defects are formed that trap H in the implanted Ge. These defects include modes assigned to Ge-H_2^* , VH_4 , V_2H_6 and IH_2 . However, there is broad background absorption from 1900 to 2050 cm^{-1} that is attributed to a broad distribution of vacancy-hydrogen defect structures of the form V_xH_y . Upon annealing, these structures are lost and the hydrogen therein is free to move through diffusion. This leads to the agglomeration of defect structures that form the precursors for internal (100) and (111) monohydride internal surfaces. It is speculated on the basis of this study and previous studies of the role of H in the exfoliation of Si, that the nucleation points for these agglomerated defect structures are (100) platelets. This hypothesis is further supported by XTEM observation of (100)-oriented defect structures typical of platelets immediately following implantation and by the possible spectroscopic signal at 1996 cm^{-1} assigned to (100) platelet structures. Upon sufficient annealing micro-cracks form along the same orientation in the crystal, lying predominantly along the (100) plane, as observed by XTEM. Simultaneously, vibrational frequencies associated with monohydride (100) Ge surfaces appear in the FTIR spectra, indicating that hydrogen provides a termination species for the internal blister structures. These micro-cracks and their agglomerated precursors serve as points for the coalescence of H_2 and the development of internal pressure sufficient to break bonds and extend

the internal fracture laterally. Upon ripening of the micro-cracks into super-critical radius internal surfaces, blisters pop-up and lead to the exfoliation of the thin Ge film.

4.2 *H-induced Exfoliation of InP*

The motion and bonding configurations of hydrogen in InP are studied after proton implantation and subsequent annealing, using Fourier Transform Infrared Spectroscopy. It is demonstrated that, as implanted, hydrogen is distributed predominantly in isolated point-like configurations with a smaller concentration of extended defects with uncompensated dangling bonds. During annealing, the bonded hydrogen is released from point defects and is recaptured at the peak of the distribution, by free internal surfaces in di-hydride configurations. At higher temperatures, immediately preceding exfoliation, rearrangement processes lead to the formation of hydrogen clusters and molecules. Reported results demonstrate that the exfoliation dynamics of hydrogen in InP and Si are markedly different, due to the higher mobility of hydrogen in InP and different implant defect characteristics leading to fundamentally differences in the chemical mechanism for exfoliation.

4.2.1 An Introduction to Hydrogen in H-implanted InP

The chemical and electrical activity of hydrogen in semiconductors is of fundamental and applied interest. This is especially true for hydrogen in III-V compound semiconductors due to its incorporation during the epitaxial growth of III-V device structures. Hydrogen can be incorporated in III-V materials as an impurity or intentionally introduced in the material to passivate the electrically active defects and other impurities.¹⁵ In the present analysis, hydrogen in III-V materials, specifically InP, is of interest for the exfoliation of thin films for use in wafer bonding applications. The H-induced exfoliation of III-V semiconductors for the layer transfer onto foreign substrates has proven to be more difficult than exfoliation of Si for fabrication of SOI. Indeed, it was only recently shown that the concept of hydrogen-induced exfoliation can be

applied to the transfer of thin films of InP^{16,17} and GaAs¹⁸ to foreign substrates. For this reason, a detailed understanding of the role of hydrogen in the exfoliation of these materials is still lacking.

As was summarized in §4.1.1, several studies have applied structural characterization and spectroscopy to understanding the evolution role of hydrogen in the exfoliation of Si. However, an understanding of the chemical and physical mechanism of H-induced exfoliation in InP cannot be deduced from previous studies in Si for several reasons. First, In and P have different valence electronic structures, which necessarily leads to a different interactions with hydrogen. Second, the different masses of In and P lead to a preferential displacement of P over In, by a factor of 1.8 as determined from a TRIM⁵ damage simulation and assuming a displacement energy of 15 eV for both In and P. Thus, a larger number of vacancies are expected to be formed in the anion sublattice with a correspondingly larger quantity of P interstitials. As a consequence, implantation of InP creates more disorder and damage in the material, and can inhibit the complete healing of the structure by thermal annealing. A consequence of extreme implantation-induced disorder for the H-induced exfoliation of InP is that the reduction of crystallographic planes, which are required for the formation of platelets and subsequent opening of micro-cracks necessary for the exfoliation process.

In contrast the wealth of reported spectroscopic information of hydrogen in Si, few infrared spectroscopy studies of hydrogen in InP exist in the literature. Prior work has focused on the study of the vibrational modes of hydrogen bonded to external surfaces of InP where hydrogen is adsorbed to well-characterized low-index crystallographic InP surfaces, such as the (100), (110), and (111) surfaces, while other studies have investigated the so-called local vibrational modes (LVM's) of H-implanted InP in which hydrogen is opportunistically incorporated in a perturbed lattice, with uncharacterized crystal structure. In our case, the study of InP implanted under conditions leading to H-induced layer exfoliation is a combination of these two conditions. On the one hand, implantation creates isolated lattice defects that lead to defect modes attributed to LVM's. However, large implantation doses that cause large densities of defects and introduce

large quantities of hydrogen that lead to the formation of internal surfaces where the hydrogen accumulates prior to the layer exfoliation.

In this section the effect of isochronal annealing on the vibrational modes of H-implanted InP is studied for the understanding of H-induced exfoliation of InP. The experimental results are discussed relative to existing microscopic models for the H-containing defect centers produced by implantation and also relative to previous studies of the H-passivation of (100), (110) and (111) InP free-surfaces. The FTIR results are complemented by hydrogen thermal evolution measurements and structural characterization by TEM and AFM of InP during the exfoliation process.

4.2.1 Experimental Procedure

InP wafers used in this study are commercially available, 500 μm thick double-side polished 50 mm un-doped (100) InP, grown by the vertical gradient freeze technique. The wafers were implanted at room temperature using the technique described in §4.1.2 with 80 keV H^+ to a dose of 10^{17} cm^{-2} , then cleaved into individual samples measuring 15 mm x 40 mm for transmission-mode and MIT-mode⁴ FTIR spectra measurements. The MIT-mode sample preparation and technique is described in §4.1.2. For transmission-mode measurements, the same sample holder was equipped with a calibrated resistance heater, allowing an *in situ* annealing inside a nitrogen purged chamber located in the spectrometer shown in Fig. 4.20. The sample was therefore not exposed to air between isochronal annealing steps and the measurements. Annealing *in situ* also guaranteed that the 45° angle of the sample relative to the IR beam and detector was not perturbed.

The hydrogen evolution measurement was performed by placing a 1 cm^2 InP sample inside a vacuum furnace equipped with a mass spectrometer with a base pressure of 10^{-9} Torr. The InP was then annealed up to 340°C at a rate of 10°C per minute, and the partial pressure of H_2 was

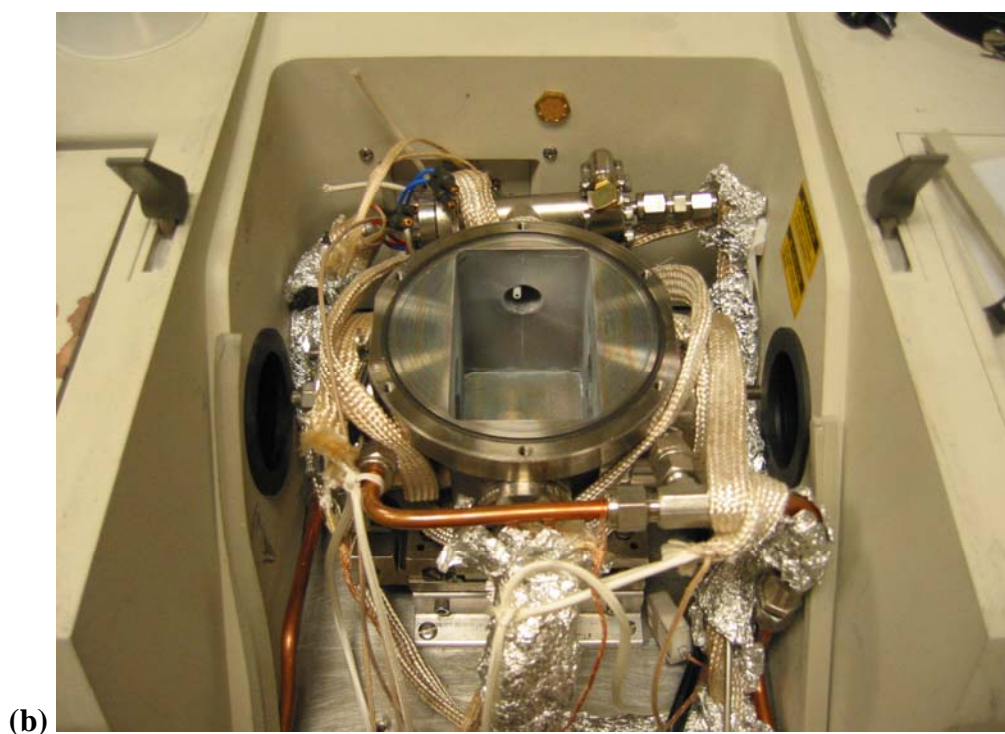
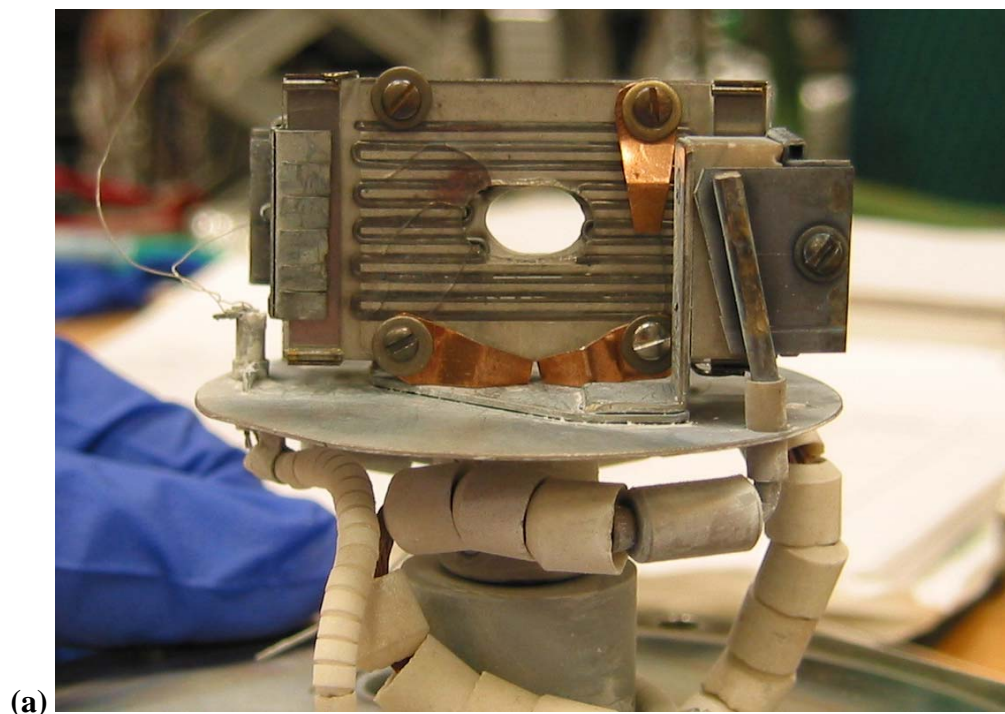


Figure 4.20 (a) The in situ resistive heater used for performing 45° incidence transmission-mode FTIR spectroscopy measurements of InP. (b) The controlled atmosphere sample holder installed in a Thermo-Nicolet mass spectrometer, enabling in situ sample annealing in an inert N_2 environment.

measured by the mass spectrometer. The temperature in the vacuum furnace for the hydrogen evolution, the FTIR sample heater and the furnace used for annealing the MIT-mode samples were all calibrated using a silicon thermocouple-instrumented wafer from Sensarray, which has an absolute temperature accuracy of 1.1°C . This calibration enables a fair comparison of the temperature-dependent behavior measured by the different techniques.

4.2.2 Results and Interpretation

4.2.2.1 Transmission Electron Microscopy

In Fig. 4.21 a XTEM micrograph reveals the presence of micro-cracks along the implanted region after annealing at greater than 350°C . As shown in the micrograph, the cracks open and extend

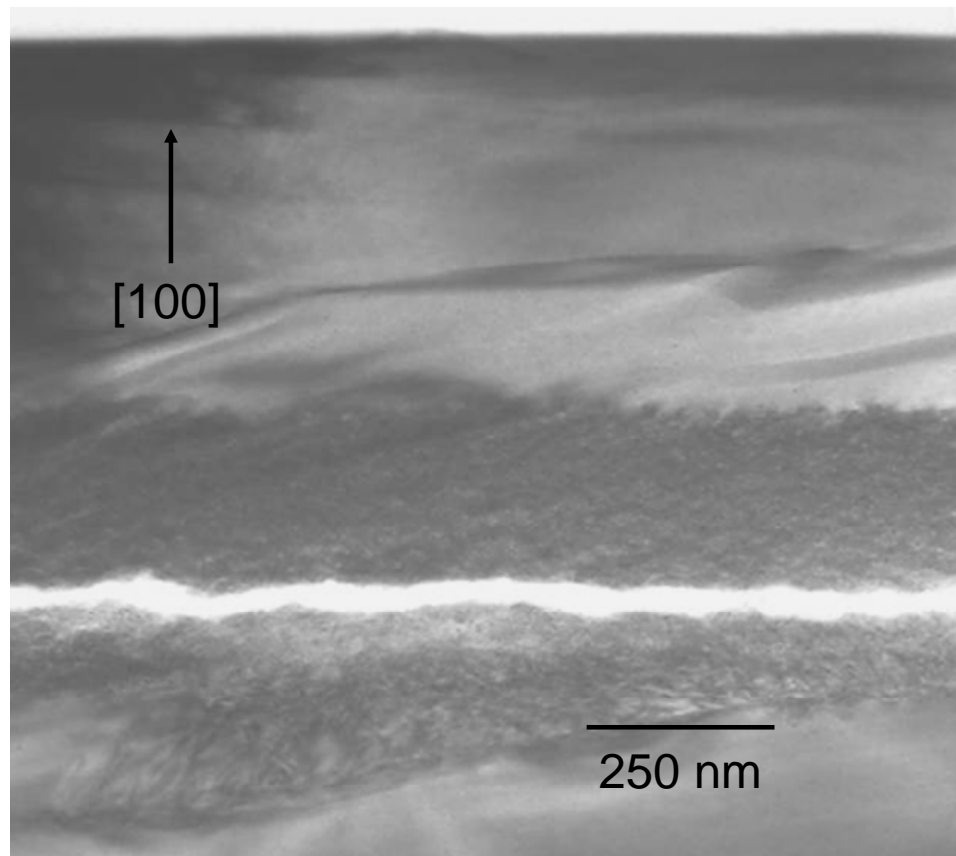


Figure 4.21 A cross-sectional TEM micrograph of H-implanted InP annealed to 350°C , showing cleavage parallel to the implanted surface.

parallel to the (100) surface indicating that the exfoliation occurs in the peak of the implanted hydrogen distribution. This observation is further corroborated by the AFM image of the blistered surface, where the presence of (100) parallel mesas are clearly present further indicating that cleavage proceeds along the (100) plane during exfoliation of InP.

4.2.2.3 Infrared Spectroscopy

H-implanted InP exhibits multiple infrared absorption peaks. These peaks are attributed to In-H and P-H stretching modes associated with both discrete defects and H-passivated internal surfaces. Transmission-mode FTIR spectra were measured from the as-implanted sample and following ten minute isochronal annealing steps in 60°C increments from 112°C to 412°C. All measurements were taken at 50°C. Modes attributed to In-H, P-H, and surface adsorbed water have differing intensities and are located in different parts of the spectrum. To better illustrate the different infrared features observed, the full spectra were divided into three graphs showing the In-H modes from 1400 to 1900 cm⁻¹ shown in Fig. 4.22, the adsorbed water modes from 3000 to 4000 cm⁻¹ shown in Fig. 4.23, and the P-H modes from 2100 to 2500cm⁻¹ in shown in Fig. 4.24.

Bands centered at 1600 and 1705 cm⁻¹ shown in Fig. 4.22 are associated with the vibration of In-H modes, specifically to a mixture of terminal and bridging In hydrides.^{19,20} The large width of the bands and their annealing behavior strongly suggests that In-H modes are not located in well-defined planes but consist of point defects, such as H-decorated phosphorous vacancies. At room temperature, these two bands seem to be merged into a single broad band. We attribute this lack of separation to the presence of a third band at 1650 cm⁻¹. This third band corresponds to the presence of water molecules adsorbed at the surface of the sample, and is attributed to the H-O-H scissor mode. The water peak at 1650 cm⁻¹ is correlated with the intensity of the H-O-H stretch modes of adsorbed water observed at 3500 cm⁻¹, as shown in Fig. 4.23. The absorption of water at the surface is a consequence of the InP surface hydrophilicity. Indeed, it has been shown that InP

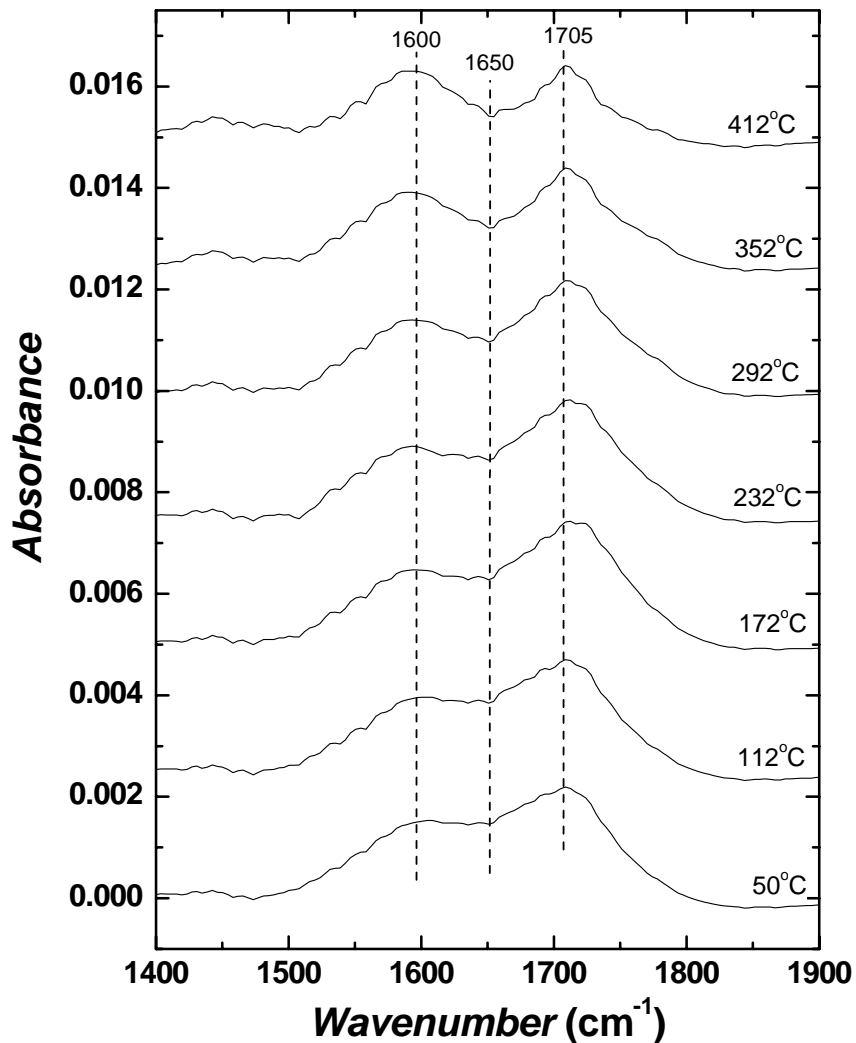


Figure 4.22 Transmission-mode FTIR spectral evolution of In-H modes at 1600 cm⁻¹ and 1705 cm⁻¹, corresponding to In-H and adsorbed water modes, overlapping with the H-O-H scissor mode of adsorbed water. The peak overlap associated with adsorbed water is lost upon annealing.

surfaces adsorb several monolayers of water following a brief exposure to air, even if H-passivated by being treated in HF.²¹ As illustrated in Fig. 4.23, all spectral bands associated with water disappear after annealing to 292°C, indicating that the water has been thermally desorbed from the surface or converted to an InPO_x surface layer. Following the loss of water at the InP surface at 292°C the bands attributed to the In-H modes shown in Fig. 4.22 become clearer and with a reduced spectral overlap.

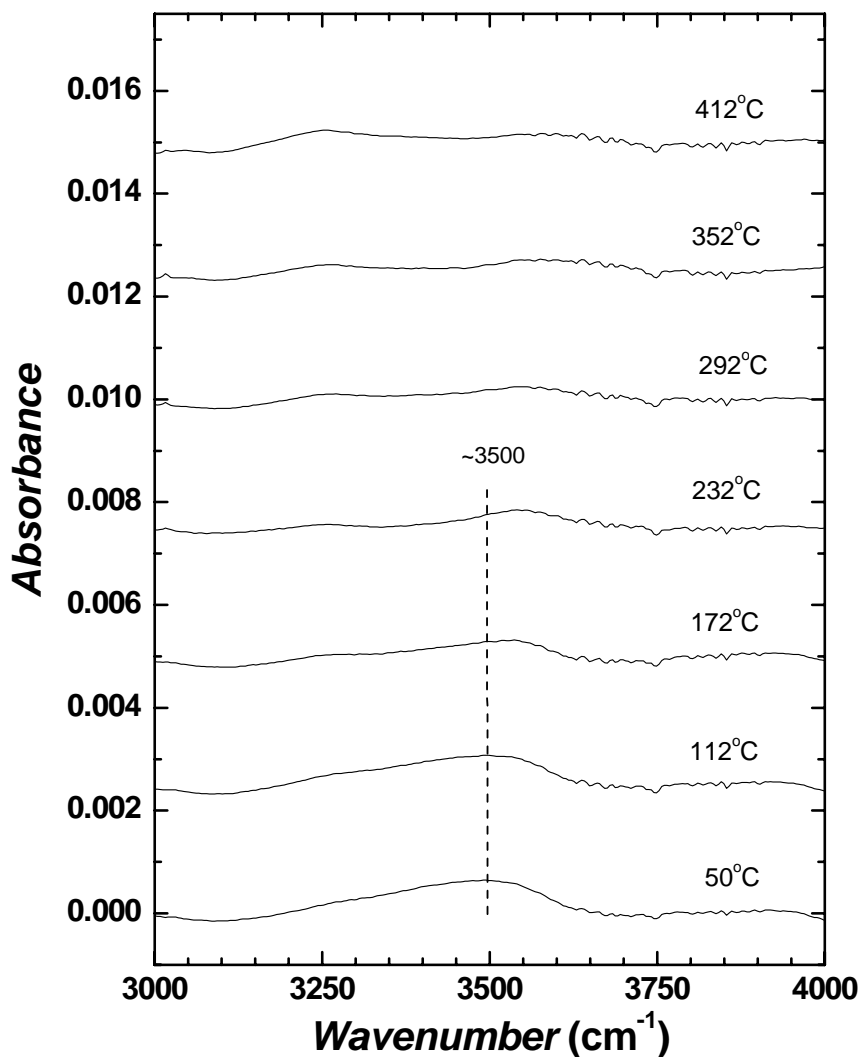


Figure 4.23 Transmission-mode FTIR spectra showing the loss of absorption at 3500 cm^{-1} associated with the H-O-H stretch mode upon annealing to 292°C , further confirming the loss of water from the surface seen in Fig. 4.22.

Interestingly, the In-H modes centered at 1600 and 1705 cm^{-1} exhibit uncorrelated annealing behavior. While the intensity of band at 1600 cm^{-1} remains nearly unaffected during annealing, the band at 1705 cm^{-1} decreases in intensity by 27% upon annealing. In both cases the bands become narrower upon annealing, but it is difficult to make a quantitative analysis, due to the presence of the H-O-H scissor-mode band at 1650 cm^{-1} present at lower temperatures. In general,

it appears that In-H complexes in implanted InP are relatively more stable than P-H complexes up to 412°C. It has been found that the insertion of hydrogen into metal dimer bonds releases a substantial amount of strain in the In-P bonds adjacent to the dimer structure, leading to an overall energy reduction of the InP defect upon H-passivation.²² The release of implantation-induced stress by hydrogen incorporation, along with the large enthalpy of formation of 52.2 kcal mol⁻¹, corresponding to a bond formation energy of 2.6eV, are possible origins of the observed thermal stability of the In-H bonding configurations.²³ This observation has important implications for the exfoliation of InP. Specifically, the relative difficulty of performing the H-induced exfoliation process in InP, as compared to Si, can be partially explained by the sequestering of hydrogen at anion vacancies that feature In-H bonds. Once In-H bonds are formed at these anion vacancies, the bonded H is no longer free to diffuse to extended defect structures where it can contribute to internal pressure that leads to exfoliation.

The evolution of P-H infrared spectra under isochronal annealing is shown in Fig. 4.24. The spectrum of the 50°C sample is composed of two clear peaks at 2306 and 2198 cm⁻¹ punctuated by a series of overlapping peaks at intermediate frequencies, specifically at 2217, 2227, 2268, and 2275 cm⁻¹. All of these peaks are associated with P-H modes that will be identified and discussed with the aid of higher resolution MIT-mode spectra in §4.2.3. Here a brief description of the evolution of the P-H during modes during sequential isochronal annealing steps is presented. There is no change in the spectrum after annealing the sample for 10 min at 112°C. After annealing at 172°C the overlapping peaks between 2217 and 2227 cm⁻¹ begin to decrease in intensity, disappearing completely after annealing to 292°C. The remaining peaks generally sharpen as annealing proceeds with each peak exhibits a unique evolution upon annealing. The intensities of the peaks at 2198, 2268, and 2275 cm⁻¹ decrease, with the peak at 2198 cm⁻¹ nearly disappearing by 352°C, while the peaks at 2268 and 2278 cm⁻¹ are still observed after annealing to 412°C. In addition, the position of the peaks at 2198, 2268, and 2275 cm⁻¹ does not change, while the position of the peak at 2306 cm⁻¹ is shifted to higher energy by 6 cm⁻¹, during which its

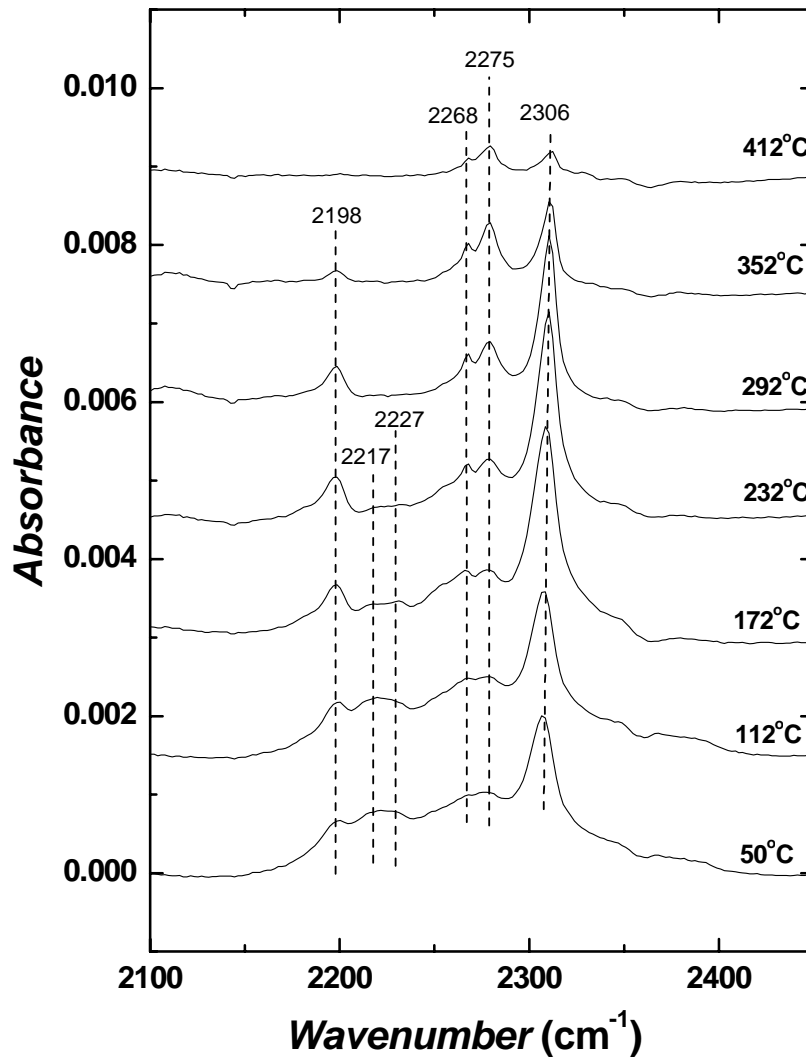


Figure 4.24 Transmission-mode FTIR spectra showing the evolution of P-H modes found in the 2100 to 2450 cm^{-1} range. Upon annealing, lower wavenumber modes associated with discrete defects are preferentially lost, while modes at higher wavenumbers associated with extended defect structures grow as they sequester mobile hydrogen that diffuses through the lattice during anneal steps.

intensity first increases, reaching a maximum at 232°C, and subsequently decreases significantly by the 412°C anneal. By comparison to previous work, it is determined that the lower frequency modes correspond to isolated H-passivated defects, whereas the higher frequency modes correspond to hydrogen complexes.^{1,10}

From these measurements several conclusions can be drawn. In the range from 50 to 292°C, the simultaneous increase of absorption in the higher wavenumber modes and decrease of absorption in the lower wavenumber modes suggests that upon annealing in this temperature range hydrogen bonded to point defects is thermally released from these structures and repopulates extended defects that it reaches during diffusion. The further decrease of the high frequency modes at higher temperatures indicates the formation of still more extended defects that contain H₂ clusters and molecules. Finally, at temperatures higher than 350°C, the pressure of H₂ inside the extended defects is sufficient to induce blistering of the material. At this point, very little hydrogen is left in the material, as shown by the reduced intensity of the high-frequency hydrogen modes attributed to the un-blistered hydrogen passivated cavities.

4.2.3 Discussion

Hydrogen forms a relatively strong chemical bond with In and P. However, the bond strength must depend on the surrounding environment and the type of defect in which the hydrogen is bound. Moreover, the evolution of the bonds is kinetically limited, with less steric hindrance to hydrogen leaving a larger position such as an In vacancy in the cation sublattice. H-covered InP free surfaces presented in the literature are ideal for research of chemisorption processes at semiconductor surfaces, but the geometry and crystallography do not correspond well to our experimental situation. Indeed, even assuming that during the H-induced exfoliation process hydrogen evolves by forming H-stabilized internal surfaces, the configuration and bonding of hydrogen to those internal surfaces is strongly influenced by the interaction of these In-H and P-H surface modes with similar modes on opposing surfaces in micro-cracks. Additionally, strain-induced vibrational shifts caused by local damage in the InP or by high pressure of trapped H₂ in internal voids can cause significant shifting of surface modes in InP micro-cracks from the measured values on ideal InP external surfaces. Moreover, it is expected that implantation will displace some In and P atoms and creating dangling bonds and damaging the structure. As the

surrounding InP is different from free surfaces, it is expected that the frequencies of In-H and P-H modes located in internal cavities and in defect structures created by implantation will be shifted and broadened relative to measurements made on free surfaces. Finally, hydrogen modes should also exhibit different annealing behavior and a different polarization response, depending on their location and surrounding environment.

In this section, we present MIT-FTIR experimental results for the purpose of elucidating the chemical states of hydrogen in H-implanted InP. As described in §4.1.2, MIT-mode FTIR spectroscopy makes this possible because of the greater signal-to-noise performance enabled by the enhancement that occurs when the IR beam makes multiple passes through the absorbing medium. Additionally, the use of the MIT geometry allows the possibility of performing polarization-dependent measurements that allow the orientation of the dipole associated with the observed modes to be determined. In the following discussion, the observed vibrational modes are related to specific positions of hydrogen in the InP lattice. This information is used to guide the discussion and interpretation of the measurements with the vibrational data already present in the literature.

In the MIT-FTIR configuration light is introduced through one bevel at the end of the prism sample and makes approximately 80 passes through the sample prior to exiting the opposite bevel and being directed to the detector. As a consequence of being a multi-pass experiment, MIT-mode measurements are more sensitive than single-pass transmission measurements, making it easier to resolve weak spectral features. As was described in §4.1.2 the geometry is denoted MIT, because the incident light is able, in each reflection, to pass through the implanted region of interest. In the case when the refractive index of the implanted region is significantly lower than that of the surrounding InP due to the formation of voids, extended defects, or micro-cracks, the IR beam arrives at the interface between this layer and the bulk InP at an angle greater than the critical angle for reflection from this interface. However, because the implanted region is much thinner than the wavelength of the radiation of interest, the IR light is able to evanescently tunnel

through the interface causing enhancement of absorption in z-axis oriented dipoles, as is described by Chabal.⁴ Additionally, by polarizing the IR beam prior to entry into the MIT prism, it is possible to deduce the dipole orientation of the observed modes, assisting in the interpretation of the spectra. However, when the implanted species are within a few wavelengths from the external surfaces, interference leads to strong intensity modulation of the polarization modes as a function of distance from the external surface of the prism. It is therefore possible in some cases to determine spatial information from the spectra. Specifically, the light intensity of each polarization is proportional to the square of the field components and is expressed as follows.

$$\left| \overline{E}_s \right|^2 = 4E_o^2 \left| \overline{e}_y \left\{ \exp \left[ik_z \cdot z + \Delta\psi + \exp(ik_z \cdot z) \right] \right\} \right|^2 \quad (4.7)$$

Thus,

$$\left| \overline{E}_s \right|^2 = 4E_o^2 \left| \sin \theta \cos \left(k_z \cdot z + \frac{\Delta\psi}{2} \right) \right|^2 \quad (4.8)$$

Where, E_o is the magnitude of the electric field vector in the incident radiation, and $k_z \cdot z$ is the z-direction component of the light propagation vector. The intensity of the z-direction component of the \bar{p} -polarized radiation is given by

$$\left| \overline{E}_p \right|^2 = 4E_o^2 \left| \overline{e}_x \left[\exp(ik_z \cdot z + \Delta\psi) + \exp(ik_z \cdot z) \right] + \overline{e}_z \left[\exp(ik_z \cdot z + \psi_p) + \exp(ik_z \cdot z) \right] \right|^2 \quad (4.9)$$

Thus,

$$\left| \overline{E}_p \right|^2 = E_o^2 \left| \sin \theta \cos \left(k_z \cdot z + \frac{\Delta\psi}{2} \right) \right|^2 + E_o^2 \left| \cos \theta \cos \left(k_z \cdot z + \frac{\Delta\psi}{2} \right) \right|^2 \quad (4.10)$$

In equations 4.4 and 4.6 the term $\Delta\psi/2$ is determined related to the phase shift of the reflected light at the outer surface due to the presence of the evanescent field protruding from the air-semiconductor interface at the outer edge of the substrate.

$$\frac{\Delta\psi}{2} = \frac{\pi}{2} - \frac{\psi_p}{2} \quad (4.11)$$

$$\frac{\psi_p}{2} = -\arctan\left(\frac{n^2\sqrt{n^2\sin^2\theta-1}}{n\cos\theta}\right) \quad (4.12)$$

Where, n is the refractive index of the semiconductor under consideration, and θ is the angle of incidence of the radiation relative to the outer surface.

The convention used for the polarization is schematically illustrated in Fig. 4.1b. In Fig. 4.25, the field intensities of the x-, y- and z-components of \vec{p} - and \vec{s} -polarized light are plotted as a function of the distance to the interface with closest outer surface of the prism. The hydrogen distribution in InP after implantation, for the implant conditions used is also shown. The peak of the H-distribution occurs where the z-component of the \vec{p} -polarized light is extinguished. As a consequence, the sensitivity to symmetric (100) P-H modes in the peak of the hydrogen

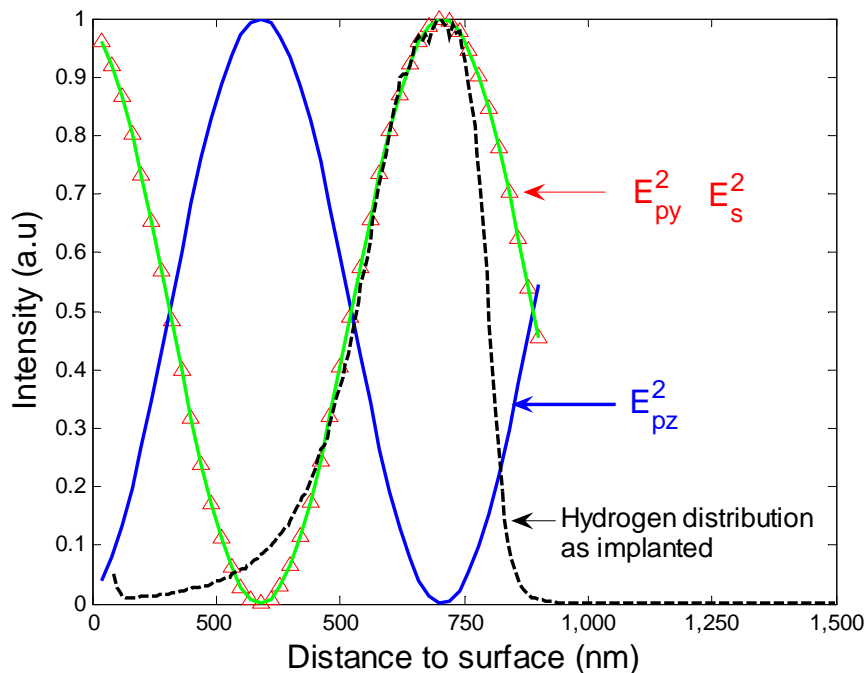


Figure 4.25 The interference effects of local field intensities for MIT-mode FTIR spectroscopy measured near the outer surface of the InP prism. The intensities shown are qualitative in nature, as they do not incorporate the predicted effect of evanescent enhancement for absorption in the buried layer.

implantation, where exfoliation occurs is zero. Interestingly, at that position the y-component of \vec{p} -polarized light and \vec{s} -polarized light are approximately equally in intensity with only minor changes in the absorption intensity due to evanescent enhancement in the lower index implanted region. Therefore, if all bound hydrogen is located at a depth of 700 nm, the \vec{s} - and \vec{p} -polarized peak intensities should be equal. For positions closer to the external surface, the z-component of the \vec{p} -polarized light increases, while the x- and y-components of the \vec{p} - and \vec{s} -polarized light, respectively, decrease. As a consequence, the spatial dependency of the field intensity can be used as a *spatial probe* for hydrogen.

Before entering into detail on the consequences of the extinguished z-component at the H-concentration peak, the origin of the peaks observed in the 2100 to 2300 cm^{-1} region as measured by MIT-FTIR is discussed. Figs. 4.26 and 4.27 show the \vec{s} - and \vec{p} -polarized absorbance spectra, respectively, of H-implanted InP after successive 10 minute isochronal annealing at temperatures of 172, 294, and 352°C. The samples were not annealed to higher temperatures required for exfoliation due to limitations in the furnace.

In comparison to the single-pass transmission-mode measurements, the MIT-mode spectra are more sensitive to defects present in small concentration. For instance, MIT-mode measurements reveal that two new absorption peaks appear at 2060 and 2250 cm^{-1} . The peak at 2250 cm^{-1} shifts to 2258 cm^{-1} upon annealing. While the mode at 2060 cm^{-1} was not observed in transmission-mode measurements presented in §4.2.2.1 due to the inferior sensitivity of single-pass transmission-mode measurements, the mode present at 2250 and 2258 cm^{-1} was not detected because it was obscured by two adjacent peaks. After implantation, all of the modes except the modes at 2060 cm^{-1} and 2198 cm^{-1} mode exhibit slightly enhanced absorbance in \vec{p} -polarization. Despite the identification of a mode at 2050 cm^{-1} in previous studies associated with the P-H stretch of a H-passivated (111) surface²⁴, the disappearance of the mode at 2060 cm^{-1} between 172 and 294°C indicates that it is a LVM associated with a discrete hydrogenated defect or

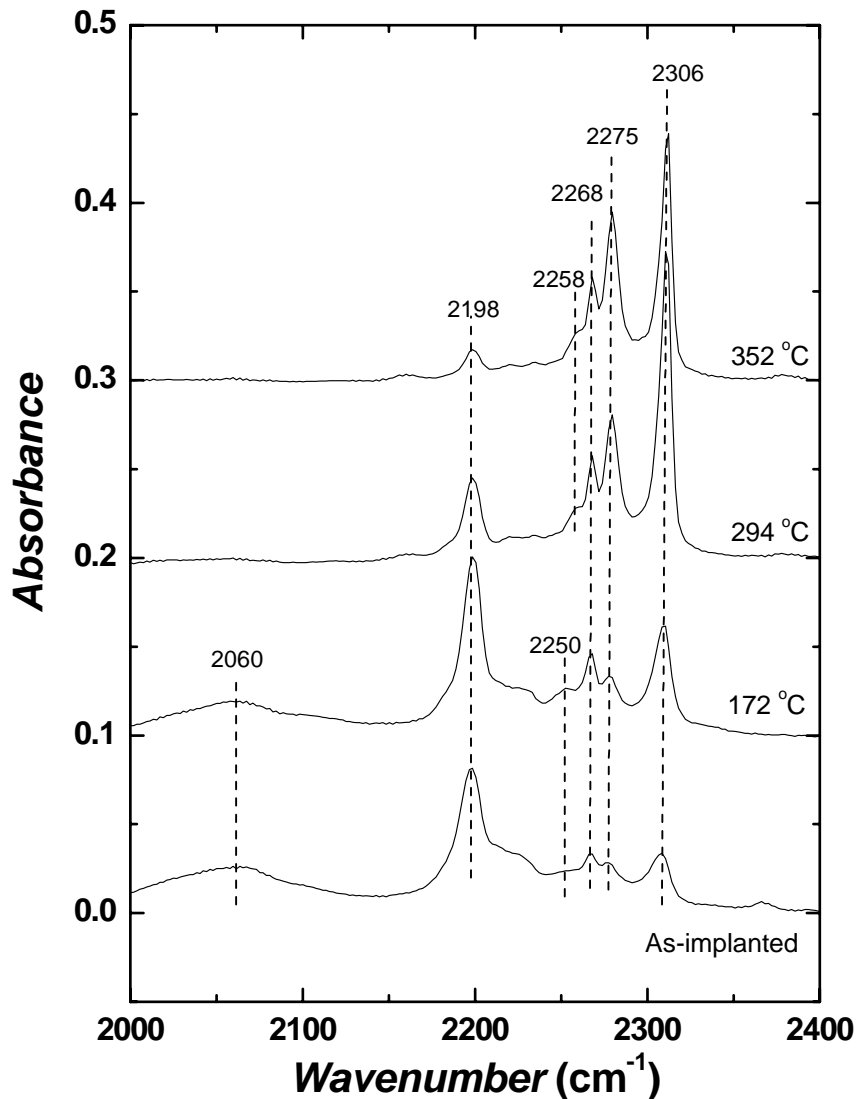


Figure 4.26 The temperature-dependent evolution of \bar{s} -polarized MIT-mode FTIR spectra showing the growth of higher wavenumber modes associated with extended defects upon annealing.

distribution of related discrete defects having similar chemical structure, such as vacancy-hydrogen or hydrogenated interstitial defects. This explanation is consistent with the fact that this mode was never observed in works where H-passivated surfaces were studied. The 2198 cm^{-1} mode is very close to the LVM at 2206 cm^{-1} measured by Fischer *et al.*²⁵⁻²⁷ and in perfect agreement with the mode measured by Riede *et al.*²⁸ In both references, this mode is attributed to P-H vibrations of a hydrogen atom localized in a cation vacancy.

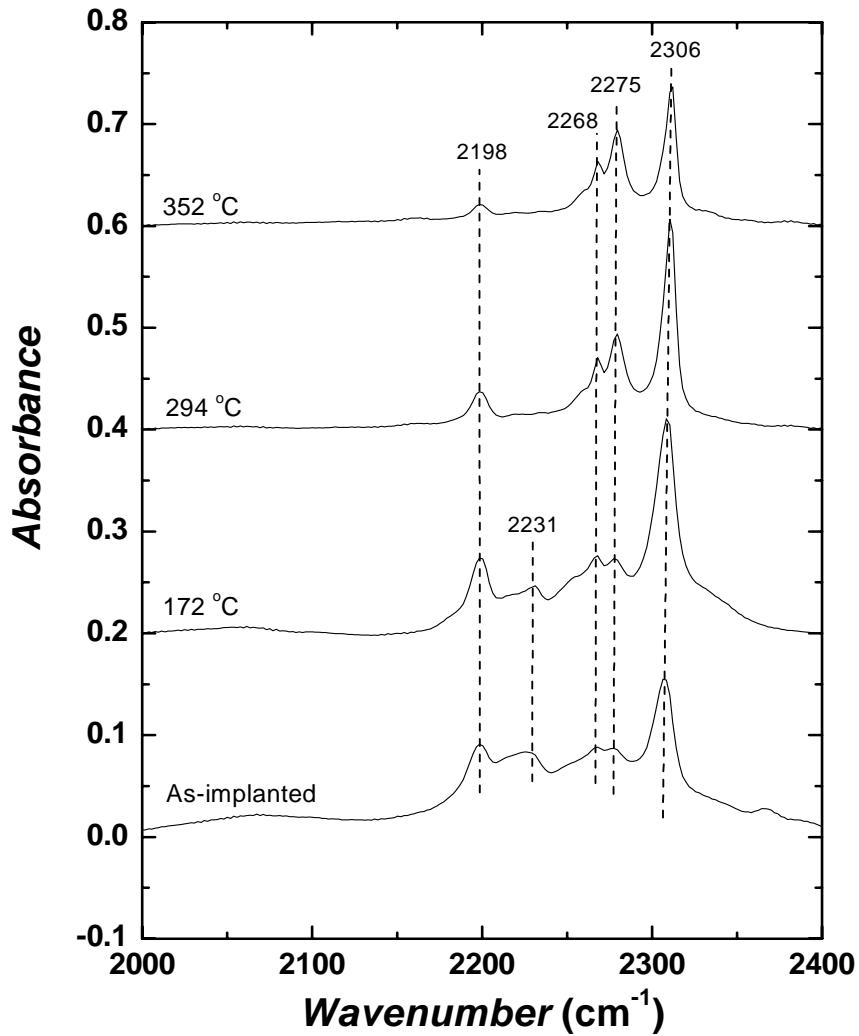


Figure 4.27 The temperature-dependent evolution of \bar{p} -polarized MIT-mode FTIR spectra showing the growth of higher wavenumber modes associated with extended defects upon annealing.

The modes at 2217 and 2227 cm⁻¹ correspond to the stretch modes of H-decorated In vacancies, denoted $V_{In}H_4$.²⁹ In this configuration, the four hydrogen atoms form a tetrahedron and the vibrational dipole is oriented along the $\langle 111 \rangle$ direction. Such vacancies are randomly distributed in depth and are located in the region above the implant end of range where the z-component of \bar{p} -polarized light is roughly three times as intense as the x-component of \bar{s} -polarized light and the y-component of \bar{p} -polarized light. This conclusion is supported by the

observation that the mode at 2198 cm^{-1} has a higher intensity in the \bar{p} -polarized spectra. The mode at 2198 cm^{-1} almost entirely disappears at 294°C , with a small peak present in the \bar{p} -polarized spectrum.

The mode at 2268 cm^{-1} is close to the frequency of 2265 cm^{-1} attributed in previous work to symmetric stretch modes of H-terminated (100) P-terminated surfaces with a 2×1 reconstruction.²² The mode corresponds to hydrogen passivated P dimers formed by bonding two adjacent surface atoms.

The mode at 2306 cm^{-1} has been theoretically predicted to be the symmetric stretching vibration of a P-H₂ complex. The anti-symmetric pair is predicted to be found at 2332 cm^{-1} with lower intensity than the symmetric mode and is not detected in our measurements. Such di-hydride complexes could be found both in cation multi-vacancies and at internal surfaces.^{30,31} This di-hydride dipole is predicted to be isotropic ally oriented, with equal contributions along all axes (x,y,z), because it is not located on a particular surface. Therefore, we can use relative polarization intensities to get spatial information. For instance, in the as-implanted spectra, the \bar{p} -polarized peak is about four times stronger than the \bar{s} -polarized peak. The difference in the absorbance between the \bar{s} - and \bar{p} -polarized spectra can be explained by the superposition of the incident and reflected light at distances close to the surface. At the implant conditions we have chosen for this study, the maximum hydrogen concentration is located at a distance to the surface corresponding to a position where the z-component of the electric field is zero and therefore \bar{p} - and \bar{s} -polarized spectra should have x- and y-component electric fields, respectively, that are of equal intensities. As indicated in Fig. 4.25, for distances closer to the external surface, the field intensity of the \bar{s} -polarized spectrum becomes weaker in comparison to the field intensity of the \bar{p} -polarized spectrum. Given the difference between the \bar{p} - and \bar{s} -polarized spectra present in the 50°C sample, it is indicated that the majority of the H-passivated vacancies are located in the regions located closer to the surface than the peak of the distribution. As the annealing proceeds,

the intensity differences between the two polarizations become less apparent, and at 352 °C they are nearly equivalent. The intensity of the peak at 2308 cm⁻¹ increases with annealing up to 294 °C, where it reaches a maximum. The simultaneous increase of the higher wavenumber LVM's and decrease of the lower wavenumber LVM's along with the equilibration of the \bar{p} - and \bar{s} - polarized spectra, suggests that the release of bonded hydrogen in regions between the hydrogen peak concentration and the outer surface is due to point defect annealing. This released hydrogen partially captured at the free internal surfaces of voids and/or extended defect structures is located at the peak of the H-implant distribution. Indeed, other studies have shown that the formation of clusters of cation vacancies including di-vacancies can be expected at sufficiently high H-implantation doses. Of these defects, the larger defects are predominantly formed in regions of the implanted layer with high damage densities close to the damage peak.³² The grouping of hydrogen into the internal surfaces at the peak of the distribution is analogous to a self-gettering process, and it is responsible for the collection of H₂ gas that provides internal pressure and leads to blister formation and exfoliation of InP films upon annealing.

4.2.4 Conclusions

FTIR measurements of H-implanted InP have been carried out to investigate the H-induced exfoliation processes in InP. As-implanted, the hydrogen is distributed in isolated discrete defects and extended defects with uncompensated dangling bonds. FTIR spectra provide insight into the predominant types of defects and consequently into the environments of bonded hydrogen in H-implanted InP. Additionally, polarized MIT-mode spectra shed light on the distribution of defects within the implanted region. The simultaneous occurrence of an increase of absorption in higher wavenumber local modes, attributed to agglomerated H-passivated defects, and of a decrease of absorption in lower wavenumber local modes, attributed to hydrogen bonded in isolated vacancies, suggests that the release of bonded hydrogen due to point defect annealing is accompanied by its capture at the free internal surfaces of extended defects. Polarization-

dependent MIT-mode spectra suggest that the desorbed atomic hydrogen from single vacancies distributed toward the outer surface of the InP substrate during annealing diffuses to internal surfaces and cavities located at the peak of the distribution. At higher temperature, there is a decrease of absorption in the highest frequency modes that is attributed to rearrangement processes that lead to trapping and buildup of H₂ molecules and their associated pressure just prior to exfoliation.

4.3 *Summary*

The role of hydrogen in the H-induced exfoliation process has been studied by application of TEM and AFM to the study of the morphology of micro-cracks that lead to the exfoliation of Ge and InP. The defect microstructure studied by XTEM shows surprising differences between the exfoliation process in Ge and InP. In Ge the implantation of a large dose of hydrogen leads to a dense defect network of platelet structures that are shown to define the cleavage plane upon annealing. In InP the same dose does not lead to the formation of clearly observed defects that are oriented along the (100) plane, but rather the H-implantation process leads to accumulation of a large amount of damage at the end of range for the implant. However, this damage does not exhibit a dominant defect structure. This difference is attributed to the fundamental difference between damage accumulation mechanisms in a pure group IV semiconductor relative to a III-V compound semiconductor.

The evolution of infrared spectra upon annealing has been used to deduce the chemical states of hydrogen in H-implanted Ge and InP that lead to the exfoliation process. The use of MIT-mode FTIR spectroscopy with polarization was used to determine the dipole orientation of defects that lead to exfoliation. This was particularly effective in the case of Ge, in which it was shown that point defects caused during implantation serve as binding sites for hydrogen during implantation and at low temperatures, but release that hydrogen upon annealing. This hydrogen then diffuses to agglomerated defect structures that trap hydrogen, either by further growth of the

defect structure or as molecular H₂ gas that then provides internal pressure required to separate internal surfaces and form micro-cracks that precede exfoliation. TEM images and comparison to previous studies of the H-induced exfoliation of Si suggest that these agglomerated defect structures that lead to micro-cracks are oriented along (100) platelet structures.

The evolution of transmission-mode FTIR spectra upon annealing in H-implanted InP show that In-H stretching modes at 1600 and 1705 cm⁻¹ are stable upon annealing. This suggests that the preferential formation of vacancies in the anion sublattice during implantation makes the H-induced exfoliation process more challenging in InP due to gettering of hydrogen at these sites from which it is not released to facilitate the exfoliation process in InP. The evolution of P-H stretching modes upon annealing suggests that hydrogen is released from discrete defects and then diffuses to extended defect structures attributed to higher wavenumber stretching modes where it facilitates the exfoliation process by providing internal pressure and passivating hydrogen necessary to enlarge these defects. The use of polarized MIT-mode spectroscopy suggests that the discrete defect distribution is skewed toward the implanted surface of the InP substrate, and the extended defects that lead to exfoliation are found at the end of range, as indicated by XTEM micrographs.

4.4 References

- ¹ M. Weldon, V. Marsico, Y. Chabal, A. Agarwal, D. Eaglesham, J. Sapjeta, W. Brown, D. Jacobson, Y. Caudano, S. Christman, and E. Chaban, *Journal of Vacuum Science and Technology B* **15**, 1065-1073 (1997).
- ² M. Weldon, M. Collot, Y. Chabal, V. Venezia, A. Agarwal, T. Haynes, D. Eaglesham, S. Christman, and E. Chaban, *Applied Physics Letters* **73**, 3721-3723 (1998).
- ³ www.ioffe.ru/SVA/NSM/Semicond/.
- ⁴ Y. Chabal, in *Handbook of Vibrational Spectroscopy; Vol. 2*, edited by J. Chalmers and P. Griffiths (John Wiley and Sons, New York, 2001), p. 1117-1123.
- ⁵ www.srim.org.
- ⁶ M. Budde, B. B. Nielsen, R. Jones, J. Goss, and S. Oberg, *Physical Review B* **54**, 5485-5494 (1996).
- ⁷ M. Budde, B. B. Nielsen, P. Leary, J. Goss, R. Jones, P. Briddon, S. Oberg, and S. Breuer, *Physical Review B* **57**, 4397-4412 (1998).
- ⁸ M. Budde, B. B. Nielsen, J. Keay, and L. Feldman, *Physica B* **273-274**, 208-211 (1999).
- ⁹ S. Myers, H. Stein, and D. Follstaedt, *Physical Review B* **51**, 9742-9751 (1995).
- ¹⁰ Y. Chabal, *Surface Science* **168**, 594-608 (1986).
- ¹¹ J. Crowell and G. Lu, *Journal of Electron Spectroscopy and Related Phenomena* **54/55**, 1045-1057 (1990).
- ¹² Y. J. Chabal, (Personal communication, 2004).

- 13 M. Weldon, V. Marsico, Y. Chabal, D. Hammann, S. Christman, and E. Chaban, *Surface Science* **368**, 163-178 (1996).
- 14 L.-J. Huang, Q.-Y. Tong, Y.-L. Chao, T.-H. Lee, T. Martini, and U. Gosele, *Applied Physics Letters* **74**, 982-984 (1999).
- 15 C. G. Van de Walle and J. Neugebauer, *Nature* **423**, 626-628 (2003).
- 16 S. Hayashi, M. S. Goorsky, R. Sandhu, and M. Wojtowicz, in *Processing issues for wafer bonded III-V on insulator structures*, Kagoshima, Japan, 2004.
- 17 A. Fontcuberta i Morral, J. M. Zahler, H. A. Atwater, M. M. Frank, Y. J. Chabal, P. Ahrenkiel, and M. W. Wanlass, in *Electrical and structural characterization of the interface of wafer bonded InP/Si*, San Francisco, 2003.
- 18 I. Radu, I. Szafraniak, R. Scholz, M. Alexe, and U. Gosele, *Journal of Applied Physics* **94**, 7820-7825 (2003).
- 19 S. Nannarone and M. Pedio, *Surface Science Reports* **51**, 1-149 (2003).
- 20 L. Li, B.-K. Han, Q. Fu, and R. F. Hicks, *Physical Review Letters* **82**, 1879-1882 (1999).
- 21 O. Pluchery, J. Eng, R. L. Opila, and Y. Chabal, *Surface Science* **502-502**, 75-80 (2002).
- 22 K. Raghavachari, Q. Fu, G. Chen, L. Li, C. H. Li, D. C. Law, and R. F. Hicks, *Journal of the American Chemical Society* **124**, 15119-15124 (2002).
- 23 V. Swaminathan and A. T. Macrancer, *Material Aspects of GaAs and InP Based Structures* (Prentice Hall, Englewood Cliffs, NJ, 1991).
- 24 M. D. McCluskey and E. E. Haller, *Semiconductors and Semimetals* **61**, 373-440 (1999).
- 25 D. Fischer, M. Manaresh, and G. Matous, *Applied Physics Letters* **63**, 3038-3039 (1993).
- 26 D. Fischer, M. Manaresh, D. Talwar, and G. Matous, *Journal of Applied Physics* **73**, 78-83 (1993).
- 27 D. Fischer, M. Manaresh, and G. Matous, *Semiconductor Science and Technology* **9**, 1-4 (1994).

- ²⁸ V. Riede, H. Sobotta, H. Neumann, C. Ascheron, C. Neelmeijer, and A. Schindler, *Physica Status Solidi A* **116**, K147-K152 (1989).
- ²⁹ D. Fischer, M. Manares, and G. Matous, *Journal of Applied Physics* **71**, 4805-4808 (1992).
- ³⁰ C. Ascheron, *Physica Status Solidi A* **124**, 11-55 (1991).
- ³¹ Q. Fu, E. Negro, G. Chen, D. C. Law, C. H. Li, R. F. Hicks, and K. Raghavachari, *Physical Review B* **65**, 075318 (2002).
- ³² G. Dlubek, C. Ascheron, R. Krause, H. Erhard, and D. Klimm, *Physica Status Solidi A* **106**, 81-88 (1988).

Chapter 5: Electrical Properties of Wafer-Bonded Interfaces

It was pointed out in Chapter 1 that the bonded interface of a Ge/Si or InP/Si replacement substrate for photovoltaics should be electrically conductive with low-resistance to minimize voltage loss in the cell during operation. This technical requirement has been accomplished by bonding heavily doped substrates and annealing the bonded structures. For Ge/Si heavily doped p^+ -Ge/ n^+ -Si and p^+ -Ge/ p^+ -Si wafer-bonded heterojunctions have been shown to exhibit low-resistance ohmic electrical contact. For InP/Si heavily doped n^+ -InP/ p^+ -Si and n^+ -InP/ n^+ -Si wafer-bonded heterojunctions have demonstrated low resistance contact upon annealing. In both material systems and all doping conditions an instrument-limited, specific interfacial resistance of less than $0.16 \Omega \text{ cm}^2$ was observed. Additionally, the effect of bonding parameters – annealing temperature and azimuthal twist angle between the bonded substrates – on interfacial electrical properties has been studied for pGe/ p^+ Si isotype-heterojunctions by observing the evolution of the J - V properties of the bonded structures. The observed J - V behavior of these structures, along with FTIR characterization of the evolution of the chemical state of the bonded interface, provide a compelling picture of the structure and electrical activity of the wafer-bonded Ge/Si interface. These measurements indicate that in as-bonded hydrophobically wafer bonded samples, the surface passivation layer at the bonded interface leads to a large potential barrier of 0.65 eV that features slow electronic trap states. Upon annealing FTIR spectroscopy suggests that this interfacial passivation layer is desorbed and subsequent J - V behavior indicates a twist-angle and

anneal-time dependent barrier height between 0.47 and 0.54 eV. Additionally, a leakage path modeled by a shunt resistance indicates that as azimuthal twist angle between the bonded substrates increases, the number of leakage paths also increases. This is in agreement with the expected change in the number of twist interfacial dislocations predicted by theory.

5.1 Electrical Properties of Heavily-Doped Wafer-Bonded Interfaces

From the perspective of the motivating technological application – alternative substrates for existing photovoltaic devices and novel wafer-bonding enabled photovoltaic devices – demonstration of low-resistance bonded interfaces is an essential step toward the implementation of these structures. For instance, in a one sun AM1.5 triple-junction solar cell, the current density is on the order of 15 mA cm^{-2} . Thus, considering Ohm's Law, a $0.10 \text{ } \Omega \text{ cm}^2$ resistance leads to a loss of 1.5 mV. This is suitable for this condition, but taking that same interface and implementing it in a 100 sun concentration system leads to a loss of 0.15 V at the bonded interface. This represents a relative efficiency loss of $\sim 7.5\%$ relative to triple-junction solar cells fabricated on bulk Ge substrates.

5.1.1 Schemes for Enabling Low-Resistance Bonded Interfaces

When attempting to establish ohmic, low-resistance electrical conductivity through wafer-bonded interfaces, there are two primary design considerations – the nature of the bond formed and the doping of the materials near the wafer-bonded interface.

First, the type of bond is important. There are several schemes for ensuring that the bond itself does not provide significant electrical resistance. For instance, the use of a metallic bonding layer ensures ohmic electrical contact, provided that the metal is chosen to have close Fermi level alignment with the substrates on either side of the bonded interface. Additionally, as was described in Chapter 3, the use of hydrophobic wafer bonding has been shown to enable direct,

covalent bonding at the bonded interface between two Si substrates.^{1,2} This property of hydrophobic wafer bonding has been shown to extend to other materials as well, such as InP/GaAs^{3,4} and InP/Si.^{5,6} This is the approach that is pursued in the present work for both Ge/Si and InP/Si.

Of equal importance is the doping of the semiconductors near the bonded interface. In general, it is desirable to have a heavily-doped bonded interface to enable tunnel-junction contact. Tunnel-junctions are the general method for ensuring low resistance at epitaxially fabricated heterojunctions, such as those used to separate the subcells in conventional triple-junction solar cells. In general the term tunnel-junction refers to p-n junctions with degenerately doped material on either side of the junction. This ensures that the junction is narrow enough to tunnel through. Furthermore, under reverse bias, the energy level of valence states of the p-type material and the conduction states of the n-type material overlap. Thus, there are available states for the tunneling of holes from the p-type material into the n-type material. Under forward bias, the valence and conduction states overlap in energy under low bias, but this overlap is lost under larger forward bias. Thus, tunneling only occurs up to a cutoff bias. At that point typical forward-biased diode behavior is followed, leading to the observation of a current valley under forward bias.

Tunnel-junctions are essential in multi-junction solar cells, because they serve as a means of switching the material type without incurring significant power loss. However, low-resistance electrical contact can also be made at heavily-doped isotype heterojunctions. In these structures conduction is predominantly by the majority carrier, and conduction occurs by tunneling through and thermionic emission over the barrier created by the band offset at heterojunctions.

Isotype and p-n heterojunctions are illustrated using the fundamental model of ideal heterojunction band alignment for Ge and Si in Figs. 2.1 and 2.2, respectively. In an ideal heterojunction the conduction band offset is equivalent to the difference between the electron affinities of the two materials.^{7,8} Thus,

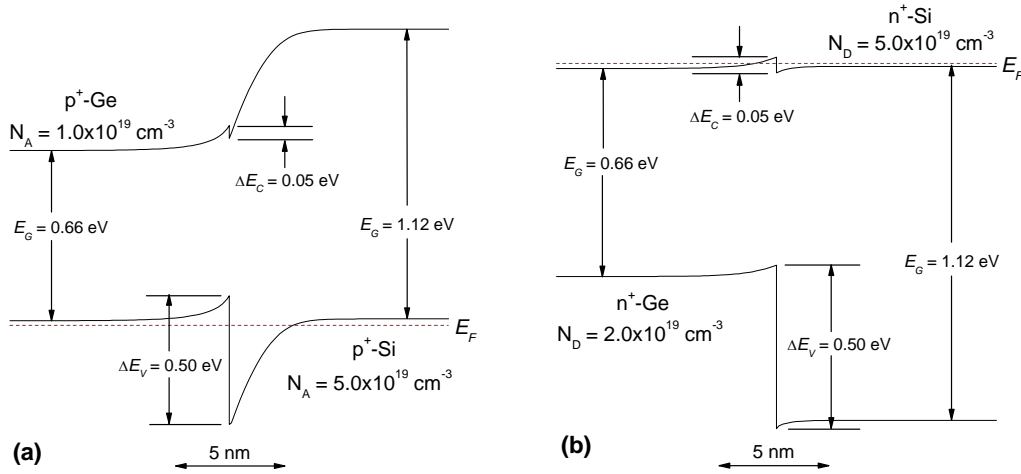


Figure 5.1 Band energy diagrams for Ge/Si isotype heterostructures suitable for tunneling between degenerately doped Ge and Si substrates based upon the ideal heterojunction band offsets showing the anticipated band diagram of (a) p⁺-Ge/p⁺-Si and (b) n⁺-Ge/n⁺-Si structures.

$$\Delta E_C = (E_C)_2 - (E_C)_1 = \chi_2 - \chi_1 = \Delta\chi \quad (5.1)$$

$$\Delta E_V = \Delta E_G + \Delta\chi \quad (5.2)$$

In the case of Ge and Si the electron affinities are 4.00 and 4.05 eV, respectively, resulting in $\Delta E_C = 0.05\text{eV}$ and $\Delta E_V = 0.50\text{eV}$.⁹ In the figures, the interface between degenerately doped semiconductors is modeled using the software package PC1D.¹⁰ Although this model of heterojunction alignment is only an approximation, it is still instructive in selecting the doping configuration most likely to yield a low-resistance bonded heterojunction. From Fig. 2.1 it is clear that the conduction band offset, and thus the barrier height, for n-n isotype heterostructures is much lower than that for p-p isotype heterostructures. For this reason, it is desirable to pursue this contact type. In Fig. 2.2 there is no obvious distinction between n-p and p-n heterojunctions. However, it should be noted that the defect states and potential contamination of wafer-bonded heterostructures can be expected to impact their electrical properties. For this reason, it may be desirable to switch doping types at epitaxially grown tunnel-junction structures and use isotype wafer-bonded heterostructures to make electrical contact at wafer bonded interfaces.

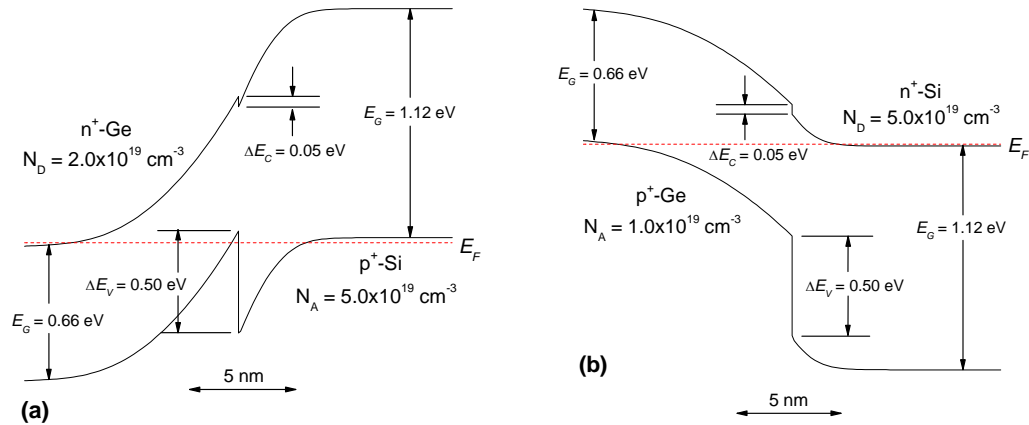


Figure 5.2 Band energy diagrams for Ge/Si heterostructures suitable for tunneling between degenerately doped Ge and Si substrates based upon the ideal heterojunction band offsets showing the anticipated band diagram of (a) n^+ -Ge/ p^+ -Si and (b) p^+ -Ge/ n^+ -Si structures.

In the subsequent sections, the measured resistance of heavily doped p-n and isotype heterojunctions will be discussed for Ge/Si and InP/Si wafer-bonded heterostructures.

5.1.2 Heavily Doped Ge/Si Wafer-Bonded Heterostructures

5.1.2.1 Experimental Procedure

As was described in the previous section, low-resistance contact can be ensured by hydrophobically bonding heavily doped semiconductors. To test this, p^+ -Ge/ p^+ -Si and p^+ -Ge/ n^+ -Si wafer-bonded heterostructures were fabricated by bonding $\sim 1.6 \text{ cm}^2$ samples of (100) p^+ -Ge (Ga-doped to $1 \times 10^{18} \text{ cm}^{-3}$), (100) p^+ -Si (B-doped to $3 \times 10^{18} \text{ cm}^{-3}$), and (100) n^+ -Si (P-doped to $3 \times 10^{19} \text{ cm}^{-3}$) using the following hydrophobic wafer bonding process. First, samples were cleaved in an acetone bath to reduce particle contamination generated during the cleaving process. The samples were subsequently cleaned by ultrasonic acetone and methanol baths consecutively for 10 min each to remove organic and particulate contamination, and followed by a one minute DI rinse. Ge samples were finally dipped in 1% HF solution for 1 min to remove any remaining chemical oxide and render the surface hydrophobic. Si samples were further cleaned in 80 °C 1:1:5 $\text{H}_2\text{O}_2:\text{NH}_4\text{OH}:\text{H}_2\text{O}$ (RCA1) solution for 10 min to remove organic surface contamination

and particles. Finally, the Si samples were dipped in a 1% HF solution for 4 min to remove a thermally grown oxide on the Si surface and to render the surface hydrophobic. After this cleaning process, both Si and Ge surfaces had a surface micro-roughness less than 0.5 nm-rms, as measured by contact mode atomic force microscopy (AFM). Following the cleaning processes, Ge and Si samples were brought into contact at room temperature with a controlled azimuthal twist angle using a modified goniometer system shown in Fig. 5.3. Bonding was initiated by ~20 MPa pressure applied over a 0.6 cm diameter region at the center of the sample. For current-voltage measurements, large area Al contacts were evaporated on the entire front and back surfaces of the wafer bonded sample. To observe the anneal time and temperature dependence of the I - V characteristics of the Ge/Si bonded interface, test samples were annealed at 400°C in N₂ furnace with varying annealing times prior to Al depositions. J - V characteristics were measured in a dark ambient in the apparatus shown in Fig. 5.4.

5.1.2.2 Results and Analysis

Representative J - V curves are shown in Fig. 5.5. These curves are relatively featureless, showing only that the specific resistance of less than 0.16 Ω cm² is achievable for both p⁺-Ge/p⁺-Si and p⁺-Ge/n⁺-Si heterostructures. Many conditions were tested by varying the anneal time and temperature as well as the azimuthal twist angle between the bonded substrates. The J - V behavior observed for all bonded samples is essentially indistinguishable with a resistance that appears to be dominated by the probe-tip to Al contact pad resistance, rather than the bonded interface resistance.

5.1.2.3 Discussion

The expected ideal heterojunction band diagrams for both p⁺-Ge/p⁺-Si and p⁺-Ge/n⁺-Si heterostructures are shown in Fig. 5.6. In the p⁺-Ge/p⁺-Si heterostructure there is no anticipated overlap of valence states on opposite sides of the junctions at zero bias. Likewise, in the p⁺-Ge/n⁺-Si heterostructure there is no overlap in the valence states of the Ge and conduction states of the

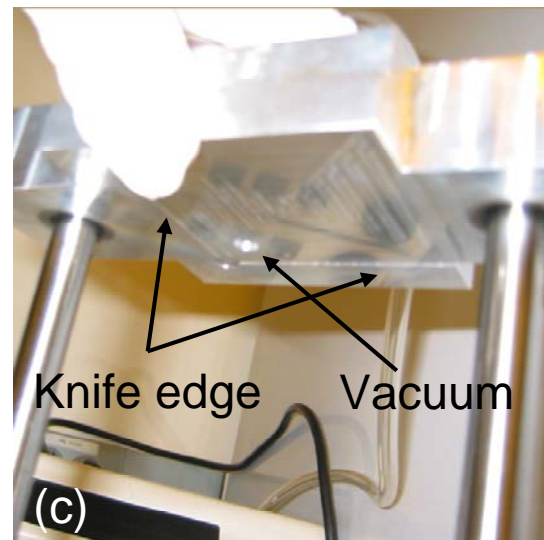
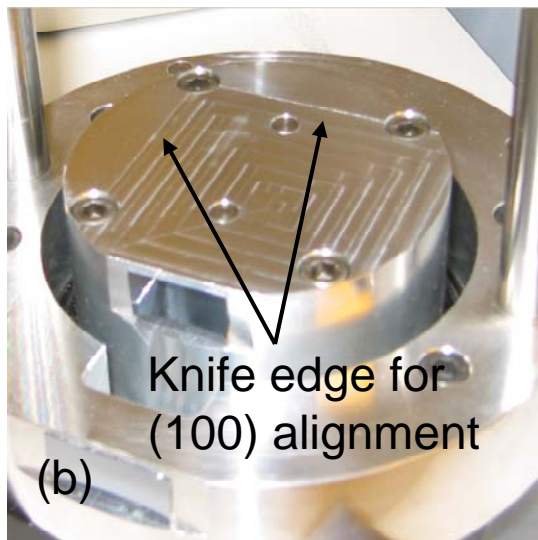
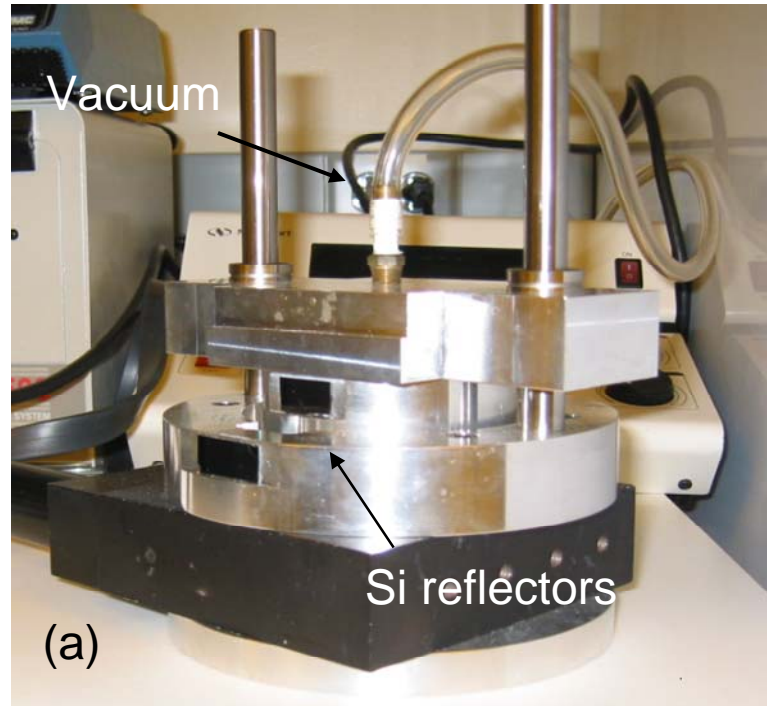


Figure 5.3 Modified goniometer stage used for precision control of the azimuthal twist angle to within $\pm 0.1^\circ$ in bonded samples showing (a) the complete device with reflective surfaces for laser alignment, (b) the rotating stage with knife-edges for {100} alignment, and (c) the top sliding sample holder with vacuum port and knife-edges for {100} alignment.

Si at zero bias. Thus, one would anticipate that, under small reverse-bias, current should not exhibit tunneling behavior. Additionally, the relatively thick barriers, especially for the $p^+-\text{Ge}/n^+-\text{Si}$ heterostructure would lead one to expect tunneling to be an inefficient process. Consistent with the interpretation that tunneling directly through the barrier makes a minimal contribution to the

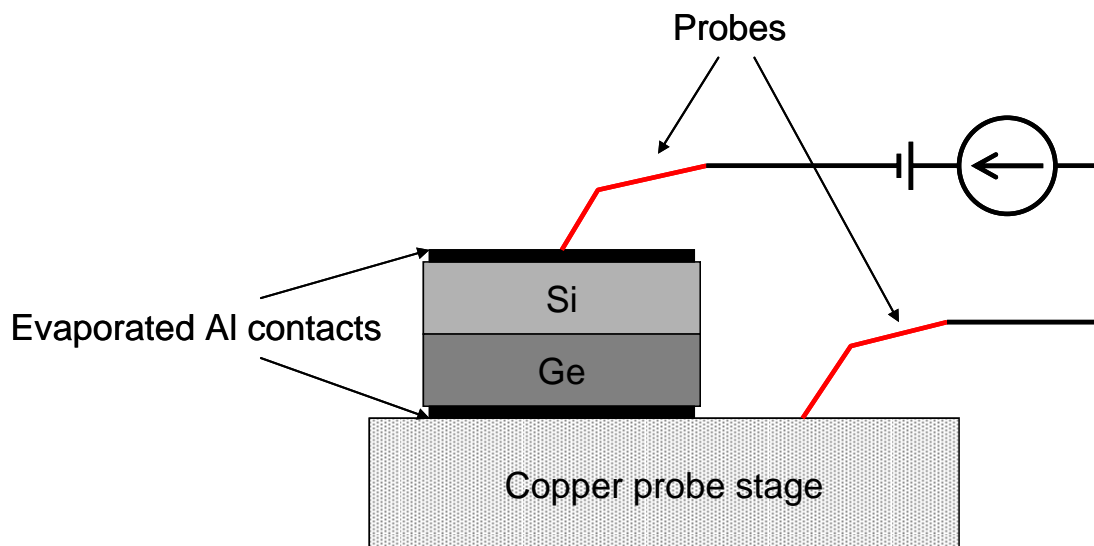


Figure 5.4 Sample measurement configuration for measuring the current-voltage behavior of a wafer bonded structure.

observed J - V behavior is the lack of a forward-biased current valley. This observation has important implications for the conduction mechanism through hydrophobically wafer-bonded interfaces. In particular, it is assumed that interface states in the bonded structures play an active role in the conduction mechanism.

The defect structure anticipated at a hydrophobically wafer-bonded interface is a function of the surface passivation of the bonded surfaces, the lattice mismatch of the bonded semiconductors, and the azimuthal twist angle between the bonded interfaces. The chemical passivation obviously impacts the type of defects at the interface and their electrical activity. For instance, for a perfect monolayer of hydride passivation of both the Ge and Si substrates, the electrical activity of the interface should be minimized. However, the observation of easy current conduction, even prior to annealing, suggests that this idealized condition does not exist. In an idealized covalent wafer bonding condition in which no interfacial contamination or passivation exists between the Ge and Si substrates, it is anticipated that an interfacial defect network will arise due to the lattice mismatch. This mismatch is expected to form a network of edge-like dislocations with a dislocation spacing in the [100] direction given by

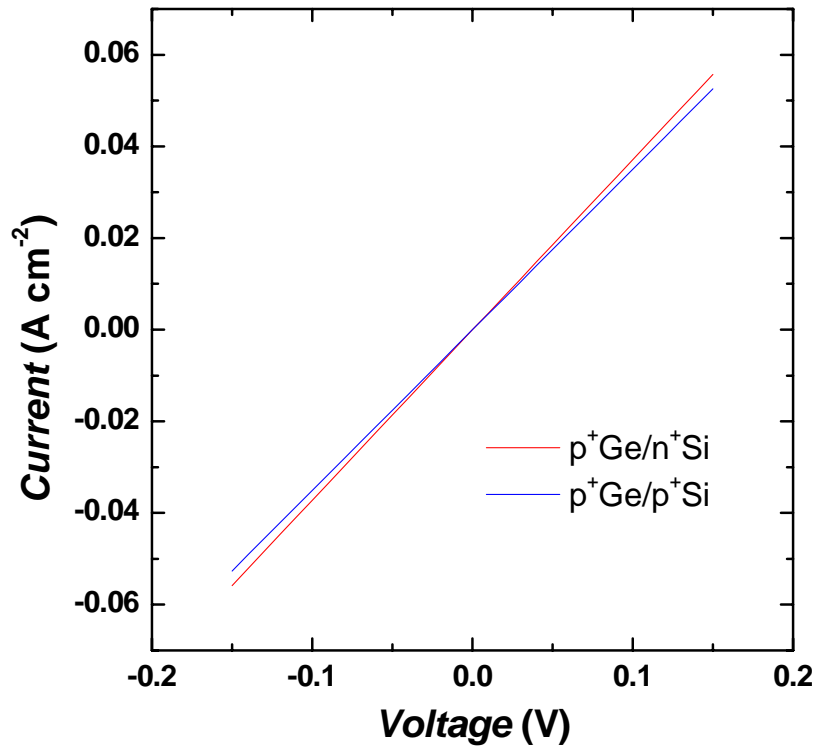


Figure 5.5 Current-voltage measurements of heavily-doped wafer-bonded Ge/Si heterostructures showing ohmic, low-resistance electrical contact.

$$d_{edge} = \frac{|\vec{b}_{edge}| a_{Si}}{\Delta a} \quad (5.3)$$

Where, $|\vec{b}_{edge}|$ is the magnitude of the Burgers vector of the edge dislocations equal to $a_{Si}/2$.

Thus,

$$d_{edge} = \frac{a_{Si}^2}{2\Delta a} = 6.85nm \quad (5.4)$$

In wafer bonded interfaces with an azimuthal twist angle, there is a twist interfacial dislocation network of screw-like dislocations due to the misalignment of the crystallographic structure of the semiconductors on either side of the interface. The spacing between these dislocations in the [110] direction is given by¹¹

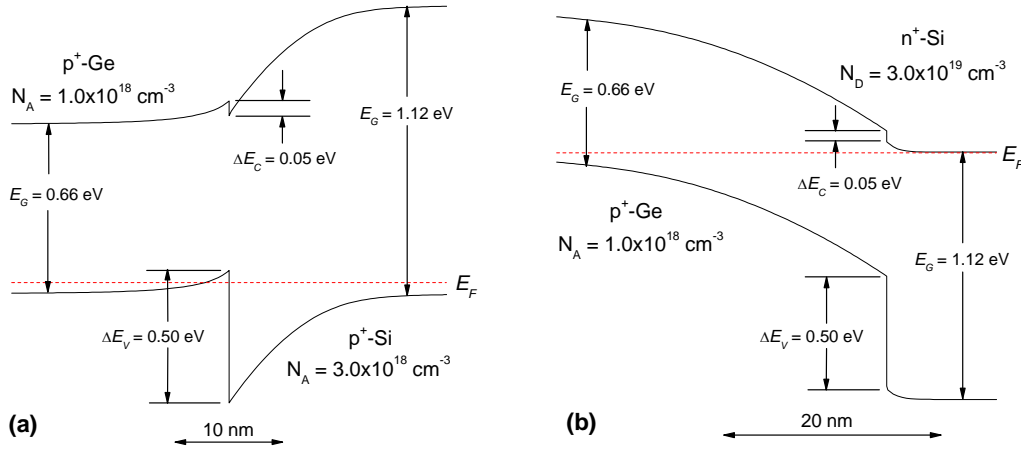


Figure 5.6 Band energy diagrams for Ge/Si wafer bonded heterostructures based upon the Anderson model of heterojunction band offsets using the doping levels described in §5.1.1.2.1 showing the anticipated band structure of (a) p⁺-Ge/p⁺-Si and (b) p⁺-Ge/n⁺-Si.

$$d_{twist} = \frac{|\vec{b}_{twist}|}{2} \csc\left(\frac{\theta_{twist}}{2}\right) \quad (5.5)$$

Where, θ_{twist} is the azimuthal twist angle between the [110] directions of the opposing bonded semiconductors and $|\vec{b}_{twist}|$ is the magnitude of the Burgers vector of the twist dislocations, equal to $a_{Si}\sqrt{2}/2$. Thus,

$$d_{twist} = \frac{a_{Si}\sqrt{2}}{4} \csc\left(\frac{\theta_{twist}}{2}\right) \quad (5.6)$$

The presence of these twist dislocations has been well studied for grain boundaries between hydrophobically wafer-bonded Si/Si substrates.^{12,13}

Clearly for large azimuthal twist angles, a dense network of closely spaced edge and twist interfacial dislocations populate the interface. A third defect type at the bonded interface, called a tilt interfacial dislocation arises due to miscut between the substrates. It is common for Ge substrates for the photovoltaic industry to have an intentional miscut of up to 15° to aid the nucleation of GaAs epitaxy. However, the substrates under consideration are nominally on-axis, and for this reason the density of these edge-like dislocations is expected to be low, relative to the

density of twist interfacial dislocations and misfit dislocations. For this reason tilt interfacial dislocations are neglected in the present analysis.

Based on the data in Fig. 5.5, it can be assumed that the defects arising from interfacial surface species, twist interfacial dislocations and misfit edge dislocations play a critical role in conduction through the bonded interface. This interpretation is solidified in §5.2 where the thermal history and azimuthal twist angle of Ge/Si bonded structures are related to the observed behavior of Schottky-like p^+ -Ge/p-Si wafer bonded structures.

The results in the present section demonstrate two very important technological requirements for use of wafer-bonded replacement substrates in photovoltaic devices. First, ohmic, low-resistance bonded interfaces can be achieved by bonding heavily doped semiconductors. Additionally, to within the resolution of measurement, the twist interfacial dislocation network in substrates bonded with an azimuthal twist angle is not observed to change the electrical properties of the bonded interface. In fact this dislocation network is assumed to facilitate current conduction through the interface. This is important for robust fabrication of bonded structures requiring controlled electrical conductivity through the interface.

5.1.3 Heavily Doped InP/Si Wafer-Bonded Heterostructures

As with Ge/Si replacement substrates for triple-junction solar cells, InP/Si wafer-bonded epitaxial templates require the demonstration of ohmic, low-resistance electrical properties of the bonded samples. However, as is shown below, the formation of ohmic contact at InP/Si wafer-bonded interfaces occurs by a different mechanism than for Ge/Si.

5.1.3.1 Experimental Procedure

n^+ -InP/ n^+ -Si and n^+ -InP/ p^+ -Si wafer-bonded heterostructures were fabricated by bonding samples of (100) n^+ -InP (Zn-doped to $1 \times 10^{17} \text{ cm}^{-3}$), (100) n^+ -Si (P-doped to $3 \times 10^{19} \text{ cm}^{-3}$), and (100) p^+ -Si (B-doped to $3 \times 10^{18} \text{ cm}^{-3}$) using a hydrophobic wafer bonding process similar to the one described in §5.1.2.1. However, for these samples, photoresist was used to protect the surface while

cleaving the InP substrates into smaller samples for wafer bonding. Also, the RCA1 clean step of the Si substrate was omitted and 5% HF was used to hydrophobically passivate both the InP and Si samples. Additionally, the azimuthal twist angle was not actively controlled. As with Ge/Si Al-contacts were evaporated on both surfaces and the J - V properties were measured. The effect of annealing was studied, and as with the Ge/Si samples, the anneal was performed prior to Al deposition.

In addition to measuring the J - V properties of the bonded interface, multiple internal transmission Fourier transform infrared (MIT-FTIR) spectroscopy was used to study the evolution of the chemical state of the bonded interface. In MIT-FTIR spectroscopy, a prism geometry is used to cause the radiation to make many passes through the material, thus enhancing absorption from the bonded interface. For the geometry under consideration, an enhancement of approximately 28 times that expected for a single pass transmission measurement is predicted. Because of the cutoff due to multi-phonon absorption, the stretch modes of the oxide species of Si and InP cannot be observed with MIT-FTIR spectroscopy. For this reason, the evolution of the bonded interface was also observed using conventional transmission-mode FTIR spectroscopy. In both geometries, spectra were collected with a liquid-nitrogen cooled HgCdTe detector. The structure of the bonded interface was also observed with cross-sectional transmission electron microscopy (XTEM).

5.1.3.2 Results and Analysis

5.1.3.2.1 Current-Voltage Data

The J - V behavior of wafer-bonded n^+ -InP/ p^+ -Si heterostructures is shown as a function of anneal time and temperature in Fig. 5.7. This figure shows that a specific resistance of less than $0.16 \Omega \text{ cm}^2$ is reached upon annealing. Once again, the measured specific resistance is thought to be primarily due to the probe-tip to Al-contact-pad resistance. While not shown, similar J - V behavior is observed for n^+ -InP/ n^+ -Si structures. In Fig. 5.7 the non-linear behavior of the J - V behavior prior to annealing to 350°C suggests that the as-bonded interface passivation is different in InP/Si relative to Ge/Si. Specifically, the passivation layer and/or defect states at the interface

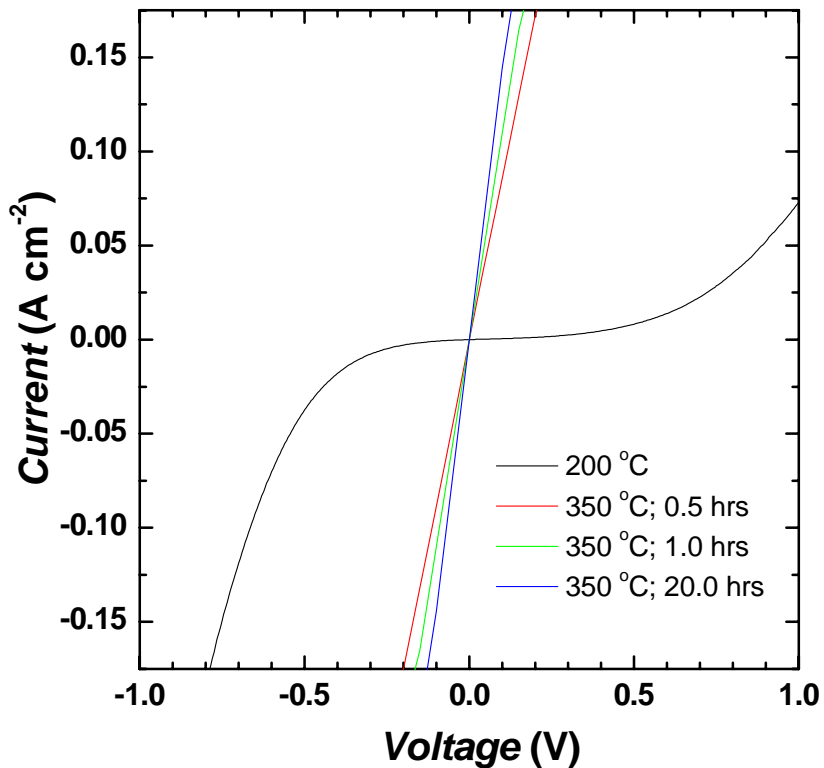


Figure 5.7 Current-voltage measurements of heavily-doped wafer-bonded InP/Si heterostructures showing ohmic, low-resistance electrical contact.

appear to form a potential barrier to current. To investigate the chemical nature of the bonded interface, FTIR spectroscopy and XTEM were employed.

5.1.3.2.2 Infrared Spectroscopy

Figure 5.8(a) shows the MIT-FTIR spectra of a InP/Si hydrophobically wafer-bonded sample. The spectra in this figure show the InP/Si structure referenced to an as-bonded InP/Si prism. Thus, the negative absorbance peaks seen in the spectra indicate a loss of the feature under consideration. The spectra show a loss of adsorbed water at the bonded interface, estimated at between seven and 11 mono-layers of adsorbed water. This result is consistent with previous observations that hydrophobic InP(100) surfaces quickly adsorb water, leading to oxidation.¹⁴

Upon the loss of water at the bonded interface, it is anticipated that an oxide is grown. The transmission mode FTIR spectra shown in Fig. 5.8(b) are referenced to an as-bonded InP-Si reference sample. Thus, the positive absorbance peaks indicate the presence of excess oxides of Si and InP relative to as-bonded samples.¹⁵ The increase upon annealing a second time indicates that these oxides are growing at the same time that MIT-FTIR spectroscopy indicates a loss of adsorbed water from the bonded interface. Based on the observed peak height following the second anneal, it is estimated that 3.5 nm InP-oxide and 0.5 nm Si-oxide are present at the bonded interface.¹⁵

5.1.3.2.3 Transmission Electron Microscopy

The FTIR spectroscopy observations in the previous section are corroborated by studying the bonded interface upon annealing with high-resolution XTEM. In Fig. 5.9 the presence of an amorphous material at the bonded interface is observed. Furthermore, the observed thickness of the bonded interface is approximately 4 nm, the thickness predicted by the absorbance observed in FTIR spectroscopy. However, the lack of z-contrast between the InP-oxide and the Si-oxide regions of this interface prevent the verification of the relative quantities of these oxide species.

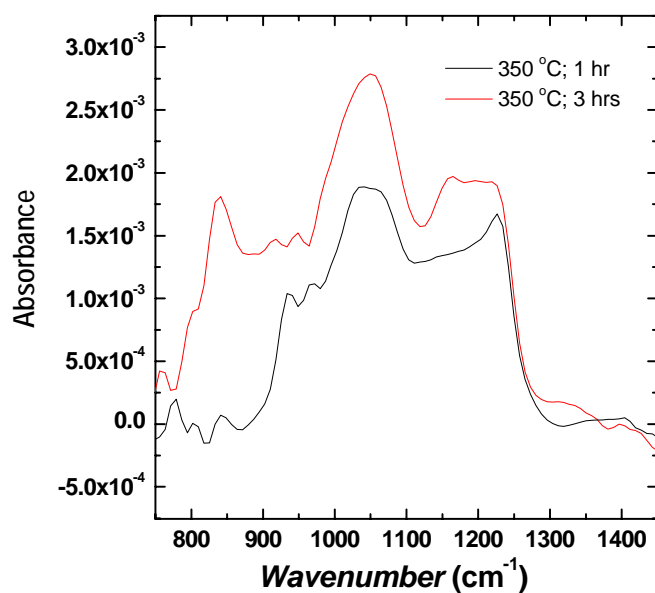
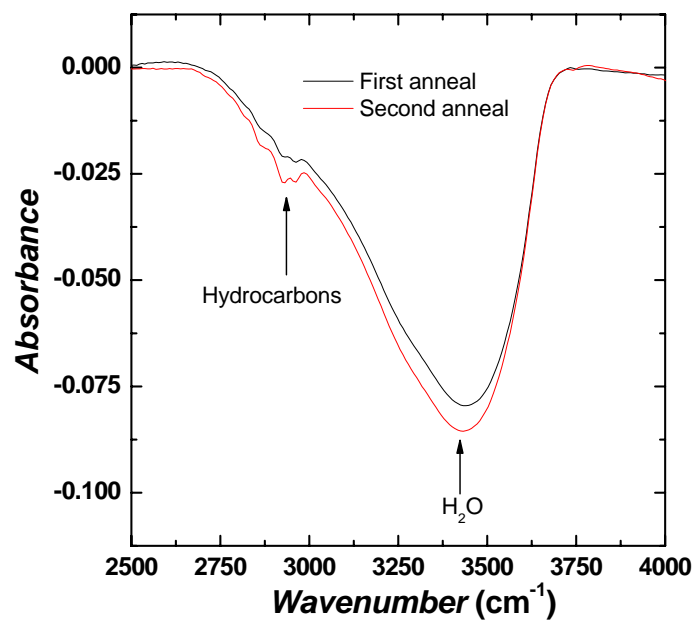


Figure 5.8 MIT-FTIR spectra of hydrophobically-bonded InP/Si heterostructures as a function of anneal time, showing the loss of between seven and 11 monolayers of adsorbed water upon annealing at 350°C.

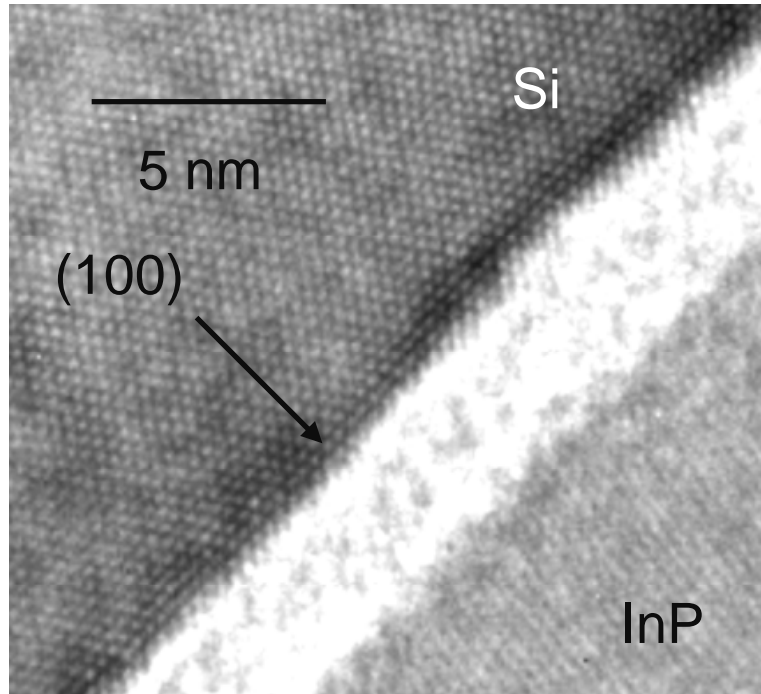


Figure 5.9 Cross-sectional TEM micrograph of an annealed wafer-bonded InP/Si interface showing the presence of a thick amorphous material determined by FTIR spectra to be primarily InPO_x with some SiO_2 present.

5.1.3.3 Discussion

The band diagrams for the n^+ -InP/ n^+ -Si and n^+ -InP/ p^+ -Si wafer-bonded heterostructures under consideration are shown in Fig. 5.10. As before, these diagrams are based upon the ideal heterojunction band alignment based upon the electron affinities of InP and Si. Electron affinities of 4.38 and 4.05 eV were used for InP and Si, respectively. Using these values a 0.56 eV valence band offset and a 0.35 eV conduction band offset are predicted. As with Ge/Si, the InP/Si wafer-bonded heterostructures studied here do not form degenerately doped tunnel junctions. However, the observed J - V behavior clearly indicates linear behavior to within the resolution of the measurement following an anneal to 350°C. The non-ohmic J - V behavior for InP/Si structures annealed to 200°C, along with the observed FTIR spectra and XTEM images indicate that a large quantity of water is adsorbed at the bonded interface at room temperature. Upon annealing the structures to 350°C the adsorbed water forms a 4 nm thick oxide layer that is predominantly InP-oxide. The oxide present at the bonded interface upon annealing does not prohibit efficient

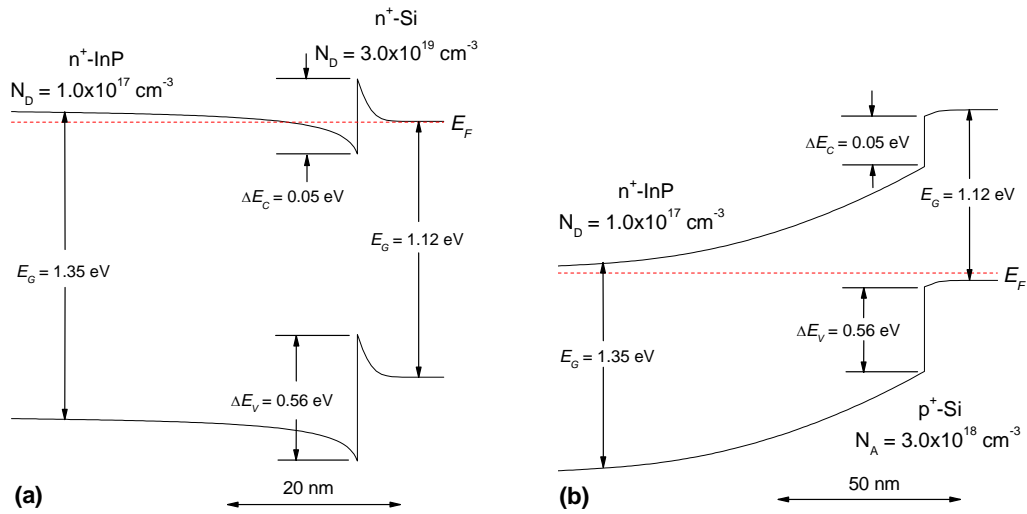


Figure 5.10 Band energy diagrams for InP/Si wafer bonded heterostructures based upon ideal heterojunction band offsets using the doping levels described in §5.1.1.2.1 showing the anticipated band structure of (a) n^+ -InP/ n^+ -Si and (b) n^+ -InP/ p^+ -Si.

conduction. This can be attributed to either a small potential barrier or a defect assisted tunneling process through the interface. As with the Ge/Si analysis, it is reasonable to assume that the oxide actually aids conduction in non-degenerately InP/Si wafer-bonded heterostructures by providing a dense distribution of defect states to which carriers can tunnel. The presence of a broad distribution of defect types and energy levels in the oxide would then allow carriers to hop by a thermal process to levels at which the barrier narrows and tunneling can occur to the other side of the junction.

5.1.4 Conclusions

The key result of the work described above is that ohmic electrical contact can be established in hydrophobically wafer-bonded Ge/Si and InP/Si heterostructures by bonding heavily, but non-degenerately, doped substrates. This is of technological importance for applying wafer bonding to reliably fabricating wafer-bonded alternative substrates for use in novel photovoltaic devices. Additionally, in light of the predicted band energy diagrams based on ideal heterojunction band offsets for both Ge/Si and InP/Si, it is speculated that the chemical and defect structure of the

wafer-bonded interface plays a critical role in the transport of carriers through the interface. In particular, the presence of misfit and twist dislocations due to the lattice mismatch and the azimuthal twist angle at the bonded Ge/Si interface appear to provide states in the band gap at the bonded interface. These defects presumably facilitate charge transport through a thermally assisted process.

In InP/Si, FTIR spectroscopy and XTEM images indicate a surprisingly different interface, relative to Ge/Si. In InP/Si structures, water adsorbed at the bonded interface leads to the formation of an InP-oxide that efficiently conducts current, presumably by the combined effects of providing available states for occupation at the interface and also by having a sufficiently low barrier height to minimize resistance of the interfacial layer.

The results for both Ge/Si and InP/Si indicate that with degenerate doping, lower interfacial specific resistances can be achieved. Additionally, the ideal band energy diagrams indicate that for both Ge/Si and InP/Si, the specific resistance could be further minimized by forming heavily doped n-n isotype heterojunctions, which features the lowest potential barrier of any conceivable bonded junction.

5.2 *Electrical Properties of Wafer-Bonded p^+ -Ge/p-Si Isotype Heterostructures*

In the previous sections the physical and chemical nature of the bonded Ge/Si interface is speculated to consist of a dense dislocation network that aids in the efficient conduction of current through the interface. By studying the interfacial electrical properties of wafer-bonded isotype heterostructures made from lightly doped p-Si and heavily-doped p^+ -Ge substrates, the impact of the bonded interface on the heterostructure can be studied with greater control. This is because of the relative insensitivity of the J - V properties of heavily doped junctions to defects at those junctions. In the following sections the impact of the thermal history and azimuthal twist angle between the bonded substrates are studied for Schottky-diode-like p^+ -Ge/p-Si wafer-bonded

heterostructures, and a more thorough model for the electrical activity of interfacial defects is presented.

5.2.1 Experimental Procedure

The experimental procedure described in §5.1.2.1 was applied to fabricate hydrophobically wafer-bonded p⁺-Ge/p-Si heterojunctions using (100)Ge (Ga-doped to $1 \times 10^{18} \text{ cm}^{-3}$) and (100)p-Si (B-doped to $8 \times 10^{14} \text{ cm}^{-3}$). A series of samples were bonded to independently study the impact of two variables – anneal time and azimuthal twist angle of the bonded pairs. The effect of the anneal time was observed by bonding samples at a 5° twist angle to control the density of twist interfacial dislocation defects governed by equation 5.6. The samples were then annealed to 400°C for 0.5, 1.0, 2.0 and 10.0 hours. Additionally a sample was measured prior to annealing. The effect of the azimuthal twist angle between the bonded samples was studied by bonding samples at angles 0.0°, 0.6°, 1.2°, 5.0°, 12.0° and 16.0° by controlling the azimuthal twist angle using the goniometer shown in Fig. 5.3. These samples were then annealed at 400°C for 4.0 hours. Following processing, Al contacts were deposited on the entire front and back surfaces of all samples, and *J-V* traces were measured using the configuration illustrated in Fig. 5.4.

The evolution of the bonded interface was observed using transmission-mode FTIR spectroscopy. In these measurements, samples were bonded using both hydrophobic and hydrophilic surface treatments prior to bonding. For hydrophilic bonding, a degreasing process similar to that described in §5.1.2.1 was employed along with a 10 minute ultra-violet ozone treatment. For hydrophobic bonding, the same process as that described in §5.1.2.1 was employed. Samples were then annealed using the heated press system shown in Fig. 3.8. Several annealing conditions were used, as there is no obvious reference sample for these measurements. Thus, these bonded samples were referenced relative to one another to assess the relative difference between the various treatments. In this way the loss of interfacial species can be confirmed relative to as-bonded Ge/Si samples.

5.2.2 Results and Analysis

5.2.2.1 Anticipated Energy Band Diagram for Wafer-Bonded p⁺-Ge/p-Si Heterostructures

The predicted band diagrams for these samples are shown in Fig. 5.11. In Fig. 5.11(a) it is clear that the dominant portion of the band bending associated with this structure occurs in the Si substrate. Thus, the bonded structures closely resemble Schottky diodes, typically formed by a metal-semiconductor junction.

5.2.2.2 p⁺-Ge/p-Si Wafer-Bonded Heterostructure Current-Voltage Data

Given the resemblance of the band diagram for p⁺-Ge/p-Si wafer-bonded heterostructures to a Shottky diode, one would expect the thermionic J - V model for Shottky diodes to be obeyed. In this model, the current has the functional form

$$J = J_0 \left[\exp\left(\frac{qV}{nkT}\right) - 1 \right] \quad (5.7)$$

Where, n is the diode ideality factor. Generally, this term is not included in the Schottky diode

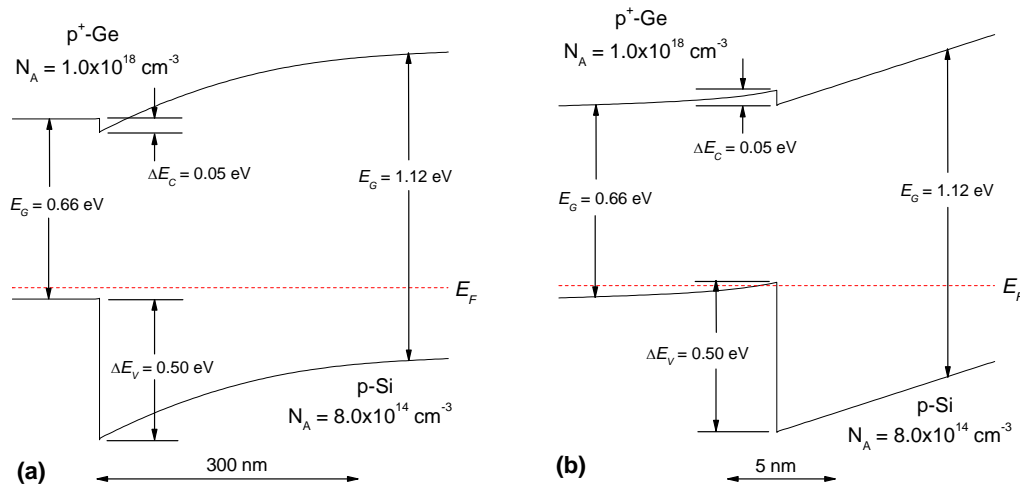


Figure 5.11 Band energy diagram for wafer-bonded p⁺-Ge/p-Si heterostructures based upon the ideal heterojunction band offsets showing (a) the full band bending and (b) a magnification of the interface region.

governing equation, because the current is dominated by a single carrier type. However, it is retained here as a fitting parameter to give more freedom in the fit process given the complexity and non-ideality of the bonded interface. J_0 is the reverse bias dark current due to carriers that can surmount the large abrupt barrier when passing from Ge to Si in reverse bias. J_0 is defined as

$$J_0 = A^* T^2 \exp\left(-\frac{\phi_{eff}}{kT}\right) \quad (5.8)$$

A^* is the Richardson constant for thermionic emission from a semiconductor. For a metal-semiconductor junction, this is a material property of the semiconductor under consideration. In the present case, the average value between Ge and Si is assumed. Thus, $A^* = 60[A \cdot cm^{-2} \cdot K^{-2}]$.

ϕ_{eff} is the effective barrier height for thermionic emission.

The anneal-dependent J - V behavior shown in Fig. 5.12(a) and the twist-angle-dependent J - V behavior shown in Fig. 5.12(b) both violate the expected behavior of a Schottky diode. In particular the reverse-biased behavior indicates that there is a linear relationship between the current and voltage of the junction. A closer look at the band diagram near the bonded interface shown in Fig. 5.11(b) reveals some degree of band bending in the Ge substrate near the bonded interface. This is consistent with the Anderson model of current conduction through an isotype heterojunction. In this model, the junction is treated as a dual-Schottky-diode structure. The J - V behavior of isotype heterojunctions has been analytically solved giving the following governing equation

$$J = J_0 \left(1 - \frac{V}{V_{bi}}\right) \left[\exp\left(\frac{qV}{kT}\right) - 1 \right] \quad (5.9)$$

Where,

$$J_0 = \frac{qA^*TV_{bi}}{k} \exp\left(-\frac{qV_{bi}}{kT}\right) \quad (5.10)$$

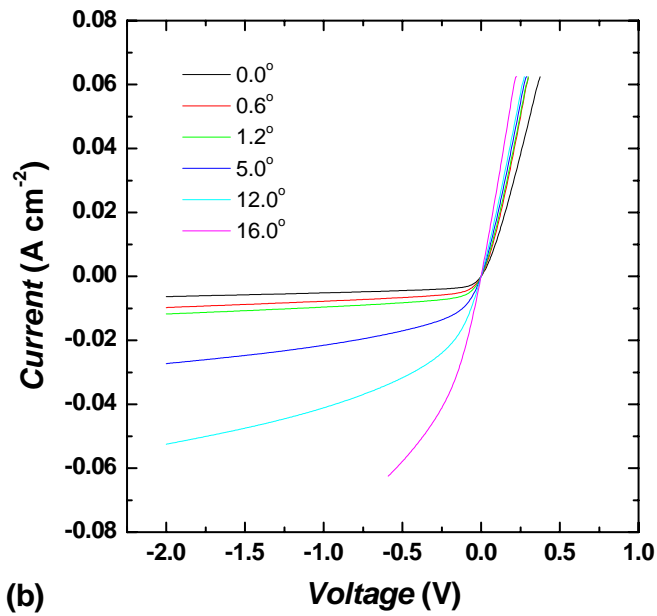
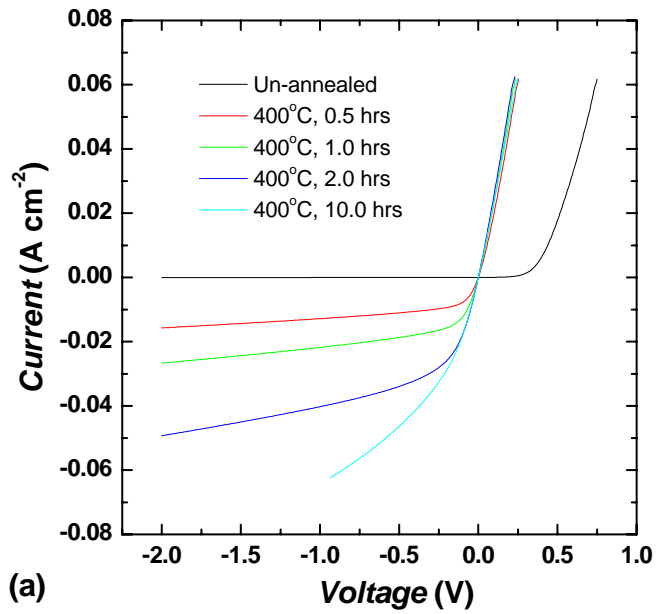


Figure 5.12 Current-voltage characteristics of p^+ -Ge/ p -Si as a function of (a) annealing time at 400°C for wafer-bonded p^+ -Ge/ p -Si heterostructures bonded with a 5° azimuthal twist angle between the substrates and (b) azimuthal twist angle for an anneal of four hours at 400°C .

Substituting ϕ_{eff} for V_{bi} gives a model with a linear reverse-bias J - V relationship. However, this analytical solution is subject to the assumption that,

$$(\epsilon N_A)_{Ge} = (\epsilon N_A)_{Si} \quad (5.11)$$

This is clearly not the case, with the acceptor concentration being three orders of magnitude higher for Ge than Si in the isotype heterojunctions under consideration.

5.2.2.3 Current-Voltage Model for a Leaky Schottky-Diode-Like Heterojunction

The models for the J - V behavior introduced in the previous section are clearly not relevant for the structures under consideration. However, by modifying the Schottky diode equation with the addition of shunt and series resistance elements as shown in Fig. 5.12, the measured J - V behavior is successfully modeled. The addition of a shunt resistance to the Schottky diode model captures the leakiness of the diode with an empirical parameter. The shunt resistance acts as a parallel leakage path for charge through the interface. In the case of Ge/Si wafer-bonded heterostructures, this leakage path is assumed to be caused by defect states at the bonded interface. The addition of a series resistance is a way to model resistances within the circuit as a whole and cannot be directly related to the electrical properties of the bonded interface. It is more likely that a significant series resistance element is caused by the measurement apparatus itself.

The governing equation for a diode such as the one shown in Fig. 5.13 can be derived from Ohm's Law by considering the resistive elements of the circuit. Thus,

$$R_{cir}(V) = R_s + \frac{R_d(V)R_{sh}}{R_d(V) + R_{sh}} \quad (5.12)$$

Where, R_s is the series resistance of the circuit; R_{sh} is the shunt resistance; $R_d(V)$ is the voltage-dependent resistance of the diode; and, $R_{cir}(V)$ is the voltage-dependent resistance of the entire circuit. Using this resistance model and Ohm's Law, one arrives at

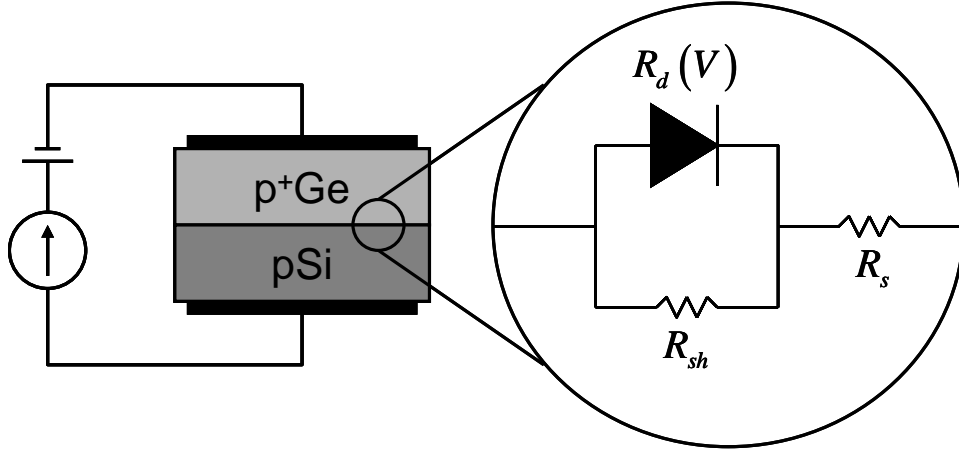


Figure 5.13 Circuit diagram for a wafer-bonded p⁺-Ge/p-Si heterostructure modeled by a leaky Schottky diode featuring a thermionic diode structure in parallel with a shunt resistance, R_{sh} , and in series with a parasitic resistance, R_s .

$$J(V) = \frac{V}{R_s + \frac{R_d(V)R_{sh}}{R_d(V) + R_{sh}}} \quad (5.13)$$

Assuming that the diode obeys the thermionic emission model given in equation 5.7, the full equation for the Schottky diode with a series and shunt resistance is

$$J(V) = \frac{V}{R_s + \frac{R_{sh} \frac{V}{J_0 \left\{ \exp \left[\frac{q(V - J(V)R_s)}{nkT} \right] - 1 \right\}}{R_{sh} + \frac{V}{J_0 \left\{ \exp \left[\frac{q(V - J(V)R_s)}{nkT} \right] - 1 \right\}}}} \quad (5.14)$$

Where, J_0 is given by the thermionic emission dark current governed by equation 5.7.

The fit to equation 5.14 is performed by considering the J - V behavior under extreme forward and reverse bias conditions. Under forward bias, $R_d(V)$ is essentially zero. Thus, linear properties are expected and the governing equation reduces to

$$J_{V \rightarrow \infty} = \frac{V}{R_s} \quad (5.15)$$

So, the series resistance is easily estimated as

$$R_s = \frac{1}{\text{Slope}} \quad (5.16)$$

Under extreme reverse bias the diode acts as an essentially infinite resistor, allowing a current of only J_0 through the diode branch of the circuit. Thus, the J - V behavior is governed by the series and shunt resistances and is expected to obey

$$J_{V \rightarrow -\infty} = \frac{V}{R_{sh} + R_s} - J_0 \quad (5.17)$$

Thus, using the estimated value of R_s from equation 5.16, the values of R_{sh} and J_0 can be estimated by

$$R_{sh} = \frac{1}{\text{Slope}} - R_s \quad (5.18)$$

$$J_0 = \text{Intercept} \quad (5.19)$$

The fitting process described above is shown for the sample condition of a 400°C one hour anneal in Fig. 5.14. Following the linear data fit, a non-linear fitting algorithm in Origin Lab is used to optimize the values of R_s , R_{sh} , and ϕ_{eff} estimated by equations 5.16, 5.18, and 5.19. When conducting this optimization, the diode ideality factor, n , is initialized at one and allowed to vary to optimize the curve fit. It is important to note that this new free parameter does not deviate into physically unrealistic values, but rather remains at around two for all of the fit curves. The original data along with the optimized fit with the leaky Schottky diode model are shown for the anneal-dependent J - V behavior in Fig. 5.15(a). The same comparison is made for the twist-angle-dependent J - V curves in Fig. 5.15(b). (In the twist dependent data, the 16° twist angle is shown, but the extracted parameters have been removed from later analyses, because the limited data range under reverse bias makes the present analysis unreliable.) For both the anneal-dependent and twist-dependent tests, the fits are excellent and the trends are consistent to within the estimated error in the extracted values.

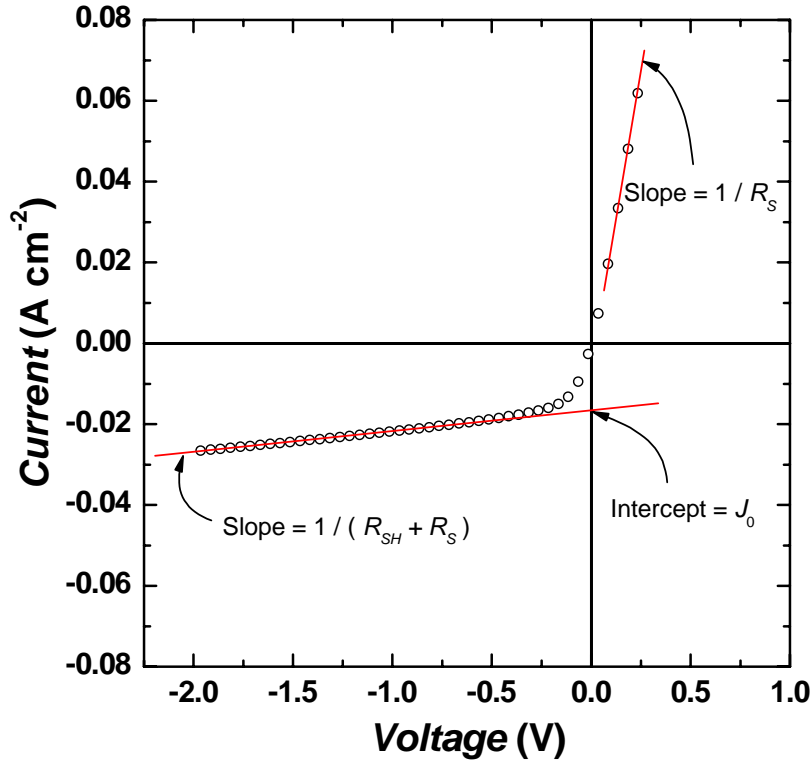


Figure 5.14 Fitting of the current-voltage curve for the sample annealed to 400°C for one hour curve to estimate the parasitic series resistance in the leaky Schottky diode model.

The dark current determined by the linear and optimized analyses was used to determine the value of ϕ_{eff} using equation 5.8. Thus,

$$\phi_{eff} = -kT \ln \left(\frac{J_0}{A^* T^2} \right) \quad (5.20)$$

The error in the extracted value of ϕ_{eff} was estimated by propagation of error assuming the following error estimates

$$\varepsilon(T) = \pm 10K \quad (5.21)$$

$$\varepsilon(J_0) = \left[\varepsilon^2(A) (AJ_0 \ln A)^2 + \varepsilon^2(AJ_0) \left(\frac{1}{A} \right)^2 \right]^{1/2} \quad (5.22)$$

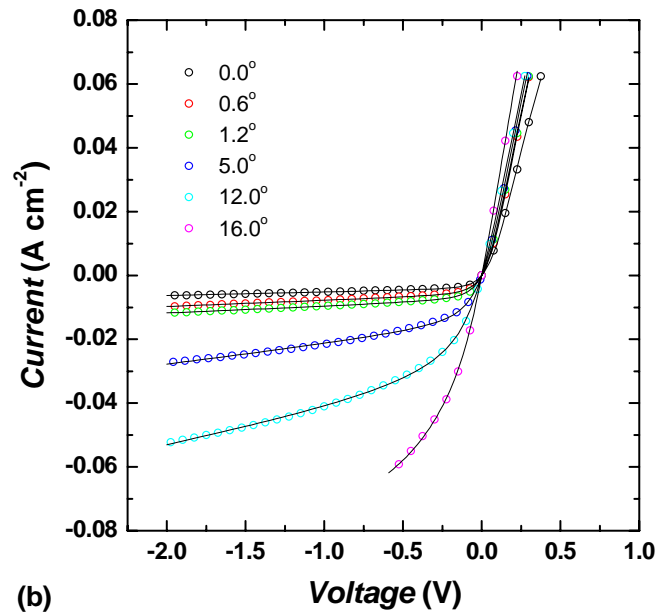
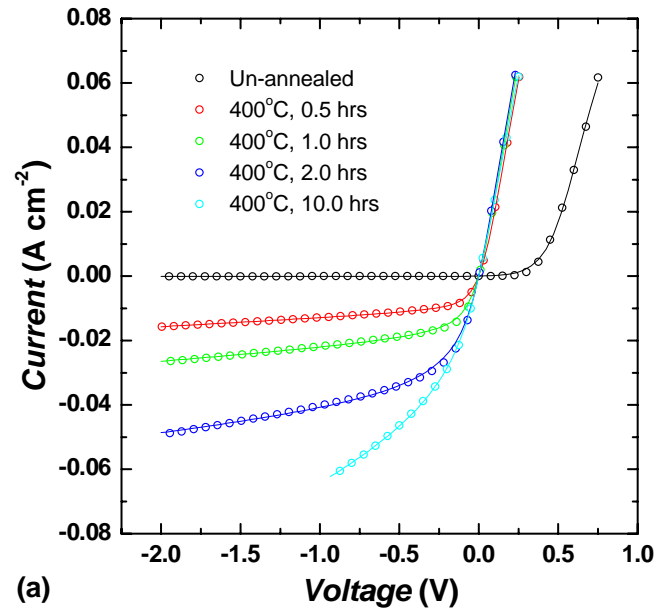


Figure 5.15 The optimized leaky Schottky diode curve fits for wafer-bonded p^+ -Ge/ p -Si heterostructures showing the model (solid curves) and data (open circles) for (a) the anneal-time-dependent J - V behavior at 400°C for heterostructures with a 5° azimuthal twist angle and (b) the twist-angle dependent J - V behavior for heterostructures annealed at 400°C for four hours.

$$\varepsilon(A^*) = \pm(A_{Ge}^* - A_{Si}^*)/2 = \pm 19.2 A \cdot cm^{-2} \cdot K^{-2} \quad (5.23)$$

The estimated temperature error was made in consideration of power dissipation at the bonded interface and the expected temperature drop across the bulk semiconductor with imperfect thermal contact at the probe stage surface. The estimated error in the measured current varies from sample to sample and combines the fitting error from the optimized fit and the estimated error in the bonded area used to calculate the current density. Because the bonded interface was not directly observed, a conservative value of $\pm 25\%$ of the sample size was used to estimate the error in the dark current, J_0 . The effective barrier heights and estimated errors are reported in Fig. 5.16 for all conditions in the anneal-dependent and twist-dependent analysis. Figure 5.17 shows the shunt resistance as a function of anneal time and twist angle. In this plot, the error bars are not based upon the propagation of error, as there is no governing equation that directly relates the shunt resistance to other experimental parameters. Rather, these shunt resistance error bars display the fitting error reported by Origin.

5.2.3 Discussion

5.2.3.1 Anneal-Dependent Evolution of the Electrical Properties of the Wafer-Bonded Interface

In the anneal-dependent barrier height evolution shown in Fig. 5.16, there is a consistent decrease in the calculated barrier height with increasing annealing time. In the as-bonded pair the barrier height is calculated to be 0.73 eV. Upon annealing to 400°C the barrier height decreases rapidly, reaching a value of 0.52 eV after a half hour anneal. Upon further annealing, there is an asymptotic decline in the barrier height with the barrier having reduced to 0.47 eV after a ten hour anneal. The 0.47 eV barrier height is close to the ideal band offset of 0.50 eV valence band offset. Also, upon annealing the shunt resistance (Fig. 5.17) evolves from an essentially infinite resistance for the as-bonded samples to a resistance of 40 $\Omega \text{ cm}^2$ following a ten hour anneal at

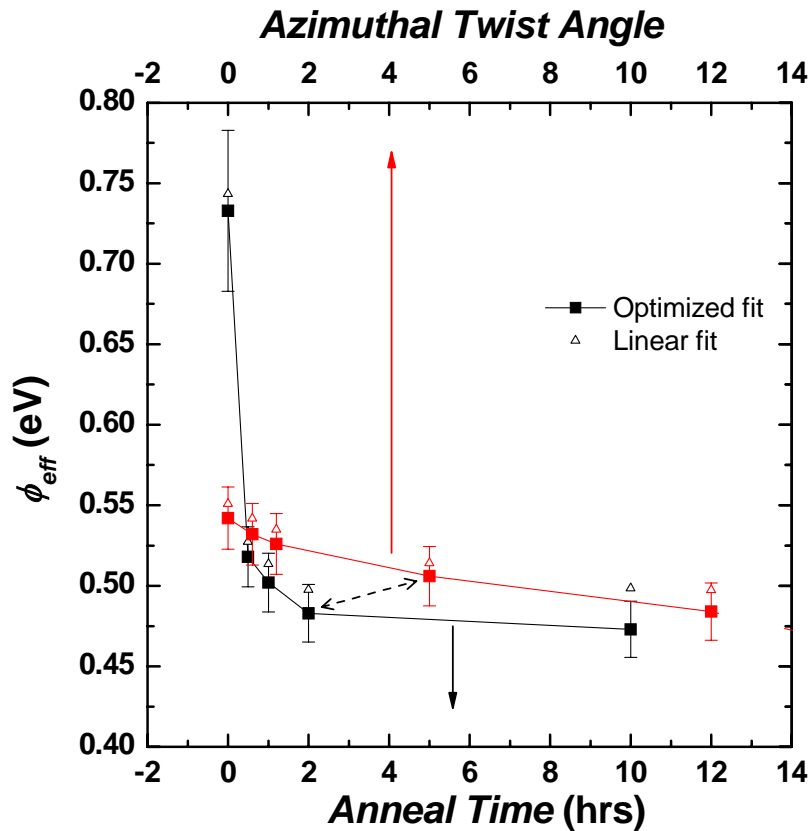


Figure 5.16 The effective barrier heights given as a function of both anneal time and azimuthal twist angle. The solid squares show the optimized fit, and the open triangles show the estimated values based on the linear analysis of the forward and reverse bias J - V behavior. The dashed arrow points out two conditions that should be reasonably well matched – the 5° sample annealed for two hours (black) and the 5° sample annealed for four hours (red). These values are not identical, but are within the estimated error bars.

400°C. Unlike the barrier height, the shunt resistance does not appear to be approaching its asymptotic limit following the ten hour anneal and could presumably drop further.

5.2.3.1.1 Electrical Properties of the As-Bonded p^+ -Ge/ p -Si Heterostructure

The substantial change in the barrier height upon annealing to 400°C, even for a brief period of time, suggests that there is a substantial change in the nature of the bonded interface. It is further observed that when measuring the J - V properties of the as-bonded interface, that the forward-bias turn-on voltage of the curve is dependent upon the voltage scan rate as shown in Fig. 5.18. In this test the same scan range and voltage step size were used, but the dwell time following current

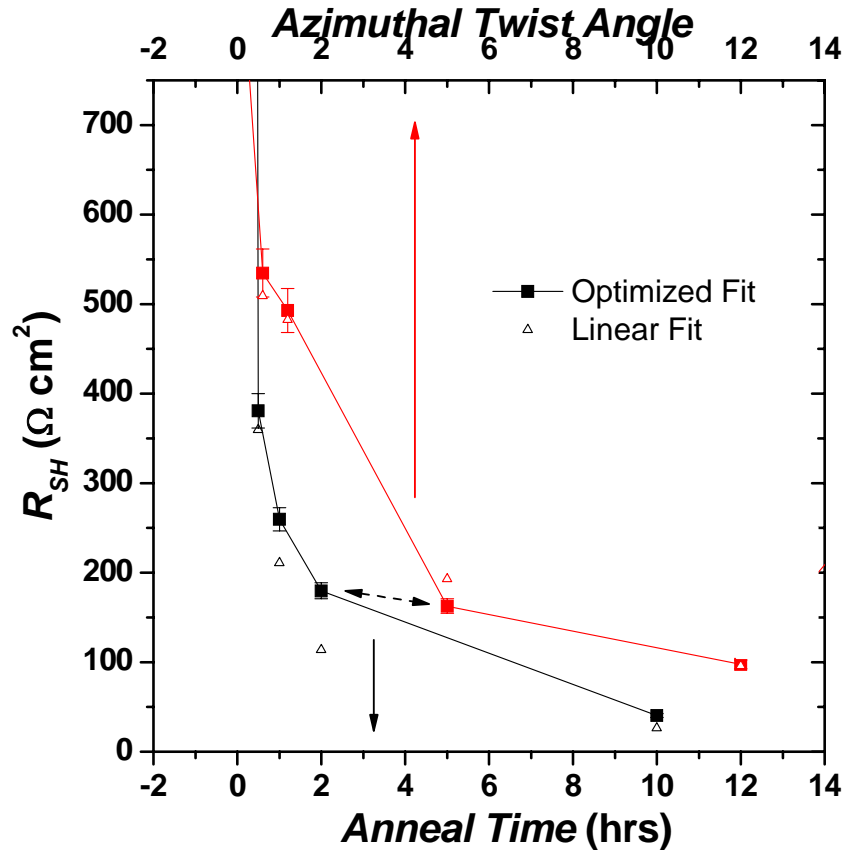


Figure 5.17 The shunt resistance given as a function of both anneal time and azimuthal twist angle. The solid squares show the optimized fit, and the open triangles show the estimated values based on the linear analysis of the forward and reverse bias J - V behavior. The dashed arrow points out two conditions that should be reasonably well matched – the 5° sample annealed for two hours (black) and the 5° sample annealed for four hours (red).

measurement at each voltage step was varied between zero and 200 ms. As the dwell time between points increases, the barrier height increases. The inset plot in Fig. 5.18 shows the increase in the effective barrier height with increasing scan delay time. This is attributed to a change in the population of trapped charge at the bonded interface in defect structures with a long time constant relative to the scan delay times.

The scan-time-dependent behavior of the as-bonded interface was also studied by observing the transient response of the measured current upon switching the bias direction. This was done

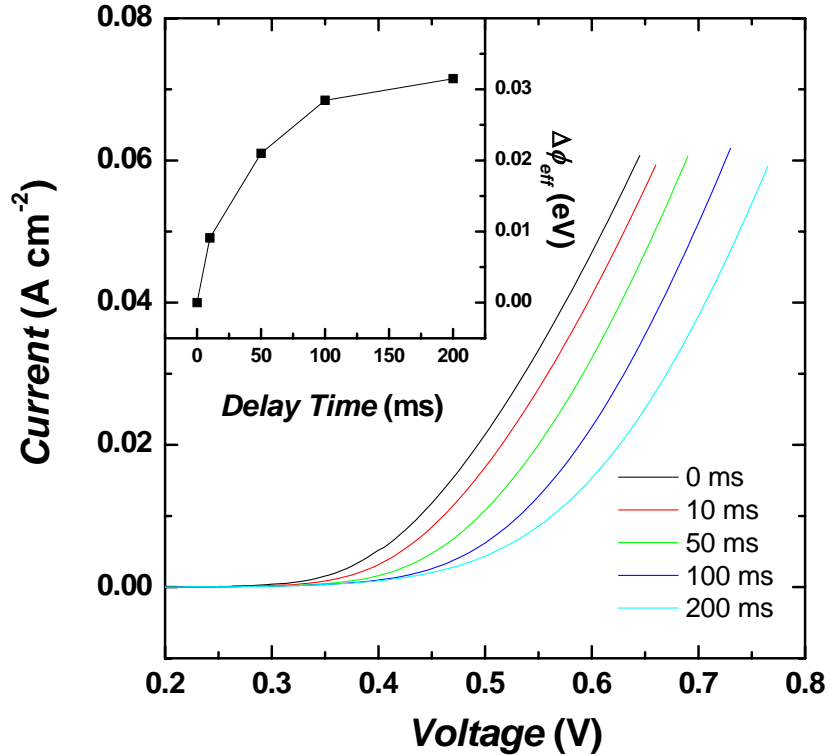


Figure 5.18 The J - V curves for 5° twisted as-bonded p^+ -Ge/ p -Si heterostructures showing the impact of the time delay between voltage steps. The inlaid plot shows the estimated effective barrier height as a function of the scan time delay.

by first allowing the sample to come to equilibrium under a forward bias voltage of 3.0 V. Then, the bias was reversed to -0.4 V, and the transient response of the reverse-biased current was observed as shown in Fig. 5.19. The effective barrier height response was also estimated by making the assumption that the current measured at this bias was near the dark current value. The calculated barrier heights were lower than those estimated by fitting the full J - V response of the heterostructure, as was done in determining the values in Fig. 5.16. However, the change in the estimated barrier height with time is assumed to be a reasonable assessment of the way in which the charge state and barrier height is evolving with time. As with the data in Fig. 5.18, this effect is assumed to be due to the slow transient associated with trap states at the as-bonded interface. Similar measurements performed on annealed samples show no long transient response

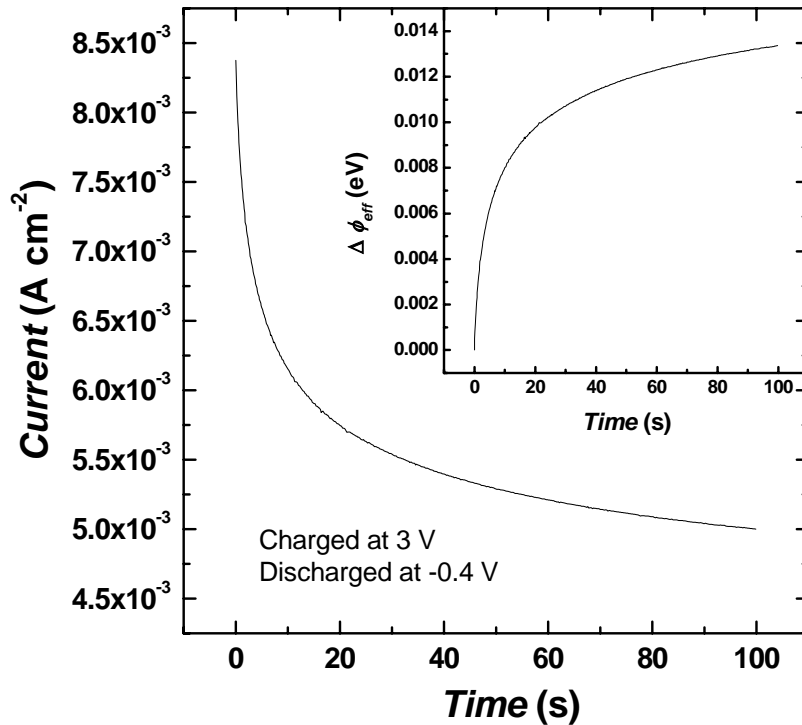


Figure 5.19 The transient response for an as-bonded p⁺-Ge/p-Si illustrating the long lifetime of defect states at the bonded interface. The sample was first allowed to come to steady state under 3 V forward bias. The bias was reversed to -0.4 V and the current was monitored as the interface states discharged. The transient response of the effective barrier height is shown in the inset plot.

In addition to indicating the presence of long lifetime trap states at the as-bonded interface, the transient response of the reverse biased structure illustrates how charged interface states might be affecting the barrier height. Under strong forward bias, the Fermi level in the Si side of the junction is below the energy level of interfacial defect states. Thus, the population of electrons in interfacial defects is expected to be relatively small for a sample at steady state under extreme forward bias. However, under a reverse bias of -0.4 V, the Fermi level is above the energy of many of the interfacial defect states. Thus, one would expect a dynamic charging effect of the interface. Thus, if one assumes that the charge states at the interface are occupied by electrons and are not holes, the transient response under reverse-bias is actually due to the long time constant of defect charging with electrons under reverse bias. This assumption further implies that

the charging of interfacial defect states causes a reduction in the valence band barrier height by inducing a local upward shift in the band structure. Extending this analysis to the observed behavior in Fig. 5.17 indicates that the defect states that are charged under reverse-bias are discharged slowly under forward bias causing the barrier height to increase with increased dwell time at voltage steps in the forward biased direction.

In both the forward- and reverse-bias behavior observed in Figs. 5.18 and 5.19, the transient behavior does not obey a simple exponential behavior. This is not surprising considering the likely number and variety of defect states at the bonded interface. The activation energy for the charging of a defect state is dependent upon the position of the defect in the band structure of the bonded structure. Furthermore, the structural nature of the defect state and its proximity to the bulk semiconductor will naturally impact its time constant for charging. Thus, the functional form of the barrier height change as a function of charging and discharging is a complicated mixture of the behavior of many states and defect structures that can not be distinguished on the basis of the data in the present study.

5.2.3.1.2 Evolution of the Bonded Interface upon Annealing

We know from the surface passivation prior to bonding that at room temperature, the bonded interface must consist of two H-passivated surfaces interacting via van der Waals forces. Furthermore, the previous section shows that this thin layer behaves much like an insulator, as indicated by the slow charging and discharging of defect states in the interfacial bonded structure. Upon annealing, the effective barrier height is dramatically reduced. This behavior is consistent with the concept of a chemical or structural rearrangement of the interface. Upon annealing to 400°C, it is assumed that the H-passivation of the Ge and Si is lost due to thermal desorption. In this process it is anticipated that Ge-Si covalent bonds form to reduce the surface energy of exposed Ge and Si surface. In this process, the insulating interfacial layer is lost and the resulting barrier height is closer to the ideal value of 0.50 eV. However, as was previously pointed out, the

resulting structure has J - V properties that are assumed to be influenced by the presence of a dense dislocation network due to twist interfacial dislocations and misfit edge dislocations.

Desorption of a hydrogen passivation layer is verified by studying the impact of annealing on the bonded interface by transmission-mode FTIR spectroscopy shown in Fig. 5.20. In this analysis three samples were fabricated from double-side polished Ge and Si – an as-bonded hydrophobically-bonded sample, an as-bonded hydrophilically-bonded sample, and a hydrophobically-bonded sample annealed to 300°C. The as-bonded samples were used as references, and the change in the absorbance spectra of the samples was studied by adjusting the

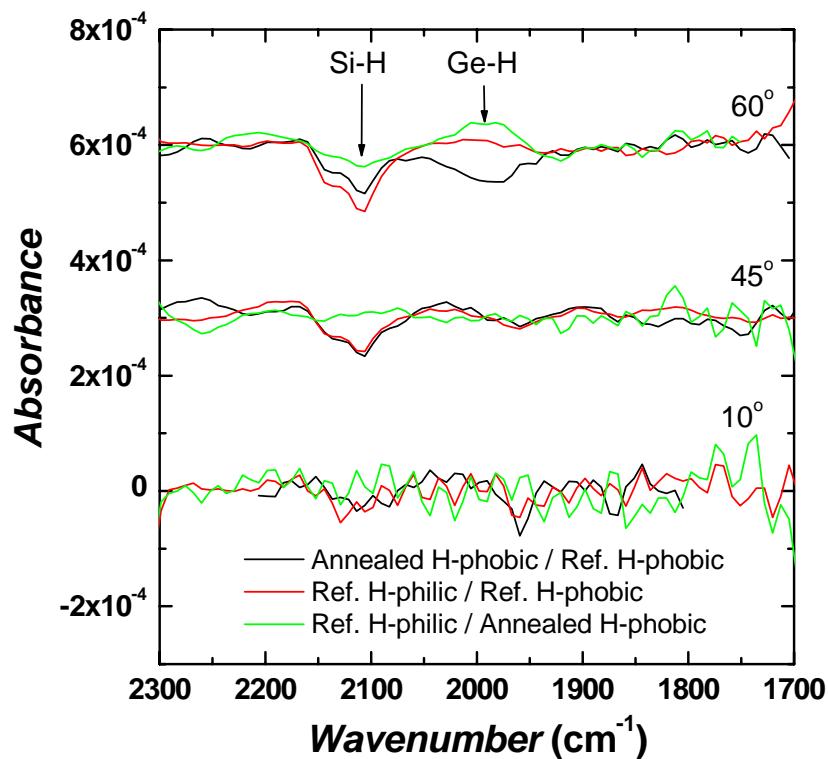


Figure 5.20 Transmission-mode FTIR spectra of wafer-bonded Ge/Si heterostructures at 10, 45, and 60° transmission angles. The different colors refer to different bonding conditions and reference spectra. In the black curve, the effects of annealing a hydrophobically-bonded sample following an anneal to 300°C referenced to an as-bonded sample. The red curve shows an as-bonded hydrophilically-bonded sample referenced to an as-bonded hydrophobically-bonded sample. And, the green curve shows an as-bonded hydrophilically-bonded sample referenced to a hydrophobically-bonded sample that has been annealed to 300°C.

reference. The spectra were collected at three angles to assess the dipole orientation of observed spectral features.

In Fig. 5.20 the black curve illustrates the change of Si-H and Ge-H stretch mode absorption peaks for the annealed hydrophobically-bonded Ge/Si sample relative to the as-bonded hydrophobically-bonded Ge/Si sample. The negative absorbance peak at 2105 cm^{-1} clearly indicates the loss of Si-H at the bonded interface upon annealing. The peak position of this vibrational mode is closest to the anti-symmetric mode of the Si(100) surface dihydride, reported at 2110 cm^{-1} at free surfaces.¹⁶ However, the transmission-angle dependence of the peak behavior is contradictory to this assignment. It is therefore more likely that the peak loss is associated with the symmetric mode of the Si(100) surface dihydride or Si(100) surface monohydride, reported at 2099 cm^{-1} for free Si surfaces.¹⁶ The shift from the anticipated value can be attributed to the interaction of this surface with the opposing Ge-H surface. The lack of an absorption peak in the 10° incidence angle suggests that the instrument sensitivity is reduced for this angle, probably due to increased reflectance of the incident radiation. The change in the Ge-H stretch mode in the 60° incidence measurement is inconclusive. This can be attributed to an imperfect Ge surface-monohydride coverage, making the loss of Ge-H species from the surface difficult to measure, despite the relatively strong dynamic dipole of Ge-H compared to Si-H.¹⁶

The red curve in Fig. 5.20 illustrates the relative difference in Si-H and Ge-H absorption intensity between hydrophilically-bonded Ge/Si structures and hydrophobically-bonded Ge/Si heterostructures. This indicates that the loss of the Si-H stretch mode upon annealing a hydrophobically-bonded sample is slightly less than all of the Si-H species anticipated to be present in the as-bonded state.

Finally, the green curve in Fig. 5.20 directly compares the Ge-H and Si-H stretch mode intensity in the annealed hydrophobically-bonded sample with an as-bonded hydrophilically-bonded sample. This again illustrates that, to within the resolution of the measurement, the H-passivation of the Si bonded interface is substantially lost upon annealing to 300°C . This result

suggests that upon annealing to 400°C the H-passivation of the interface is substantially removed in the present study. Thus, the substantial decrease in the effective barrier height and the loss of the slow transient response of the J - V characteristics can be attributed to the loss of this interfacial passivation.

In addition to the loss of the interfacial passivation layer and its associated large potential barrier, annealing of the Ge/Si wafer-bonded heterostructures to 400°C also increases leakage of the interface as indicated by the reduced shunt resistance upon annealing. This is presumably due to the formation of a twist interfacial dislocation network related to the azimuthal twist of the bonded structures along with the formation of an edge dislocation network caused by the misfit of the Ge and Si lattices. The continuous decline in the shunt resistance and effective barrier height with increasing annealing time suggests, along with the FTIR spectroscopy observations of the bonded interface, that desorption of interfacial passivation species occurs rapidly upon annealing to 400°C. However, reordering of the interfacial structure to form dislocations continues to occur upon extended annealing. The impact of interfacial dislocations on the electrical properties is verified in the following section by studying the impact of the twist-angle on the shunt resistance and barrier height of the bonded structures.

5.2.3.2 Twist-Dependent Electrical Properties of the Wafer-Bonded Interface

The J - V behavior as a function of twist-angle summarized in Figs. 5.15(b), 5.16, and 5.17 indicates that as the twist angle increases the barrier height and shunt resistance decrease. This behavior is best explained by the formation of a twist-angle-dependent defect network at the bonded interface consisting of misfit edge-like dislocations (equation 5.4) and twist interfacial dislocations (equation 5.6). Both the effective barrier height and the shunt conductivity are expected to be related to the density of these defects. The density of defects is specified in total defect length per unit area, as it is anticipated that the number of states or leakage paths per unit

length is relatively independent of the spacing of these defects. The density of defects in nm cm^{-2} is thus given by

$$\rho = \frac{2L^2}{d} = \frac{2(10^7)^2}{d[\text{nm}]} \frac{\text{nm}}{\text{cm}^2} \quad (5.24)$$

Thus, the density of misfit dislocations and edge dislocations are

$$\rho_{\text{edge}} = \frac{4(10^7)^2 \Delta a[\text{nm}]}{a_{\text{Si}}^2[\text{nm}]} = 2.92 \times 10^{13} \frac{\text{nm}}{\text{cm}^2} \quad (5.25)$$

$$\rho_{\text{twist}}(\theta_{\text{twist}}) = \frac{4\sqrt{2}(10^7)^2}{a_{\text{Si}}} \sin\left(\frac{\theta_{\text{twist}}}{2}\right) = 1.04 \times 10^{15} \sin\left(\frac{\theta_{\text{twist}}}{2}\right) \frac{\text{nm}}{\text{cm}^2} \quad (5.26)$$

The effect of the azimuthal twist angle and affiliated twist interfacial dislocation network was studied by analyzing the change in the barrier height and shunt conductance as a function of $\sin(\theta_{\text{twist}}/2)$, the functional argument of the change in the twist interfacial dislocation network. In this analysis the misfit dislocation network should not impact the change in the measured barrier height and shunt conductance, as it is independent of the twist angle.

In Fig. 5.21 $-\Delta\phi_{\text{eff}}$ is plotted as a function of $\sin(\theta_{\text{twist}}/2)$. $-\Delta\phi_{\text{eff}}$ has a sub-linear response to increasing values of $\sin(\theta_{\text{twist}}/2)$ that is modeled by an asymptotic exponential approach to a maximum barrier height increase of 0.062 eV. As was determined in §5.2.3.1.1, the change in barrier height for annealed structures with increasing twist angle is attributed to the increased density of defect states at the bonded interface that are populated by electrons, leading to barrier lowering. Presumably the density of these states is linear with the increasing density of twist interfacial dislocations. However, it is not unreasonable to assume that Coulombic repulsion of charged interface states prevents the lowering of the barrier height from being linear with respect to the density of charge states at the interface, as is observed here.

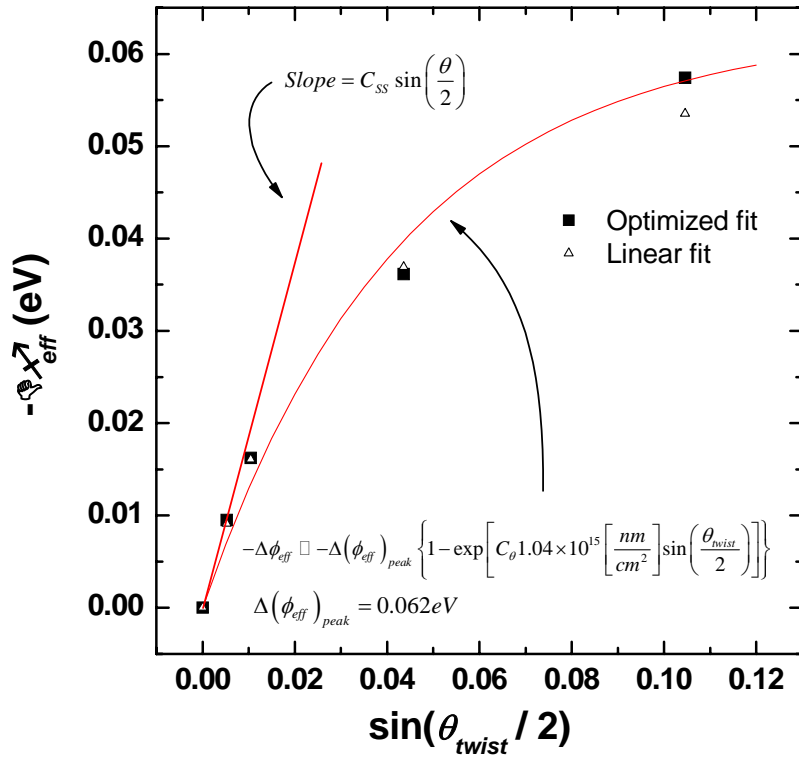


Figure 5.21 Change in barrier height at an anneal time of two hours at 400°C for Ge/Si bonded interfaces as a function of $\sin(\theta_{\text{twist}}/2)$, the argument of the expected change in the twist interfacial dislocation density, as expressed in total dislocation length per cm^2 . The sub-linear behavior is consistent with the suppression of defect decoration due to Coulombic repulsion in closely spaced defects.

Figure 5.22 shows the change in the shunt conductance, $\Delta\sigma_{\text{shunt}} = \Delta(1/R_{\text{sh}})$, as a function of $\sin(\theta_{\text{twist}}/2)$. The linear relationship between these parameters is consistent with the notion of defect states at the bonded interface providing a leakage path for conduction of charge through the bonded interface. Unlike a barrier height reduction due to trapped charge, leakage does not result from the sustained occupation of defect states at the bonded interface. On the contrary, the presence of vacant defect states is more conducive to this conduction mechanism. Because the occupation of these states during conduction of current through them need not increase substantially, Coulombic repulsion is not expected to suppress this conduction mechanism. Thus,

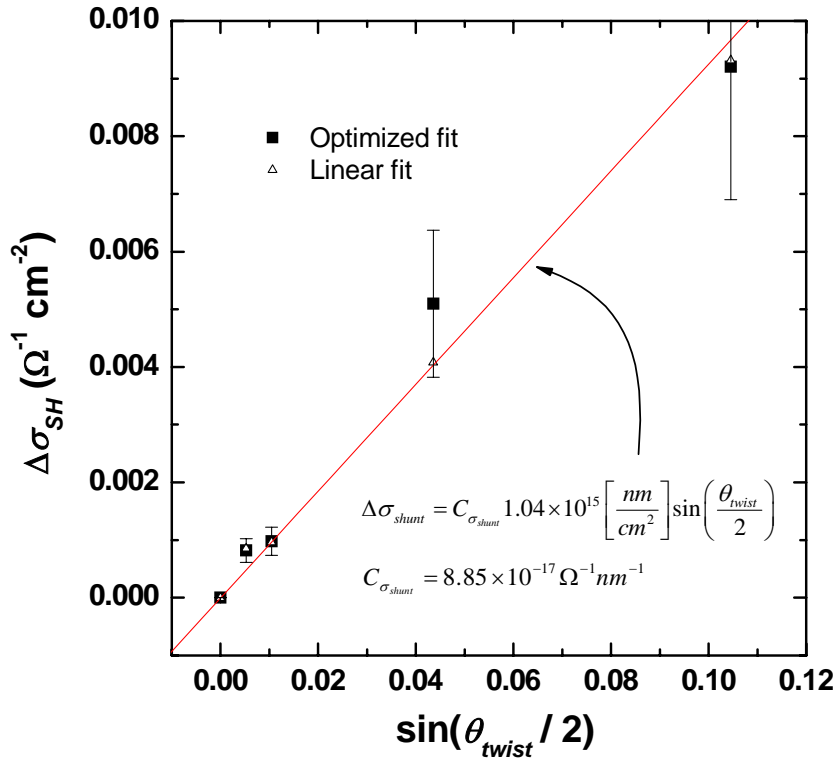


Figure 5.22 Change in shunt conductivity at an anneal time of two hours at 400°C for Ge/Si bonded interfaces as a function of $\sin(\theta_{twist}/2)$, the argument of the expected change in the twist interfacial dislocation density, as expressed in total dislocation length per cm^2 . The approximately linear behavior is consistent with the expectation that defect states that are transiently occupied during conduction through the interface are not sensitive to the occupation level.

the increased density of defect states at the interface increases the probability of carriers transitioning into and through the defect states at the bonded interface, resulting in an increased conduction path.

5.2.3.3 Comparison of Present Results to Theoretical and Experimental Results in the Literature

Heterojunction band offsets have been studied theoretically and experimentally to determine their offsets. Despite over 30 years of study, there is no conclusively accepted value for the valence band offset between Ge and Si. Table 5.1 catalogs the theoretical and measured values of the

Table 5.1 Summarized barrier heights for the present study and previously reported theoretical and experimental estimates of the valence band offsets at Ge/Si heterojunctions. The literature values highlighted in bold correspond to those conditions that most closely correspond to the measurement conditions of the present work.

Fabrication Method (Theoretical Structure)	Measurement Technique (Theoretical Method)	ΔE_V	Pub. Year	Authors
-----	$\Delta E_V = \Delta E_G + \Delta\chi$	0.50 eV	-----	-----
Alloyed n-n Ge/Si junction grown on Si by GeI ₂ disproportionation; presumably relaxed	C-V profiling	0.40 eV	1976	van Opdorp and Kanerva
(Unstrained Ge/Si)	(Linear combination of atomic orbitals)	0.38 eV	1977	Harrison
(Unstrained Ge/Si)	(Tersoff's Theory – Interface dipole states)	0.18 eV	1984	Tersoff
(Coherently strained Ge/Si)	(Pseudopotential Theory)	0.84 eV	1986	Van de Walle and Martin
(Fully relaxed Ge/Si)	(Pseudopotential Theory)	0.31 eV	1986	Van de Walle and Martin
Strained Ge/Si grown by epitaxy	XPS photoemission	0.74 eV	1988	Schwartz <i>et al.</i>
(Coherently strained Ge/Si)	(Density Functional Theory w/ Linear Response Theory)	0.47 eV	1991	Colombo <i>et al.</i>
(Fully relaxed Ge/Si)	(Density Functional Theory w/ Linear Response Theory)	0.41 eV	1991	Colombo <i>et al.</i>
(Coherently strained Ge/Si)	(Empirical Pseudopotential Method)	0.74 eV	1993	Rieger and Vogl
(Coherently strained Ge/Si)	(Tersoff's Theory w/ Strain)	0.61 eV	1998	Ohler <i>et al.</i>
Strained Ge/H/Si(100)2x1 grown by epitaxy	XPS photoemission	0.71 eV	1999	Almeida <i>et al.</i>
Wafer-bonded Ge/Si; unannealed	J-V modeling	0.65 to 0.73 eV		
Wafer-bonded Ge/Si; annealed	J-V modeling	0.47 to 0.54 eV		

Present Work

valence band offset between Ge and Si.¹⁷⁻²⁴ This is not meant to be an exhaustive list of all reported values. The listing here serves to highlight the conditions under which the band offsets at Ge/Si heterojunctions have been measured and how the present results compare.

It has been noted that the J - V behavior of Shottky-like isotype heterojunctions does not accurately reflect the actual band offset value of the heterojunction, because a relatively small density of defect states at the interface can lead to charging that causes substantial changes in the barrier height to thermionic emission.²⁵ Thus, the present comparison of the measured thermionic emission barrier heights to reported values of the valence band offset are expected to disagree, because the present analysis is not a direct measurement of the band offset. That being said, there is generally such disagreement over the correct value of the valence band offset in the literature that the measured values here easily fall within the range of reported values. For coherently strained Ge/Si interfaces, the reported theoretical and experimental values of the valence band offset range from 0.47 to 0.84 eV. The reported values of the valence band offset for unstrained Ge/Si heterojunctions range from 0.18 to 0.50 eV. The reported values in the present study for annealed samples in the range from 0.47 to 0.54 eV are in good agreement with values reported in the literature.

5.2.4 Conclusions

The analysis of the anneal-dependent and twist-angle-dependent behavior of the J - V behavior of the bonded interface shows that in the as-bonded p^+ -Ge/ p -Si heterostructure, there is minimal shunt conductance due to leakage, but there are slow trap states that cause the effective barrier height to decrease when charged. Upon annealing the bonded heterostructures, the interfacial passivation layer giving rise to the slow traps and high potential barrier height is lost, leaving the Ge and Si substrates in intimate contact. The loss of the interfacial passivation layer leads to increased shunt conductance through defect states. These same defect states cause a slight lowering of the potential barrier when charged. The density of this dislocation network has been

shown to be dependent on the azimuthal twist angle between the bonded substrates. When the twist angle is increased, the dislocation network due to twist interfacial dislocations becomes more dense leading to a decrease in the barrier height and an increase in the shunt conductance. These mechanisms are graphically summarized in Fig. 5.23.

5.3 Summary

Ohmic, low-resistance wafer-bonded interfaces were demonstrated for heavily doped Ge/Si and InP/Si hydrophobically wafer bonded pairs. Furthermore, the measured specific resistance of less than $0.16 \Omega \text{ cm}^{-2}$ was shown to be independent of the azimuthal twist angle orientation. The observed linear J - V behavior for both Ge/Si and InP/Si is surprising in light of the anticipated band offset diagrams of these structures. Leakage paths due to interfacial defect states are indicated as a possible explanation for this linear J - V behavior. However, the nature of these defects is different in the two structures, with the defects in Ge/Si attributed to interfacial dislocation structures and the defects in InP/Si related to defect states in an InP-oxide that forms

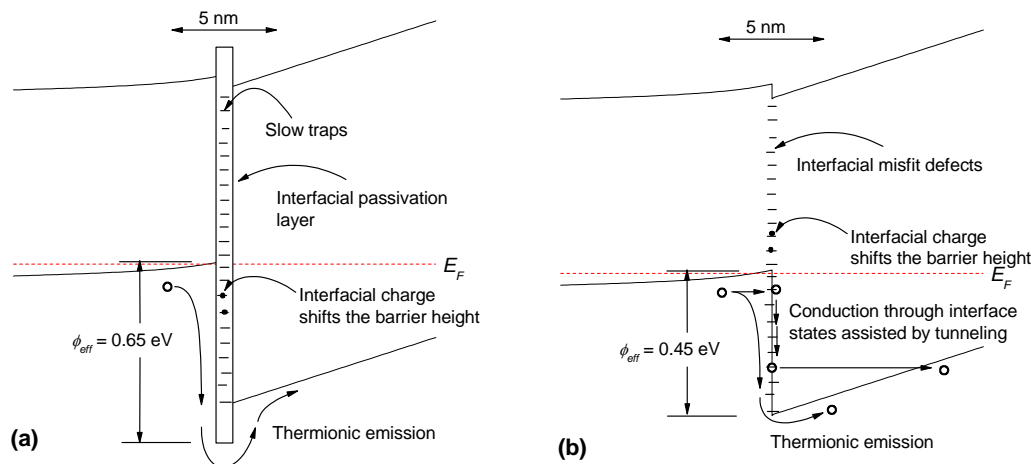


Figure 5.23 Band energy diagram for wafer-bonded p^+ -Ge/ p -Si heterostructures illustrating the conceptual model for thermionic and tunneling conduction mechanisms as they relate to the anneal-dependent interface states and barrier height in (a) an as-bonded unannealed heterostructure featuring slow defect states in a surface passivation interfacial layer and (b) an annealed sample having lost the passivation layer but replaced it with a network of twist and anneal dependent interfacial misfit dislocation defect states that lead to shunt conductivity and barrier height reduction.

upon annealing.

The role of interfacial dislocations in the electrical properties of Ge/Si wafer-bonded heterostructures was elucidated by studying Schottky-like p^+ -Ge/p-Si wafer-bonded isotype heterostructures. As-bonded, these structures have an effective barrier height of 0.74 eV. Upon annealing the effective barrier height is reduced to the 0.47 to 0.54 eV range depending on anneal time and azimuthal twist angle of the bonded structures. Additionally, the annealed samples indicate that a shunt leakage path is present that is dependent upon the anneal-time duration and the azimuthal twist angle. These results suggest that the electrical properties of the effective barrier height and the shunt leakage are attributable to the interfacial dislocation network present in wafer-bonded heterostructures.

5.4 *References*

- ¹ Q.-Y. Tong, E. Schmidt, U. Gosele, and M. Reiche, *Applied Physics Letters* **64**, 625-627 (1994).
- ² M. Weldon, Y. Chabal, D. Hamann, S. Christman, E. Chaban, and L. Feldman, *Journal of Vacuum Science and Technology B* **14**, 3095-3106 (1996).
- ³ G. Patriarche, F. Jeannes, J.-L. Oudar, and F. Glas, *Journal of Applied Physics* **82**, 4892-4903 (1997).
- ⁴ T. Akatsu, A. Plossl, R. Schloz, H. Stenzel, and U. Gosele, *Journal of Applied Physics* **90**, 3856-3862 (2001).
- ⁵ D. Pasquariello and K. Hjort, *IEEE Journal on Selected Topics in Quantum Electronics* **8**, 118-131 (2002).
- ⁶ D. Pasquariello, M. Camacho, K. Hjort, L. Dozsa, and B. Szentpali, *Materials Science and Engineering* **B80**, 134-137 (2001).
- ⁷ A. G. Milnes and D. L. Feucht, *Heterojunctions and Metal-Semiconductor Junctions* (Academic Press, New York, 1972).
- ⁸ S. M. Sze, *Physics of Semiconductor Devices*, 2nd ed. (John Wiley & Sons, New York, 1981).
- ⁹ www.ioffe.ru/SVA/NSM/Semicond/.
- ¹⁰ www.pv.unsw.edu.au/Links/pc1d.asp.

- 11 J. W. Christian, *The Theory of Transformations in Metals and Alloys*, 2nd ed. (Pergamon Press, New York, 1981).
- 12 J. L. Rouviere, K. Rousseau, F. Fournel, and H. Moriceau, *Applied Physics Letters* **77**, 1135-1137 (2000).
- 13 A. E. Romanov, P. M. Petroff, and J. S. Speck, *Applied Physics Letters* **74**, 2280-2282 (1999).
- 14 O. Pluchery, J. Eng, R. L. Opila, and Y. Chabal, *Surface Science* **502-502**, 75-80 (2002).
- 15 A. Fontcuberta i Morral, J. M. Zahler, H. A. Atwater, M. M. Frank, Y. J. Chabal, P. Ahrenkiel, and M. W. Wanlass, in *Electrical and structural characterization of the interface of wafer bonded InP/Si*, San Francisco, 2003.
- 16 Y. Chabal, *Surface Science* **168**, 594-608 (1986).
- 17 W. A. Harrison, *Journal of Vacuum Science and Technology* **14**, 1016-1021 (1977).
- 18 J. Tersoff, *Physical Review B* **30**, 4874-4877 (1984).
- 19 C. G. Van de Walle and R. M. Martin, *Physical Review B* **34**, 5621-5634 (1986).
- 20 G. P. Schwartz, M. S. Hybertsen, J. Bevk, R. G. Nuzzo, J. P. Mannaerts, and G. J. Gaultieri, *Physical Review B* **39**, 1235-1241 (1989).
- 21 L. Colombo, R. Resta, and S. Baroni, *Physical Review B* **44**, 5572-5579 (1991).
- 22 M. M. Rieger and P. Vogl, *Physical Review B* **48**, 276-287 (1993).
- 23 C. Ohler, C. Daniels, A. Forster, and H. Luth, *Physical Review B* **58**, 7864-7871 (1998).
- 24 J. Almeida, L. Sirigu, G. Margaritondo, P. Da Padova, C. Quaresima, and P. Perfetti, *Journal of Physics D: Applied Physics* **32**, 191-194 (1999).
- 25 H. Kroemer, *Surface Science* **174**, 299-306 (1986).

Chapter 6: Demonstration of Epitaxial Growth on Wafer-Bonded Templates

In this chapter the suitability of Ge/Si and InP/Si wafer-bonded epitaxial templates is studied by metal-organic vapor-phase epitaxy (MOVPE) growth of triple-junction solar cell structures and InP/In_{0.53}Ga_{0.47}As/InP double-heterostructures (DHs) on Ge/Si and InP/Si, respectively. The optical quality of these epitaxially-grown structures is studied by photoluminescence (PL) measurement. Additionally, the surface morphologies and defect densities of the Ge/Si and InP/Si structures are described. Ge homoepitaxy on Ge/Si wafer-bonded structures is also explored as a means of surface improvement and as a proxy for the study of threading dislocation propagation in III-V heteroepitaxial films. These structures clearly show that removal of the implant damage is essential to the growth of high-quality films. In the case of InP/Si wafer-bonded structures wet chemical etching with various ratios of a HCl:H₃PO₄:H₂O₂ solution and chemical mechanical polishing (CMP) with a sodium hypochlorite slurry is shown to improve the PL emission intensity relative to structures grown on an as-transferred InP/Si wafer-bonded structure.

6.1 *Epitaxy on Ge/Si Heterostructures*

6.1.1 Growth Surface

In §3.2.1.1 the surface morphology of as-transferred Ge/Si wafer-bonded epitaxial templates as measured by contact mode atomic force microscopy (AFM) was reported. The surface of the as-transferred Ge layer has a roughness of 10 to 20 nm-rms, depending on the substrate miscut, with

increasing miscut angle resulting in increasing as-transferred surface roughness. The surface morphology of as-transferred Ge/Si wafer-bonded epitaxial templates is of concern in the growth of GaAs-lattice-matched epitaxial films on the templates, because the local surface morphology strongly influences the nucleation of the GaAs film, as described in §1.2.1.3.1.

Samples used for the study of the heteroepitaxy of triple-junction solar cell structures on Ge/Si samples were fabricated from Ge(100) substrates miscut by 7° at an angle between the [110] and [111] crystallographic directions. (The exact orientation of the miscut is proprietary knowledge of Tecstar, now owned by Emcore.) The miscut was optimized to result in a step-edge spacing on the surface that is ideal for nucleation using the Tecstar MOVPE growth process for triple-junction solar cell fabrication. The presence of substantial surface undulations due to the exfoliation process causes local deviation of the crystallographic orientation of the Ge surface from the intentional miscut of an epi-ready bulk Ge substrate. In Fig. 6.1 a single AFM line scan is analyzed to estimate the local variation in miscut angle. In this analysis, Origin was used to take a local numerical derivative of the surface morphology. This was converted to a local miscut angle, called the local roughness-induced miscut in the subsequent discussion, using simple trigonometry.

The local roughness-induced miscut is influenced by measurement noise in the AFM scan in such a way that large spikes in the data are observed. To verify that measurement noise was not a substantial factor in the calculation of the mean and standard deviation of the local roughness-induced miscut angle, a low-pass FFT filter was used to remove high-frequency noise from the line scan. The mean and standard deviation of the local roughness-induced miscut for the filtered line scan were within 1% of these values for the unfiltered line scan. The mean value of the local roughness-induced miscut for five line scans was 0.55° , in addition to the 7° miscut of the Ge surface. The standard deviation of the local roughness-induced miscut was 11.11° . This value has significant implications for the nucleation and growth of GaAs on as-transferred Ge/Si wafer-bonded epitaxial template structures. The magnitude of the variation of the local roughness-

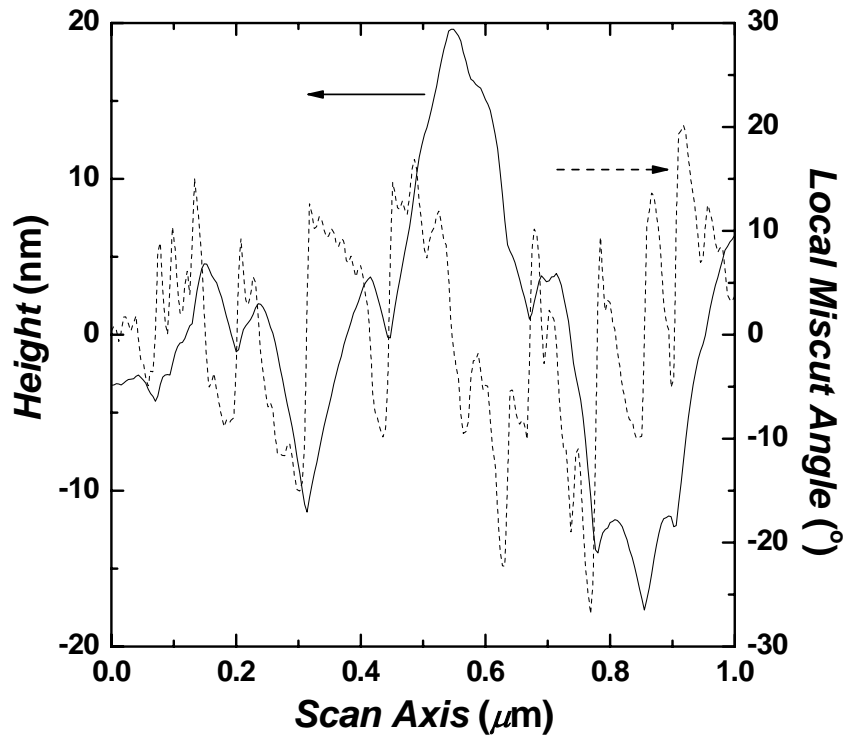


Figure 6.1 A cross-sectional view of the AFM-measured surface morphology for one of the lines in the scan direction of the AFM image shown in Fig. 3.12. The derivative of the scan has been converted into a local miscut angle value, assuming that there is no miscut in the direction of the scan. For directions offset by ϕ from the miscut direction, the local miscut has an angle of $|\theta_{miscut} \cos \phi|$ added to the local miscut.

induced miscut suggests that significant fractions of the as-transferred Ge surface have a local miscut that has a significantly lower coverage of step edges than an epi-ready Ge substrate with a 7° miscut, while other regions can be expected to have a step-edge density that is substantially higher than an epi-ready Ge substrate. These surface undulations are anticipated to degrade the quality of epitaxial GaAs-like structures grown on as-transferred Ge/Si wafer-bonded epitaxial templates.

6.1.2 Epitaxially Grown Structures

6.1.2.1 Triple-Junction Solar Cell Structures

MOVPE growth of triple-junction solar cell heterostructures on as-bonded Ge/Si epitaxial templates was performed using $(\text{CH}_3)_3\text{Ga}$ and AsH_3 precursors for GaAs cell growth and $(\text{CH}_3)_3\text{Ga}$, $(\text{CH}_3)_3\text{In}$, and PH_3 precursors for GaInP cell growth. The peak temperature during the process was 750°C with a growth temperature of $\sim 650^\circ\text{C}$. The triple-junction solar cell structure consists of a GaAs buffer layer followed by two active subcell regions – a GaAs subcell and a $\text{Ga}_{0.5}\text{In}_{0.5}\text{P}$ subcell – with each subcell consisting of thin heavily-doped n-type emitters on a thick p-type base. The active subcells are separated by tunnel-junction structures. (Once again, the precise growth and structure details are proprietary knowledge of Tecstar, now owned by Emcore.)¹

Figure 6.2 shows a cross-sectional scanning electron microscope (SEM) image of the triple-junction solar cell structure grown on an epi-ready bulk Ge substrate and on an as-transferred Ge/Si wafer-bonded epitaxial template. The structure grown on the bulk Ge substrate shows

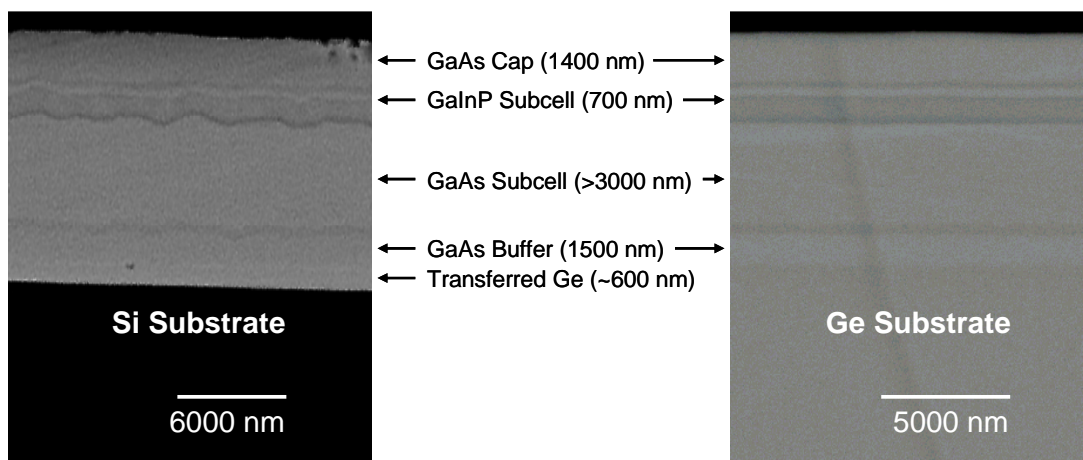


Figure 6.2 A cross-sectional SEM image of a triple-junction solar cell structure fabricated on an as-transferred Ge/Si wafer-bonded epitaxial template (left) and a bulk Ge substrate (right), showing the transferred Ge film, the GaAs buffer layer, the GaAs and GaInP subcells, and the GaAs cap layer, as well as the intervening tunnel junctions.

greater growth uniformity relative to the structure grown on the as-transferred Ge/Si wafer-bonded epitaxial template. This is especially apparent in the interface between the GaAs and GaInP subcells, where the roughness of the interface in the solar cell fabricated on the Ge/Si structure has a roughness of >300 nm, while the same interface in the solar cell grown on bulk epi-ready Ge is smooth to within the resolution of the SEM.

PL spectra and time resolved photoluminescence (TRPL) spectra were measured in the heavily-doped GaAs top contact layer in a control sample grown on bulk Ge and structures grown on Ge/Si wafer-bonded epitaxial templates. PL measurements were performed with an argon pump laser operated at 457 nm and a power of 25 mW with a 50 μm diameter spot size. PL spectra of the top GaAs contact layer indicate comparable GaAs band-edge emission intensity at ~ 880 nm for the solar cell structure grown on the bulk Ge control and the best performing solar cell structure grown a Ge/Si wafer-bonded epitaxial template (see Fig. 6.3). Because the heavily-doped GaAs contact layer was optically thick at this wavelength, PL was not observed in the $\text{Ga}_{0.5}\text{In}_{0.5}\text{P}$ or the GaAs bases of their respective subcells, both of which are expected to exhibit higher lifetime and superior material quality to the heavily-doped GaAs contact layer.

TRPL measurements were performed at National Renewable Energy Laboratory (NREL) with a 600 nm pump laser operated at a repetition rate of 1000 kHz. The samples were maintained at 293 K during the measurement. TRPL measurements of the GaAs top contact layer shown in Fig. 6.4 indicate short but comparable decay time constants of 0.23 ns for the bulk Ge sample and 0.20 ns for the best performing Ge/Si sample measured, indicating comparable minority carrier lifetimes in the two structures. However, the GaAs contact layer is not passivated by wide-bandgap cladding layers, thus shortening the minority carrier lifetime due to a high recombination velocity at the exposed surface. Additionally, the heavy doping in the GaAs contact layer also limits the minority carrier lifetime in this layer. It is likely that these factors limit the lifetime in the control sample grown on bulk epi-ready Ge, degrading the quantitative value of the lifetime comparison. The use of GaAs DHs for future testing will improve the quantitative nature of the

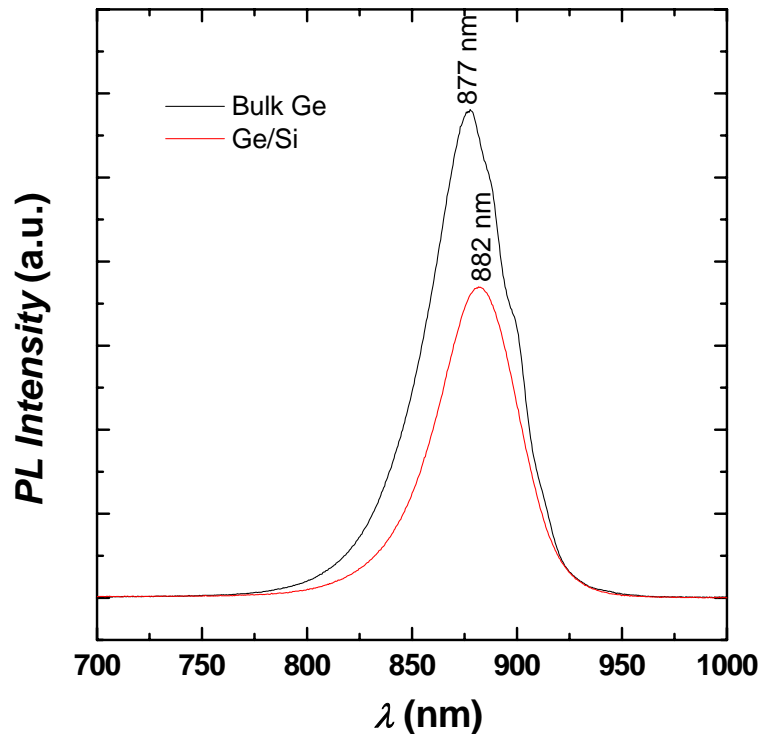


Figure 6.3 Representative PL spectra from the GaAs capping layer of a triple-junction solar cell structure grown on a Ge/Si wafer-bonded epitaxial template and a bulk Ge substrate, showing comparable intensity between the two structures.

lifetime measurements. By varying the base thickness in such structures, the GaAs minority carrier lifetime can be extracted from the measured decay time which is impacted by both the minority carrier lifetime due to recombination within the bulk GaAs and surface recombination at the GaAs top surface.^{2,3}

Selective etching was used to expose the $\text{Ga}_{0.5}\text{In}_{0.5}\text{P}$ subcell, and PL spectra, shown in Fig. 6.5, were obtained using the same pump probe conditions as described above for measurement of the GaAs contact layer. The PL spectra show comparable $\text{Ga}_{0.5}\text{In}_{0.5}\text{P}$ band-edge emission intensity in triple-junction solar cell structures grown on bulk Ge and Ge/Si wafer-bonded epitaxial templates, with the integrated intensity for the $\text{Ga}_{0.5}\text{In}_{0.5}\text{P}$ subcell grown bulk Ge having approximately twice the integrated PL intensity of the subcell grown on the Ge/Si wafer-bonded

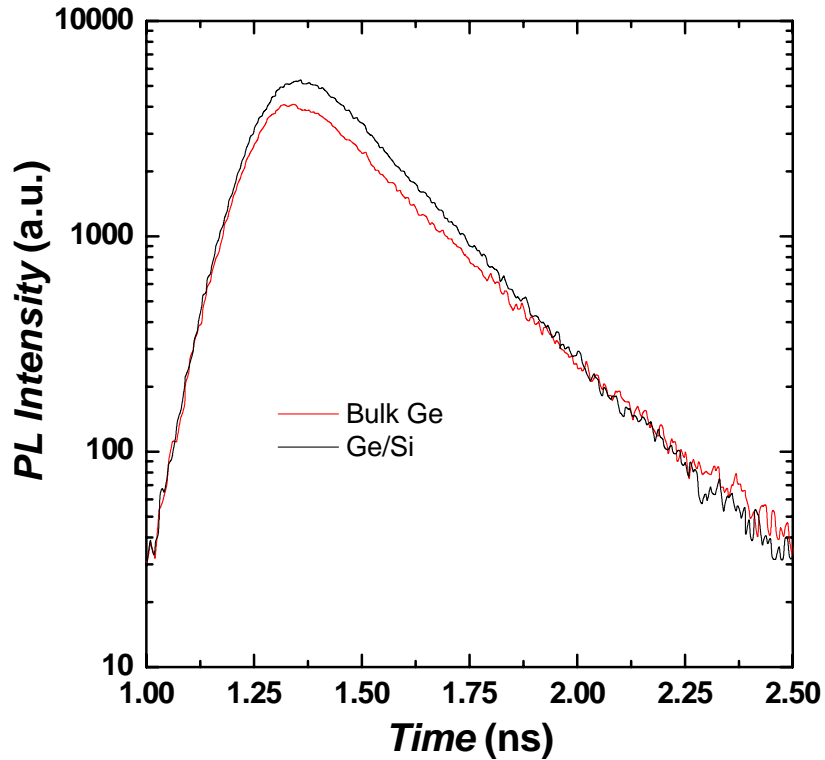


Figure 6.4 TRPL data for the best measured photoluminescence decay for the GaAs capping layer in a triple-junction solar cell structure grown on both a Ge/Si wafer-bonded epitaxial template and a bulk Ge control.

epitaxial template. The double peak at the top of the $\text{Ga}_{0.5}\text{In}_{0.5}\text{P}$ PL peak on the Ge/Si wafer-bonded epitaxial template is not fully understood, but is possibly an optical artifact due to scattering of the pump laser at the rough surface relative to the structure grown on bulk Ge. The red-shift of the $\text{Ga}_{0.5}\text{In}_{0.5}\text{P}$ emission on the Ge/Si structure is possibly due to the presence of increased strain in the $\text{Ga}_{0.5}\text{In}_{0.5}\text{P}$ subcell grown on the Ge/Si wafer-bonded epitaxial template or to the presence of ordering of the cation sublattice in the $\text{Ga}_{0.5}\text{In}_{0.5}\text{P}$ subcell on the Ge/Si wafer-bonded epitaxial template, both of which are known to cause bandgap narrowing.⁴⁻⁷

The growth of triple-junction solar cell structures on wafer-bonded Ge/Si templates has shown that optically-active III-V semiconductors can be epitaxially grown on the surface of Ge/Si wafer-bonded epitaxial templates. However, the diminished optical and electrical performance

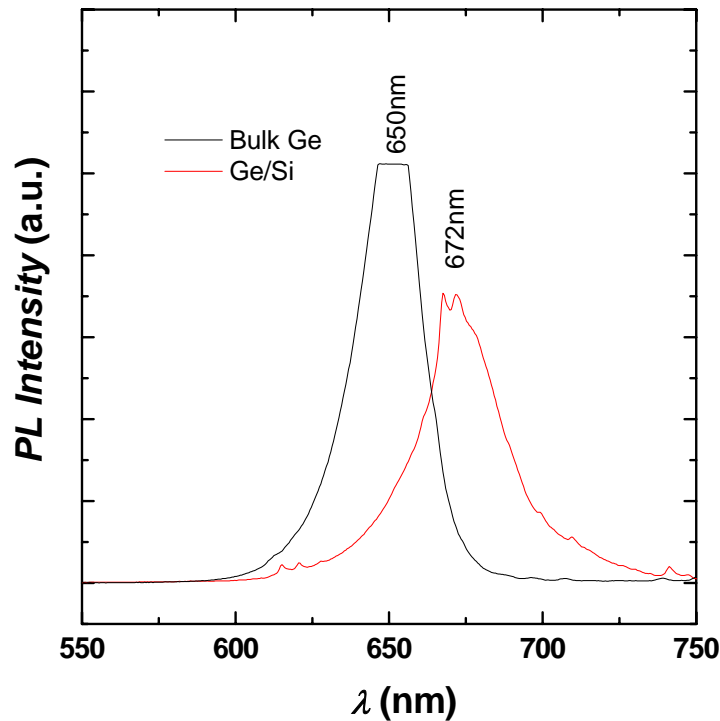


Figure 6.5 Representative PL spectra from the GaInP subcell of a triple-junction solar cell structure grown on a Ge/Si wafer-bonded epitaxial template and a bulk Ge substrate, showing comparable intensity between the two structures, but with a significant red shift of the peak position for the GaInP layer grown on a Ge/Si .

relative to the control grown on bulk epi-ready Ge illustrates the need for further improvement of the epitaxial surface of the Ge/Si wafer-bonded epitaxial templates.

6.1.2.2 Ge Homoepitaxy

As was mentioned in §6.1.1, the as-transferred Ge/Si surface morphology is undesirable for GaAs heteroepitaxy. Additionally, as the transmission electron microscopy (TEM) study of the exfoliation process in §4.1.3.1 showed, the ion-implantation and subsequent H-induced exfoliation process results in a dense network of surface fractures and extended defect structures such as H platelets. The presence of these defects, along with the extreme surface morphology of as-transferred Ge/Si wafer-bonded epitaxial templates, degrades the quality of subsequent

epitaxy. Ge homoepitaxy on as-transferred Ge/Si wafer-bonded epitaxial templates was used to improve the surface morphology. Additionally, the propagation of threading dislocations from the heavily-damaged as-transferred Ge/Si surface was studied using this model system in which the surface morphology of the as-transferred Ge film does not lead to the formation of defects during epitaxy nucleation.

Ge homoepitaxial films were grown on as-transferred Ge/Si wafer-bonded epitaxial templates using molecular beam epitaxy (MBE). The Ge homoepitaxy was grown on samples at both 450 and 500°C with growth rates of 0.1 nm s⁻¹. The homoepitaxial films of a total thickness of both 250 and 500 nm were grown. *In-situ* reflection high-energy electron diffraction (RHEED) monitoring showed diffraction spots at the onset of growth indicating that the as-transferred Ge surface is rough and the diffraction is occurring three-dimensionally. Figure 6.6 shows the post-growth RHEED pattern for a 250 nm thick Ge homoepitaxial film grown at 450°C. The observation of Bragg rods indicates that the post-growth surface is sufficiently smooth to form a two-dimensional diffraction surface. The appearance of two diffraction rings is attributed to an azimuthal twist between the Ge transferred film and the underlying Si substrate. The ring offset to the right is caused by diffraction from Ge heteroepitaxially grown on the Si handle substrate. The thickness of the film is such that the Ge film on the Si substrate has relaxed to the Ge lattice constant, resulting in the same spacing between the Bragg rods for the MBE Ge film grown on the Si substrate as the Ge film grown on the as-transferred Ge/Si surface.

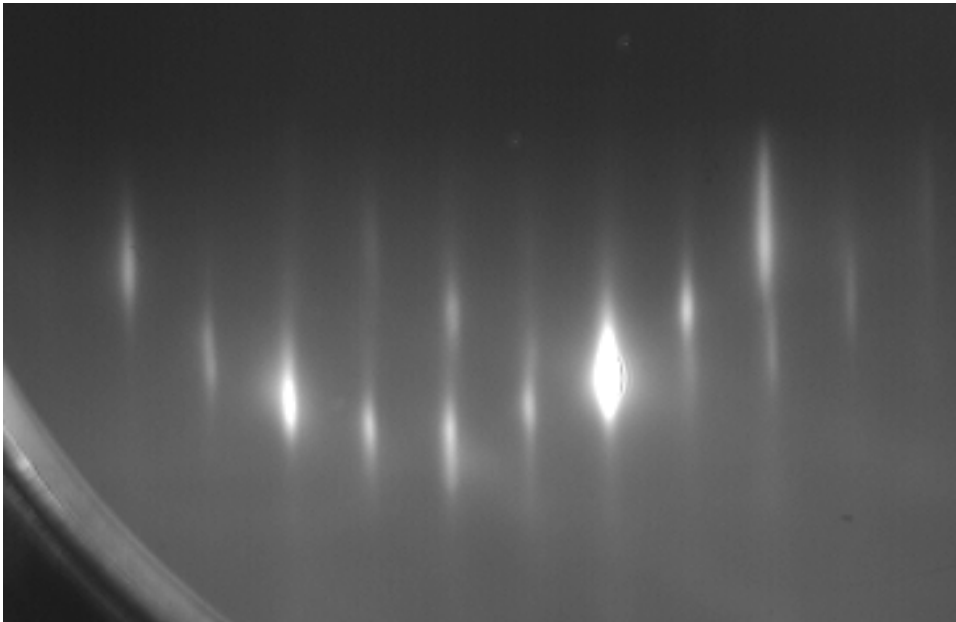


Figure 6.6 The post-growth RHEED pattern of a 250 nm thick Ge homoepitaxial layer grown at 450°C on a Ge/Si substrate at 0.1 nm s⁻¹. The primary RHEED pattern is formed by diffraction from the Ge transferred film, while the offset RHEED pattern is formed by diffraction from Ge grown epitaxially on the Si handle wafer. The offset is attributed to the slight twist between the substrates.

AFM analysis of the surface of the Ge homoepitaxial film shows a significant reduction of the surface roughness from ~10 nm-rms to 2.3 nm-rms for a 250 nm thick film grown at 450°C and 4.5 nm rms for a 250 nm thick film grown at 500°C. As shown in Fig. 6.7, the surface of the film exhibits a mesa-like morphology with extended regions of smooth surface punctuated with deep surface depressions attributed to minimization of the strain energy surrounding threading dislocations during Ge epitaxy. It is estimated that the Ge homoepitaxial films have a threading dislocation density of $>10^7$ cm⁻². This dislocation density has been shown to significantly degrade the minority carrier lifetime of GaAs with reported values of less than 2 ns.⁸ The cross-sectional TEM (XTEM) micrograph in Fig. 6.8 shows that the origin of these threading dislocations is at the interface between the as-transferred Ge/Si surface and the homoepitaxial Ge film. This suggests that the density of threading dislocations can be reduced by removal of the near-surface damage present in the as-transferred Ge film.

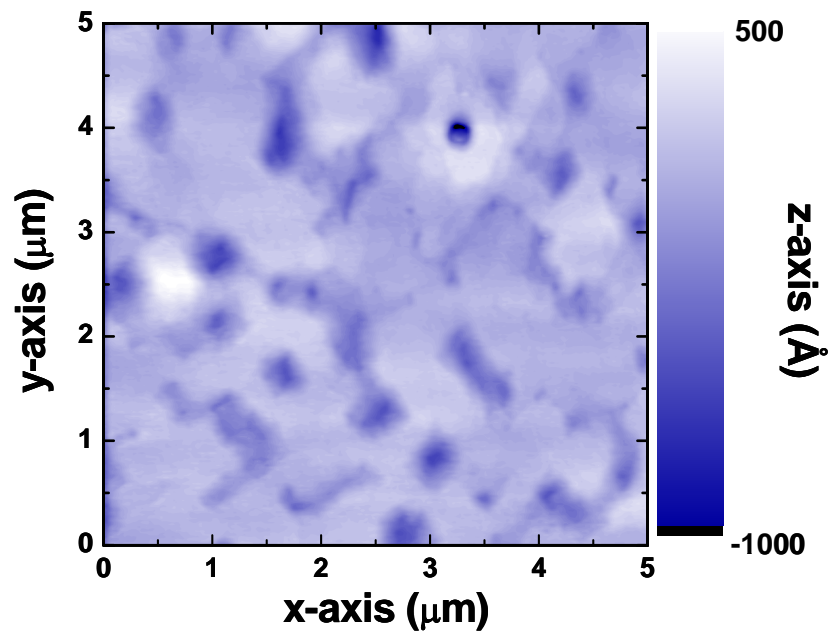


Figure 6.7 AFM images of the surface of a 250 nm thick Ge homoepitaxial buffer layer grown on a Ge/Si wafer-bonded structure at a growth rate of 0.1 nm s^{-1} and a growth temperature of 450°C .

6.1.3 Conclusions

Epitaxial templates fabricated using wafer bonding and H-induced layer transfer have been used for the growth of III-V compound-semiconductor triple-junction solar cell structures. Characterization of these structures shows that the GaAs and $\text{Ga}_{0.5}\text{In}_{0.5}\text{P}$ constituents are optically active. This is the first known demonstration of optically active III-V semiconductors grown on Ge/Si wafer-bonded epitaxial templates formed using H-induced exfoliation. However, the optical and electrical properties of the III-V materials are of lower performance than control structures grown on bulk Ge. The study of the surface with AFM and the use of Ge homoepitaxy and XTEM suggest that the cause of the reduced material performance is two-fold:

- the as-transferred Ge surface has significantly higher roughness and local variation of miscut angle relative to bulk Ge leading to poor nucleation of the GaAs epitaxial layer relative to a bulk Ge substrate; and ,

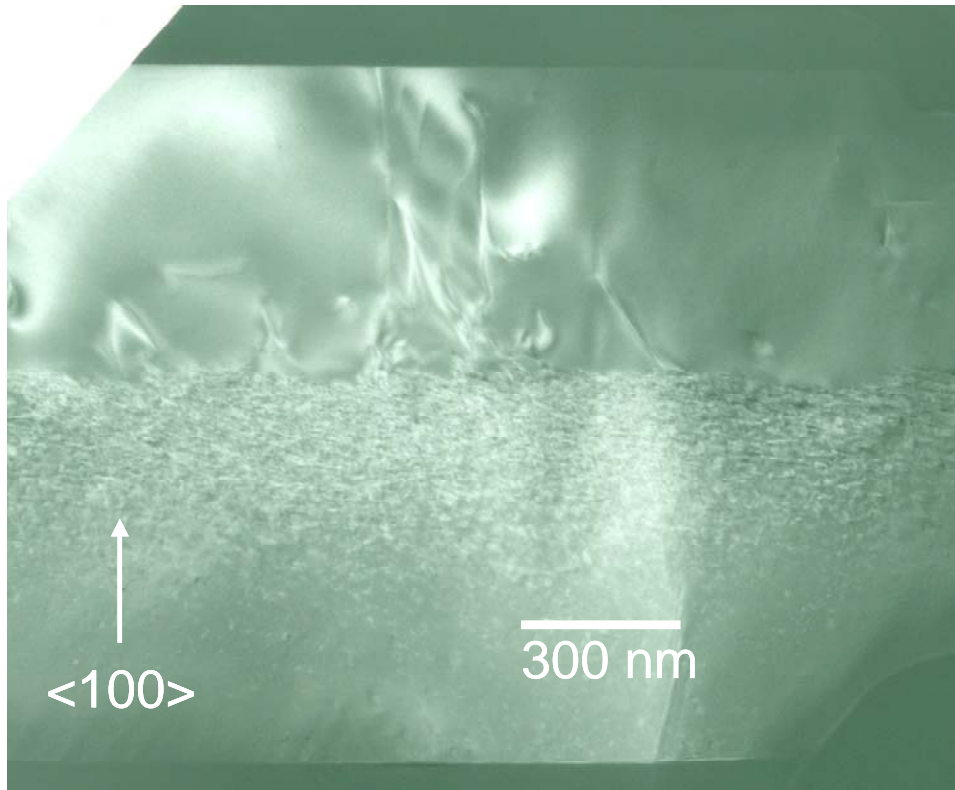


Figure 6.8 XTEM image of a ~500 nm thick Ge homoepitaxial film grown at a temperature of 500°C and a growth rate of 0.1 nm s^{-1} on a Ge/Si wafer-bonded epitaxial template, showing the origin of threading dislocations at the interface between the transferred film and the homoepitaxial layer.

- damage in the near surface region of the as-transferred Ge layer caused by the ion implantation and fracture processes leads to propagation of threading dislocations in the epitaxial film.

However, these challenges associated with epitaxial growth on Ge/Si are of a technical nature. They are not fundamental limitations of the Ge/Si system and can be overcome by the removal of damage and roughness from the near surface region of the transferred Ge film.

6.2 *Epitaxy on InP/Si Heterostructures*

The growth of III-V semiconductors on Ge/Si wafer-bonded epitaxial templates shows the promise of using wafer bonding and layer transfer to enable the integration of traditional multi-junction solar cell structures with optimized handle substrates. In this section the growth of

optically active III-V semiconductors on InP/Si wafer-bonded epitaxial templates is demonstrated. Heteroepitaxial growth on InP/Si wafer-bonded epitaxial templates is essential for enabling the fabrication of the novel four-junction solar cell structure described in §1.3.2.^{9,10} Additionally, such structures could improve the economics of radiation-hard InP-based multi-junction cells by reducing the considerable cost of the epitaxial substrate.¹¹

6.2.1 Growth Surface

6.2.1.1 As-Transferred InP/Si Surface

The nucleation of III-V semiconductors during homoepitaxial or heteroepitaxial growth is generally less complicated than the nucleation of III-V semiconductors in polar on non-polar epitaxy characteristic of the GaAs/Ge system. This is primarily due to the lower propensity for the epitaxial layer to form anti-phase domain boundaries at the edge of surface steps on the epitaxial template. However, three-dimensional growth can arise from the ripening of growth islands on a rough surface. For these reasons it is less essential, but still desirable, that the growth surface of InP/Si wafer-bonded epitaxial templates be reasonably smooth. As reported in §3.2.2.1, AFM measurements indicate that the as-transferred roughness of InP/Si wafer-bonded epitaxial templates is ~10 nm-rms.

6.2.1.2 Surface Modification for Epitaxy

In addition to studying III-V epitaxy on the as-transferred surface, two methods were utilized both to improve the surface morphology for epitaxy and to remove the heavily-damaged near-surface region of the transferred InP film.

The first damage removal and surface modification method used was the wet chemical etching of the surface with various ratios of 50% HCl, H₃PO₄, and 30% H₂O₂. The time-dependent surface roughness was measured by AFM for dilution ratios of 1:2:2, 1:2:4, and 1:2:5

HCl: H₃PO₄: H₂O₂ and is reported in Fig. 6.9. XTEM was used to verify that the heavily-damaged surface layer of the transferred InP film was removed by 20 seconds of etch time.

Also shown in Fig. 6.9 is the roughness measured by AFM following chemical mechanical polishing (CMP) using a Logitech PM5 polisher with a colloidal alumina slurry in a sodium hypochlorite solution. Following CMP the InP surface is relatively smooth, but the polish process leaves scratches in the surface observable by AFM. These scratches are possibly due to film delamination that releases pieces of film that scratch the InP surface as the delaminated InP film is dragged across the InP surface by the pad rotation. The presence of these scratches could also be attributed to general cleanliness problems with the polish system. Recent results by Hayashi *et*

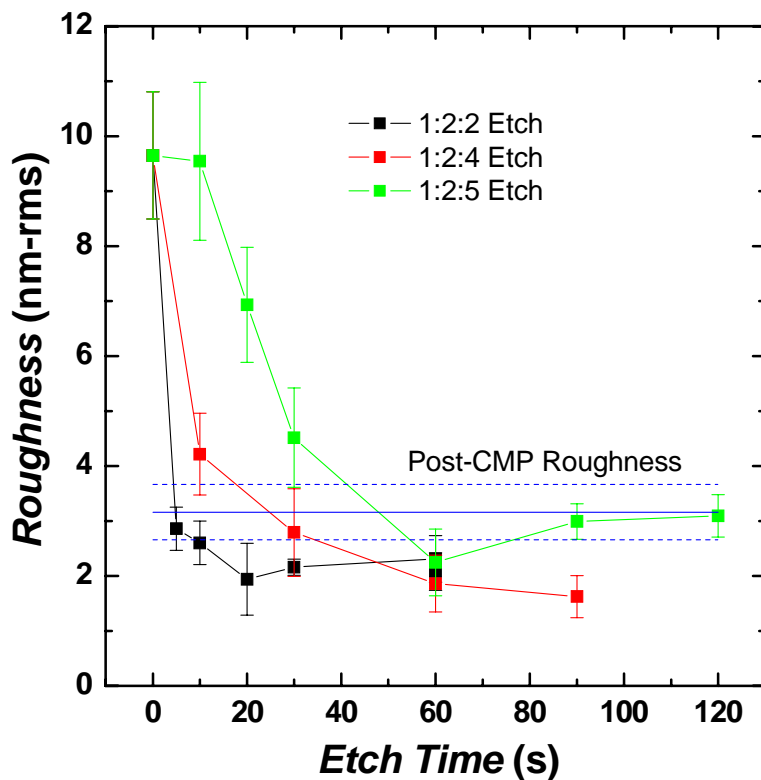


Figure 6.9 InP/Si surface roughness as a function of etch time and dilution ratio for a HCl:H₃PO₄:H₂O₂ wet etch, showing up to an 80% reduction in roughness. Also shown is the post-polish roughness (shown in blue) of an InP/Si wafer-bonded heterostructure following a CMP process, with error bars illustrated by dashed lines.

al. indicate that the use of a zero-solids polish solution yields superior surface morphology with less scratching than standard sodium hypochlorite slurries.¹²

6.2.2 Epitaxial Growth of InGaAs Double-Heterostructures

The suitability of InP/Si wafer-bonded epitaxial templates for InP growth was investigated by growing a lattice-matched InP/In_{0.53}Ga_{0.47}As/InP DH with atmospheric-pressure MOVPE. Structures were grown on an as-transferred InP/Si wafer-bonded template along with InP/Si wafer-bonded templates following surface modification with either an HCl: H₃PO₄: H₂O₂ chemical etch or a CMP process. All InP/Si wafer-bonded templates were fabricated with (100)InP. A DH was also grown on a bulk (100)InP control substrate. In all cases the growth was performed at 620°C with a V/III ratio of 120 for the growth of InP and 10 for the growth of In_{0.53}Ga_{0.47}As. The growth rate in both cases was 100 nm min⁻¹. Each layer of the DH is 1000 nm thick.

PL spectra of In_{0.53}Ga_{0.47}As DHs grown on a variety of InP/Si wafer-bonded epitaxial templates and bulk InP test samples, shown in Fig. 6.10, were measured at room temperature with a 1064 nm pump wavelength with a 10 μm diameter spot with a pump power of 25 mW. Shown in Fig. 6.10 are spectra for the following conditions:

- bulk (100)InP control,
- bulk (100)InP etched for 45 seconds in 1:2:2 HCl: H₃PO₄: H₂O₂,
- bulk (100)InP etched for 60 seconds in 1:2:4 HCl: H₃PO₄: H₂O₂,
- bulk (100)InP processed by CMP,
- wafer-bonded InP/Si as-transferred,
- wafer-bonded InP/Si etched for 45 seconds in 1:2:2 HCl: H₃PO₄: H₂O₂,
- wafer-bonded InP/Si etched for 60 seconds in 1:2:4 HCl: H₃PO₄: H₂O₂, and
- wafer-bonded InP/Si processed by CMP.

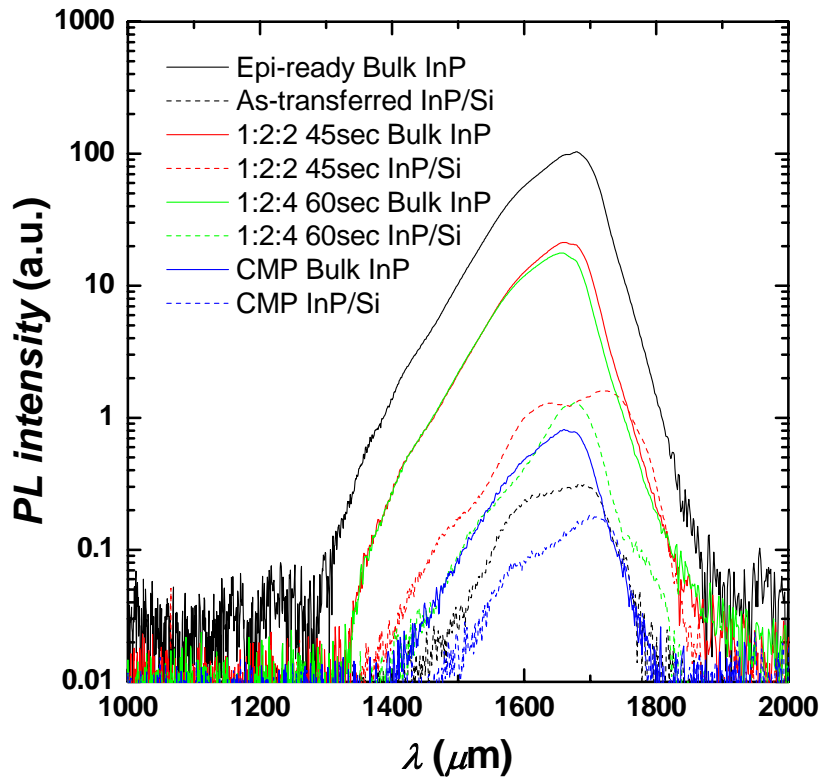


Figure 6.10 PL spectra from InP/In_{0.53}Ga_{0.47}As/InP DHs grown on bulk InP and InP/Si wafer-bonded epitaxial templates both unprocessed and processed with chemical etching with 1:2:2 and 1:2:4 ratios of the HCl: H₃PO₄: H₂O₂ etch or CMP with a sodium hypochlorite slurry.

The observed band-edge emission from the In_{0.53}Ga_{0.47}As base in these structures varies in shape and intensity depending on the processing of the sample. As is shown in Fig. 6.10, the strongest, most regular band-edge emission is observed for the bulk epi-ready InP control. The PL spectra show that any additional processing degrades the optical quality of the DH structure. The PL peak intensity and emission wavelength information is summarized for each condition in Tab. 6.1.

The origin of the observed degradation of PL intensity can be attributed either to optical geometry changes from sample to sample or to degradation of the electrical properties of the In_{0.53}Ga_{0.47}As base. Variations in the DH surface morphology lead to variation of the coupling efficiency of the pump laser into the DH and to variation of the coupling efficiency of PL out of

the structure to the detector. To make sense of the results it is assumed that this is a secondary effect relative to the degradation of the optical and electrical properties of the $\text{In}_{0.53}\text{Ga}_{0.47}\text{As}$ base that are correlated with decreased minority carrier lifetime. The decreased minority carrier lifetime of the DH is, in turn, attributed to defects that are incorporated in the $\text{In}_{0.53}\text{Ga}_{0.47}\text{As}$ base during growth. Defects that degrade minority carrier lifetime in the $\text{In}_{0.53}\text{Ga}_{0.47}\text{As}$ DH can originate from the following conditions:

- threading dislocations in the bulk in the InP substrate or InP transferred film that propagate up through the DH,
- dislocations that originate from the growth surface caused by surface contamination or epitaxy nucleation, or
- dislocations that form to relieve strain during growth.

It is likely that plastic deformation to relieve strain during growth does not impact the lifetime of these structures, because the $\text{In}_{0.53}\text{Ga}_{0.47}\text{As}$ composition was selected to be lattice matched to bulk InP at the growth temperature. There is strain in the InP thin film in wafer-bonded InP/Si structures at the growth temperature due to the differences in the coefficient of thermal expansion between the two materials. Assuming that the zero-stress temperature is approximately the bonding temperature of 25°C, the InP film should be compressively strained at the growth temperature of 620°C by 0.066%. The critical thickness of a compressively strained InP epitaxial film grown at this strain is >300 nm.¹³

The fact that damage removal by both chemical etching and CMP processing of bulk InP degrades the optical properties of DHs grown on these structures suggests that these etch processes are introducing defects that originate at the growth surface. These defects are due to changes in the nucleation of the InP epitaxial film caused by surface contaminants, surface imperfections, or changed surface morphology. For any material removal process it is assumed that there is a limiting surface morphology that forms after the removal of a substantial amount of material. This limiting surface morphology should be independent of the starting surface

morphology. One possible explanation for the weak PL intensity from DHs grown on the chemically etched and CMP processed InP/Si wafer-bonded epitaxial templates relative to DHs grown on bulk InP that received the same surface treatment is that the surface has not yet reached the limiting surface morphology. This would suggest that the processes pursued in this study should be further optimized to result in surfaces that are optimized for III-V heteroepitaxy on InP.

As shown in Fig. 6.10 and Tab. 6.1, in addition to reduced PL emission intensity in DHs grown on InP/Si wafer-bonded epitaxial templates relative to DHs grown on bulk InP, the peak position of the $\text{In}_{0.53}\text{Ga}_{0.47}\text{As}$ emission varies from condition to condition. The origin of this variation is not yet fully understood, but as with triple-junction solar cells grown on Ge/Si wafer-bonded epitaxial templates described in §6.1.2.1, it is reasonable that the variation of the peak intensity is attributable to strain in the epitaxial structure or to ordering of the cation sublattice. In addition to the variation of the peak position, there are multiple-peaks observed in some of the spectra. The observation of multiple peaks in spectra from DHs grown on InP/Si wafer-bonded epitaxial templates could be due to scattering from the DH surface, but it is also possible that these peaks are associated with defect states in the $\text{In}_{0.53}\text{Ga}_{0.47}\text{As}$ base that change the mode of PL emission.

Table 6.1 The $\text{In}_{0.53}\text{Ga}_{0.47}\text{As}$ PL emission peak position and intensity relative to a control DH grown on bulk epi-ready InP for all of the surface conditions tested.

Sample Condition	Peak Position (nm)	Relative Peak Intensity
Bulk InP	1679	1.0000
As-transferred InP/Si	1687	0.0031
1:2:2 45 sec etched bulk InP	1660	0.2068
1:2:2 45 sec etched InP/Si	1722	0.0155
1:2:4 60 sec etched bulk InP	1657	0.1715
1:2:4 60 sec etched InP/Si	1679	0.0126
CMP processed bulk InP	1661	0.0079
CMP processed InP/Si	1706	0.0018

6.2.3 Conclusions

The first known demonstration of III-V epitaxy on InP/Si structures formed by wafer bonding and H-induced exfoliation has been achieved by fabrication of optically-active InP/In_{0.53}Ga_{0.47}As/InP DHs. The intensity of the band-edge emission from the In_{0.53}Ga_{0.47}As base on these structures is significantly diminished relative to structures grown on bulk InP control substrates. However, the application of damage removal and surface smoothing processes to the transferred InP film has been shown to reduce the surface roughness and improve the emission intensity of DHs grown on InP/Si wafer-bonded structures.

6.3 Summary

Ge/Si and InP/Si wafer-bonded templates have been used to demonstrate the first known III-V epitaxy on structures fabricated using H-induced exfoliation. The PL emission intensity is reduced on wafer-bonded templates relative to emission from III-V epitaxy grown on bulk semiconductor control samples. However, in the case of InP/Si, damage removal and surface modification with chemical etching and CMP has been shown to enable significant improvement of the emission intensity. Further optimization of the damage removal technique and its application to Ge/Si structures holds the promise of improved performance of wafer-bonded epitaxial templates. The results presented in this chapter represent an important step toward wafer-bonding enabled material integration for revolutionary photovoltaic structure fabrication.

6.4 *References*

- ¹ J. M. Zahler, C.-G. Ahn, S. Zaghi, H. A. Atwater, C. Chu, and P. A. Iles, *Thin Solid Films* **403-404**, 558-562 (2002).
- ² R. R. King, J. H. Ermer, D. E. Joslin, M. Haddad, J. W. Eldredge, N. H. Karam, B. M. Keyes, and R. K. Ahrenkiel, in *Double heterostructures for characterization of bulk lifetime and interface recombination velocity in III-V multijunction solar cells*, Vienna, Austria, 1998, p. 86-90.
- ³ R. K. Ahrenkiel, B. M. Keyes, and S. Johnston, *Surface Engineering* **16**, 1-7 (2000).
- ⁴ G. B. Stringfellow, *MRS Bulletin* **22**, 27-32 (1997).
- ⁵ E. Zolotoyabko, A. Godner, and Y. Komem, *Physical Review B* **60**, 11014-11025 (1999).
- ⁶ K. Uchida, P. Y. Yu, N. Noto, Z. Lilientalweber, and E. R. Weber, *Philosophical Magazine B* **70**, 453-466 (1994).
- ⁷ K. Uchida, P. Y. Yu, N. Noto, and E. R. Weber, *Applied Physics Letters* **64**, 2858-2860 (1994).
- ⁸ R. M. Sieg, J. A. Carlin, J. J. Boeckl, S. A. Ringel, M. T. Currie, S. M. Ting, T. A. Langdo, G. Taraschi, E. A. Fitzgerald, and B. M. Keyes, *Applied Physics Letters* **73**, 3111-3113 (1998).
- ⁹ J. M. Zahler, A. Fontcuberta i Morral, C.-G. Ahn, H. A. Atwater, M. W. Wanlass, C. Chu, and P. A. Iles, in *Wafer bonding and layer transfer processes for 4-junction high efficiency solar cells*, New Orleans, 2002.

- ¹⁰ A. Fontcuberta i Morral, J. M. Zahler, H. A. Atwater, M. M. Frank, Y. J. Chabal, P. Ahrenkiel, and M. W. Wanlass, in *Electrical and structural characterization of the interface of wafer bonded InP/Si*, San Francisco, 2003.
- ¹¹ G. P. Summers, R. J. Walters, S. R. Messenger, and E. A. Burke, *Progress in Photovoltaics: Research and Applications* **4**, 147-154 (1996).
- ¹² S. Hayashi, M. S. Goorsky, R. Sandhu, and M. Wojtowicz, in *Processing issues for wafer bonded III-V on insulator structures*, Kagoshima, Japan, 2004.
- ¹³ J. Y. Tsao, *Materials Fundamentals of Molecular Beam Epitaxy* (Academic Press, Boston, 1993).

Chapter 7: Conclusions and Future Work

In the preceding chapters, the promise of wafer-bonding enabled photovoltaic devices was explored. Furthermore, the basic processes necessary for the fabrication of these structures were demonstrated, while fundamental physical mechanisms of the exfoliation process and the electrical properties of the bonded interface were explored. In the following section, the key conclusions of the previous chapters are reiterated. In §7.2 future work necessary to advance both the practice and understanding of materials integration through wafer bonding and layer transfer is proposed.

7.1 Conclusions and Key Results

In Chapter 2 fundamental limitations of photovoltaic efficiency were explored using the detailed-balance method. The detailed-balance analysis for single-junction solar cells illustrates the effects of temperature, concentration and optical geometry on the performance of the cell. Generally speaking, it is desirable to operate a solar cell at low temperatures under extreme concentration. In addition to the single-junction cell, conventional dual- and triple-junction cells were evaluated to assess the performance improvements that are achievable in these devices through wafer-bonded integration of non-lattice-matched semiconductors.

The limiting efficiency for several wafer-bonding enabled solar cell designs were explored with the detailed-balance model. These calculated efficiencies show the merit of pursuing the development of these devices. The use of an active Si subcell in a replacement Ge/Si substrate for

a triple-junction solar cell was shown to improve performance relative to a dual-junction solar cell. Despite this gain in efficiency, an active-Si wafer-bonded triple-junction solar cell still underperforms a conventional triple-junction. However, the added benefits of higher specific power and better thermal conductivity of the handle substrate offset these slight efficiency performance losses for terrestrial use under concentration. Additionally, wafer-bonding enabled four-junction designs were proposed that would enable record-setting efficiencies. Of particular promise is the idea of using a Si substrate that doubles as an active subcell along with a Ge subcell on the back surface. This Si/Ge support substrate would be used as a handle for a GaAs thin epitaxial template on which to epitaxially grow III-V compound semiconductor subcells of 2.00 and 1.49 eV bandgaps to fabricate a cell that very nearly matches the subcell band gaps of an optimal four-junction cell. Finally, the promise of a five-junction solar cell consisting of independently-connected subcells wafer bonded in a mechanical stack that separates the subcells with a low refractive index material such as sapphire was demonstrated, and a limiting efficiency in excess of 60% was predicted.

In Chapter 3 a generalized wafer bonding process was described for the fabrication of Ge/Si and InP/Si virtual substrates. This method and several variations on the method were shown to enable transfer of thin Ge and InP films on the order of mm^2 to cm^2 to Si handle substrates. The surface morphology of these structures was shown to have a surface roughness of 10 to 20 nm rms. The degree of roughness was shown to be a function of the miscut angle in the material system. Additionally, the general challenges for wafer bonding were summarized as they apply to the Ge/Si and InP/Si materials systems, and specific challenges associated with the bonding of dissimilar materials were also evaluated for Ge/Si and InP/Si structures. Specifically, it was shown that not only must the bonding surface roughness be minimized, but also the lateral wavelength of surface roughness must be maximized to facilitate bonding. Additionally, particles with diameters in excess of $0.2 \mu\text{m}$ were shown to be unacceptable at the bonded interface. The coefficient of thermal expansion mismatch associated with wafer bonding of dissimilar materials

was shown to be especially problematic for the Ge/Si system, where temperature excursions of more than 150°C from the bond initiation temperature can not be tolerated in large area substrates.

In Chapter 4 the evolution of infrared spectra upon annealing was used to deduce the chemical states of hydrogen in H-implanted Ge and InP that lead to the exfoliation process. The use of MIT-mode FTIR spectroscopy with polarization was used to determine the dipole orientation of defects that lead to exfoliation. This was particularly effective in the case of Ge, in which it was shown that point defects caused during implantation serve as binding sites for hydrogen during implantation and at low temperatures, but release that hydrogen upon annealing. This hydrogen then diffuses to agglomerated defect structures that trap hydrogen, either by further growth of the defect structure or as molecular H₂ gas that then provides the internal pressure required to separate internal surfaces and form micro-cracks that precede exfoliation. TEM images and a comparison to previous studies of the H-induced exfoliation of Si suggest that these agglomerated defect structures that lead to micro-cracks are oriented along (100) platelet structures.

The evolution of transmission-mode FTIR spectra upon annealing in H-implanted InP show that In-H stretching modes at 1600 and 1705 cm⁻¹ are stable upon annealing. This suggests that the preferential formation of vacancies in the anion sublattice during implantation makes the H-induced exfoliation process more challenging in InP due to gettering of hydrogen at these sites from which it is not released to facilitate the exfoliation process in InP. The evolution of P-H stretching modes upon annealing suggests that hydrogen is released from discrete defects and then diffuses to extended defect structures where it facilitates the exfoliation process by providing the internal pressure and passivating hydrogen necessary to enlarge these defects. The use of polarized MIT-mode spectroscopy suggests that the discrete defect distribution is skewed toward the implanted surface of the InP substrate, and the extended defects that lead to exfoliation are found at the end of range, as indicated by XTEM micrographs.

In Chapter 5, Ohmic, low-resistance wafer-bonded interfaces were demonstrated for heavily doped Ge/Si and InP/Si hydrophobically wafer bonded pairs. Furthermore, the measured specific resistance of less than $0.16 \Omega \text{ cm}^{-2}$ was shown to be independent of the azimuthal twist angle orientation. The observed linear J - V behavior for both Ge/Si and InP/Si is surprising in light of the anticipated band offset diagrams of these structures. Leakage paths due to interfacial defect states are indicated as a possible explanation for this linear J - V behavior. However, the nature of these defects is different in the two structures, with the defects in Ge/Si attributed to interfacial dislocation structures and the defects in InP/Si related to defect states in an InP-oxide that forms upon annealing.

The role of interfacial dislocations in the electrical properties of Ge/Si wafer-bonded heterostructures was elucidated by studying Schottky-like p^+ -Ge/ p -Si wafer-bonded isotype heterostructures. As-bonded, these p^+ -Ge/ p -Si structures have an effective barrier height of 0.74 eV. Upon annealing the effective barrier height is reduced to 0.47 to 0.54 eV depending on anneal time and azimuthal twist angle of the bonded structures. Additionally, the annealed samples indicated that a shunt leakage path is present that is dependent upon the anneal-time duration and the azimuthal twist angle. These results suggest that the electrical properties of the effective barrier height and the shunt leakage are attributable to an interfacial dislocation network present in wafer-bonded heterostructures and the corresponding leakage paths associated with these defects.

In Chapter 6 Ge/Si and InP/Si wafer-bonded templates were used to demonstrate the first known III-V epitaxy on structures fabricated using H-induced exfoliation. The PL emission intensity was reduced on wafer-bonded templates relative to emission from III-V epitaxy grown on bulk semiconductor control samples. However, in the case of InP/Si, damage removal and surface modification with chemical etching and CMP was shown to enable significant improvement of the emission intensity.

7.2 *Future Work*

While the work of this thesis has shown the feasibility of wafer bonding and layer transfer with H-induced layer exfoliation as a means of high-performance photovoltaic device fabrication, there is ample room for improvement in both the fundamental understanding of the processes involved and in reduction of the processes to practice for the economical fabrication of next generation high performance photovoltaics.

The detailed balance reported in Chapter 2 proves the theoretical efficiency gain achievable through the integration of non-lattice-matched semiconductors to fabricate novel multi-junction solar cells. However, empirical models of solar cell efficiency are much more informative for design of real functioning devices. Such empirical models based on numerical solution of the drift and diffusion equations of carriers in a solar cell along with the optical and recombination processes in the absorber along with many other properties derived from characterization of real materials are instructive in selecting the bandgap and the doping level and thicknesses of the emitter and base of a subcell. In the case of wafer-bonding enabled solar cell designs such models can be used to determine “break-even” properties for the wafer bonded interface, such as the maximum tolerable optical power loss at wafer-bonded interfaces through due to free-carrier absorption and reflectance loss. Additionally, such empirical models can be used to establish material performance limits necessary for the addition of a new subcell to add to the power conversion of the solar cell structure. Such an analysis is essential to the further refinement of wafer-bonding enabled solar cell designs.

The wafer bonding and layer transfer processes for Ge/Si and InP/Si described in Chapter 3 demonstrate feasibility. However, much work can be done to understand the bonding process and to improve the robustness of the fabricated structures. In particular, moving to larger area substrates with more refined experimental apparatuses should improve the reproducibility of the experiments, leading to statistically significant interpretations of the bonding and layer transfer

process and ultimately to process optimization. Additionally, more robust samples would improve the results of subsequent chapters, in particular the MOCVD growth results of Chapter 6.

The spectroscopic study of the exfoliation process presented in Chapter 4 is relatively complete with respect to the spectra obtained. However, in the case of the Ge exfoliation process, better temperature and dose resolution might improve the spectral quality. Additionally, the surface contamination during caused due to background pressure during implantation could be avoided by implantation through a protective film of SiO₂. These suggestions could lead to improved spectral quality, which may in turn improve the certainty of the interpretation. However, the greatest limitation of this study is the lack of reference spectra in the literature for the specific modes shown to lead to exfoliation. To improve this situation, theoretical calculations of the vibrational modes of defect structures might shed some light, but the broad peak shape and the relative complexity of the defect structures leading to these modes could make this prohibitively difficult. To better corroborate the interpretation of the Ge exfoliation process given in Chapter 4, a forward recoil scattering analysis of the integrated hydrogen content of the implanted Ge samples as a function of annealing should be performed. Additionally, cross-sectional transmission electron microscopy (XTEM) images at all or the intermediate temperature cycles might shed some light on the structures that lead to absorption in the 2010 to 2030 cm⁻¹ range and form the precursors to exfoliation.

In the study of InP exfoliation, improved resolution of the temperature steps and dose conditions would once again improve the interpretation of the chemical states that lead to exfoliation. Additionally, as was pointed out in §4.2.3, the implant depth selected for this experiment is near an extinction node for the z-component of the electric field in the P-H stretching mode range of the FTIR spectra. By increasing (or decreasing) the implant energy, the z-axis enhancement observed for Ge exfoliation might be observed for InP, making the specific modes leading to exfoliation much more clear as was observed for Ge exfoliation.

In Chapter 5 the electrical properties of InP/Si and Ge/Si were studied as a function of the bonding process and semiconductor doping level. It is of importance for any eventual photovoltaic device fabricated on Ge/Si or InP/Si wafer-bonded structures that the bonded interface has a resistance well below the $0.16 \Omega \text{ cm}^2$ observed in the present study. However, it was noted that the materials used in the bonded structures studied here were not degenerately doped. Thus, any linear J - V behavior observed p-n heterojunctions can be attributed to leakage paths attributed to defects at the bonded interface. To improve on the specific resistance of the bonded interface, ion implantation of dopants in the shallow region near the bonded interface should reduce the resistance of the interface by enabling tunneling to occur.

The study of Schottky-like p-p isotype heterojunctions in Ge/Si would be aided by additional measurements of the temperature-dependent J - V behavior of the bonded interface. Additionally, the interpretation of the bonding process using FTIR spectra would be greatly enhanced by employing multiple internal transmission-mode FTIR to enhance the modes at the bonded interface. Additionally, the speculated mechanism of barrier height reduction proposed could be further corroborated by studying the bonded interface as a function of bond temperature using plan-view or cross-sectional TEM. This analysis was prohibited in the present study due to the fragility of the bonded structures attributed to the weak bond in the as-bonded condition and poor bonding due to thermal strain for samples annealed to 400°C . By using a focused ion beam sample preparation process, such samples should be possible to prepare.

The results of Chapter 6 are the most significant of this thesis, and yet they are the most preliminary. The fabrication of more robust wafer bonded structures is the first step toward improved demonstrations of epitaxially grown III-V semiconductors on wafer-bonded Ge/Si and InP/Si epitaxial templates. While preliminary and relatively promising studies were made for damage removal in InP/Si structures, there is much room for improvement. Much iteration is likely needed to remove the damage caused by implantation and exfoliation of the Ge and InP,

while leaving the surfaces of the transferred films suitable for epitaxy. Improved epitaxy is under continuing development.

This list of suggested future work is not intended to be exhaustive. As wafer bonding technology for photovoltaic applications evolves, particularly if it becomes commercially compelling, the depth of knowledge about the fundamental processes studied in the present study will naturally improve. However, it is my sincere belief that the work presented here demonstrates a proof of concept for the technology that can be used as a stepping stone to future development.

Appendix: MatLab Code for Detailed Balance Calculation

In the interest of space, the code used to calculate the efficiency of a four-junction solar cell operated in series connection is given. This code can be easily modified to calculate the efficiency of a different multi-junction structure or of a single-junction cell as was done in Chapter 2. The spectrum input file can be downloaded from the National Renewable Energy Laboratory.

```

clear all;

% 4-Junction series connected wafer wafer bonded solar cell model.
% The limiting current is set as the minimum operating current of the cell.

% Variable definitions:
% LL = expanded wavelength vector in microns
% PP = Watts / m^2 / micron
% T = cell operating temperature
% C = concentration of the illumination
% ni = semiconductor refractive index
% no = refractive index of covering layer
% e_em = etendue for emission from the cell
% e_int = etendue for emission internal to the cell
% E1 = top cell band gap
% E2 = bottom cell band gap
% dE = integration element for determining the radiative reemission
% Emax = energy above the band gap at which emission is assumed to stop
% Js_i = photocurrent for cell i
% dJs = photocurrent vector for integration of photocurrent
%

L = CSVREAD('AM15wavelength.txt');           %Reading wavelengths (um)
LL = CSVREAD('AM15wavelengthexpand.txt');    %Reading expanded wavelength file
(um)
P = CSVREAD('AM15power.txt');                 %Reading power (W/m2/um)

T = 300;                                     %Setting temperature to 80C
C = 100;                                     %Setting concentration
ni = 3.5;
no = 1.75;
e_em = pi;                                  %Etendue of a free surface
e_int = pi*ni^2;                             %Etendue between internal
semiconductor surfaces

%Assigning Cell Eg arrays. Ei(r,s,t,u) = bandgap of cell i for cell 1 index r,
%cell 2 index s, cell 3 index t, and cell 4 index u.

for r = 1:3,
    for s = 1:3,
        for t = 1:3,
            for u = 1:3,
                E1(r,s,t,u) = 2.05 + 0.05*(r-1);
                E2(r,s,t,u) = 1.60 + 0.05*(s-1);
                E3(r,s,t,u) = 1.10 + 0.05*(t-1);
                E4(r,s,t,u) = 0.65 + 0.05*(u-1);
            end
        end
    end
end

%Black body radiation integration interval

dE = 0.001;
Emax = 1.000;
E_index = round(Emax/dE);

%Interpolating the power spectrum data

PP = spline(L,P,LL);
for i = 1:3741,                               %Setting minimum value at zero
    if PP(i) < 0,
        PP(i) = 0;
    end
end

```

```

end
end

%Populating differential elements of the solar spectrum photon flux
for i = 1:3741,

    if i == 1,
        dJs(i) = C*0.001*(PP(i)*LL(i)+PP(i+1)*LL(i+1))/(2*1.24);
    elseif i == 3741,
        dJs(i) = C*0.001*(PP(i-1)*LL(i-1)+PP(i)*LL(i))/(2*1.24);
    else
        dJs(i) = C*0.001*(PP(i-1)*LL(i-1)+PP(i+1)*LL(i+1))/(2*1.24);
    end
end

end

%Calculating each cell operating parameters

for r = 1:3, %E1 index
    for s = 1:3, %E2 index
        for t = 1:3, %E3 index
            for u = 1:3, %E4 index

% Calculating the photocurrent

                lower_1 = 1;
                upper_1 = round((1.24/E1(r,s,t,u) - 0.305)*1000.534);
                lower_2 = upper_1 + 1;
                upper_2 = round((1.24/E2(r,s,t,u) - 0.305)*1000.534);
                lower_3 = upper_2 + 1;
                upper_3 = round((1.24/E3(r,s,t,u) - 0.305)*1000.534);
                lower_4 = upper_3 + 1;
                upper_4 = round((1.24/E4(r,s,t,u) - 0.305)*1000.534);

                Js_1(r,s,t,u) = sum(dJs(lower_1:upper_1));
                Js_2(r,s,t,u) = sum(dJs(lower_2:upper_2));
                Js_3(r,s,t,u) = sum(dJs(lower_3:upper_3));
                Js_4(r,s,t,u) = sum(dJs(lower_4:upper_4));

%Setting up integration elements for radiation.

                dm_1 = 0.001*E1(r,s,t,u);
                m_index_1 = round(0.745*E1(r,s,t,u)/dm_1);
                dm_2 = 0.001*E2(r,s,t,u);
                m_index_2 = round(0.745*E2(r,s,t,u)/dm_2);
                dm_3 = 0.001*E3(r,s,t,u);
                m_index_3 = round(0.745*E3(r,s,t,u)/dm_3);
                dm_4 = 0.001*E4(r,s,t,u);
                m_index_4 = round(0.745*E4(r,s,t,u)/dm_4);

%Calculating the radiative current and operating point for cell 1

                for j = 3:m_index_1,

                    m_1(j,r,s,t,u) = 0.25*E1(r,s,t,u)+j*dm_1;

                    for k = 1:E_index,
                        dJ_1_out(k) =
(e_em+e_int)*5.033e7*dE*((E1(r,s,t,u)+dE*(k-1))^2*(exp(((E1(r,s,t,u)+dE*(k-1))-
m_1(j,r,s,t,u))/(8.616e-5*T))-1)^-
1+(E1(r,s,t,u)+dE*(k+1))^2*(exp(((E1(r,s,t,u)+dE*(k+1))-
m_1(j,r,s,t,u))/(8.616e-5*T))-1)^-1)/2;

```

```

end
J_1(j,r,s,t,u) = Js_1(r,s,t,u) - sum(dJ_1_out(1:E_index));

P_1(j,r,s,t,u) = m_1(j,r,s,t,u)*J_1(j,r,s,t,u);

%Determining the maximum power point for cell 1

if P_1(j,r,s,t,u) < P_1(j-1,r,s,t,u),
    if P_1(j-1,r,s,t,u) > P_1(j-2,r,s,t,u),
        J_1_max(r,s,t,u) = J_1(j-1,r,s,t,u);
        J_1_rad_max(r,s,t,u) = sum(dJ_1_out(1:E_index));
        V_1_max(r,s,t,u) = m_1(j-1,r,s,t,u);
        P_1_max(r,s,t,u) = m_1(j-1,r,s,t,u)*J_1(j-
1,r,s,t,u);
        m_1_index_max(r,s,t,u) = j-1;
    end
end

%Determining the open circuit voltage point for cell 1

if P_1(j,r,s,t,u) < 0,
    V_1_oc(r,s,t,u) = (m_1(j-1,r,s,t,u)+m_1(j,r,s,t,u))/2;
    m_1_index_oc(r,s,t,u) = j;
    break;
end

end
J_1(1:2,r,s,t,u) = J_1(3,r,s,t,u);

%Calculating the radiative current and operating point for cell 2

for j = 3:m_index_2,

    m_2(j,r,s,t,u) = 0.25*E2(r,s,t,u)+j*dm_2;

    for k = 1:E_index,
        dJ_2_out(k) =
(e_em+e_int)*5.033e7*dE*((E2(r,s,t,u)+dE*(k-1))^2*(exp(((E2(r,s,t,u)+dE*(k-1))-
m_2(j,r,s,t,u))/(8.616e-5*T))-1)^-
1+(E2(r,s,t,u)+dE*(k+1))^2*(exp(((E2(r,s,t,u)+dE*(k+1))-
m_2(j,r,s,t,u))/(8.616e-5*T))-1)^-1)/2;
    end
    J_2(j,r,s,t,u) = Js_2(r,s,t,u) - sum(dJ_2_out(1:E_index)) +
J_1_rad_max(r,s,t,u)*(e_int/(e_int+e_em));

    P_2(j,r,s,t,u) = m_2(j,r,s,t,u)*J_2(j,r,s,t,u);

%Determining the maximum power point for cell 2

if P_2(j,r,s,t,u) < P_2(j-1,r,s,t,u),
    if P_2(j-1,r,s,t,u) > P_2(j-2,r,s,t,u),
        J_2_max(r,s,t,u) = J_2(j-1,r,s,t,u);
        J_2_rad_max(r,s,t,u) = sum(dJ_2_out(1:E_index));
        V_2_max(r,s,t,u) = m_2(j-1,r,s,t,u);
        P_2_max(r,s,t,u) = m_2(j-1,r,s,t,u)*J_2(j-
1,r,s,t,u);
        m_2_index_max(r,s,t,u) = j-1;
    end
end

%Determining the open circuit voltage point for cell 2

if P_2(j,r,s,t,u) < 0,

```

```

        V_2_oc(r,s,t,u) = (m_2(j-1,r,s,t,u)+m_2(j,r,s,t,u))/2;
        m_2_index_oc(r,s,t,u) = j;
        break;
    end

end

J_2(1:2,r,s,t,u) = J_2(3,r,s,t,u);

%Calculating the radiative current and operating point for cell 3

for j = 3:m_index_3,

    m_3(j,r,s,t,u) = 0.25*E3(r,s,t,u)+j*dm_2;

    for k = 1:E_index,
        dJ_3_out(k) =
        (e_em+e_int)*5.033e7*dE*((E3(r,s,t,u)+dE*(k-1))^2*(exp(((E3(r,s,t,u)+dE*(k-1))-
        m_3(j,r,s,t,u))/(8.616e-5*T))-1)^-
        1+(E3(r,s,t,u)+dE*(k+1))^2*(exp(((E3(r,s,t,u)+dE*(k+1))-
        m_3(j,r,s,t,u))/(8.616e-5*T))-1)^-1)/2;
    end
    J_3(j,r,s,t,u) = Js_3(r,s,t,u) - sum(dJ_3_out(1:E_index)) +
    J_2_rad_max(r,s,t,u)*(e_int/(e_int+e_em));

    P_3(j,r,s,t,u) = m_3(j,r,s,t,u)*J_3(j,r,s,t,u);

%Determining the maximum power point for cell 3

    if P_3(j,r,s,t,u) < P_3(j-1,r,s,t,u),
        if P_3(j-1,r,s,t,u) > P_3(j-2,r,s,t,u),
            J_3_max(r,s,t,u) = J_3(j-1,r,s,t,u);
            J_3_rad_max(r,s,t,u) = sum(dJ_3_out(1:E_index));
            V_3_max(r,s,t,u) = m_3(j-1,r,s,t,u);
            P_3_max(r,s,t,u) = m_3(j-1,r,s,t,u)*J_3(j-
1,r,s,t,u);
            m_3_index_max(r,s,t,u) = j-1;
        end
    end

%Determining the open circuit voltage point for cell 3

    if P_3(j,r,s,t,u) < 0,
        V_3_oc(r,s,t,u) = (m_3(j-1,r,s,t,u)+m_3(j,r,s,t,u))/2;
        m_3_index_oc(r,s,t,u) = j;
        break;
    end

end

J_3(1:2,r,s,t,u) = J_3(3,r,s,t,u);

%Calculating the radiative current and operating point for cell 4

for j = 3:m_index_4,

    m_4(j,r,s,t,u) = 0.25*E4(r,s,t,u)+j*dm_2;

    for k = 1:E_index,
        dJ_4_out(k) =
        (e_em+e_int)*5.033e7*dE*((E4(r,s,t,u)+dE*(k-1))^2*(exp(((E4(r,s,t,u)+dE*(k-1))-
        m_4(j,r,s,t,u))/(8.616e-5*T))-1)^-
        1+(E4(r,s,t,u)+dE*(k+1))^2*(exp(((E4(r,s,t,u)+dE*(k+1))-
        m_4(j,r,s,t,u))/(8.616e-5*T))-1)^-1)/2;
    end

```

```

J_4(j,r,s,t,u) = Js_4(r,s,t,u) - sum(dJ_4_out(1:E_index)) +
J_2_rad_max(r,s,t,u)*(e_int/(e_int+e_em));

P_4(j,r,s,t,u) = m_4(j,r,s,t,u)*J_4(j,r,s,t,u);

%Determining the maximum power point for cell 4

if P_4(j,r,s,t,u) < P_4(j-1,r,s,t,u),
    if P_4(j-1,r,s,t,u) > P_4(j-2,r,s,t,u),
        J_4_max(r,s,t,u) = J_4(j-1,r,s,t,u);
        J_4_rad_max(r,s,t,u) = sum(dJ_4_out(1:E_index));
        V_4_max(r,s,t,u) = m_4(j-1,r,s,t,u);
        P_4_max(r,s,t,u) = m_4(j-1,r,s,t,u)*J_4(j-
1,r,s,t,u);
        m_4_index_max(r,s,t,u) = j-1;
    end
end

%Determining the open circuit voltage point for cell 4

if P_4(j,r,s,t,u) < 0,
    V_4_oc(r,s,t,u) = (m_4(j-1,r,s,t,u)+m_4(j,r,s,t,u))/2;
    m_4_index_oc(r,s,t,u) = j;
    break;
end

end
J_4(1:2,r,s,t,u) = J_4(3,r,s,t,u);

%Determinating series connected operating current

J_op_dummy(r,s,t,u) = min(J_1_max(r,s,t,u),J_2_max(r,s,t,u));
J_op_dummy(r,s,t,u) =
min(J_op_dummy(r,s,t,u),J_3_max(r,s,t,u));
J_op(r,s,t,u) = min(J_op_dummy(r,s,t,u),J_3_max(r,s,t,u));

if J_1_max(r,s,t,u) == J_op(r,s,t,u),
    J_1_op_index = find(J_1(:,r,s,t,u) == J_1_max(r,s,t,u));
    J_2_op_index = find(J_2(:,r,s,t,u) > J_op(r,s,t,u));
    J_3_op_index = find(J_3(:,r,s,t,u) > J_op(r,s,t,u));
    J_4_op_index = find(J_4(:,r,s,t,u) > J_op(r,s,t,u));
elseif J_2_max(r,s,t,u) == J_op(r,s,t,u),
    J_1_op_index = find(J_1(:,r,s,t,u) > J_op(r,s,t,u));
    J_2_op_index = find(J_2(:,r,s,t,u) == J_2_max(r,s,t,u));
    J_3_op_index = find(J_3(:,r,s,t,u) > J_op(r,s,t,u));
    J_4_op_index = find(J_4(:,r,s,t,u) > J_op(r,s,t,u));
elseif J_3_max(r,s,t,u) == J_op(r,s,t,u),
    J_1_op_index = find(J_1(:,r,s,t,u) > J_op(r,s,t,u));
    J_2_op_index = find(J_2(:,r,s,t,u) > J_op(r,s,t,u));
    J_3_op_index = find(J_3(:,r,s,t,u) == J_3_max(r,s,t,u));
    J_4_op_index = find(J_4(:,r,s,t,u) > J_op(r,s,t,u));
else
    J_1_op_index = find(J_1(:,r,s,t,u) > J_op(r,s,t,u));
    J_2_op_index = find(J_2(:,r,s,t,u) > J_op(r,s,t,u));
    J_3_op_index = find(J_3(:,r,s,t,u) > J_op(r,s,t,u));
    J_4_op_index = find(J_4(:,r,s,t,u) == J_4_max(r,s,t,u));
end

V_1_op(r,s,t,u) = m_1(max(J_1_op_index),r,s,t,u);
V_2_op(r,s,t,u) = m_2(max(J_2_op_index),r,s,t,u);
V_3_op(r,s,t,u) = m_3(max(J_3_op_index),r,s,t,u);
V_4_op(r,s,t,u) = m_4(max(J_4_op_index),r,s,t,u);

```

```

        P_op(r,s,t,u) = J_op(r,s,t,u)*(V_1_op(r,s,t,u) +
V_2_op(r,s,t,u) + V_3_op(r,s,t,u) + V_4_op(r,s,t,u));
        Eff_op(r,s,t,u) = P_op(r,s,t,u)/(C*976);

        Eff_op

            end
        end
    end
end

save FourJunctionSeries Eff_op -mat;
```